

Aberration Corrected *In-Situ* Electron
Microscopy of Nanoparticle Catalysts

Michael James Walsh

Submitted for the degree of
Ph D

University of York
Department of Physics

August 2012

Abstract

Catalysts play a crucial role in much of the world's energy, chemical processing and manufacturing technologies, whilst the development of more efficient, economical and durable catalysts is a prerequisite for the widespread introduction of future energy solutions such as fuel cells and biofuels. In this thesis, aberration corrected *in-situ* electron microscopy is used to provide atomic scale insights into the structure-property relationships of catalytic nanoparticles, as well as the deactivation mechanisms that affect them under reaction conditions.

When reduced to just a few nanometres, gold nanoparticles have been reported to show remarkable catalytic activity for the low temperature oxidation of carbon monoxide. In this size range, one of the most energetically favourable morphologies is the decahedra, and through direct measurements of atomic column positions, we quantify the substantial inherent surface strain that results from the non-space filling structure. Density functional theory calculations based on the experimentally observed atomic displacements predict significantly enhanced activity for CO oxidation due to strain induced electronic band structure modifications. This is a new mechanism for the reactivity of gold nanoparticles and provides further explanation of the surprising activities reported.

Exceptional catalytic properties for the water-gas shift reaction have been reported for cationic gold supported on ceria, although the nature of the active species and its interaction with the ceria support is uncertain. Atomic resolution Z contrast images reveal significant intensity increases for certain atomic columns', suggesting the cationic Au is in the form of highly dispersed single atoms that substitute for Ce sites.

The activation of Ni catalysts is observed *in-situ*, and a size dependent defect reduction mechanism is suggested. Upon reduction, the Ni particles are observed to sinter via an Ostwald ripening mechanism, and the effect of surface energetics is discussed to explain the variety of particle stabilities observed.

Contents

Abstract	2
Contents	3
List of figures	6
Acknowledgements	12
Declarations	13
1. Introduction	14
1.1 Overview of the thesis	15
2. An introduction to heterogeneous catalysis	16
2.1 Nanocatalysis	18
2.2 Activation: Formation of the active phase.....	20
2.2.1 Reduction of metal-oxides	21
2.3 Deactivation mechanisms	23
2.3.1 Sintering by particle migration and coalescence.....	25
2.3.2 Sintering by Ostwald ripening.....	28
3. Gold nanoparticles and catalysis	34
3.1 Catalysis by gold.....	34
3.1.1 Pollution and emission control.....	34
3.1.2 Chemical processing	36
3.1.3 The hydrogen economy and fuel cells.....	37
3.2 On the origin of gold's catalytic activity	38
3.2.1 Particle size effects.....	39
3.2.2 Low co-ordinated sites and the d band model.....	41
3.2.3 The effect of strain	46
3.2.4 Particle Morphologies	47
3.2.5 Role of the particle support	52
3.2.6 CeO ₂ based catalysis	54

4. Electron microscopy	61
4.1 Transmission electron microscopy	63
4.1.1 Limits to resolution	66
4.1.2 Spherical aberration correction	71
4.1.3 Aberration corrected atomic resolution imaging.....	72
4.2 Scanning transmission electron microscopy.....	73
4.2.1 Z contrast imaging in HAADF STEM	76
4.3 In-situ electron microscopy	78
4.3.1 Double aberration corrected environmental EM at York.....	79
5. Structural studies of gold nanoparticles	83
5.1 Sample preparation	83
5.2 Gold particle structures.....	84
5.3 The structural origin of gold nano-catalysis	86
5.3.1 The effect of strain on catalytic properties.....	87
5.3.2 Quantitative strain analysis through a real space approach.....	89
5.3.3 Calculations on the effect of strain on catalysis.....	96
5.4 Chapter conclusions.....	100
6. In-situ heating of model gold catalysts	101
6.1 Structural deactivation mechanisms	101
6.1.1 Loss of low co-ordinated sites.....	101
6.1.2 Relaxation of strain	104
6.2 Sintering of gold nanoparticles.....	106
6.2.1 Particle migration and coalescence	106
6.2.2 Ostwald Ripening.....	109
6.3 Chapter conclusions.....	111
7. Nano-ceria supported gold catalysts	113
7.1 Sample preparation	113
7.2 Structural analysis through electron microscopy.....	114
7.2.1 Imaging oxygen atoms in AC-HRTEM	117
7.2.2 Identifying the active site – single atom detection through HAADF STEM	120
7.2.3 Stability of the active site under simulated reaction conditions.....	124
7.3 Chapter conclusions.....	127

8. Activation and deactivation of Ni catalysts.....	129
8.1 Sample preparation and initial characterisation.....	129
8.2 Reduction of NiO to the active phase.....	133
8.2.1 Reduction of industrial NiO/Alumina catalysts.....	133
8.2.2 In-situ reduction of model NiO particles.....	136
8.2.3 Towards a reduction mechanism.....	139
8.3 Sintering of Ni catalysts	141
8.4 Chapter conclusions.....	148
9. Final remarks and further work.....	150
List of acronyms	154
List of symbols.....	156
Bibliography	159

List of figures

Figure 2.1 Schematic energy diagrams of simple catalytic and non-catalytic reaction pathways.....	17
Figure 2.2. Surface to volume ratio as a function of particle size.....	19
Figure 2.3. Schematic representation of sintering via particle migration and coalescence.....	26
Figure 2.4. The expected particle size distribution measured from a system that has sintered via particle migration and coalescence.....	27
Figure 2.5. Sintering by Ostwald Ripening, in which atomic or cluster transport occurs between particles, leading to the growth of larger particles at the expense of others.....	28
Figure 2.6. The expected particle size distribution measured from a system that has sintered via an Ostwald ripening mechanism, as predicted by the Lifshitz-Slyozov-Wagner model	30
Figure 3.1 CO oxidation turnover frequencies (TOFs) as a function of the Au cluster size supported on TiO ₂ . Reproduced from Lai <i>et al</i> [71].....	40
Figure 3.2 The correlation between binding energy for CO molecules and O atoms, with respect to the co-ordination number of Au atoms in a series of environments. Reproduced from Lopez <i>et al</i> [81].	41
Figure 3.3 Activity for CO oxidation at room temperature as a function of Au coverage. Reproduced from Chen <i>et al</i> [83].	42
Figure 3.4 Schematic model of Goodman's bilayer Au structures on TiO ₂ and on a single TiO _x layer. Reproduced from Rashkeev <i>et al</i> [78].	43
Figure 3.5 The desorption energy, E_d of an O ₂ molecule and the reaction barrier, E_r as a function of the average coordination number for Au/TiO ₂ and Pt/TiO ₂ . Reproduced from Rashkeev <i>et al</i> [78].	44
Figure 3.6. Narrowing and subsequent up-shift of the d band towards the Fermi level as a result of reducing co-ordination number.....	45
Figure 3.7 The dependence of binding energy of O on Au with the position of the d band relative to the Fermi level. Reproduced from Lopez <i>et al</i> [81].....	47

Figure 3.8 Various shapes exhibited by gold nanoparticles. Reproduced from Barnard <i>et al</i> [97].	48
Figure 3.9 A quantitative phase map of gold nanoparticles based on relativistic first principles calculations. Reproduced from Barnard <i>et al</i> [97].	52
Figure 3.10 Measured activities for CO oxidation at 273 K over Au-based catalysts on various supports as a function of the average particle size. Reproduced from Lopez <i>et al</i> [81] with data from [4, 46, 47, 81, 115-120].	53
Figure 3.11 XPS spectra observed before and after exposure of a AuO _x /CeO ₂ interface to a CO/H ₂ O mixture at 300°C. Reproduced from Wang <i>et al</i> [138].	57
Figure 3.12 Schematic of the proposed structural deactivation mechanism as a result of a reduced interaction with the support. Reproduced from Goguet <i>et al</i> [140].	58
Figure 3.13 Reaction mechanism and energetics of proposed CO oxidation promoted by an Au cation in an Au _x Ce _{1-x} O ₂ catalyst. Reproduced from Camellone <i>et al</i> [136].	59
Figure 4.1. Ray diagram of the TEM in imaging mode and diffraction mode. Switching between modes is done by changing the strength of the intermediate lens.	64
Figure 4.2. Ray diagram showing the effect of spherical aberration in the objective lens. High angle electrons entering a lens with spherical aberration are focussed more strongly than lower angle electrons, resulting in a distorted wavefront and limited resolution.	67
Figure 4.3. Contrast Transfer Function (CTF) of a conventional and C _s corrected TEM at optimum defocus. Reproduced from Gai and Boyes [187], with examples of bright atom contrast and dark atom contrast for TEM images of CeO ₂ nanoparticles.	70
Figure 4.4. Spherical aberration that results from cylindrically symmetrical lenses can be corrected by the addition of lower symmetry lenses with non-uniform magnetic fields.	71
Figure 4.5. Schematic diagram showing the probe formation and scanning process in the STEM	74
Figure 4.6. Schematic diagram of the double aberration corrected E(S)TEM at the University of York. Reproduced from Gai and Boyes [189].	80
Figure 4.7. Probe corrected atomic resolution HAADF ESTEM of a multiply twinned gold nanoparticle in hydrogen	81
Figure 4.8. Comparison of BF and HAADF ESTEM images of gold nanoparticles in hydrogen shows the advantage of Z contrast for imaging small particles and clusters.	81

Figure 5.1. Low Magnification image recorded at x10k showing gold nanoparticles on thin carbon film supported on a holey carbon grid.	84
Figure 5.2. Gold nanoparticles in the [110] orientation exhibiting single crystal and single twinned structures.	85
Figure 5.3. Icosahedral gold nanoparticles in or near the 2 fold , 3 fold, and 5 fold axes.	85
Figure 5.4. A decahedral Au nanoparticle in the [011] orientation with re-entrant facets at the twin boundaries and corresponding FFT and structure schematic.	86
Figure 5.5. An as-deposited gold nanoparticle with internal dislocation and surface steps. The dislocation results in streaking between the (111) diffraction spots.	87
Figure 5.6. A 3 nm Au decahedron with re-entrant facets.	88
Figure 5.7. Geometrical phase analysis of D_{xy} strain in both decahedral and single crystal structures. Scale bars indicate 2 nm.	89
Figure 5.8. Atomic column displacements are measured by identifying the x-y coordinates of each column and measuring the distances from one co-ordinate to the next, correcting for crystallographic orientation.	91
Figure 5.9. Distribution of nearest neighbour distances measured for a 3 nm decahedral particle and a 4 nm single crystal particle.	91
Figure 5.10 Average strain measured as a function of distance from the fivefold axis in a 3 nm decahedral particle.	92
Figure 5.11. AC-TEM images of a decahedral particle and single crystal particle with corresponding strain distributions. Scale markers indicate 2 nm.	93
Figure 5.12. 2D strain maps of both decahedral and single crystal structures.	94
Figure 5.13. GPA and in house strain maps of a Marks decahedral nanoparticle.	95
Figure 5.14. Strain measured as a function of distance from the fivefold axis for 3 nm and 9 nm Au decahedra.	96
Figure 5.15. Au c(4×8) (111) surface cell used for adsorption.	97
Figure 5.16. Initial configuration of the 15% strained gold slab used.	98
Figure 5.17. DFT calculations of the effect of strain on the adsorption energy for carbon monoxide.	99
Figure 5.18. Restructuring of 15% strained Au(111) surface upon CO adsorption calculated by DFT.	99

Figure 6.1. Re-arrangement of Au surface atoms towards high co-ordination planar {111} surface facets as a result of heating by 200kV electron beam.....	103
Figure 6.2. A cuboctahedral nanoparticle in the [011] orientation with atomically clean facets observed after heating to 600°C, with GPA analysis showing minimal strain.....	103
Figure 6.3 <i>In-situ</i> heating shows transition from icosahedral to decahedral structure at ~400°C, followed by shifting of the fivefold axis between 750°C and 800°C.	104
Figure 6.4. A decahedral particle with fivefold axis shifted close to the surface with average surface strain as a function of distance to the axis.....	105
Figure 6.5. ADF STEM image of a decahedral particle. Z contrast dependent intensity reveals maximum thickness at the off-centre fivefold axis.	106
Figure 6.6. <i>In-Situ</i> ADF-STEM of Au on Si ₃ N ₄	107
Figure 6.7. <i>In-Situ</i> TEM of Au on carbon	108
Figure 6.8. <i>In-Situ</i> TEM shows Au nanoparticles coalescence via the parallel alignment of {111} planes.	108
Figure 6.9. <i>In-Situ</i> TEM of 5 nm Au on Si ₃ N ₄ . Red circles indicate clusters < 1 nm...	109
Figure 6.10. Two small nanoparticles are observed to change structure as a result of heating. Evidence of the migration of single atoms is seen in (b), with single atoms appearing as black dots in the under focussed condition.....	111
Figure 7.1. TEM images showing the nano-crystalline ceria support.....	114
Figure 7.2. Electron beam induced surface atom movement of nano-ceria.....	115
Figure 7.3. TEM observations of metallic Au particles on ceria.	116
Figure 7.4. HAADF STEM identifies Au nanoparticles in the precursor sample.	116
Figure 7.5. STEM-EDX of the calcined sample shows the presence of metallic gold particles.	117
Figure 7.6. Revealing oxygen atoms through AC-HRTEM	118
Figure 7.7. Imaging of bulk oxygen atoms in CeO ₂ [001] with corresponding multislice simulation (inset).	118
Figure 7.8. Bulk oxygen atoms in CeO ₂ observed <i>in-situ</i> in Hydrogen.....	119
Figure 7.9. AC-HRTEM reveals bulk oxygen atoms, but surface oxygen atoms remain elusive from the single image.	120

Figure 7.10. Z contrast STEM is sensitive to thickness variations as well as increasing atomic number.	121
Figure 7.11. Atomic resolution HAADF-STEM imaging reveals bright columns, indicating the presence of single Au atoms.....	122
Figure 7.12. Small Au particle after <i>in-situ</i> heating to 400°C in H ₂	125
Figure 7.13. Bright contrast from some columns suggests some single Au atoms remain stable after heating in H ₂ to 400°C.....	126
Figure 7.14. Large intensity increase even with reducing crystal thickness, observed after heating in H ₂ to 400°C.....	127
Figure 8.1. XRD analysis identifies the Al ₂ O ₃ support as a mixed phase delta-theta alumina. TEM and HAADF STEM show the crystallite size of both the support and NiO particles present in the precursor.	130
Figure 8.2. AC-HRTEM with analysis of the corresponding FFTs clearly reveal the small particles are NiO, imaged here in the [011] and [001] orientations.	131
Figure 8.3. XRD analysis provided by JM shows the support is alpha alumina. HRTEM and HAADF STEM images show the large crystallite size of the α -alumina support as well as the distribution of the NiO.....	132
Figure 8.4. Very small NiO particles are observed on the surface of the α -alumina by AC-HRTEM, whilst other areas suggest the presence of highly dispersed layers of NiO on the support.	133
Figure 8.5. A sequence of images of the same particle at 600°C in vacuum taken 9 minutes apart, showing the transformation of NiO to Ni	134
Figure 8.6. The formation of discrete Ni particles is observed upon heating to 400°C in H ₂	135
Figure 8.7. Measurements of the observed lattice spacings confirm the particles are metallic Ni, whilst they are ~ hemispherical with a diameter of 2-5 nm.	136
Figure 8.8. Diffraction patterns obtained at room temperature and at 400°C in H ₂ of NiO powder provide unambiguous proof of the reduction of NiO to Ni.....	137
Figure 8.9. <i>In-situ</i> selected area diffraction clearly shows the reduction of NiO to Ni at ~400°C, as the NiO(111) ring disappears and the Ni(200) ring appears.	137
Figure 8.10. A large NiO particle after heating to 500°C in H ₂ . The particle is still NiO, however symmetry related defects are observed along the <111> directions. The defects appear to start from the surface, suggesting they are formed as a result of the reduction process.	138
Figure 8.11. Analysis of a particle heated to 600°C in vacuum shows that it is predominantly reduced Ni, however an internal section reveals lattice spacings	

greater than can be attributed to Ni, suggesting the presence of some remaining NiO.....	139
Figure 8.12. Sintering of Ni particles at 400°C over the course of 4 hours showed significant sintering and loss of surface area over the first 90 mins, followed by much improved stability.....	142
Figure 8.13. A reference area only exposed to the electron beam at the start and end points showed significant sintering as a result of the reaction conditions.	143
Figure 8.14. <i>In-situ</i> observations of the same area in H ₂ at 400°C reveal sintering through an Ostwald ripening process. The observations do not match the theoretical models of Ostwald ripening, as clearly more than just size determines the particle stability.	144
Figure 8.15. Particle size distributions of the same area as shown in figure 8.14 at t = 0 and t = 1 hour.	147
Figure 8.16. AC-HRTEM images after heating reveal the presence of some NiO remaining, suggesting that not all the NiO was reduced.....	148

Acknowledgements

The work in this thesis has been made possible by the contribution, both directly and otherwise, of many people. First and foremost I would like to thank my supervisors Profs Ed Boyes and Pratibha Gai, whose wisdom, infectious enthusiasm and generosity with time has been invaluable. I would also like to thank my industrial supervisors, Dr Mike Watson and Dr Dogan Ozkaya, for access to their expertise and providing me with an insight into the catalysis industry, as well as Johnson Matthey Plc and the EPSRC for funding.

I would especially like to thank Dr Kenta Yoshida, whose tuition, guidance and good company were a huge help during his time at York. I am also grateful to both Kenta and Dr Kuwabara for their help with DFT calculations, whilst Dr Mungo Pay's programming skills were essential for the development of our own strain analysis program and his generous help is much appreciated.

My research project has been all the more enjoyable due to the good company of many colleagues at the York Nanocentre, and I would particularly like to thank Michael and Luke for keeping me entertained during these past few years.

Finally, I would like to say a huge thank you to my parents, whose hard work, guidance and encouragement have afforded me every opportunity to pursue whichever path I chose. For better or worse, this has led to the production of this thesis, and I will be forever in their debt.

Declarations

I declare that the work presented in this thesis, except where otherwise stated, is based purely on my own research and has not been submitted for a degree in this or any other university. Parts of the work reported in this thesis have been previously published in:

M. J. Walsh, K. Yoshida, A. Kuwabara, M. L. Pay, P. L. Gai, E. D. Boyes. *On the Structural Origin of the Catalytic Properties of Inherently Strained Ultrasmall Decahedral Gold Nanoparticles*. Nano Letters, 2012. **12**. 2027-2031

M. J. Walsh, K. Yoshida, M. L. Pay, P. L. Gai, E. D. Boyes. *On the Effect of Atomic Structure on the Activity and Deactivation of Catalytic Gold Nanoparticles*. ChemCatChem. 2012. **4**. 1638-1644

M. J. Walsh, P. L. Gai and E. D. Boyes, *On the effect of atomic structure on the deactivation of catalytic gold nanoparticles*. J. Phys. Conf. Ser. 2012. 371. 012048.

M. J. Walsh, K. Yoshida, P. L. Gai and E. D. Boyes. *In-situ heating studies of gold nanoparticles in an aberration corrected microscope*. J. Phys. Conf. Ser. 2010. 241. 012058

P. L. Gai, K. Yoshida, C. Shute, X. Jia, M. J. Walsh, M. Ward, M. S. Dresselhaus, J. R. Weertman and E. D. Boyes. *Probing structures of nanomaterials using advanced electron microscopy methods including aberration-corrected electron microscopy at the Angstrom scale*. Microsc. Res. Tech. 2011.74. 664-70.

Signed

Michael James Walsh

August 2012

Chapter 1

Introduction

A recent report valued the total global demand on catalysts at US\$29.5 billion [1], and it is estimated that around 90% of the multi trillion dollar chemical industry is underpinned by catalysis. Demand in existing markets is expected to continue to grow in the coming years, and the increasing need for environmentally sustainable energy solutions requires catalysts that provide the requisite performance whilst remaining economically feasible; with both lower precious metal loadings and increased durability often needed.

Many heterogeneous catalysts consist of a precious metal, distributed in the form of nanoparticles on a support material. As such, the processes that govern their catalytic properties and subsequent deactivation occur as a result of atomic scale interactions between the particles, support and environment. Through understanding these processes it is possible to identify the nature of the active site, as well as the subsequent deactivation mechanisms that lead to fewer of them being available for reactions. Armed with this knowledge, catalysts can be designed specifically for certain reactions, with the composition, size and structure of the particles, as well their interaction with the support, all tuneable parameters that can be modified in order to present the desired electronic band structure with which the reactant molecules can interact. Through the optimisation of such parameters, more active, selective, durable and economical

catalysts can be produced; potentially enabling the commercial viability of alternative energy sources such as fuel cells and biofuels.

Electron microscopy promises to play a critical role towards achieving this goal, and direct characterisation with atomic resolution of the structure and chemical composition of nanomaterials is routinely possible. The recent widespread introduction of spherical aberration correctors has led to significantly improved resolution and interpretability of electron micrographs, as well as freeing up the space around the sample in the microscope. This has enabled the introduction of heating holders and a controlled gas environment with minimal effect on performance, allowing *in-situ* observations of the nano-catalysts under simulated reaction conditions with directly interpretable atomic resolution images. The work presented in this thesis is the application of this technique to several catalyst systems, and seeks to address questions regarding the origins of catalytic activity and the deactivation mechanisms that occur in the reaction environment.

1.1 Overview of the thesis

An introduction to the principles of heterogeneous catalysis is given in Chapter 2, followed by an overview of common activation and deactivation processes. Chapter 3 contains a literature review of the unusual case of gold catalysis, and various reported causes for the sudden change in gold's chemical properties when reduced to a few nanometres in size are discussed. Chapter 4 gives a brief overview of electron microscopy techniques, with particular emphasis on the methodologies relevant to the following results chapters. Chapter 5 reports results on the structure of gold nanoparticles in the catalytically active size regime, and a new mechanism based on band structure modifications that result from common particle morphologies is presented to further explain the reported enhanced activity. Chapter 6 shows results from *in-situ* studies on the effect of heating on gold nanoparticle structures, whilst the nature of the active site in Au/ceria catalysts is investigated using Z contrast imaging in Chapter 7. Chapter 8 presents results on the activation and deactivation mechanisms that affect industrial Ni based catalysts provided by Johnson Matthey Plc. Finally, Chapter 9 gives some concluding remarks and suggestions for further work.

Chapter 2

An introduction to heterogeneous catalysis

The term ‘catalysis’ was first coined in the 1830s by Berzelius [2], who along with Davy [3], Faraday [4] and others, pioneered the first experimental observations and understanding of the role catalytic materials can play in chemical reactions. As these first observations were of decomposition reactions, the word *catalysis* derives its origins from the Greek ‘kata’ - meaning ‘down’, and ‘lysis’ – meaning ‘to loosen’ or ‘to break’. The Oxford English Dictionary defines a catalyst in principle as:

*“A substance that increases the rate of a chemical reaction
without itself undergoing any permanent change.”*

Unfortunately, the second half of this definition is rarely true in practice, as we shall see later in this chapter. However, we first consider how the catalyst can dramatically increase the rate of the reaction, and therefore productivity, as well as possibly contributing to the selectivity of the reaction products.

Perhaps the most obvious role of the catalyst is to significantly increase the probability of interaction between two or more reactant molecules. By providing a localised surface upon which the molecules may reside for some time (known as residency time), the cross-section for interaction is greatly increased compared to the situation without a catalyst, in which the reactant molecules are highly mobile in their gas or liquid medium. However, perhaps most importantly, the presence of a catalyst opens up

alternative reaction mechanisms involving transitional states; in which one or more of the reactant molecules may bond with the catalyst. As a result of such bonding the adsorbed molecules have a lower associated potential energy, allowing for an alternative reaction pathway with reduced activation energy.

This process is shown schematically in Figure 2.1. In order for the reaction to proceed without a catalyst, a very large energy barrier must be overcome; and the height of this barrier is known as the activation energy, E_a . This large activation energy may prevent the reaction from occurring, or may mean very high temperatures are needed to enable the reaction. This is often impractical, expensive and likely to give little control over the selectivity of the reaction products.

However, the introduction of a catalytic surface allows for adsorption of a reactant molecule; creating a transitional state with reduced potential energy. Importantly, the activation energy required to overcome the energy barrier for this transitional state is significantly reduced from the case without a catalyst. Depending on the nature of the reaction, the catalysed reaction pathway will then progress through either further

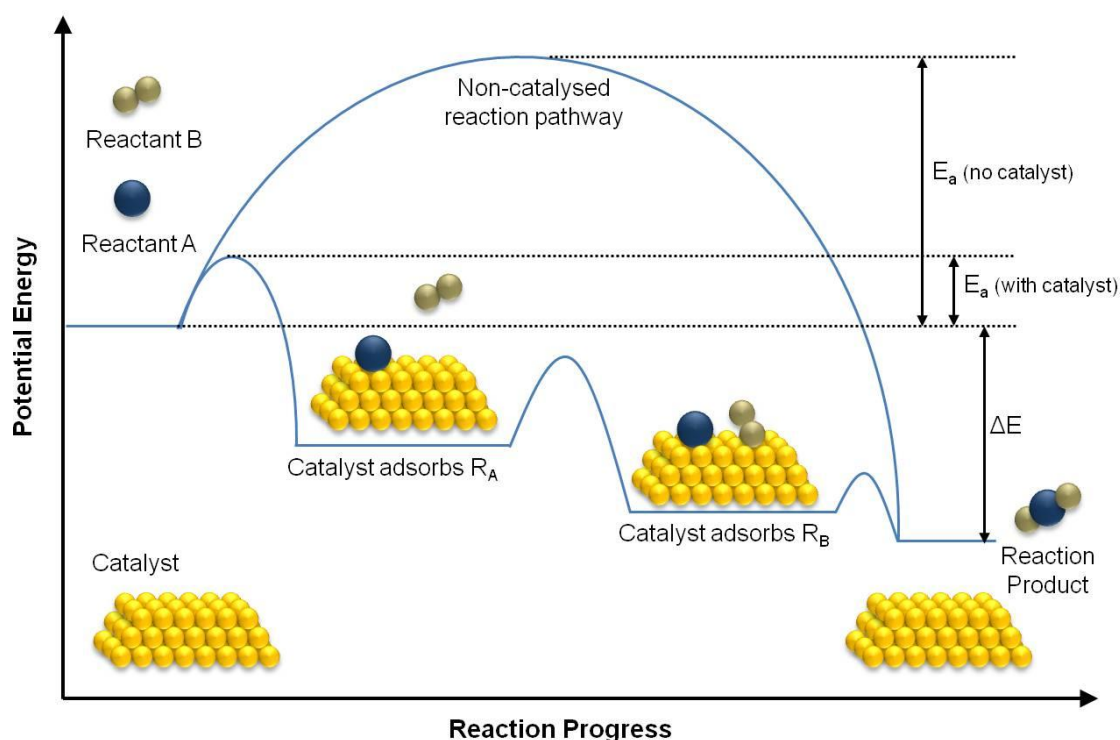


Figure 2.1 Schematic energy diagrams of simple catalytic and non-catalytic reaction pathways.

adsorption or dissociation of one or more of the reactant molecules, followed finally by desorption of the final reaction product. The reaction is energetically favourable, as the potential energy of the product is much less than that of the initial reactant molecules, and whilst each of the reaction steps has an associated activation energy, the total activation energy required with the catalyst is much less than in the case of the non-catalysed reaction. An appropriate catalyst can therefore greatly increase the rate of the reaction, whilst possibly allowing greater product selectivity by operating at lower temperatures and thereby altering the thermodynamics of the reaction.

Catalysis can be divided into two categories: homogeneous catalysis – involving a catalyst that is in the same phase as the reactants; and heterogeneous catalysis – involving a catalyst in a different phase to the reactants. Typically, a homogenous catalyst would be co-dissolved with the reactants into a solvent. In contrast, heterogeneous catalysts usually consist of a solid catalytic material, often dispersed on a support material, which then offers adsorption sites for incoming reactant molecules. Industrial reactions involving heterogeneous catalysis are generally gas-solid and liquid-solid, with the catalyst often consisting of a ceramic, or as is the case with the materials studied here, nanoparticulate metal distributed on a metal oxide or carbon support.

2.1 Nanocatalysis

The development of industrial heterogeneous catalysts has seen a trend towards smaller and smaller particle sizes, with the use of small nanoparticles common place in various applications for many years. This reduction in size of the metallic particles was largely driven by economic motives, as catalysts are often made up of platinum or other precious metals. If we consider the metallic particles to be spherical with radius r , the surface area to volume ratio is:

$$4\pi r^2 : \frac{4}{3}\pi r^3 \quad (2.1)$$

$$\frac{\text{Surface area}}{\text{Volume}} = \frac{3}{r} \quad (2.2)$$

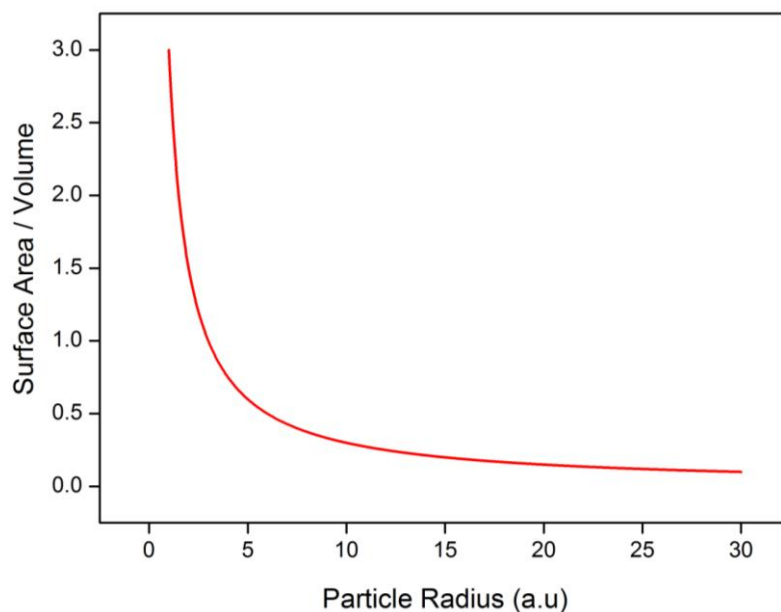


Figure 2.2. Surface to volume ratio as a function of particle size.

By plotting this relationship in Figure 2.2 we can clearly see the effect of particle size on the surface to volume ratio. Therefore reducing the individual particle size to just a few nanometres, the total surface area available for a given volume (and cost) of the precious metal catalyst is maximised.

The often complex nature of heterogeneous reactions – with many variables involved – makes identification of the catalysts properties with subsequent reaction mechanisms difficult. However, in recent years a wealth of both academic and industrial research has led to an understanding of additional effects that occur in the nano regime that may further modify and enhance catalytic properties. These effects are often intrinsic to the few nanometres size range and can go much beyond the added benefit of increasing the total surface area. Such nanoscale effects include quantum size effects, the role of under co-ordinated corner and edge atoms, modified interactions with the support and alternative surfaces and particle morphologies. All of these factors result in modifications to the particles electronic structure and therefore chemical properties, and many of these factors are considered further in this thesis. Perhaps the most striking example of this nanoscale effect is the curious case of gold, which goes from being the noblest of all metals in bulk form to an extremely active catalyst for many reactions when reduced to < 5 nm in size [5]; and this phenomenon will be used as a case study for detailed discussion of such size related effects in Chapter 3.

However, maintaining such small particle sizes under reaction conditions is a major challenge due to the inherent instability of small nanoparticles. Additionally, the chemically active phase of an as-prepared catalyst may not be stable under ambient conditions experienced during transport. Therefore before bringing the catalyst online, the catalyst must first go through an activation process to convert the precursor to achieve the required active and selective formulation.

2.2 Activation: Formation of the active phase

Synthesis of supported heterogeneous catalysts typically go through a catalyst precursor route, allowing ease of handling and transportation from point of manufacture to point of use, as the more robust precursor can be exposed to air and moisture. The precursor will then need to go through an activation process, such as heating in a suitable environment, to make sure the active phase is present before the catalyst is brought online.

Activation procedures vary depending on the nature of the reaction and catalyst. In some cases, the metal-oxide may be the active phase, therefore requiring oxidation of the metal to the active metal oxide. Other supported catalysts may be prepared as bulk alloys that then need to be transformed to the active phase. An example of this is the Raney nickel catalyst, which is prepared as a bulk Ni-Al alloy, before being activated by leaching with sodium hydroxide [6]. This activation process acts to remove most of the aluminium, leaving behind the active nickel supported on highly porous and high surface area aluminium [7].

The activation environment and temperature will help determine both the physical and chemical nature of the active species, and as such they play an important role in controlling the activity, selectivity and durability of the final catalyst. In some cases, such as in gold catalysis, the active phase may be stable under atmospheric conditions and therefore the catalyst requires no activation, whilst other catalysts may be activated by the reaction conditions themselves. However, many supported heterogeneous catalysts are prepared as metal-oxides, which are then activated by reduction to the active metal.

2.2.1 Reduction of metal-oxides

The reduction of the metal-oxide present in the precursor to the active metal is done by heating in a reducing environment, such as hydrogen. The temperature and mechanism by which this reduction takes place varies depending on the material and this can have significant consequences for the resulting catalyst. Higher activation temperatures may lead to thermal deactivation upon reduction and possible formation of non-active phases, whilst the mechanism through which oxygen is removed can lead to re-dispersion of the metal as well as determining the final particle size, morphology and interaction with the support.

Due to its industrial importance in hydrogenation and steam reforming reactions, the reduction of NiO to Ni is perhaps the most widely studied of the metal oxide reduction processes. Upon heating to above 300°C in hydrogen, NiO will reduce to metallic Ni through the following reaction:



In contrast other oxides, such as cobalt oxide, are known to reduce through an intermediate phase [8]:



Clearly the required formation of an intermediate phase will influence the kinetics of the reduction process as well as possibly affecting the physical form of the reduced metal [8]. Additionally, the significantly smaller volume of reduced metals, such as Ni and Co, from their metal-oxide counterparts can lead to significant contraction of the original particle volume upon reduction. For catalysts that undergo several redox cycles, this contraction and expansion can have major consequences for both the sizes and shapes of the particles as well as their interactions with the support. This was clearly shown through TEM analysis of reduced cobalt oxide [8] and *in-situ* TEM analysis of redox cycles in Ni catalysts [9]; both clearly showing the formation of voids inside the reduced metal particles.

Studies of model NiO(100) surfaces [10] have shown that upon heating and exposure to hydrogen, the reduction process goes through an induction period, during which

minimal metallic Ni is produced. In order for reduction to occur, the incoming H₂ must first be adsorbed and dissociated, allowing for hydrogen atoms to react with the oxygen. However, NiO(100) has negligible activity for the dissociation of H₂, meaning that the rate of reduction is very slow whilst little metallic Ni is present. Once some metallic areas are present, these then act to dissociate the H₂ and therefore enable the reaction to proceed more quickly.

Similar studies of a defective NiO surface [10] showed that the resulting induction period was much shorter, indicating surface defects may play a crucial role in the reduction process. The presence of oxygen vacancies results in much stronger adsorption of H₂ and a reduced activation energy for dissociation [10]. These vacancies therefore quickly facilitate the production of areas of metallic Ni; allowing reduction to proceed with a much shorter induction period. However, studies of nanoparticulate NiO [11] showed no sign of an induction period, suggesting that in more realistic catalytic systems, the high proportion of surface defects and under co-ordinated atoms found at corners, edges and surface steps may more readily dissociate the H₂, meaning that this may no longer be the rate limiting step.

In order to explain the wide range of activation energies for NiO reduction reported in the literature, Syed-Hassan *et al* [12] considered the effect of particle size on the resulting reduction mechanism and kinetics. They postulate that as well as the dissociation of H₂, the migration distance of H radicals may also be a rate determining step, possibly leading to different reduction mechanisms as a function of particle size. Upon production of an H radical at the H₂-Ni adsorption site, the radical will react with an oxygen atom, most likely forming an OH intermediate, before further reaction and subsequent desorption of the H₂O molecule [12]. This process will be facile at the particle surface, and indeed may remain so for very small particles. However, for larger particles the migration of the H radical into the particle, as required to reach the Ni/NiO reaction interface, may not be straightforward.

Although the activation energy for the breaking and reforming of Ni-H bonds is small, the potential large number of these steps required for the H radical to travel to the interior of a large particle to reach the NiO may result in a significant contribution to the

overall activation energy required for the reaction. Once reaching the NiO and forming OH, the hydroxyl species will then need to migrate back out of the particle to the surface before reacting with another H radical to form H₂O. This migration of the reaction product out of the particle will require a similar number of Ni-OH bond forming and breaking steps, again possibly leading to a significant contribution towards the overall activation energy [12]. The migration of species inside the particle is likely to lead to internal restructuring of the Ni, which again comes at an energy cost, although this may be partially compensated for by the formation of defects. Based on this reduction mechanism, we can expect very different activation energies for the reduction of very small NiO crystallites – for which the migration distance of H radicals is a significant proportion of the NiO particle radius – as opposed to much larger particles with a radius many times greater than the migration distance of the H or OH species.

Upon reduction, the metallic Ni species may be free to migrate on the support before reaching a nucleation site and forming small particles [13]. This mechanism explains the observed dispersion of metallic Ni upon reduction [11, 14], and allows the production of highly dispersed metallic particles, the size of which may be controlled by the original NiO loading and density on the support. However, in order to maintain the excellent catalytic properties of such highly dispersed small nanoparticles, they must remain stable in that form under reaction conditions.

2.3 Deactivation mechanisms

The deactivation of nano-catalysts is known to occur through a variety of mechanisms that can be mechanical, chemical or thermal in nature. Mechanical deactivation processes include fouling of the catalyst, resulting in the catalyst surface becoming covered in reaction by-products that are deposited over time. A well known example of mechanical deactivation is coking, in which carbonaceous material is deposited on the catalyst surface. Poisoning is an example of chemical deactivation and may result from irreversible chemisorption of either the reactant molecules, products or impurities in the reaction feed. When such strong chemisorption occurs, the energy barrier for desorption becomes too high, meaning that the active site remains blocked for subsequent reactions. As well as blocking the active site, knock on effects may include

modifications to the surrounding surface or the electronic band structure of neighbouring atoms, causing a further loss of active sites. Another example of chemical deactivation is the transformation of the catalyst away from the active phase. This may include oxidation of the active metal, reduction of the active metal-oxide or formation of alternative species as a result of reactions between the catalyst and a mixture of the reaction feed, the reaction products, any contaminants and the catalyst support. Depending on the nature of the metal, support and reaction conditions, a strong metal support interaction (SMSI) may also exist, and the strength of this interaction may lead to the support enveloping the metal particle, therefore preventing adsorption of reactant molecules. Both poisoning and fouling can be somewhat alleviated through careful control of the reaction feed – such as the use of filters and additional catalysts to remove any contamination – as well as regeneration of the catalyst in a suitable environment.

Thermal deactivation, or *sintering*, typically leads to an irreversible loss of catalytic surface area through the growth of the mean particle size, causing a loss of the surface to volume ratio of the catalyst. Furthermore, for size or structure sensitive catalysts, such as the gold nanoparticles discussed in the following chapter, sintering not only leads to a loss of surface area, but can easily cause further deactivation by changes in the particles' size or morphology away from the catalytically active range, and in the process also reduce the selectivity. Sintering to some extent is often an inevitable consequence of the elevated operating temperatures required for either activation of the active phase of the catalyst, or for the provision of sufficient energy to overcome the activation energy for the reaction. As such, sintering perhaps presents the biggest challenge to the manufacturing of highly active and selective catalysts that maintain the desired chemical properties for extended periods of time under reaction conditions.

The intrinsic instability of nano-catalysts is a result of their increased Gibbs free energy with decreasing particle size. This can be described by the Gibbs-Thomson relation, which states that the difference between the chemical potential of a metal atom in a particle of radius r , $\mu(r)$, and that of a metal atom in the bulk, $\mu(\infty)$, is:

$$\mu(r) - \mu(\infty) = \frac{2\gamma\rho}{r} \quad (2.5)$$

Where γ is the surface free energy of the metal particle, and ρ is the bulk volume per atom of the metal. Therefore the chemical potential of a given particle is inversely proportional to its radius, and an increase in the mean particle size will lead to a reduction in the total surface free energy of the system.

There are two main mechanisms by which the system will seek to minimise its surface area and therefore Gibbs free energy, and these are known as particle migration followed by coalescence; and Ostwald Ripening [15, 16]. These processes involve the diffusion of either entire particles or the inter-particle transport of atomic species across the support, and as such their rate and extent will be determined by the strength of the particle support interaction; the initial size, morphology and energetics of the particles; the local particle density; the support topography; and the local temperature and environment.

2.3.1 Sintering by particle migration and coalescence

The application of both temperature and a gas environment can induce movement of atoms and species on the surface of a metal particle. Over time, random accumulations of adatoms on one side of the particle can cause the particle to begin a random walk, which, given enough energy, will lead to the migration of the particle on the support in a Brownian type motion. If, as a result of this motion, two particles come into contact, they will coalesce in order to reduce their overall surface free energy. This leads to a loss of catalytically available surface area, as well as a potentially deleterious change in the form of the surfaces presented for reaction. If we consider spherical particles that do not wet the support, particle migration and coalescence can be thought of as being analogous to the motion of bubbles in a solid, allowing us to apply Gruber's model [17], which expresses the ability of particles to migrate as a particle diffusion coefficient, which for an FCC metal is:

$$D_p = 0.301D_s \left(\frac{d_{atom}}{r} \right)^4 \quad (2.6)$$

where d_{atom} is the atomic diameter, r is the particle radius and D_s is the diffusion coefficient of an atom on the surface of the particle, given by:

$$D_s = D_0 e^{\left(\frac{-Q}{RT}\right)} \quad (2.7)$$

where D_0 is a constant, Q is the activation energy for surface diffusion, R is the gas constant and T is the temperature [17]. However, the assumption in Gruber's theory that the particles are spherical is not generally true for small nanoparticles, as surface energy anisotropy will often lead to faceted surfaces. Additionally, depending on the type of particle and support, there will be some degree of particle-support interaction, often leading to approximately hemispherical particles with a contact angle θ , as shown in Figure 2.3. Therefore other models have been developed to include the effect of surface faceting, such as those presented by Willertz and Shewmon [18]; and Chen and Cost [19]. However, all of these models show the general result that the particle diffusivity decreases strongly with increasing particle size and particles become effectively immobile at larger sizes.

Providing there is sufficient coverage of the support with metal particles, the random migration of individual particles will lead to particle collisions and subsequent coalescence, as shown schematically in Figure 2.3. Coalescence between two particles is known to occur through the formation of a neck between the particles, which then facilitates movement of the centre of mass of the two particles to eliminate the neck, followed finally by restructuring of the particle towards a new minimum energy morphology [20, 21]. When considering the effects of crystal structure and anisotropic surface energies, an additional stage may be needed in order for the two particles to align their crystal planes to facilitate the formation of a neck between the two particles. The driving force for each of these stages is the minimisation of the overall surface free energy, which occurs initially by minimising the total surface area of the particles, followed by restructuring towards low surface energy facets. The time taken for each of

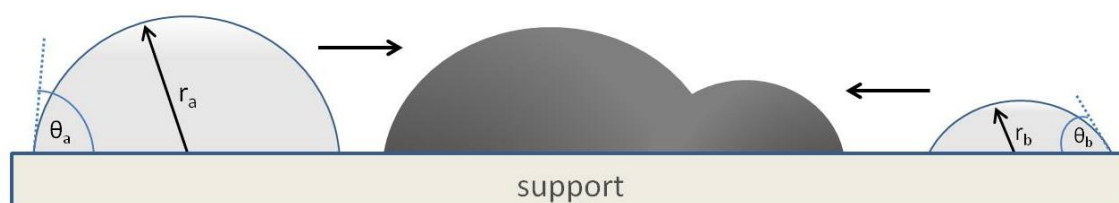


Figure 2.3. Schematic representation of sintering via particle migration and coalescence.

these stages is generally of the order of seconds or less [22], meaning that diffusion of the particle across the support is the rate limiting step in sintering by particle migration and coalescence.

The resulting particle size distribution measured from a sample that has sintered via a particle migration and coalescence process is usually log-normal in nature [23], as demonstrated in Figure 2.4. Empirical models, such as power-law expressions [24], can be used to empirically fit the measured data and extract values such as sintering rate constants and sintering order. The dispersion, dis , is defined as the fraction of metal atoms of the active phase exposed to the surface, and using dispersion instead of particle diameter, the general power law expression [25] gives the time dependence of metal dispersion as:

$$-\frac{d(dis/dis_0)}{dt} = k_s \left(\frac{dis}{dis_0} - \frac{dis_{eq}}{dis_0} \right)^m \quad (2.8)$$

where dis_0 is the initial dispersion, dis_{eq} is the dispersion at infinite time, k_s is the sintering rate constant and m is the sintering order.

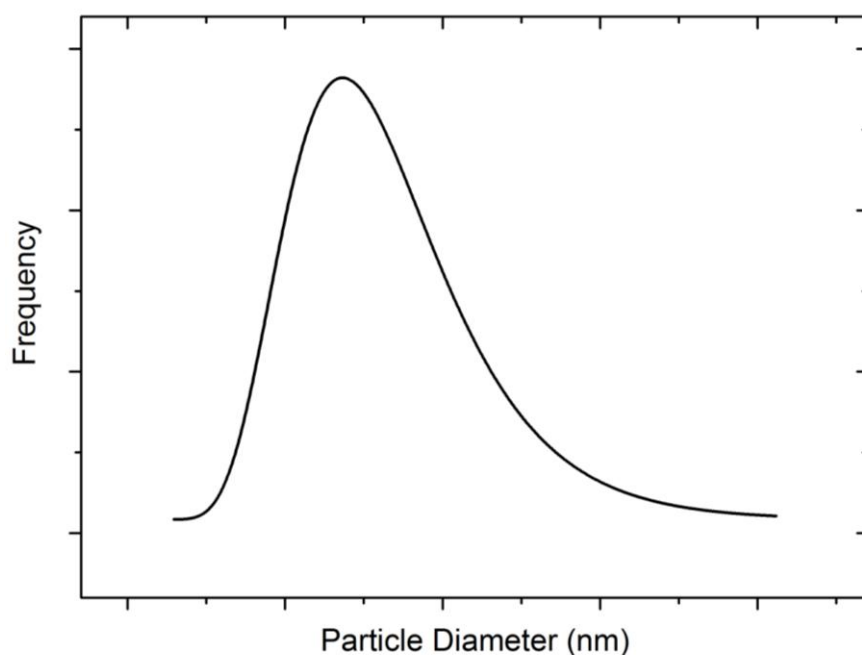


Figure 2.4. The expected particle size distribution measured from a system that has sintered via particle migration and coalescence.

Whilst such empirical laws can often provide good fits with experimental data, they clearly lack fundamental understanding of the key parameters involved, as well as no adjustable parameters that can be specific to the experimental conditions. In order to address this problem, Sehested *et al* [26] proposed an alternative model, based on density functional theory, to include terms related to the partial pressures of the gases present; sintering time; initial surface area; and metal loading. This model was developed specifically for application to Ni catalysts for steam reforming, but in principle can be adopted for a variety of catalysts in various conditions. However, fitting of experimental data to such a model can prove difficult, as it is not always possible to obtain accurate values for all the parameters needed. Whilst the model has been shown to agree with some experimental results [26], when applying to other systems, different values of the constant have been needed in order to fit the experimental data [27]. Additional factors may further complicate accurate modelling of observed sintering results, such as a particle size dependency of the contact angle, θ , between the particle and the support. Additionally, the inhomogeneous nature of the support may result in local variations of the particle-support interaction, possibly causing smaller particles to be anchored on defect sites. Such factors may lead to particle stabilities and diffusion coefficients very different to that predicted by equations such as Equation 2.6 [27].

2.3.2 Sintering by Ostwald ripening

Ostwald Ripening is a sintering mechanism that leads to a minimisation of surface free energy through the exchange of atomic species and clusters between particles, causing the growth of some particles at the expense of others, as shown schematically in Figure 2.5.

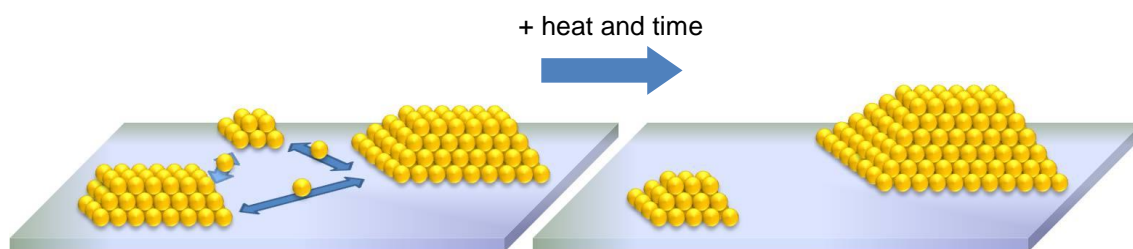


Figure 2.5. Sintering by Ostwald Ripening, in which atomic or cluster transport occurs between particles, leading to the growth of larger particles at the expense of others.

In order to reduce its own surface energy, a particle may emit either single atoms or small clusters of atoms, particularly those that are under co-ordinated and therefore causing a large increase in surface energy, such as adatoms, surface steps and kinks. Additionally, adsorption and desorption of reactant molecules and products may cause further surface rearrangements, leading to an increased migration of atomic species from the original particle. As we saw from the Gibbs-Thomson relation in equation 2.5, the free energy of the particle is inversely proportional to the particle size, meaning the smaller that particle, the less stable the surface atoms, therefore making atomic migration more likely. The result is a net transport of mass from the smaller to the larger particles, causing some particles to grow whilst others will shrink and may eventually disappear.

Due to the continuously decreasing frequency of small particles, sintering through an Ostwald ripening mechanism is expected to result in a particle size distribution described by the Lifshitz-Slyozov-Wagner (L-S-W) model [28, 29], in which the distribution has an extended tail on the small particle diameter range, as shown in Figure 2.6. Whilst simulations of sintering via Ostwald ripening do indeed result in the expected L-S-W distribution [30], experimental data does not always agree [31]. Further simulations with no prior assumption as to the sintering mechanism at work showed the development of a bimodal particle size distribution [32], which was attributed to some particle migration and coalescence occurring in the small particle size regime, followed by Ostwald ripening at larger particle sizes. The experimental observation of bimodal particle size distributions [33, 34] may therefore be a result of competitive sintering processes, or possible changes in the particle support interaction with decreasing particle size, leading to a trapping of small clusters and particles [27]. Other work, based on model two dimensional amorphous supports, did indeed reproduce the L-S-W distribution after extended periods (6 hours) of sintering [35].

However, a detailed study [36] of particle size distributions that result from a variety of sintering mechanisms on real catalyst samples showed that for all samples, the measured particle size distribution remained lognormal, independent of the reaction conditions or the sintering mechanism at work. Datye *et al* therefore concluded that sintering mechanisms could not be reliably inferred based on the resulting particle size

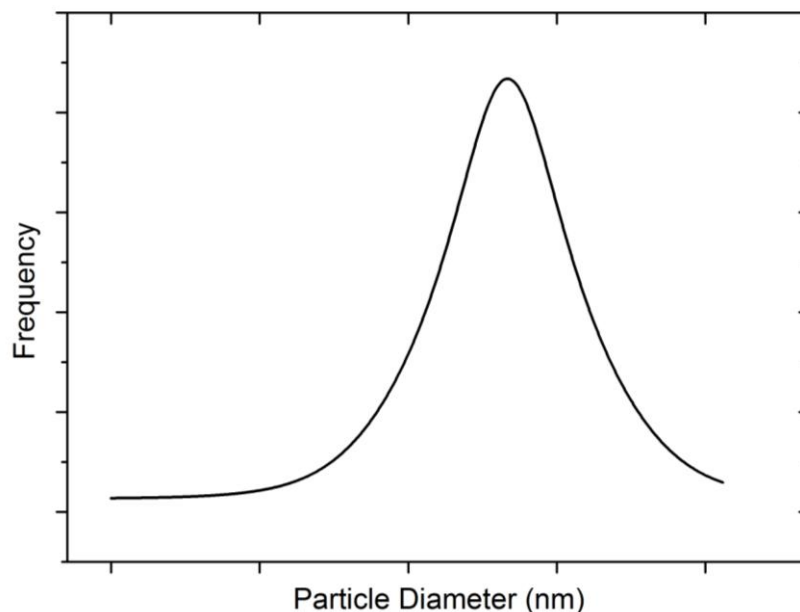


Figure 2.6. The expected particle size distribution measured from a system that has sintered via an Ostwald ripening mechanism, as predicted by the Lifshitz-Slyozov-Wagner model .

distribution [36]. Additionally, both the nature of the initial particle size distribution and the time dependency of the evolution of that distribution must also be carefully considered.

If we consider the Ostwald ripening process at the atomic scale, it is clear that the main factors governing the onset of migration of atoms from particles will be the energy barrier for surface atom movement – which will be given by the strength of the atom’s binding energy to the particle surface – and the strength of the interaction between the metal and the support. The relative importance of these parameters will determine the rate limiting step in the Ostwald ripening process, and as such Wynblatt and Gjostein [15, 22] suggest both an interface controlled model and a diffusion controlled model, depending on which is the more dominant. It has been shown that for typical metal catalysts supported on metal-oxides, the energy barrier for diffusion of a metal atom from a metal particle onto the substrate is around 5-10 times greater than the subsequent barrier for diffusion of the metal adatom on the substrate [37, 38]. Therefore the initial migration of the metal atom from the particle can be thought of as the rate determining step, and it is the ‘interface controlled’ model that is likely to be most applicable.

Wynblatt and Gjostein give the energy of a metal atom diffusing on the support as:

$$E_{Tot} = \Delta H_{sub} - (E_{ad} + E_{diff}) \quad (2.9)$$

Where ΔH_{sub} is the metal's bulk sublimation enthalpy, E_{ad} is the adsorption energy of a monomer on the support and E_{diff} is the diffusion activation energy of a monomer on the support. By substituting the Gibbs-Thomson relation into Wynblatt and Gjostein's interface controlled Ostwald ripening model [15], the rate of change of a particle's radius, r , is given by:

$$\frac{dr}{dt} = \left[\frac{2\gamma\rho K}{k_B T r^2} \right] \left(e^{-\frac{E_{Tot}}{k_B T}} \right) \left[\frac{r}{r^*} - 1 \right] \quad (2.10)$$

where, k_B is Boltzmann's constant, T is the temperature of the substrate and K is a system specific parameter to include the particle support interaction, and is defined as:

$$K = \left[\frac{(2 \sin \theta) v_p \rho}{[(2 - 3 \cos \theta + 3 \cos^3 \theta)(a)]} \right] \quad (2.11)$$

where v_p is a prefactor determining the rate at which a metal atom moving on the surface of a particle may diffuse onto the support, a is the particle's interatomic spacing and θ is the contact angle between the particle and the support, which in turn is a measure of the strength of the particle-support interaction. r^* is the critical radius, above which the particle will grow, and below which the particle will shrink. When the total mass of the metal is conserved, r^* can be shown to be equal to the mean particle diameter, which is time dependent [39].

Crucially, Campbell *et al* [40] go on to show that in the small nanoparticle size regime, the metal atoms energy does not scale linearly with size, as predicted by the Gibbs-Thomson relation. They show experimentally that the surface energy of metal nanoparticles increases significantly as the particle radius decreases below a few nanometres, and attribute this to the non-negligible contribution of under co-ordinated corner and edge atoms in this size range. Therefore, the Wynblatt-Gjostein model [15] will significantly over-estimate the stability of particles just a few nanometres in diameter, as the Gibbs-Thomson relation is no longer directly applicable. This in part explains the often large discrepancies between sintering models and the experimental

data, and further highlights the flaws in assuming sintering mechanisms based on resulting particle size distributions [41].

Modifying Wynblatt and Gjostein's interface controlled model to include a non-linear Gibbs-Thomson relation [40], equation 2.10 becomes [41]:

$$\frac{dr}{dt} = \frac{K_{int}}{r} \left[\exp\left(\frac{2\gamma\rho}{r^*k_B T}\right) - \exp\left(\frac{2\gamma\rho}{rk_B T}\right) \right] \quad (2.12)$$

where K_{int} is:

$$K_{int} = \frac{2v_p\rho \sin\theta}{a(2 - 3\cos\theta + \cos^3\theta)} e^{-\frac{E_{Tot}}{k_B T}} \quad (2.13)$$

Challa *et al* [42] recently reported Ostwald ripening of Ni nanoparticles on MgAl₂O₄ through *in-situ* TEM observations under simulated methane steam reforming conditions (3.6mbar of H₂:H₂O at 750°C). They observed small Ni particles to be stable for extended periods of time, before rapidly shrinking and disappearing, and attribute the sudden decrease in size as occurring once the particle goes below a critical value (~ 1.5 nm).

By considering a small nanoparticle that will shrink with time, and assuming the number of atoms being received by the shrinking nanoparticle is negligible, Challa *et al* simplify equation 2.12 to give the rate of decay of an individual nanoparticle as [42]:

$$\frac{dr}{dt} = -\frac{K_{int}}{r} \exp\left(\frac{2\gamma\rho}{rk_B T}\right) \quad (2.14)$$

By either assuming or fitting reasonable (but constant) values for the parameters in the K_{int} term, equation 2.14 can be shown to agree with the experimentally observed particle decay rate. However, a few other particles observed did not agree with the same theoretical treatment, with one small particle appearing to be significantly more stable than its larger neighbour [42].

The observed stability of some small nanoparticles, as compared with others of a similar or even larger size that are less stable is yet to be explained in the literature. Challa *et al* [42] acknowledge that the assumption of θ as being constant will not always be valid, as

it can be expected to vary with either particle size [43] or as a result of any local variations in the support. Additionally, it can be expected that the v_p term in equation 2.11 will play a crucial role, as it will determine the rate at which a metal atom will leave the surface of the nanoparticle. Clearly, this energy barrier will be equal to the binding energy of the atom in question, and will therefore be determined by the local atomic surface structure of the particle.

By comparing the parameters governing sintering by both particle migration and coalescence and Ostwald ripening we can expect certain conditions to favour one or other of the sintering mechanisms. By increasing the strength of the particle-support interaction, the particles can become well anchored on the support and therefore unlikely to sinter through particle migration and coalescence. However, such an increased particle-support interaction is likely to increase the v_p term in equation 2.11 and 2.13, as there will be a stronger attraction between the particle's surface atoms and the support, with the net result being more atoms migrating away from their original particle and therefore sintering through Ostwald Ripening. What is abundantly clear is that particle radius is by no means the only variable in nanoparticle sintering, and insights at the atomic scale, alongside further consideration of the driving forces for atomic migration are needed in order to more fully explain the instability of small metal nanoparticles. Such developments could lead to more stable and durable nanocatalysts that would not only save huge costs associated with current catalyst deactivation, but may also open up new possibilities for highly active catalysts that are currently too unstable for viable commercial use.

Chapter 3

Gold nanoparticles and catalysis

3.1 Catalysis by gold

Whilst the catalytic properties of platinum and other transition metals have been known since the first concepts of catalysis were put forward in the early 1800s [4], it wasn't for another 150 years that the surprising catalytic properties of gold were first reported. Traditionally believed to be an inert noble metal, the pioneering work of Haruta *et al* [44] and Hutchings [45] showed that when reduced to the nanoscale, gold had some exceptional catalytic properties, and this has since triggered a wealth of research into the area. Haruta and colleagues [5, 46-49] went on to show that when reduced to less than 5 nm in diameter, gold is in fact a more active catalyst than other metals for many applications. These range from automotive and industrial emission control, chemical processing, use in the hydrogen economy and fuel cells.

3.1.1 Pollution and emission control

In the current automotive industry three way catalysts (TWC) based on platinum group metals (PGM), particularly platinum, palladium and rhodium, are used on a global scale to good effect [50]. However such catalytic systems lack low temperature start up and this, coupled with idling problems, causes the catalyst monolith not to operate until the light-off temperature of $\sim 300^{\circ}\text{C}$ required for oxidation of hydrocarbons is reached. Therefore improvements are needed to the low temperature start up performance. The

work of Haruta's group showed that gold nanoparticles less than 5 nm in diameter exhibited exceptional catalytic activity for CO oxidation, even at low temperatures [46]. However, the relatively low melting point of gold (1064°C compared to 1769°C of platinum, with this temperature significantly reduced for nanoparticles) means that it is not really suitable for use in TWCs themselves as stoichiometric-burn exhaust temperatures typically exceed 600°C [51], causing the gold nanoparticles to sinter and deactivate. One possible solution is the use of gold based catalysts in conjunction with PGM based TWCs to overcome the cold engine problem. If improvements can be made to the stability of gold catalysts, there is further potential for use in diesel exhaust systems, with typical operating temperatures between 80-230°C and reaching a maximum of approximately 440°C [52, 53].

Conventional PGM based TWC systems are also capable of reducing NO_x to N₂ using unburnt CO, H₂ or hydrocarbons. However petrol and particularly diesel engines often operate under lean burn conditions, where there is 10-20% more oxygen present than is required to combust all the fuel. Under such conditions the reduction of NO_x by conventional means is less effective. Gold based catalysts have shown activity for the lean burn reduction of NO_x through a wide range of temperatures [51] and show a greater selectivity for NO_x reduction to N₂ than platinum based catalysts [54].

The oxidation of CO and nitrogen containing odour compounds at room temperature by catalytic gold nanoparticles offers further applications in air purification and removal of malodours. This is a use for which gold is particularly suited, due to its high activity at low temperatures [5].

Pollution and emission control is perhaps the greatest commercial area of interest in gold nanoparticle catalysis, with the comparatively lower price of gold to platinum providing strong economic benefits alongside the environmental ones previously outlined. However the stability of gold based nano-catalysts needs to be improved before widespread implementation in industry is possible, and this may be achieved through further understanding of the active site, more sophisticated supports to prevent sintering and possibly alloying or use in conjunction with other metal to provide bi-functionality.

3.1.2 Chemical processing

There are many examples in which the catalytic properties of gold nanoparticles can be used for a wide variety of chemical processing. One of the first demonstrations of this was by Hutchings, who showed gold catalysts were about three times more active than commercial mercuric chloride catalysts used in the conversion of acetylene (C_2H_2) to vinyl chloride ($H_2C:CHCl$) for the production of polyvinyl chloride (PVC) [55, 56].

The oxidation of methane (CH_4), propane (C_3H_8) and propene (C_3H_6) can be achieved using gold based catalysts, with gold shown to match the activity of commercial platinum catalysts [57]. Also, gold catalysts have been shown to be uniquely selective for the partial oxidation of propene to propene oxide – used for the production of polyurethanes – with certain conditions giving rise to 99% selectivity to propene oxide [58]. It is clear that the nature of catalysis by gold is dependent on particle size, with further work by Haruta's group showing oxidation to propene oxide by particles larger than 2 nm in diameter, whereas reduction to propane occurs below this size [59].

Production of hydrogen peroxide ($H_2 + O_2 \rightarrow H_2O_2$) is currently achieved on a large scale by the sequential hydrogenation and oxidation of anthraquinone ($C_{14}H_8O_2$) or a related alkyl derivative, and demands are steadily increasing as an environmentally friendly alternative to chlorine is sought. However, hydrogen peroxide is a hazardous material, leading to high costs in transportation from point of manufacture to point of use. Gold and Au/Pd alloy catalysts [60] offer a potential solution for the safe, cost effective local production of H_2O_2 .

Other areas of chemical processing in which the use of gold based catalysts are being investigated include selective hydrogenation of dienes in the presence of monoenes [49], the oxidation of glucose to the widely used food additive gluconic acid [61] and the conversion of alkynes (C_nH_{2n-2}) to alkenes (C_nH_{2n}) [62]. However, for many of the reactions mentioned above, further understanding of the cause of the nanoparticle's activity and selectivity is needed in order to produce efficient and economical catalysts for a given reaction, whilst deactivation processes need further study in order to improve catalyst durability.

3.1.3 The hydrogen economy and fuel cells

The potential use of fuel cells within a hydrogen based economy would greatly reduce both fossil fuel consumption and CO₂ emissions from the transportation industry. However for this to become practical there are many remaining technical barriers, including the need for a vast reduction of production cost and an increase in the durability and performance of fuel cells. The US Department of Energy's Fuel Cell Report [63] highlighted the need for a significant reduction in the cost of fuel cell catalysts. Gold nanoparticles offer several advantages over conventional catalytic systems, with their unique properties showing promise for greater selectivity and activity at lower temperatures, whilst the relatively low cost of gold compared to platinum would significantly reduce the current overall system cost.

Hydrogen for fuel cells is typically produced by steam reforming an organic fuel such as methane, followed by the water gas shift (WGS) reaction:



The thermodynamics of this reaction means that a smaller ratio of CO to H₂ will be produced as the temperature is reduced. As the platinum catalysts currently used inside the fuel cell are easily poisoned and deactivated by CO, a low operating temperature during the WGS reaction is desirable. Catalysts for the low temperature WGS reaction in fuel cells not only need to be highly active but also need to be able to endure repeated start up and shut down cycles; thus making traditional copper based catalysts used in industry unsuitable for fuel cell applications. Since early work showed that catalysts of gold supported on Fe₂O₃ (Au/Fe₂O₃) could exceed the activity of commercial copper systems [52], much research has been done in the area, with the current emphasis being on Au/CeO₂ catalysts, due to their high activity and greater stability [64-66].

As gold is a highly effective catalyst for the oxidation of CO, it has great potential for the removal of CO impurities from the hydrogen feed in fuel cells. In polymer electrolyte membrane (PEM) and other low temperature fuel cells, CO is preferentially adsorbed, often leading to poisoning of the Pt catalyst. In order to counter this, small

amounts of oxygen are added to the hydrogen stream and passed over a catalyst to oxidise the CO before the stream reaches the fuel cell stacks. As gold shows exceptional activity for the preferential oxidation of carbon monoxide (PROX), even at low temperatures, the use of gold based catalysts would allow PEM type fuel cells to run more efficiently whilst mid-temperature fuel cells could operate at reduced temperatures, leading to greater durability.

Research has shown that gold based catalysts are capable of selective carbon monoxide oxidation (SCO) in hydrogen rich gas [67]. Kung *et al* went on to show that the presence of hydrogen during SCO actually prevented deactivation, and that deactivated catalysts could be regenerated by exposure to hydrogen at room temperature [68]. These results, coupled with the low temperatures required, suggests that stability and sintering of the particles should not be a serious issue for SCO in hydrogen streams in PEM fuel cells. However, clarification in the literature is required on the effect of the support and particle size in relation to activity, whilst the nature of the active site for such reactions is still not fully understood.

A further potential application of catalytic gold nanoparticles within fuel cell systems is as an alloy with platinum as an electrocatalyst. A Pt/Au alloy could potentially create unique bi-functional catalytic properties, with the platinum acting as the main catalyst for the fuel cell reaction, whilst the gold would oxidise any carbon monoxide present. Such a bimetallic catalyst could significantly increase the lifetime of the platinum by preventing poisoning by carbon monoxide, whilst the current prohibitive cost of the fuel cell catalyst could be reduced by a reduction in the required platinum loadings [51].

3.2 On the origin of gold's catalytic activity

Although supported gold nanoparticles have been one of the most widely studied catalytic systems in recent years, agreement is yet to be reached in the literature on what exactly causes the exceptional catalytic properties of gold nano-catalysts. Understanding exactly where the active sites are, what role the particle structure has and what role the support plays has proven difficult, with several conflicting theories having

been put forward. However one thing that is well accepted is that particle size plays a crucial role.

3.2.1 Particle size effects

It has long been known that gold particles must be less than around 5 nm in size for them to achieve catalytic activities suitable for commercial use. As the particle size is reduced down to the few nanometres range, several factors give rise to their striking difference in chemical properties from bulk gold. Firstly, as the average particle size becomes smaller, the surface to volume ratio of the system is increased, thus providing more reaction sites for a given total volume of catalytic material. However, gold's surprising change in chemical properties cannot be attributed to just an increased surface to volume ratio, and intrinsic nanoscale effects must also be considered. A particle size of just a few nanometres leads to an increased proportion of under coordinated surface atoms – with fewer inter-atomic bonds – resulting in a reduced overlap of electron orbital's [69]. This causes the particle's constituent atoms, and particularly those at the surface, to begin to behave more as individual atoms rather than as part of a metallic bulk. As a result, the introduction of a band gap and therefore a metal-insulator transition can be expected for particles below approximately 3 nm in diameter and 1 nm in height [70]. This quantum size effect has also been shown by Haruta's group [71] and similar effects have been observed in Pd and Ag particles. Work by Goodman's group on the oxidation of carbon monoxide by gold catalysts (see Figure 3.1) showed that the activity, described as turnover frequency (TOF):

$$TOF = \frac{\text{product molecules}}{\text{total gold atoms} \times \text{seconds}} \quad (3.3)$$

was strongly sensitive to particle size, with a peak activity occurring at 3.2 nm [72, 73].

Due to the strong correlation in peak activity and the metal-insulator transition, it was proposed that quantum size effects were the cause of the strong sensitivity of activity on particle size, with particles that exhibit a large band gap unlike bulk metal being particularly active for the catalysis of CO oxidation [70].

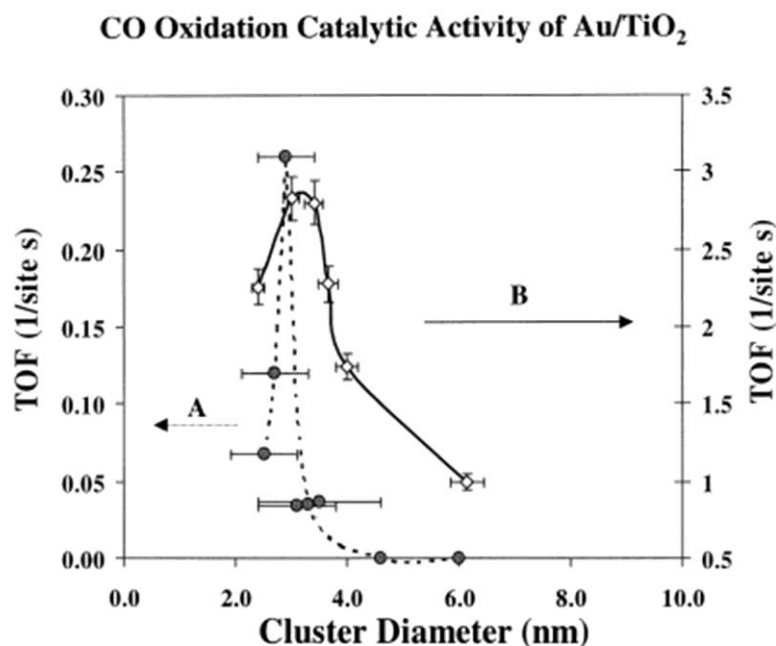


Figure 3.1 CO oxidation turnover frequencies (TOFs) as a function of the Au cluster size supported on TiO₂. (A) The Au/TiO₂ catalysts were prepared by a precipitation method [45]. (B) The Au/TiO₂ catalysts were prepared by vapor-deposited Au atoms on planar TiO₂ films on Mo(100). Reproduced from Lai *et al* [72].

However, traditional particle size analysis techniques such as conventional TEM may not be sensitive to detecting small clusters or single atoms present in the catalyst [74]. In contrast, more recent work by Herzing *et al* [75] using aberration corrected HAADF STEM reported a direct correlation of activity for CO oxidation with the presence of bilayer clusters each containing approximately 10 atoms, supported on iron oxide. They therefore suggest that these bilayer clusters, as opposed to single atoms, monolayer clusters or larger particles, are the key active species for CO oxidation. The bilayer clusters provide an abundance of low co-ordinated surface atoms, as well as multiple adjacent active sites that they claim are required for the simultaneous adsorption of CO and O atoms, O₂ or H₂O molecules. While alternative effects that may occur as a result of a differing supporting material or under different reaction conditions are not considered in their study, clearly the catalytic properties of small nanoparticles are strongly influenced by particle size and structure.

3.2.2 Low co-ordinated sites and the *d* band model

Other properties that vary as a function of particle size have been proposed as the active site key to catalytic activity. In particular perimeter sites [76], particle-support interfaces [77] and low co-ordinated edge atoms [78, 79] have all been suggested to be the cause of the catalytic properties of small gold nanoparticles. Strong support for under co-ordinated atoms providing the key active sites comes from both theoretical and experimental evidence that shows CO and O₂ can chemisorb on rough or stepped Au surfaces, but cannot on planar Au surfaces [80, 81]. Lopez *et al* have described the chemical activity of gold as being strongly dependent on the co-ordination number of gold atoms, and have shown that the strength of the Au-CO and Au-O bond varies with Au co-ordination number (see Figure 3.2) [82]. They explain this by the weak bonding between Au(111) and O relative to the stronger interaction between O and Au atoms of lower co-ordination number found at steps and corners of small particles. The atoms in the Au(111) surface have *d* states that are too low in energy to interact with the O 2*p* valence states, and are therefore unable to dissociate O₂. In contrast, the lower co-ordination atoms have *d* states that are closer to the Fermi level, resulting in a stronger interaction and therefore reaction. Furthermore, Zanella *et al* [83] correlated a loss of activity as a result of increasing calcination temperature with a greater proportion of strongly faceted particles that exhibited fewer low co-ordination surface sites.

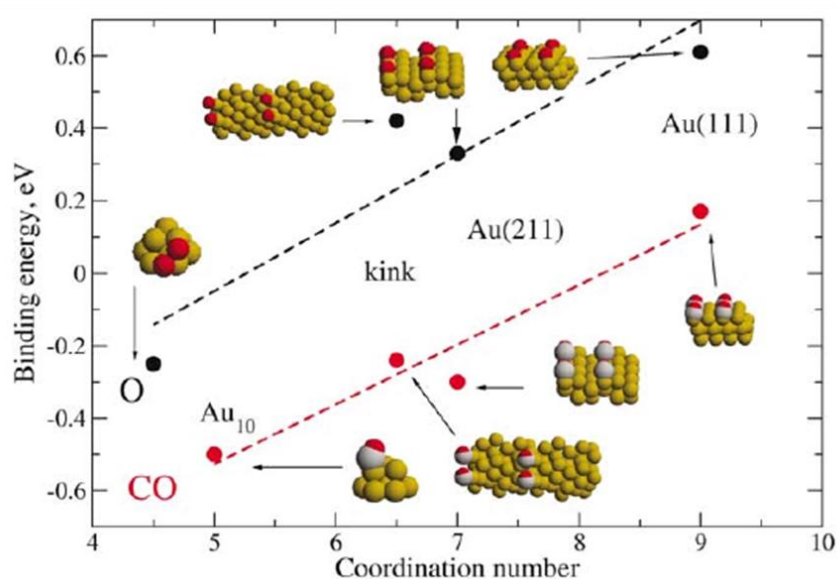


Figure 3.2 The correlation between binding energy for CO molecules and O atoms, with respect to the co-ordination number of Au atoms in a series of environments. Reproduced from Lopez *et al* [82].

Further work by Goodman's group reported exceptional catalytic activities for the oxidation of carbon monoxide by gold films. They grew two Au films, a (1x1) monolayer and a (1x3) bilayer, that completely wet an ultrathin titanium dioxide surface, supported on a Mo (112) surface, as shown in Figure 3.3. Their results showed that the bilayer produced a TOF 45 times greater than the previous most active Au/TiO₂ catalyst [84]. While they did not go on to describe the exact cause of the high activity of the Au bilayer, their results did show that TiO_x cannot be directly involved in the bonding of CO or O₂, as the Au overlayer precludes access to the Ti cation sites. They also claimed that the co-ordination numbers of atoms in the monolayer and atoms in the top layer of the (1x3) bilayer structure were the same, thus arguing that a combination of first and second layer gold sites is required to promote activity.

However Rashkeev *et al* [79] went on to explain that the co-ordination numbers of the surface atoms of the two films were in fact different, with this being the cause behind the vastly increased activity. Their schematic model of such structures, seen in Figure 3.4, shows Au atoms on a TiO₂ substrate with a row of O vacancies underneath each

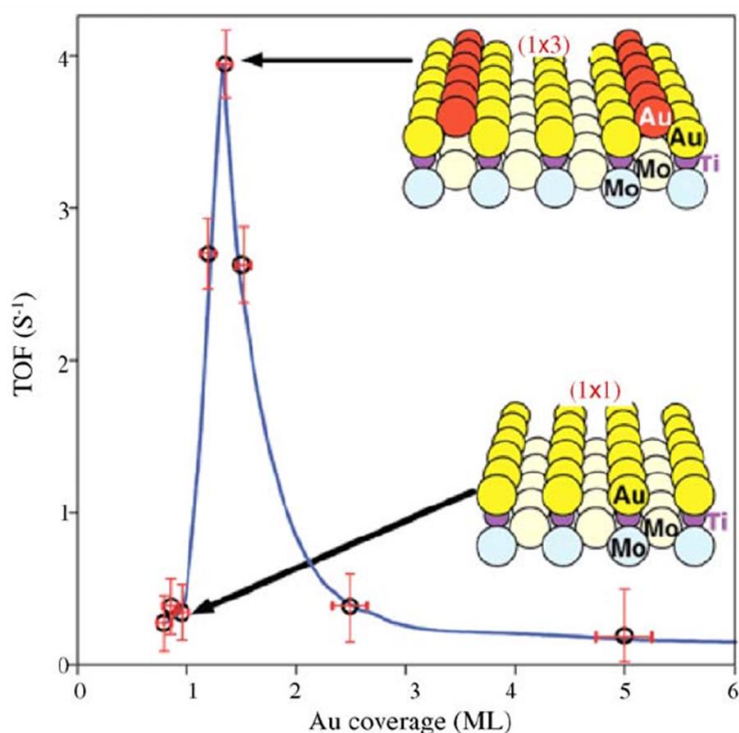


Figure 3.3 Activity for CO oxidation at room temperature as a function of Au coverage above the monolayer on Mo(1 1 2)-(8 × 2)-TiO_x. Insets: schematic models for the (1 × 1) and (1 × 3)-Au/TiO_x surfaces. Reproduced from Chen *et al* [84].

first layer Au chain. The top layer of gold atoms has a co-ordination number of 6, suggesting lower catalytic activity than was measured. However Rashkeev *et al* showed that the Au-Au spacing dictated by the TiO_2 support is $\sim 12\%$ longer than the spacing for bulk gold, causing the Au chains to be unstable against local reconstruction. As a result of this local reconstruction, short chains with decreased Au-Au spacing and lower co-ordination atoms are produced, as seen in Figure 3.4(b). Their model is extended in Figure 3.4(c) to include just a single layer of TiO_x supported on Mo(112). Figure 3.4(d) shows that the Au chains buckle as O atoms are introduced in the Ti rows, creating further low co-ordination Au sites. Their conclusion is that the exceptionally high catalytic activity of Goodman *et al*'s bilayer Au films is caused by O atoms on the substrate surface that lead to reconstructions of the gold layer, producing low co-ordination surface gold atoms.

The difference between catalytic Au and Pt nanoparticles was studied by Raskeev *et al* [79], as the activity of Pt nanoparticles shows no strong size dependence, in stark contrast to the size dependence of catalytic gold nanoparticles previously described. They found that the presence of low co-ordination atoms is necessary for the activity of

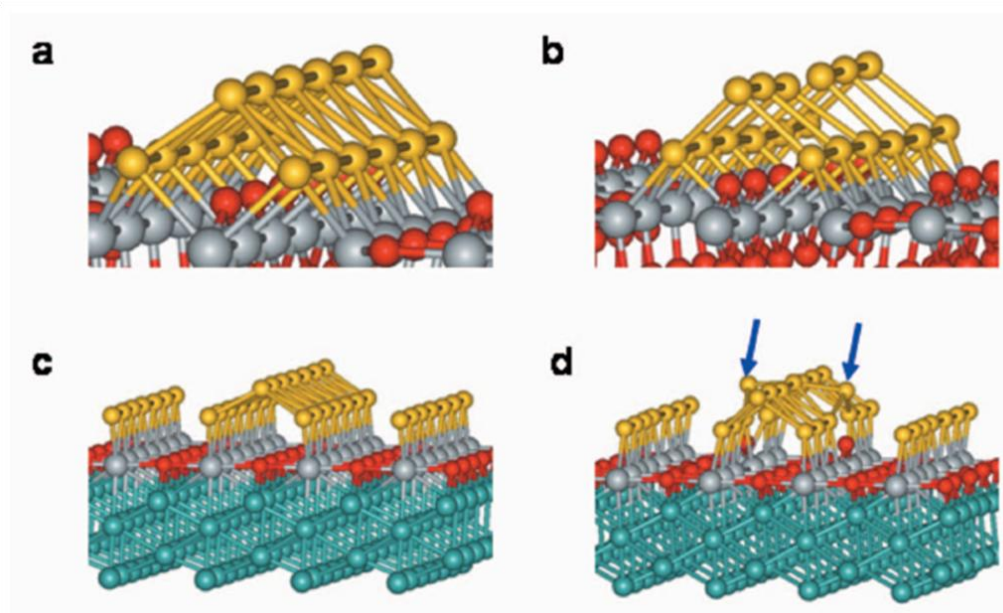


Figure 3.4 Schematic model of Goodman's bilayer Au structures on TiO_2 and on a single TiO_x layer. (a) All Au atoms are sixfold and sevenfold co-ordinated. (b) Low co-ordination sites are formed as the top Au chain is unstable against reconstruction. (c) Au bilayer structure on single TiO_x layer supported on Mo(112). (d) O is introduced under the chains, causing them to buckle and produce further low co-ordination gold sites (indicated by blue arrows). Reproduced from Rashkeev *et al* [79].

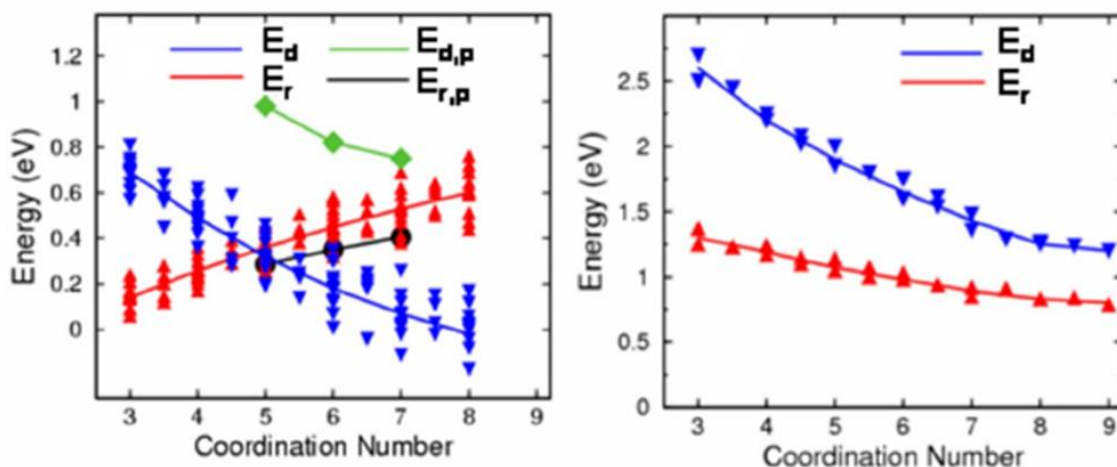


Figure 3.5 The desorption energy, E_d of an O₂ molecule and the reaction barrier, E_r as a function of the average coordination number for Au/TiO₂ (left) and Pt/TiO₂ (right). Reproduced from Rashkeev *et al* [79].

gold but is not the reason behind the difference in activity of Au and Pt. As shown earlier, the bonding of CO or O₂ to Au results in a weakening of the Au-Au bond, whereas Pt-Pt bonds become more rigid, thus preventing the strongly absorbed molecules from interacting. As the bonds become longer and weaker, the particle becomes more catalytically active as less energy is required for the rotation and stretching needed for the reaction [79].

The crossover of the reaction barrier, E_r and desorption energy, E_d curves for O₂ on Au show that reaction is only favoured over desorption when the average co-ordination number is less than 5, ie when $E_r < E_d$. At this point the time for reaction is less than the residence time of the adsorbed molecule. In contrast E_r is always less than E_d for Pt, meaning that catalysis by larger particles is always possible. Also, the perimeter sites on Pt are not thought to be catalytically active, as the dissociated oxygen is bound too strongly, preventing desorption and blocking the site for further adsorption events. Therefore a decrease in particle size does not necessarily promote activity, as opposed to Au, where a reduction in particle size is needed to increase the proportion of low co-ordination atoms.

Although the origins of gold's catalytic activity are still being debated, there is a large amount of evidence in the literature to support under co-ordinated atoms as being key for high activity. The effect of reducing the atoms co-ordination number is attributed to

a modification of the band structure, in which reducing co-ordination shifts the d states closer to the Fermi level. This effect is explained by the d -band model [85], where a reduced overlap of the d state electron wavefunctions leads to a narrowing of the d band and a subsequent increase in the bands population. In order to preserve the degree of filling of the d band, its centre, ε_d , is shifted up towards the Fermi level (as shown in Figure 3.6), leading to an increase in strength of the surface-molecule interaction as fewer of the anti-bonding states are occupied [86]. In this model a reduction in co-ordination number and an increase in tensile strain have the same effect on the d band of transition metals.

Hammer *et al* [87] go on to quantify the effect of the shift in d band centre on the chemisorption strength by considering the change in electronic structure of a CO molecule during adsorption. By calculating the shift in the filled d states and the lowest unoccupied molecular orbits after coupling, perturbation theory gives a linear relationship between chemisorption strength, ΔE_d , and shift in the d band centre, $\delta\varepsilon_d$:

$$\Delta E_d = -\frac{V^2}{|\varepsilon_d - \varepsilon_a|^2} \delta\varepsilon_d \quad (3.4)$$

where ε_a is an electronic adsorbate level and V is a coupling matrix element [88].

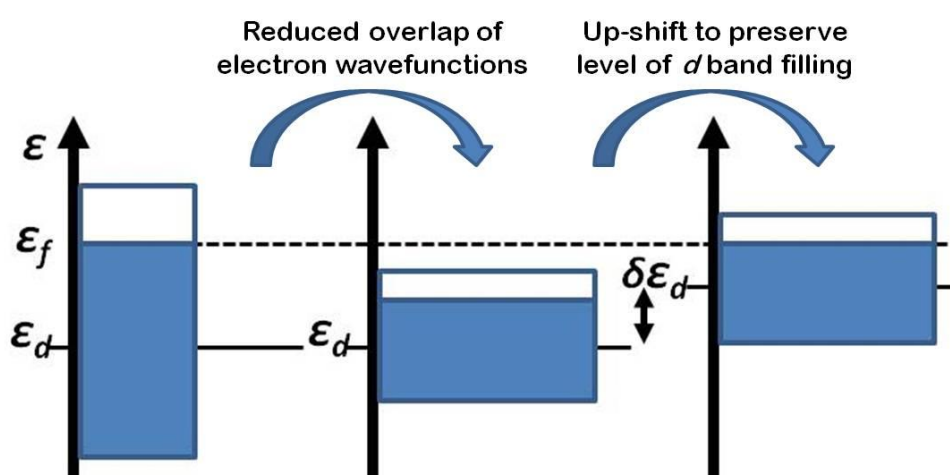


Figure 3.6. Narrowing and subsequent up-shift of the d band towards the Fermi level as a result of reducing co-ordination number for metallic gold.

3.2.3 The effect of strain

Mavrikakis *et al* have used DFT calculations to confirm that inducing a strain in a metal surface has an effect on the d states similar to that of reducing the co-ordination number. Their results show that there is a considerable variation in adsorption energies with strain for CO and O on Ru, and that as the lattice constant is increased, the chemisorption bond becomes stronger. They go on to attribute this effect to a shift in the centre of the metal d bands (ϵ_d) with strain [89]. Furthermore, Gsell *et al* provided direct evidence of oxygen being preferentially adsorbed on areas of Ru that have been strained by subsurface Ar bubbles [90], whilst later studies have shown stronger binding of adsorbates on layers of Pd, Pt and Ni that are strained as a result of a lattice mismatch with the support [91-93].

Giorgio *et al* [94] found that for Au supported on TiO₂, the Au particle may be strained at the support interface by up to 12.5% due to the lattice mismatch between Au(111) and anatase(004). Following this work Mavrikakis *et al* used DFT to investigate the effect of strain at the Au-support interface and found that a theoretical 10% strain induced by the support would significantly enhance the adsorption of O and O₂ on gold [95]. Further DFT calculations on the adsorption energies for atomic and molecular oxygen on both relaxed and strained Au surfaces are summarised in table 1. The use of Au(111) surfaces represents the most common surface facet present in Au nanoparticles, whilst (211) surfaces are used to model adsorption to an under co-ordinated atom found at a surface step.

Surface	Stretched (%)	Atomic Oxygen E _b (eV)	Molecular Oxygen E _b (eV)
(111)	0	-2.54	n/a
(111)	10	-3.14	-0.08
(211)	0	-2.77	-0.15
(211)	10	-3.07	-0.26

Table 1. Binding energies for atomic and molecular oxygen on relaxed and strained gold surfaces calculated by DFT. Based on data from Xu *et al* [95].

Clearly the introduction of significant surface strain enhances the adsorption energy and therefore catalytic activity of the Au surfaces. Also, we can see that the adsorption energies on the Au(211) surface are affected less than the usually inactive Au(111) surface, as the d band of the (211) surface has already been shifted towards the Fermi level as a result of its under co-ordinated nature. These results are shown graphically in Figure 3.7, in which the adsorption energy of atomic oxygen with respect to molecular oxygen is plotted as a function of separation between the d band centre and Fermi level for the Au surfaces considered. For CO oxidation and the water-gas shift reaction, the adsorption energies of CO on various Au sites will perhaps be the most important step, as atomic oxygen may be supplied by the formation and filling of oxygen vacancies on reducible metal oxide supports or the presence of hydroxyl groups.

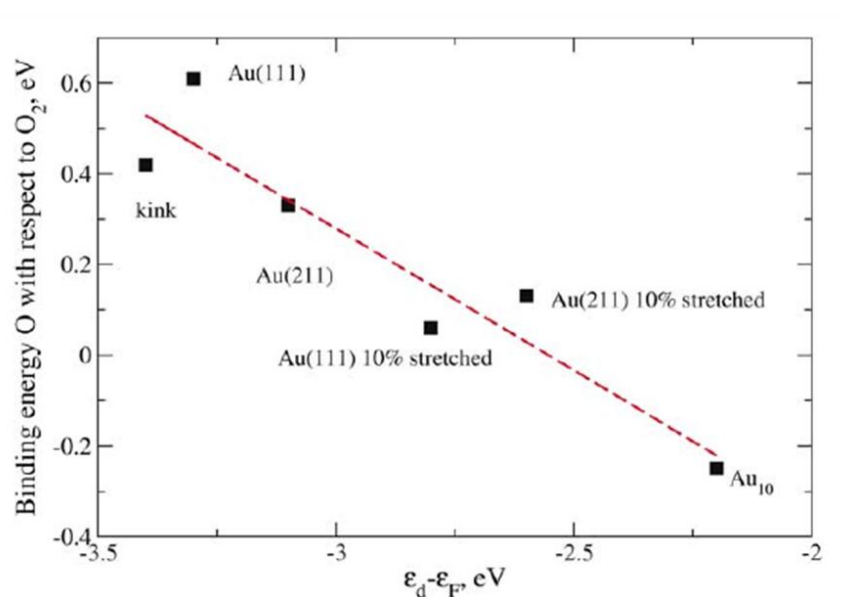


Figure 3.7 The dependence of binding energy of atomic oxygen, with respect to O_2 , with the position of the d band relative to the Fermi level for Au. Reproduced from Lopez *et al* [82].

3.2.4 Particle Morphologies

If a material's surface energy is isotropic, the equilibrium shape will be one that simply minimises surface area; resulting in a sphere. However, as crystalline solids have anisotropic surface energies, the equilibrium morphology will be one that minimises the total free surface energy for a crystal of given volume at a given temperature. The solution to this problem was first given by Wulff [96], who showed that:

$$\frac{\gamma_i}{h_i} = \text{constant} \quad (3.5)$$

where γ_i is the surface energy and h_i the distance from the particle centre to the facet i . Using this principle, Wulff found that for an FCC crystal such as gold, the equilibrium morphology is a truncated octahedron bound by eight $\{111\}$ and six $\{100\}$ faces [97], as shown in Figure 3.8(e) [98]. Such particle morphologies, in which the particle is free from any internal twin boundaries, are commonly referred to as single crystals. However, thermodynamic effects cause the surface energy anisotropy – and therefore potentially the equilibrium morphology – to change, going towards a sphere near the melting point, as surface energy anisotropy then tends to zero.

In the case of supported particles, the interfacial energy between the particle and the support can also play a crucial role in determining the equilibrium particle structure. This was considered by Winterbottom [99], leading to a modified Wulff construction to include the effect of the support interaction. For nanoparticles, the increased surface to volume ratio and surface tension allows for minimisation of surface energy terms through adopting twinned and multiply twinned morphologies, even at the energy cost

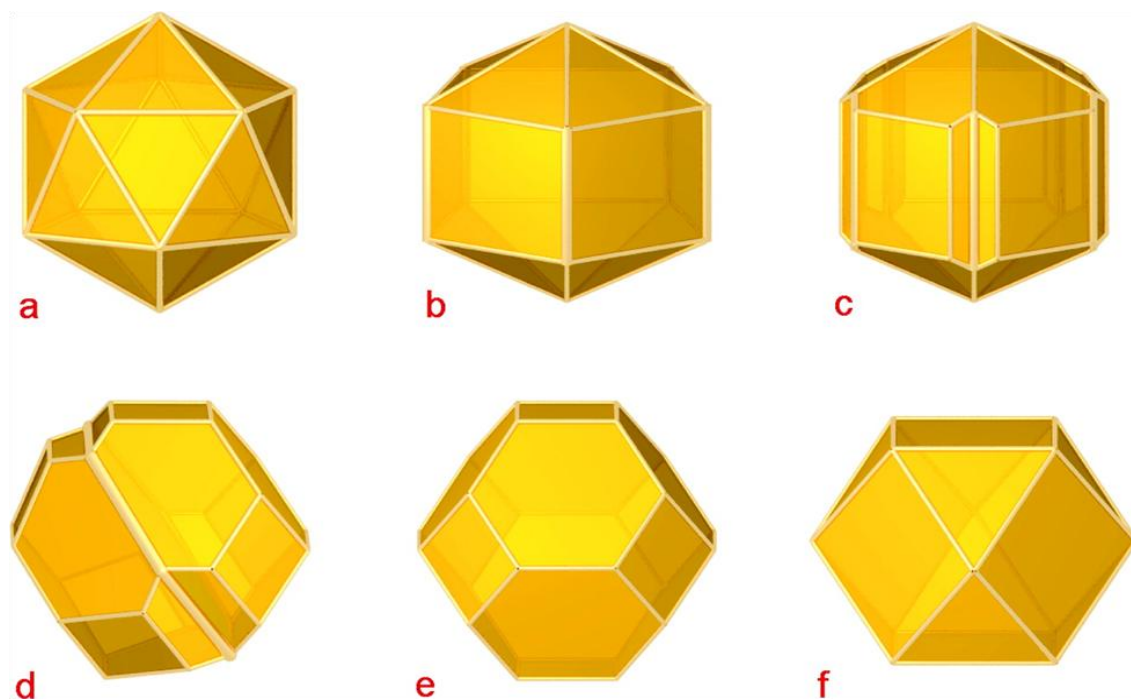


Figure 3.8 Various shapes exhibited by gold nanoparticles: the Mackay icosahedron (a), the Ino (b) and Marks (c) (truncated) decahedra, the symmetrically twinned truncated octahedron (d), the ideal truncated octahedron (e), and the ideal cuboctahedron (f). Reproduced from Barnard *et al* [98].

of an increase in surface area or elastic energy. Additionally, in this size range the contribution of under co-ordinated corner and edge atoms is no longer negligible, whilst sphere packing corrections may lead to further structural deviations from those predicted by the Wulff model [100]. Therefore, the equilibrium shape is no longer size independent, and many crystal forms have been observed for small nanoparticles [101-103]. Furthermore, in heterogeneous catalysis, the effect of the gas environment may cause additional modifications to both the external surfaces [104] and particle morphology [105].

Whilst the extremely small size of such nanoparticles can make accurate characterisation of the structure difficult, various particle morphologies have been both theoretically modelled and experimentally observed, and the more common structures are shown in Figure 3.8. [98]. It is clear that the energies of such configurations are very similar, as they become hard to differentiate and indeed transitions between different morphologies often occur [103].

Icosahedral (Figure 3.8a) and decahedral particles (Figure 3.8b-c) have non-space filling, crystallographically forbidden morphologies, in which intrinsic strain must be incorporated into the structure. In the case of the icosahedra a balance exists between surface area and packing density; whereas decahedra exhibit fivefold twinning and re-entrant facets may further minimise surface energy [106]. Such particles are often referred to as multiply twinned particles (MTPs). Perfect shapes exist only in particles with a ‘magic’ number of atoms, (13, 55, 147, 309... for icosahedra [107]) meaning that particles with slightly more or less atoms than the magic number will extend from their ideal structure to one of a lower order of symmetry, possibly exhibiting complex twinning or stepped surfaces [108]. Perfect cuboctahedral particles (Figure 3.8f) share the same series of magic numbers as icosahedra, whilst ideal octahedral (Figure 3.8d) and truncated octahedral (Figure 3.8e) FCC crystal structures occur for different sets of magic numbers [108].

Galanakis *et al* [109] show that by considering the number of broken bonds between first neighbours, the surface energy can be expressed as:

$$\sigma_{(hkl)} = \frac{1}{2} \frac{N_{(hkl)}}{Z_B} E_{coh} \quad (3.6)$$

where Z_B is the bulk co-ordination number, E_{coh} is the cohesive energy between neighbouring atoms and N is the number of broken bonds for a surface with Miller indices (hkl). Therefore the most closely packed {111} gold surfaces are the lowest in energy. Marks shows that by considering the three most common morphologies for small gold nanoparticles, the total particle surface energy goes in the order *single crystal* > *decahedral* > *icosahedral*, in line with the proportion of {111} surfaces present [106]. The reduction in total surface energy is the driving force for the adoption of multiply twinned morphologies.

The energy cost of these MTP's comes in the form of internal elastic strain energy that is required to account for the strain inherent to their non-space filling structures. For example, the decahedron is made up of five crystal segments bound by {111} twin planes. The angle between these {111} twin planes should be 70.53° , leaving a missing angle of 7.35° . This is accounted for by a disclination (rotational dislocation) about the fivefold axis in order to incorporate the necessary strain. The icosahedron is made up of 20 tetrahedra and exhibits exclusively {111} surface facets, whilst six disclinations make up for its non-space filling nature [110].

By modelling the decahedron as a cylinder with a single disclination in the centre, both Howie and Marks [110] and Richter *et al* [111] provide numerical solutions for the strain energy associated with the disclination through analysis of the stress tensor components. This results in a strain energy of:

$$E_s = \frac{G\omega^2}{4\pi(1-\nu)} d^2 \quad (3.7)$$

where G is the shear modulus, ω is the strength of the disclination, ν is Poisson's ratio and d is the diameter of the cylinder. The result is tensile strain at the surface that decreases logarithmically and becomes compressive towards the centre. In larger decahedra this therefore provides a driving force for stress relief by vacancies or climb dislocations migrating into the particle [110]. Richter *et al* go on to show that if the

disclination axis is moved away from the centre of the cylinder, the strain energy becomes:

$$E_s = \frac{G\omega^2}{16\pi(1-\nu)} r^2 \left[1 - \left(\frac{x}{r} \right)^2 \right]^2 \quad (3.8)$$

where x is the distance of the disclination from the centre of the cylinder and r is the radius of the cylinder [111]. Therefore the elastic energy associated with the disclination can be reduced by shifting the disclination axis towards the surface of the particle.

Gold based catalytic systems often exhibit a relatively broad range of particle sizes, resulting in various particle structures, whilst even particles of a given size have shown a range of morphologies and internal structures [112] – proving that it is not just particle size that determines morphology. The particles' interaction with the support [113] can play a key role in deciding both the particles structure and orientation, whilst the surface properties of small nanoparticles are often dependent on the plane of the crystal facets, with {111} planes being the most commonly observed due to their lower energy. Previous research into small gold clusters and nanoparticles has shown that they are very rarely perfect crystals, and a high density of stacking faults, twins and other defects can be expected [59, 112, 114]. Also, the average co-ordination number of atoms in a particle has been shown to change with structure, with cuboctahedral particles giving a lower average co-ordination number than an icosahedral with the same number of atoms [115]. These factors can be expected to have a large impact on the catalytic activity of a particular nanoparticle.

Different morphologies are adopted in order to minimise the free energy of a particle. Therefore the addition or removal of atoms from the particle or a change in the particles temperature can lead to structural transformations in order for the particle to adopt a more energetically favourable morphology. Figure 3.9 [98] shows a quantitative phase map that predicts the most thermodynamically stable Au structure for a given particle size and temperature. This phase map can be used to predict how the structure of gold nanoparticles will change as a function of temperature, whilst being a useful guide as to what structure can be expected for a given particle size. However, as this phase map is based on a thermodynamical model, it does not take into account any kinetic effects on

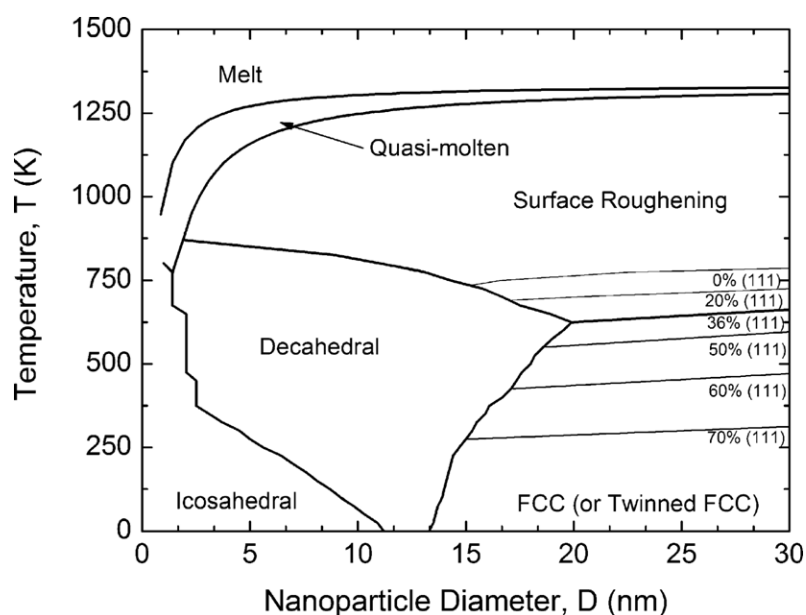


Figure 3.9 A quantitative phase map of gold nanoparticles based on relativistic first principles calculations. Reproduced from Barnard *et al* [98].

the particle shape. As it is known that the different morphologies have very similar free energies, a kinetic force can easily induce a structural transformation to a morphology that is predicted to be slightly less thermodynamically stable than the one predicted by the phase map. Also, as we consider more complex systems with many particles, interactions between particles will occur as a function of temperature, whilst the support will have a large effect on the nature of these reactions and the temperature regimes at which they occur.

3.2.5 Role of the particle support

Earlier work on gold catalyst systems [5, 46, 48, 116] noted the large effect the particle support could have on activity. Reducible metal oxide supports such as TiO_2 and Fe_2O_3 proved to be the most active, with differing reasons suggested as to the cause of this. However, it is now clear that a direct interaction with the support is not required for high activity, as demonstrated by Goodman *et al*s bilayer catalysts [84]. This rules out the particle support interface being a necessary active site for the reaction, as had been previously suggested [77]. A summary by Lopez *et al* [82] of the activity of different supports as a function of particle size can be seen in Figure 3.10, where data from several independent studies [5, 47, 48, 82, 116-121] has been collected, indicating that the effect of the support is secondary to the activities dependence on particle diameter,

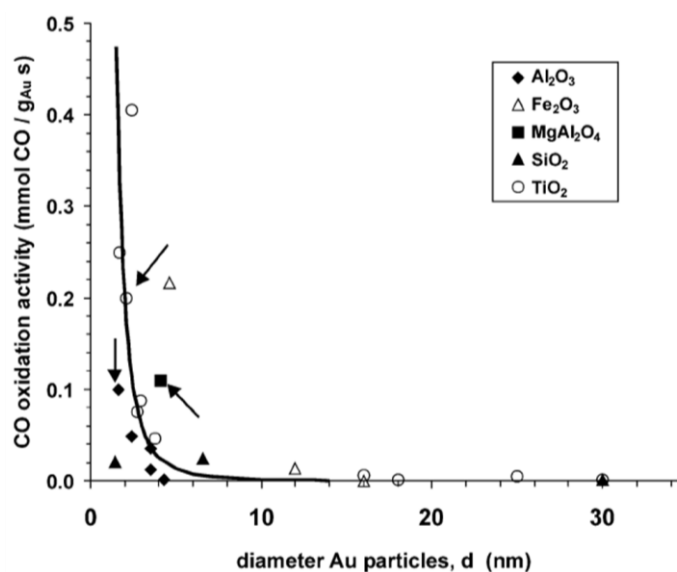


Figure 3.10 Measured activities (in $\text{mmol CO}/(\text{g}_{\text{Au}}\text{s})$) for CO oxidation at 273 K over different Au-based catalysts as a function of the average particle size (d , in nm). Supports are indicated by the symbol shape. Open symbols are used for reducible supports; solid symbols for irreducible supports. Reproduced from Lopez *et al* [82] with data from [5, 47, 48, 82, 116-121].

d. The curve roughly shows a $1/d^3$ relationship, showing that the activity of gold catalysts is approximately proportional to the number of low co-ordinated atoms at the corners of the gold particles. This is further supported by more recent work from Williams *et al* [122].

Grunwaldt *et al* [123] showed that although they both had the same mean Au particle size, Au/TiO₂ samples exhibited significantly higher activity for the oxidation of carbon monoxide than Au/ZrO₂. Further studies explained the large difference in activity was caused by the two different support interactions leading to a difference in the number of low co-ordinated gold sites present [124]. However, the regular higher activity measured on TiO₂ and to a lesser extent on Fe₂O₃ suggests the partial reducibility of these supports opens up alternative reaction mechanisms that may directly involve the support, such as the creation of oxygen vacancies in the support material in order to provide atomic oxygen to facilitate the oxidation of the adsorbed CO. The role of reducible supports is further highlighted by the remarkable catalytic activities reported on CeO₂, as discussed in detail in the following section.

As well as supplying atomic oxygen for oxidation reactions, reducible supports will also create oxygen vacancies, which may significantly affect the adsorption energy and

electronic structure of an Au adlayer, whilst it is known that gold particles will bind more strongly to a defective surface. A high concentration of oxygen vacancies may provide trapping sites for migrating atomic species or small clusters, therefore stabilising small particles and preventing coalescence or acting as nucleation sites for cluster growth during the migration of atomic species in Ostwald ripening. These factors demonstrate that the support can play a key role in determining the possible reaction mechanisms; the morphology of the particle – which will in turn determine the concentration of low co-ordination sites; as well as having a large effect on the stability of the nanoparticles under reaction conditions.

3.2.6 CeO₂ based catalysis

Cerium dioxide is widely used as a catalyst support for three-way auto-catalysts, as its oxygen storage capabilities readily allow the release and capture of oxygen in the exhaust gas stream in either fuel rich or lean conditions. This ability to readily store and donate oxygen as needed occurs through the formation and filling of oxygen vacancies, such that:



A renewed interest in the water-gas shift reaction for hydrogen production and the removal of poisonous CO from hydrogen streams in fuel cells has recently triggered a wealth of research into ceria based catalysis. It was found that by reducing the ceria crystallite size to the nanoscale, the CO oxidation rate was increased by two orders of magnitude for Au supported on nano-ceria compared to similar Au on bulk ceria [125]. This result was attributed to the greatly facilitated formation of oxygen vacancies on nano-ceria crystals as opposed to extended CeO₂ surfaces, due to the very small energy cost of removing oxygen atoms from low co-ordinated sites such as those found at the corners of the small ceria nanoparticles [126, 127]. Furthermore, the observation of CO₂ formation during CO adsorption experiments over Au/ceria catalysts, despite the absence of oxygen in the gas stream, directly shows that the participating reactive oxygen is supplied by the supporting nano-ceria [128].

The addition of dopants to ceria (such as zirconia and/or lanthanum) was also found to increase the reducibility and therefore activity of ceria based catalysts [129, 130], whilst

the presence of gold nanoparticles on nano-ceria was found to lower the reduction temperature of surface oxygen to $\sim 100^\circ\text{C}$ or less and as a result dramatically increase the low temperature activity for the water-gas shift reaction [131].

Fu *et al* went on to identify the active species in Au-ceria water-gas shift catalysis as non-metallic Au associated with the cerium-oxygen surface groups [132]. In their study, they take a conventional 4.4 atom % Au catalyst and leach it with sodium cyanide to remove the metallic gold, before drying and calcination in air at 400°C . The remaining 0.44 atom % catalyst exhibited no loss of activity, with XPS showing that the remaining gold species were in the Au^{+1} and Au^{+3} states. Therefore they conclude that it is these cationic species that are the key for activity. Similar results were also found for Pt/ceria catalysts, with the remaining Pt being in the Pt^{+2} and Pt^{+4} states [132].

Following this work, theoretical studies investigated the energetics and oxidation states of both gold single atoms and small clusters on CeO_2 in order to try and establish the likely nature of the active gold cations. Liu *et al* use DFT calculations to study the oxidation of gold on ceria [133]. They state that single gold atoms will mainly occupy oxygen vacancy sites and find the resulting Au-O_{vac} to be strongly negatively charged. Therefore they “rule out any catalytic mechanism based upon only a gold single atom” and go on to find that Au atoms bound to oxygen vacancies will act as nucleation sites for the growth of small Au clusters. After finding such gold clusters ($4 \leq n \leq 6$) to be cationic, they conclude that these are the active species in water-gas shift catalysis by Au/ceria.

However, Fu *et al* speculate that $\text{Au}^{+\delta}$ may partially fill vacant Ce sites and therefore create further oxygen vacancies. The resulting $\text{Au}_x\text{Ce}_{1-x}\text{O}_2$ surface has increased weakly bound surface oxygen [132], and this is the source of the exceptional activity. XPS and diffraction data from Venezia *et al* [134] was consistent with this hypothesis, whilst DFT calculations from Zhang *et al* [135] give the adsorption energy for a Au atom into a Ce vacancy as -5.68eV , making this energetically favourable, even when considering the 4.85eV energy cost of creating the Ce vacancy. Similar DFT results from Tibiletti *et al* [136] give the chemisorption energies of Au on both (111) and (110) CeO_2 as being in the order $E_{ad}(\text{Ce-vacancy}) > E_{ad}(\text{O-vacancy}) > E_{ad}(\text{perfect surface})$.

Camellone and Fabris [137] provide DFT calculations to investigate both the possibility of single Au atoms filling vacant Ce sites; as well as conditions similar to those considered by Liu *et al* previously. In agreement with Liu *et al*, they find that a single Au atom bound to an oxygen vacancy will become negatively charged and therefore deactivate after one CO oxidation cycle, with this situation being recovered for gold clusters as small as Au₂ that maintain their Au⁺ oxidation state throughout multiple cycles. For the case of Au atoms partially filling vacant Ce sites, they find that the Au⁺³ ions are stable throughout the oxidation cycle, and predict a regenerative mechanism based on CO adsorption on single Au atoms.

Further work by Tibiletti *et al* [136] and Fonseca *et al* [138] also correlate high activity with the presence of Au⁺³ in the as-prepared catalysts, with the turnover frequency found to be at a maximum in the sample with the lowest loading, where the Au present is almost exclusively found to be in the Au⁺³ state. However, through *in-situ* EXAFS measurements under water-gas shift conditions of CO and H₂O, they find that by just 100°C there is complete reduction of Au⁺³ to metallic gold, and therefore suggest that metallic Au is the active phase under reaction conditions. They go on to attribute the active species to approximately 50 atom clusters in ‘intimate contact’ with the support. This is clearly in direct contrast with the conclusions of Fu *et al*, and whilst the presence of cationic gold directly correlates with activity in the as-prepared samples, they conclude that the Au cations act as a precursor to small metallic cluster formation and this is the real active phase [136].

These results are supported by Wang *et al*, who come to similar conclusions based on *in-situ* X-ray adsorption spectroscopy [139]. They also observe complete reduction of AuO_x to Au under simulated WGS conditions, and therefore conclude that “*cationic Au^{δ+} species cannot be the key sites responsible for the WGS activity, since they do not exist under reaction conditions.*” Photoemission spectroscopy corroborates this finding, showing a shift from cationic to zero-valent Au after exposure to CO/H₂O and heating to 300°C, shown in Figure 3.11.

Comparison of these reported results is not straightforward, as subtle differences in both sample preparation and analysis techniques used may lead to some discrepancies.

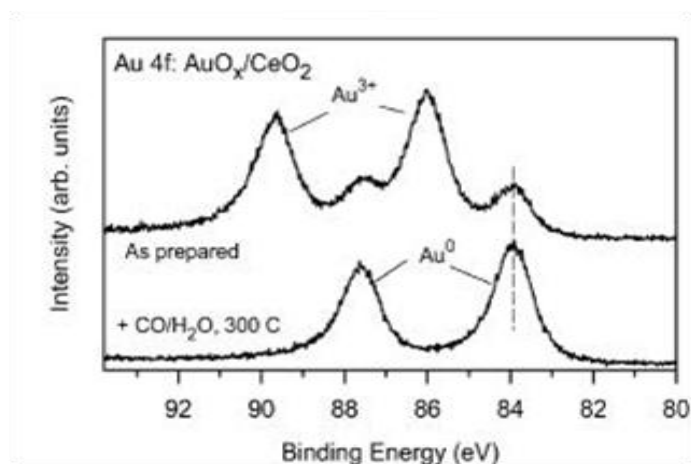


Figure 3.11 XPS spectra observed before and after exposure of a AuO_x/CeO₂ interface to a CO/H₂O mixture at 300°C. Reproduced from Wang *et al* [139].

However, the presence of Au⁺³ is ubiquitous in the highly active as-prepared catalysts, and clearly plays an important role, whether it is as the active phase or a precursor. If gold is reduced to metallic Au under WGS conditions, the nature of the Au/ceria interface seems to govern both the source of activity as well as the stability of the catalyst. Cationic Au atoms in Ce vacancies are expected to act as nucleation points for small clusters and particles, with the strong particle-support interaction known to promote oxygen vacancy formation and hence activity. Scanning transmission electron microscopy data [138] provides some evidence for the presence of single atoms as well as small clusters and nanoparticles in the as-prepared catalyst. However, identification of the single atoms is ambiguous, whilst it was not possible to resolve the position and therefore interaction of the single atoms with the support. Additionally, the multitude of Au species observed in the micrographs of the catalyst makes direct links between any particular form of gold and the measured catalytic activity difficult.

More recent work from Flytzani-Stephanopoulos and co-workers agrees with the findings that Au^{+δ} is largely reduced to zero-valent Au under water gas shift conditions, however, instead of attributing this metallic Au to being the active species, they correlate the Au reduction with an observed deactivation of the catalyst [140]. They go on to show that the surface oxygen and hence activity is recovered after a 400°C oxygen treatment of the reduced Au catalyst, and claim that reduced gold in the form of metallic clusters is not-active, and regeneration occurs through a reversible redispersion of the gold in oxygen.

Alternatively, similar observations of deactivation with time on stream under WGS conditions by Goguet *et al* are explained very differently [141]. They maintain that reduction to metallic Au clusters occurs rapidly and that this reduction of the Au^{+3} is an activation process to reach the active phase. The subsequent loss of activity is attributed to a reduced interaction and therefore a loss of the ‘intimate contact’ between the Au cluster and the support. As deactivation is also observed to directly correlate with the concentration of H_2O in the gas stream, they propose that the particle will detach from the support, either through hydrolysis at $< 250^\circ\text{C}$ or as a result of heating at higher temperatures. DFT calculations show that the presence of OH-terminated surfaces under water rich conditions leads to an increased Au-surface distance upon H_2O dissociation. The proposed removal of Au atoms from Ce vacancies and reduction in particle-support interaction is described schematically in Figure 3.12 [141].

Both Deng *et al* [140] and Goguet *et al* [141] find that the addition of oxygen to the gas stream suppresses deactivation, although this is consistent with both the suggested mechanisms for activity and subsequent deactivation. Without any direct observation of the deactivation process or processes, the proposed mechanisms remain somewhat speculative.

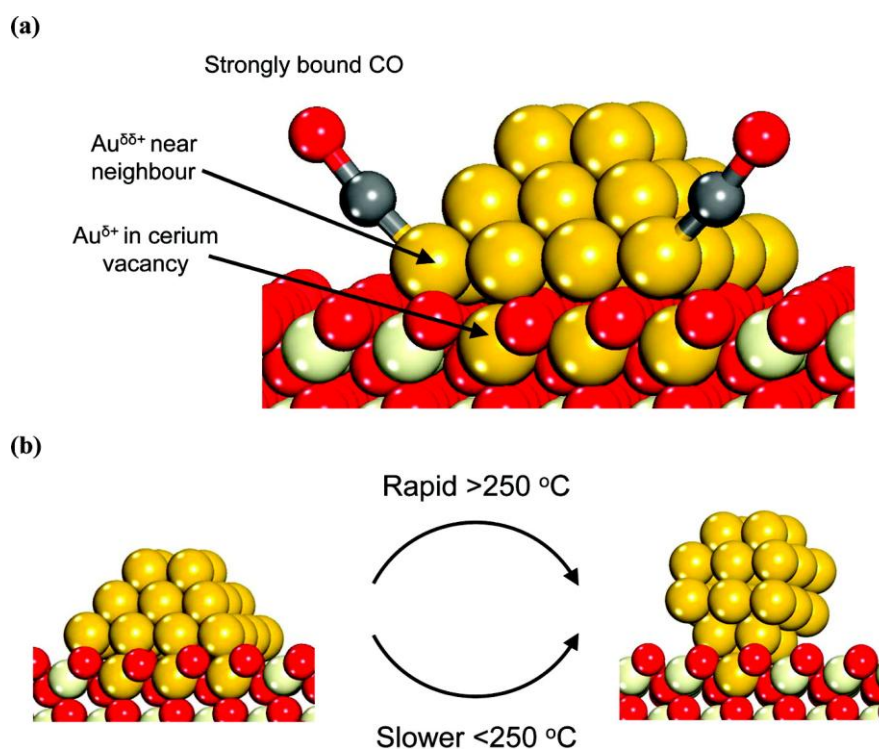


Figure 3.12 Schematic of the proposed structural deactivation mechanism as a result of a reduced interaction with the support. Reproduced from Goguet *et al* [141].

After finding that the most stable site for an Au cation is substituting for a Ce atom, Camellone and Fabris calculate that the oxidation of CO can occur through a three step mechanism, as shown in Figure 3.13 [137]. In this regenerative, or redox, mechanism, an adsorbed CO molecule is oxidised by an oxygen atom from the $\text{Au}_x\text{Ce}_{1-x}\text{O}_2$ surface, thus leaving behind an oxygen vacancy. This oxygen vacancy is filled by an adsorbed O_2 or H_2O molecule, resulting in either an extra O adspecies that enables a second CO oxidation event, or the production of H_2 .

Alternatively, an associative mechanism has been proposed, in which hydroxyl or carbonate groups formed after adsorption of CO are decomposed to produce H_2 and CO_2 [142-144]. As both mechanisms are supported in the literature it is clear that both are possible, and that the reaction conditions may govern which is more prominent. Burch goes on to suggest a universal reaction mechanism, involving the regenerative and associative mechanisms in differing proportions as a function of temperature and environment [65]. At lower temperatures, the formation of surface species is expected, with the ratio of CO to H_2O in the initial gas stream determining whether carbonate (high CO) or formate (high H_2O) decomposition will be the rate determining step. At higher temperatures, the redox mechanism is expected to become dominant, although expected mechanism is unclear.

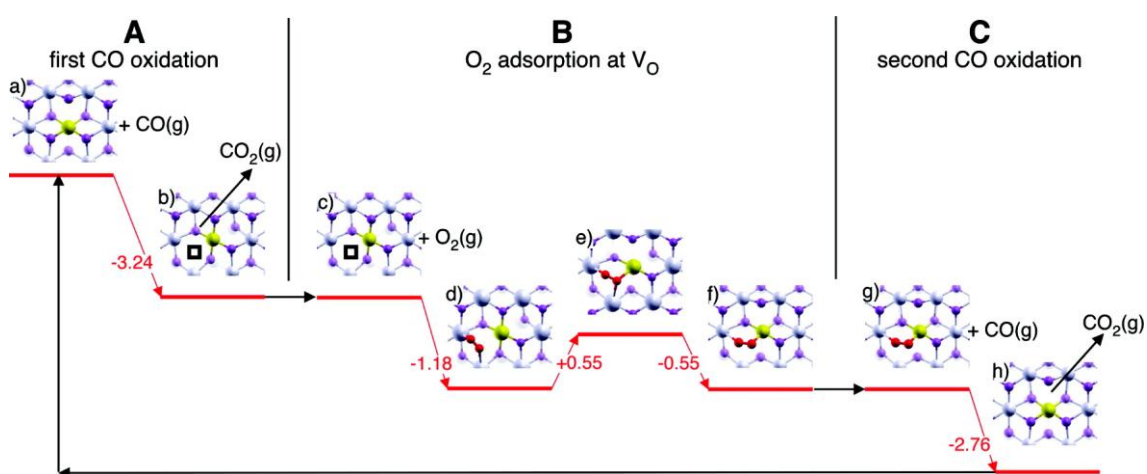


Figure 3.13 Reaction mechanism and energetics (in eV) of proposed CO oxidation promoted by an Au cation in an $\text{Au}_x\text{Ce}_{1-x}\text{O}_2$ catalyst. Square indicates an O vacancy and red molecular O_2 . Reproduced from Camellone *et al* [137].

The remarkable catalytic properties of such Au/ceria systems offers great potential for applications in the production of hydrogen and the removal of CO in hydrogen streams in fuel cells, whilst the reported 90% reduction in Au loading promises a significant advance in the economic viability of fuel cells as an alternative energy source. In contrast to conventional Cu based systems, Au/ceria catalysts have shown excellent stability under repeated start up/shut down cycles, and require either no activation or are activated by the WGS conditions, making them applicable for use in fuel cells under realistic operating conditions [145]. However, despite the wealth of research into Au/ceria catalysis in recent years, there is still no consensus on the exact nature of the active site; namely, is it Au⁺¹ or Au⁺³ cations or metallic gold, and are these small Au clusters, single Au atoms or a combination of both? Furthermore, where do these single atoms or clusters sit on the supporting crystal, what is the resulting reaction mechanism and what deactivation processes affect them?

Based on the work of Fu *et al* it seems certain that the presence of Au⁺³ in the as-prepared catalysts is crucial for activity, whilst DFT calculations predict that such species are either Au single atoms substituting for Ce atoms, or small Au clusters nucleated on an oxygen vacancy. Whether these single atoms or small cationic clusters remain stable and act as active sites by themselves, or promote the nucleation of small metallic clusters under reaction conditions is still unclear. If the latter, the anchoring of the cluster at an Au cation can be expected not only to improve stability, but to have a crucial effect on the reducibility of the surrounding oxygen due to the associated charge transfer. As yet, no direct experimental evidence exists to definitively resolve the nature of the active form of gold, whilst the stability of such single atoms and small clusters is uncertain. Without direct identification at the nanoscale of the active species of gold and any deactivation processes that may occur, differing theories remain somewhat speculative and agreement in the literature is unlikely. These systems will be the subject of study in Chapter 7, in which *in-situ* HAADF-STEM is employed to address some of these questions.

Chapter 4

Electron Microscopy

The development of the light microscope brought with it unprecedented insight into the micro-world, and discoveries such as bacteria and the structure of the cell led to revolutions in many areas of science. However, the resolution of a microscope is fundamentally limited by the wavelength of the illuminating radiation, as shown by the classical Rayleigh criterion, which states that the smallest distance that can be resolved, δ , is:

$$\delta = \frac{0.61\lambda}{n \sin \beta} \quad (4.1)$$

where λ is the wavelength of the radiation, n is the refractive index of the medium and β is the semi angle of collection of the magnifying lens. The result is that when using light as the illuminating radiation, resolution is limited to ~ 200 nm, and clearly an alternative is needed for the observation of materials at the nanoscale.

In 1924, following Einstein's discovery that light also acted as a particle [146], de Broglie famously introduced the concept of particle-wave duality, meaning that the electron could also be thought of as a wave. Correcting for relativity, de Broglie showed the wavelength of a particle of rest mass, m_0 , and energy, eV , is [147]:

$$\lambda = \frac{h}{\sqrt{2m_0eV\left(1 + \frac{eV}{2m_0c^2}\right)}} \quad (4.2)$$

where h is Planck's constant and c is the speed of light. This means that electrons exhibit much shorter wavelengths than light, with an electron accelerated through 200kV having a wavelength of just 0.00251 nm.

Electrons also offer advantages over other short wavelength forms of radiation, such as X-rays, the most obvious of which is that they have an inherent charge. This offers two key advantages: they will interact strongly with the electrostatic potential of the constituent protons and electrons of atoms in a sample; and their trajectory can be easily influenced by the application of external electric or magnetic fields. The force, \mathbf{F} , on an electron travelling through a magnetic field, \mathbf{B} , is given by the Lorentz equation:

$$\mathbf{F} = -e(\mathbf{E} + \mathbf{v} \times \mathbf{B}) \quad (4.3)$$

where e is the charge of the electron, \mathbf{E} is the strength of the electric field and \mathbf{v} is the velocity of the electron.

The combination of both the electrons short wavelength and the possibility of using magnetic fields to act as focussing and magnifying lenses led Ernst Ruska and Max Knoll to make the first electron microscope in 1931 – eventually leading to Ruska winning the Nobel prize in 1986. The theoretical resolution limit of an electron microscope based on the Rayleigh criteria is much below the inter-atomic spacings found in crystalline materials, therefore opening up the possibility of atomic resolution microscopy. However, as we shall see in the following chapter, other factors limit the resolution and interpretability of images produced by electron microscopes, and it is only through understanding and control of these parameters that materials can be studied at the atomic scale.

There have been many comprehensive texts written on the subject of electron microscopy, including [34, 148-153]. Therefore the following chapter will not seek to give a broad detailed account of electron microscopy and electron scattering, but instead provide a brief overview of the electron microscopy techniques that will be used in

Chapters 5-8, whilst identifying some of the key parameters and imaging conditions that will need to be considered for analysis and interpretation of the resulting data.

4.1 Transmission electron microscopy

The transmission electron microscope uses high energy electrons (typically 100-300 keV), generated by an electron gun through either heating (thermionic emission) or the application of an electric field (field emission), followed by acceleration through the applied accelerating voltage. The electron beam then passes through a series of condenser lenses that are used to spread or collimate the beam and transmit it to the sample. A condenser aperture is also typically used to provide the desired beam convergence angle.

The electrons are then transmitted as a parallel beam through an electron transparent sample, with the electron-sample interaction resulting in a variety of scattering events. The objective lens collects the transmitted electrons and focuses them into a diffraction pattern in the back focal plane and an image in the image plane. Additional intermediate and projector lenses provide further magnification before the electrons are projected on to a variety of possible detectors. A simple schematic representation of this process is shown in Figure 4.1, in which the microscope can be switched between imaging and diffraction modes by changing the strength of the intermediate lens. It should be noted that the angles depicted both here and in other ray diagrams used to represent the path of electrons through various lenses in this chapter are exaggerated in order to clearly display what are typically only small deviations from the optical axis.

There are several ways in which the incoming electron may interact with the sample, as described in detail in [148], and these interactions produce a variety of signals which may be usefully detected. If the electron interacts with the electrostatic potential of an atom it may undergo inelastic scattering, resulting in a change in energy of the transmitted electron, that can in turn be measured by a spectrometer in electron energy loss spectroscopy (EELS). Also, inelastic interaction between the sample and the electron beam will cause a transfer of energy, resulting in an atom in the specimen entering an excited state. The atom will then return to its ground state via the transition

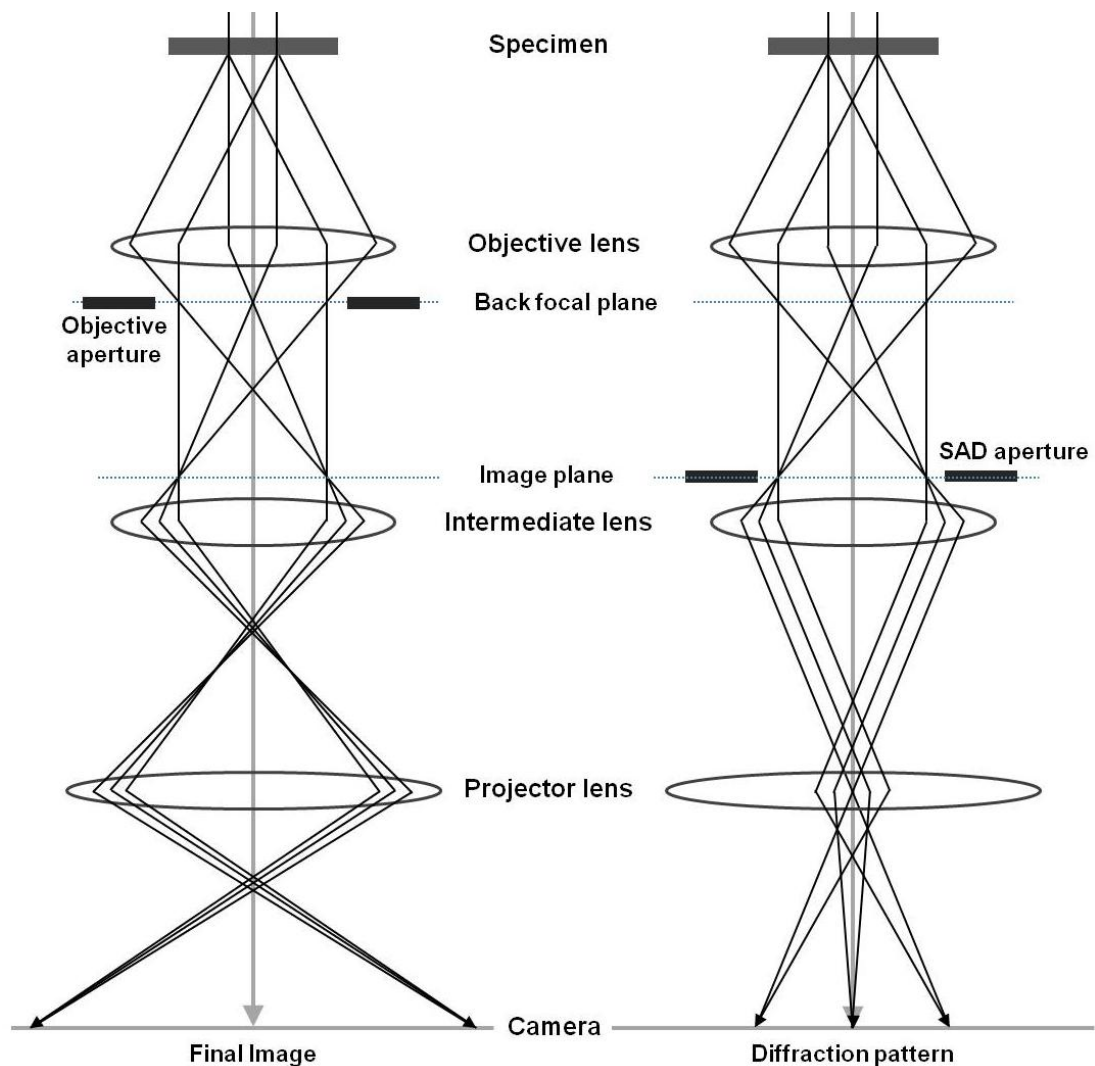


Figure 4.1. Ray diagram of the TEM in imaging mode (left) and diffraction mode (right). Switching between modes is done by changing the strength of the intermediate lens.

of an electron from a higher to a lower energy level. In order to conserve energy, this transition will necessitate the emission of an X-ray with energy characteristic to the energy difference between electron shells for that particular element [154]. Therefore by detecting and measuring the energy of these X-rays, it is possible to determine the chemical composition of the sample; and this process known as energy dispersive X-ray (EDX) spectroscopy.

Electrons that are forward scattered through low angles may be usefully detected for imaging, in which the contrast may come from incoherent elastically scattered electrons (mass-thickness contrast) or coherent inelastically scattered electrons. These coherent electrons have a wavefunction with both amplitude and phase components, and both can

be used to provide intensity in the image. However, for atomic resolution images, it is the effect of the atoms' potential on the phase of the electron beam that is measured. The transfer of phase information has been described in detail by Van Dyck and de Jong [155] and also in [151], and some of the key results are briefly summarised below.

After interacting with the sample, the transmitted coherent electrons are of the form:

$$F(x, y) = A(x, y) \exp(i\varphi_t(x, y)) \quad (4.4)$$

where $A(x, y)$ is the amplitude and $\varphi_t(x, y)$ is the phase that is dependent on the specimen thickness, t . For phase contrast imaging used in atomic resolution TEM, Equation 4.4 is simplified by setting the amplitude of the incident wave, and therefore $A(x, y) = 1$. The phase of the electrons will be modified as a result of interactions with the potential, $V(x, y, z)$, of the sample. Therefore when in the sample, and ignoring relativistic effects for simplicity, equation 4.2 becomes:

$$\lambda' = \frac{h}{\sqrt{2me(E + V(x, y, z))}} \quad (4.5)$$

The phase change that results from passing through a section of the sample, dz , can be written as:

$$d\varphi = 2\pi \frac{dz}{\lambda'} - 2\pi \frac{dz}{\lambda} \quad (4.6)$$

$$d\varphi = 2\pi \frac{dz}{\lambda} \left[\frac{\sqrt{E + V(x, y, z)}}{\sqrt{E}} - 1 \right] \quad (4.7)$$

which for a thin sample can be simplified to:

$$d\varphi \cong \frac{\pi}{\lambda E} V_t(x, y) \quad (4.8)$$

Therefore, the change in phase is dependent only on the projected potential of the specimen, $V_t(x, y)$, where:

$$V_t(x, y) = \int_0^t V(x, y, z) dz \quad (4.9)$$

For a very thin specimen, in which $V(x, y) \ll 1$, Equation 4.4 can be further simplified by expanding the exponential term, such that:

$$F(x, y) = 1 + i \frac{\pi}{\lambda E} V_t(x, y) \quad (4.10)$$

This is the weak phase approximation [151, 155], and shows that for very thin specimens, the amplitude of the transmitted wavefunction will vary linearly with the projected potential. This approximation only holds true for very thin specimens, and will be used for interpretation of phase contrast images of very small nanoparticles discussed in Chapters 5 and 6.

Applying the above argument to the resulting TEM image, the wavefunction as measured in the image plane will be the convolution of the exit wavefunction with the point spread function $h(x, y)$:

$$\Psi(x, y) = 1 + i \frac{\pi}{\lambda E} V_t(x, y) * h(x, y) \quad (4.11)$$

where $h(x, y)$ describes the way a point in the object is spread into a disk in the image plane as a result of imperfections in the transfer of the exit wavefunction through the optical system, as discussed in more detail in the following section. The resulting intensity in the phase contrast image is then given by:

$$I = \Psi\Psi^* = |\Psi|^2 \quad (4.12)$$

4.1.1 Limits to resolution

There are several factors that have so far prevented electron microscopes from reaching their theoretical resolving potential, which is ultimately limited by the size of the electrostatic potential and thermal motion of atoms (~ 0.02 nm) [156]. These limiting factors include stability issues, such as stabilities in voltage supplies and lens currents, as well as mechanical and thermal stabilities in the microscope environment. However, the most prohibitive aspect of conventional electron microscopes has been aberrations that are inherent to cylindrically symmetrical magnetic lenses. In light microscopy, the focal length of a lens is many times greater than its aberration coefficients, and any aberrations can be routinely corrected by the incorporation of both convex and concave lenses. However, in an electron optical system, the focal length of the lens may be comparable to the aberration coefficients, whilst Scherzer showed that cylindrically symmetrical magnetic lenses were always additive in terms of their aberrations. This results in a significant limitation on the resolution of the electron microscope [157].

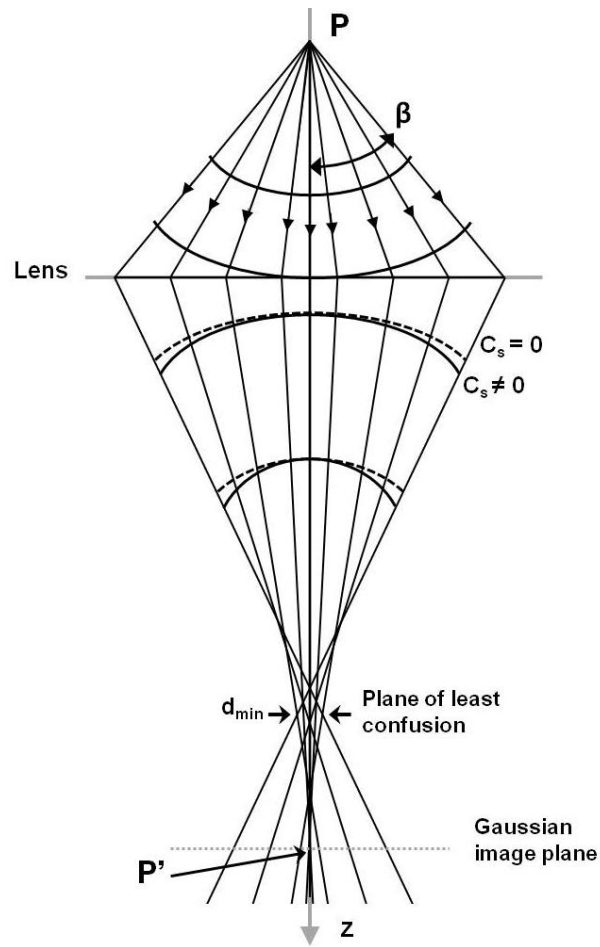


Figure 4.2. Ray diagram showing the effect of spherical aberration in the objective lens. High angle electrons entering a lens with spherical aberration are focussed more strongly than lower angle electrons, resulting in a distorted wavefront and limited resolution.

The effect of spherical aberration is shown schematically in Figure 4.2. Here we can see that electrons entering the lens at higher angles are focussed more strongly than those that are closer to the optical axis, causing the electron wavefront to become more curved than the original wavefront exiting the specimen. The result is that a point P in the specimen is imaged in the Gaussian image plane at P'; appearing as a disk of radius:

$$r_{sph} = C_s \beta^3 \quad (4.13)$$

where β is the semi angle of collection of the objective lens and C_s is the spherical aberration coefficient.

Chromatic aberration occurs as a result of energy differences in the electrons entering the objective lens. These energy differences may arise from either the energy spread of the source electrons or as a result of inelastic scattering upon interaction with the

sample. Electrons with reduced energy will be focussed more strongly by the objective lens, again resulting in electrons from a point in the sample being imaged as a disk, the radius of which is:

$$r_c = C_c \frac{\Delta E}{E_0} \beta \quad (4.14)$$

where C_c is the chromatic aberration coefficient, ΔE is the energy loss of the electrons and E_0 is the initial beam energy. Therefore the effect of chromatic aberration can be reduced by using higher beam energies, E_0 or minimising power supply instabilities, whilst the addition of a monochromator or energy filter can reduce the energy spread of the electrons.

Magnetic lenses can also introduce astigmatism, which occurs due to any imperfections in the lens and causes the electrons to experience a cylindrically non-uniform magnetic field, resulting in some deviation in the electrons ideal trajectory and therefore distortion in the image. However, adjustable stigmators comprised of small compensating magnetic fields can be used to straightforwardly correct any astigmatism in the image.

Therefore, despite the small wavelength of the electrons, the parameters above limit the resolution of the electron microscope well above the diffraction limit given by the Rayleigh criterion in equation 4.1. In the case of the transmission electron microscope, the high beam energies used mean that the chromatic aberration will be reduced, as the $\Delta E/E$ ratio in equation 4.14 will be small. This means the spherical aberration of the objective lens is the dominant limit to resolution, whilst in the case of the scanning transmission electron microscope, similar lens aberrations will be present in the probe forming lenses, leading to a broadening of the electron probe.

The information transferred from the specimen to the image is described by the contrast transfer function, $T(k)$, where k is a spatial frequency. This transfer function can be expressed as the product of three parameters, such that:

$$T(k) = A(k)E(k)B(k) \quad (4.15)$$

where $A(k)$ is a function of the aperture contribution, $E(k)$ is an envelope function to describe the attenuation of the electron wave and $B(k)$ is the aberration function that

results from aberrations in the lenses. The envelope function $E(k)$ results from the instabilities in the lens currents and high voltage supply; mechanical instabilities in the specimen; the energy spread and spatial coherence of the source; as well as the effect of chromatic aberration. In modern microscopes, these stabilities can be controlled to less than one part per million, giving an information limit well below 0.1 nm.

In the case of high resolution phase contrast imaging, the aberration function can be expressed as:

$$B(k) = \exp(-i\chi(k)) \quad (4.16)$$

where $\chi(k)$ is the total phase shift that occurs at defocus, Δf , and can be shown to be:

$$\chi(k) = \frac{1}{2}\pi C_s \lambda^3 k^4 + \pi \Delta f \lambda k^2 \quad (4.17)$$

where k is spatial frequency, C_s is the spherical aberration coefficient and λ the wavelength of the electron beam. Figure 4.3 shows a plot of the phase contrast transfer function (CTF) for a conventional TEM at optimum defocus. The most notable result of this plot is that for the critical range in which the interatomic spacings lie, the CTF oscillates many times, with each crossing of the x axis resulting in a phase contrast reversal. When $T(k)$ is positive we are in a negative phase contrast condition, meaning atoms will appear as bright spots in the image. Alternatively, when $T(k)$ is negative, the resulting positive phase contrast gives dark atoms on a bright background. For a given defocus value, these contrast reversals result in complex image interpretation, whilst at the points where $T(k) = 0$, no contrast is given, resulting in blind spots in some spatial frequency components to the image [151]. The position and frequency of the CTF oscillations can be adjusted by changing the defocus value, and a through focal series of images is required to build up an interpretable representation of the specimen.

The point at which the CTF first crosses the x axis is known as the *first zero*, and is often used to describe the point limit to which useful information can be obtained from the image. As we can see from equation 4.17, the contrast transfer function is dependent on the defocus value, Δf , and Scherzer [158] showed that for a given value of C_s , there would be an optimum defocus value. At this point, the phase will be as

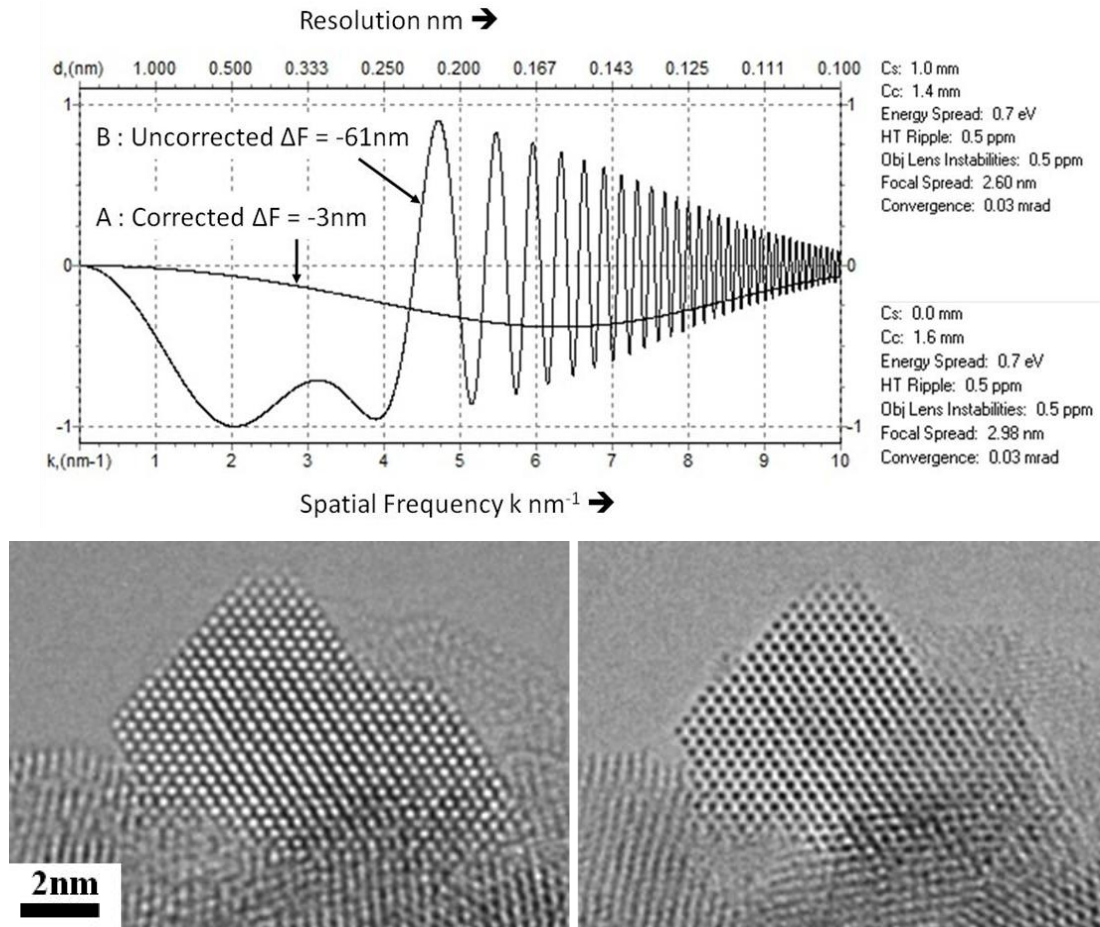


Figure 4.3. (Above) Contrast Transfer Function (CTF) of a conventional and C_s corrected TEM at optimum defocus. Reproduced from Gai and Boyes [188]. Examples of bright atom contrast (left) and dark atom contrast (right) for TEM images of CeO₂ nanoparticles.

consistent as possible out to the first zero, thus giving the image with the maximum amount of information for that particular optical system. This defocus value is known as the optimum defocus modification of the *Scherzer defocus*, and is given by [158]:

$$\Delta f_{Sch} = -1.2(C_s \lambda)^{1/2} \quad (4.18)$$

Also shown in Figure 4.3 is the phase contrast transfer function for a microscope with negligible spherical aberration. The resulting plot of $T(k)$ shows a continuous transfer function that incorporates the entire range of spatial frequencies down to the information limit set by the envelope terms. Additionally, correction of the spherical aberration allows use of minimal defocus values and delocalisation effects, with the combined result of interpretable single images with improved resolution. It is only relatively recently that correction of the spherical aberration has become possible, leading to huge leap forward in the performance of electron microscopes.

4.1.2 Spherical aberration correction

Scherzer showed back in 1947 [157] that it would, in principle, be possible to correct the aberrations inherent to a symmetrical magnetic lens, and whilst a detailed design of such a corrector was proposed by Rose [159] in the early 1990s, it would still be several years until the first working C_s corrector would be built [160, 161]. This lengthy delay in the development of the aberration corrector was largely due to the difficulty in simultaneously controlling the many necessary variable parameters to the required precision, and it is only thanks to the increased processing power of modern computers that it is now possible.

The basic principle of the C_s corrector is to incorporate additional lower symmetry lenses through the use of a double hexapole [159] (or similar) system in order to create non-uniform magnetic fields immediately below the objective lens. The net effect of these lower-symmetry lenses is to act as a concave lens, and therefore compensate for the spherical aberration in the cylindrically symmetric (convex) objective lens. This process is shown schematically in Figure 4.4, in which the strength of the additional lower symmetry lenses can be adjusted in order to compensate for the effect of spherical aberration, therefore focussing electrons from a wide range of scattering angles to the same point. As a result, point P is imaged as a sharp point P' in the Gaussian image plane, as opposed to a delocalised disk in the uncorrected objective lens, the radius of

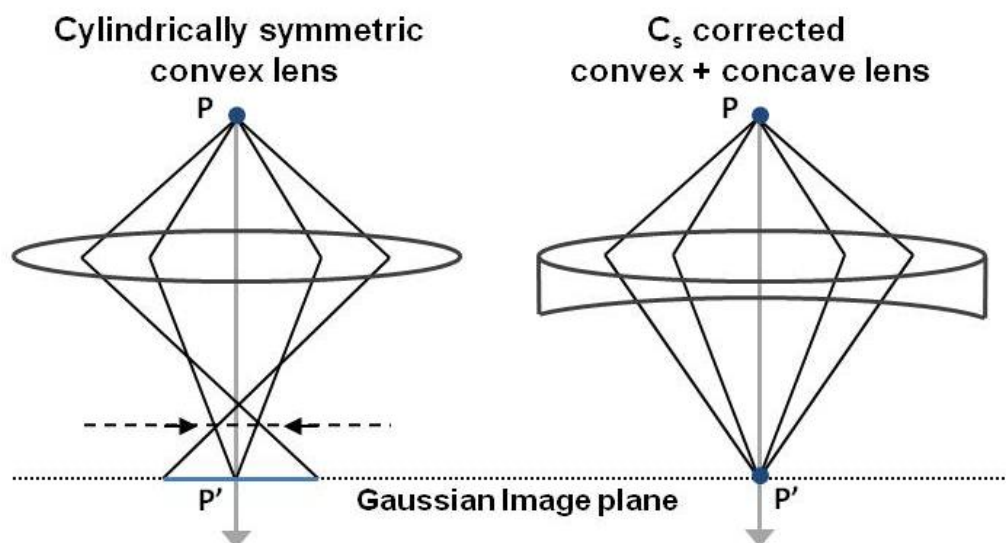


Figure 4.4. Cylindrically symmetrical lenses lead to spherical aberration (left). This can be corrected by the addition of lower symmetry lenses with non-uniform magnetic fields (right).

which is given by equation 4.13. A comprehensive review of the optical arrangements of the Rose corrector can be found in [162], and based on this design, the incorporation of spherical aberration correctors has become increasingly widespread in commercially available modern microscopes.

4.1.3 Aberration corrected atomic resolution imaging

As can be seen in Figure 4.3, in a C_s corrected instrument there are no phase contrast reversals, meaning the first zero – and therefore the amount of interpretable information in the image – is extended out to the information limit. This results in a huge improvement in the interpretable resolution of the microscope. Additionally, the removal of zero contrast points means that there is consistent phase contrast throughout the entire range of spatial frequencies, allowing for directly interpretable single images.

However, perhaps the greatest advantage of C_s corrected TEMs is that the point spread function is greatly reduced in the absence of spherical aberration, resulting in minimal delocalisation effects. This dramatically improves the interpretability of the images; as in a weak phase object, the intensity of the imaged atomic columns will result directly from phase changes induced by that particular atomic column in the sample. This is in contrast to the case in an uncorrected microscope, where the atomic column intensity includes contributions of neighbouring columns that are imaged as a delocalised disk due to point spread induced by the lens aberrations. Therefore the aberration corrected electron microscope can provide us with a true representation of the sufficiently thin sample with atomic resolution.

An unforeseen but welcome effect of the aberration corrector is that it opens up new imaging conditions not previously accessible in conventional microscopes. Scherzer's [158] equation (4.18) was derived based on a set value for C_s . However, with the addition of a C_s corrector, we can treat defocus, Δf , and C_s as adjustable parameters that can be used to optimise the contrast that results from equation 4.17. This leads to very different optimum imaging conditions operating at close to zero defocus, as described by Lentzen [163]. Additionally, the strength of the C_s corrector can be increased to over

compensate for the spherical aberration of the objective lens, therefore creating negative spherical aberration imaging (NCSI) conditions [164].

Under conditions of negative spherical aberration and positive defocus, the contrast transfer function shown in Figure 4.3 is inverted, meaning we are in a negative phase contrast condition, with atoms appearing as bright spots on a dark background. In this situation, Urban and co-workers have demonstrated significantly enhanced contrast when compared with the equivalent positive C_s and negative defocus parameters [164-166]. It should be noted that whilst a small amount of negative C_s (not possible without aberration compensating lenses) is being deliberately added to the system, the magnitude of the spherical aberration coefficient is only a small fraction of that in an uncorrected microscope (typically $\sim 2\%$), and the benefit of the resulting enhanced contrast far outweighs the minimal detrimental effect on resolution.

The cause of the enhanced contrast through NCSI can only be understood by removing the weak phase approximation and instead considering a full treatment of electron scattering from a ‘not so weak’ object [167]. The result is that when expanding equation 4.10 to include non-linear terms, the phase contributions from the first and second order terms are additive in the case of negative phase contrast, whereas for positive phase contrast, the second order term detracts from the image contrast. Additionally, the effect of amplitude contrast should be considered. The amplitude contrast results from small variations in the specimen thickness, as well as electron channelling by the atomic columns – in which the electrostatic potential of each atom acts as a mini lens. This amplitude contribution is again additive for contrast in the NCSI conditions, as both the phase and amplitude components give bright atom contrast. A full description of enhanced contrast with NCSI is given in [164, 167], whilst important effects of the improved contrast include enabling the direct imaging of light atoms, such as oxygen, even when surrounded by much heavier neighbours [166].

4.2 Scanning transmission electron microscopy

Scanning transmission electron microscopy (STEM) uses a small probe of electrons focussed on to the specimen and then raster scanned across the sample. The resulting

scattered electrons are then transmitted by the image forming lenses below the specimen and used to build up an image of that particular beam position. Therefore, over the course of a scan, the image is built up pixel by pixel as a result of each probe position. Additionally, the probe can be positioned on certain areas of the sample for extended periods in order to collect localised chemical information through either EDX or EELS techniques, or local crystallography through diffraction.

The resolution of the STEM is limited by the size of the electron probe, and as such is determined by the probe forming lenses and the characteristics of the high brightness field emission gun (FEG). Figure 4.5 shows this process schematically, in which condenser lenses and a condenser aperture are used to define the beam convergence angles, whilst the objective lens is again the most important lens in the imaging system,

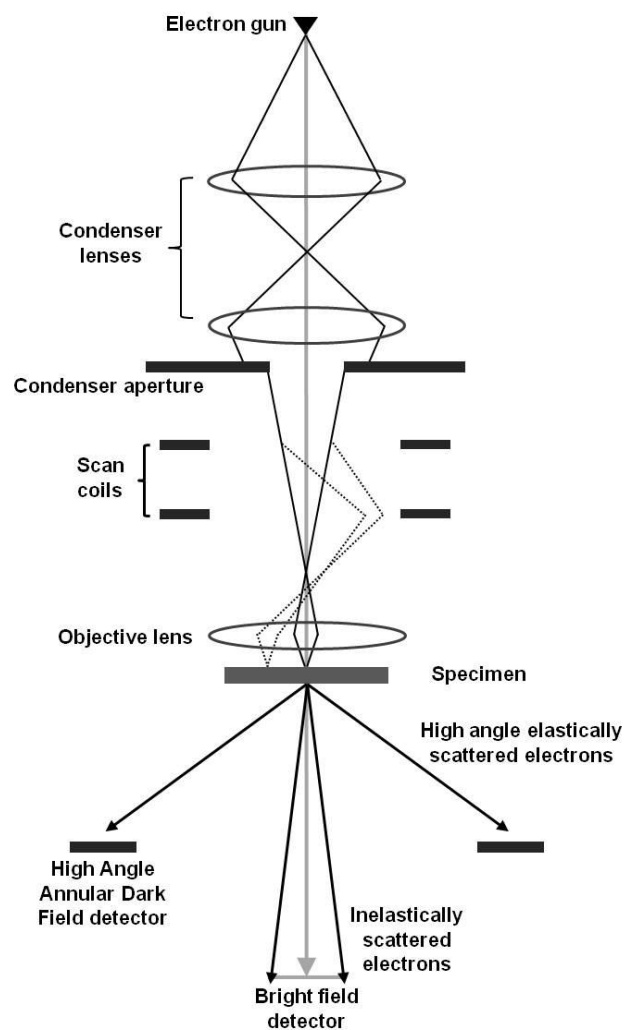


Figure 4.5. Schematic diagram showing the probe formation and scanning process in the STEM

as it is responsible for focussing the electrons to a spot – the size of which is determined by the quality of the electron-optics and the FEG. The lens aberrations affecting the STEM are analogous to the case of the TEM, with the spherical aberration here causing a broadening of the probe as opposed to a delocalisation of an object point. As such, they can be treated in much the same way as aberrations in the TEM, and a probe C_s corrector can be placed before the specimen in order to allow the beam to be focussed to a much smaller point. As with TEM, aberration correction in the STEM has led to a dramatic improvement in performance, with probe sizes of less than 0.1 nm – and therefore considerably less than typical interatomic spacings – now possible [153]. The significant reduction in probe size not only gives improved resolution, but has the added benefit of increasing the peak intensity of the probe, resulting in a better signal to noise ratio and therefore contrast in the image.

One major advantage of the STEM over the TEM is that the performance determining optics are before the specimen, meaning there is much greater flexibility in the imaging conditions used post interaction with the sample. Electrons undergoing low angle scattering can be used to build up a bright field (BF) image using a coherent phase contrast imaging process similar to the case of HRTEM. However, incoherent elastically scattered electrons are also generated by the electron-nucleus interaction, and these can be collected by a High Angle Annular Dark Field (HAADF) detector. By using an annular detector with an inner collection angle $> \sim 50$ mrad, the electrons undergoing Bragg diffraction can be discarded, leading to an image made up almost entirely of incoherent elastically scattered electrons. This imaging technique is known as HAADF STEM and is the most common mode of operation of the STEM, with its major advantage being that the intensity in the image is strongly sensitive to atomic number of the atoms in the specimen. As the electrons used for BF and HAADF imaging are collected by different detectors, it is possible to record both simultaneously, whilst the combination of HAADF imaging with EELS allows for the simultaneous acquisition of structural and chemical information, resulting in atomically resolved elemental maps [168, 169].

4.2.1 *Z* contrast imaging in HAADF STEM

Electrons collected by the HAADF detector are the result of elastic scattering following interaction with the atomic nucleus, and as such can be thought of as being analogous to Rutherford scattering. Geiger, Rutherford and his student Marsden famously discovered the atomic nucleus by measuring high angle elastic scattering from a thin gold foil. This observation led Rutherford to derive the differential cross section for elastic scattering with a nucleus of atomic number Z as:

$$\frac{d\sigma(\theta)}{d\Omega} = \frac{e^4 Z^2}{16(E_0)^2 \sin^4 \frac{\theta}{2}} \quad (4.19)$$

where θ is the scattering angle, Ω is the solid angle of collection, e is the electron charge, and E_0 is the energy of the incident radiation. When applied to electron microscopy, this expression should be corrected for electron screening and relativistic effects, however the proportion of high angle electrons collected can be thought of as being strongly dependent on the atomic number, Z .

Crewe and co-workers [170] would use this principle in their newly developed field emission gun (FEG) STEM to take the first high resolution ADF-STEM images. After using an annular detector to collect the elastically scattered electrons resulting from interactions with uranium atoms on a thin carbon support, the Z contrast nature of the image intensity enabled Crewe to provide the first images through electron microscopy of single atoms [170]. In today's aberration corrected microscopes, the incoherent nature of the HAADF STEM imaging process has recently seen the resolution of STEM overtake TEM, and resolutions of < 0.05 nm have been reported [171].

For a crystalline material imaged in HAADF STEM, the intensity of a particular atomic column will be directly dependent on the number of protons in that column, and is therefore a function of both the atomic number of the element, Z , and the number of atoms in the column. As such, HAADF STEM images contain information about the direction parallel to the beam previously inaccessible from other single transmission imaging techniques. Coupled with atomic resolution in the x - y plane, the Z contrast nature of the image therefore opens up the possibility of quantitative analysis of the 3D structure of nanomaterials with atomic resolution [172]. Also, the Z dependency of the

contrast in HAADF STEM provides a chemical sensitivity to the image, allowing clear identification of the size, structure and position of highly dispersed additional elements, crucial for understanding the role of dopant atoms in semiconductors [173] or supported single atoms [174] and clusters [75] in heterogeneous catalysis.

By using an annular detector with a high inner collection angle, the image intensity will result from electrons having undergone Rutherford scattering, and therefore should have a Z^2 intensity dependence. However, in the experimental HAADF STEM image the Z dependency is measured as being somewhat less than Z^2 , and this discrepancy between the expected and observed intensity has led to difficulties in quantifying the Z contrast image, and therefore the type and number of the atoms present. For example, recent results [175] of atomically resolved boron-nitride doped with carbon and oxygen found that the intensity of the atoms in the HAADF STEM image varied with $Z^{1.64}$, and indeed this is a fairly typical reported Z dependency of the experimental image. The difference between the observed experimental and theoretical intensity is known as the Stobbs factor [176], and its physical origins in HAADF STEM are thought to result from possible combinations of electron screening effects, the inclusion of some inelastic signal, and reduced intensity due to the signal to noise ratio of the image; whilst remaining intensity discrepancies are thought to originate from the nature of thermal diffuse scattering [177].

An additional complication comes from the observed saturation of image intensity with sample thickness, and this is again thought to be due to the effects of thermal diffuse scattering, coupled with electron channelling effects, causing both absorption and oscillations of the electron beam along the column [178]. The non-linear nature of intensity with thickness necessitates the close comparison of images with simulations that include the effects of thermal diffuse scattering and accurate Debye-Waller factors in order to obtain quantitative information from the Z contrast image.

The uncertainty over the Z contrast dependence has therefore meant fully quantitative interpretation of intensities in HAADF STEM images has proven difficult. Traditionally, comparison between experimental images and simulations required the use of an empirical intensity scaling factor [179] used to provide semi-quantitative

agreement. However, recent advances in both the simulation and imaging techniques have led to the reports of fully quantitative Z contrast imaging [180], leading to the ability to count the number of atoms in each column to ± 1 atom, as well as the previously discussed sub atomic resolution in the x - y plane.

The most successful technique used to date has been to place the image intensity on an absolute scale by plotting it as a fraction of the incident probe intensity. This then allows direct comparison with simulations, in which the intensity given is normalised to the incident beam intensity. For this to be possible, several careful calibrations are first required, including knowledge of the probe width, convergence angle and current; the linearity of the HAADF detector response; a preamplifier with sufficient dynamic range to include the intensity of the incident probe; and careful control of the image processing conditions to ensure no saturation of the contrast with output voltage [181]. In addition, more accurate simulations of the elastic scattering events are needed. These are now provided by the frozen phonon model [182, 183], using accurate Debye-Waller factors that vary as a function of atomic position [184], coupled with incorporating the effect of spatial incoherence that results from the finite probe size [184]. Through a combination of these experimental and theoretical techniques, it is now possible to quantify the number of atoms in a column with up to single atom sensitivity [180].

4.3 *In-situ* electron microscopy

The sub angstrom resolution provided by electron microscopy offers a powerful tool for determining the local atomic structure of materials. However, in the case of heterogeneous catalysis, the nature of the atomic structure will be strongly influenced by the surrounding environment. Therefore, to understand the structure-property relationships of a working catalyst, information at the atomic scale under simulated reaction conditions is needed. This is the driving force for the development of *in-situ* environmental electron microscopy techniques under controlled conditions of gas atmosphere and specimen temperature.

Traditionally there have been two approaches towards simulating reaction conditions inside what is usually a high vacuum instrument. The first is through the use of a

specially designed holder [185], in which the sample is trapped between two electron transparent windows that enclose the gas environment. One advantage of such a technique is that it allows for reasonably high gas pressures, as well as exposure of some gases or liquids to the sample which may not be possible using an alternative approach. This makes such environmental cells particularly useful for high pressure reactions, or for study of biological specimens in which the presence of water may be a necessity. However, one danger of such a technique is that the thin windows used to encapsulate the gas or liquid medium are liable to ruptures, leading to severe potential consequences for the microscope. Thicker windows can be used to somewhat mitigate this risk, but will have a detrimental effect on the possible imaging resolution.

The second approach is to use a differential pumping system [186, 187], in which gas is inserted into the sample area but then rapidly pumped out above and below the sample by additional gas tolerant turbomolecular pumps, quickly recovering the high vacuum condition in the rest of the column. The resulting usable pressure range at the sample is somewhat limited in comparison with the environmental cell holder, but essentially the performance of the microscope can be maintained to provide clear insight at the atomic scale under simulated reaction conditions.

4.3.1 Double aberration corrected environmental EM at York

The development of aberration corrected microscopes has had important consequences for environmental transmission electron microscopy. In a conventional TEM, the spherical aberration coefficient was minimised by reducing the size of the objective lens polepiece, meaning there was as a consequence little space to work with around the sample. In order to incorporate additional gas diffusion limiting apertures, or the use of a regular heating holder, a sacrifice in the performance of the microscope as a result of increased spherical aberration was needed. However, by subsequent correction of the spherical aberration, the polepiece gap can be increased with only a marginal detrimental increase in the chromatic aberration coefficient – providing the polepiece gap stays within a critical range (2-5 mm at 200kV) [188, 189] – thereby allowing much greater flexibility in the microscope design.

As well as much improved resolution, aberration correction gives minimal delocalisation and a complete range of contributing spatial frequencies in each image frame. The resulting directly interpretable image allows for accurate studies of dynamic processes under a controlled environment at the atomic scale, and as such represents a major advance for *in-situ* microscopy. Additionally, the consistent phase contrast means that through-focal series are no longer always necessary; allowing for minimal exposure of the sample to the potentially invasive electron beam.

Figure 4.6 is a schematic representation of the environmental (scanning) transmission electron microscope, or E(S)TEM, recently developed at the University of York. The design is based on the previous differentially pumped ETEM design of Boyes and Gai [186] (and later commercialised by FEI), modified to be compatible with a JEOL 2200FS FEG (S)TEM equipped with both probe and image C_s correctors. As such, this microscope represents the world's first double aberration corrected E(S)TEM, with resolution of < 0.1 nm in both TEM and STEM modes [188].

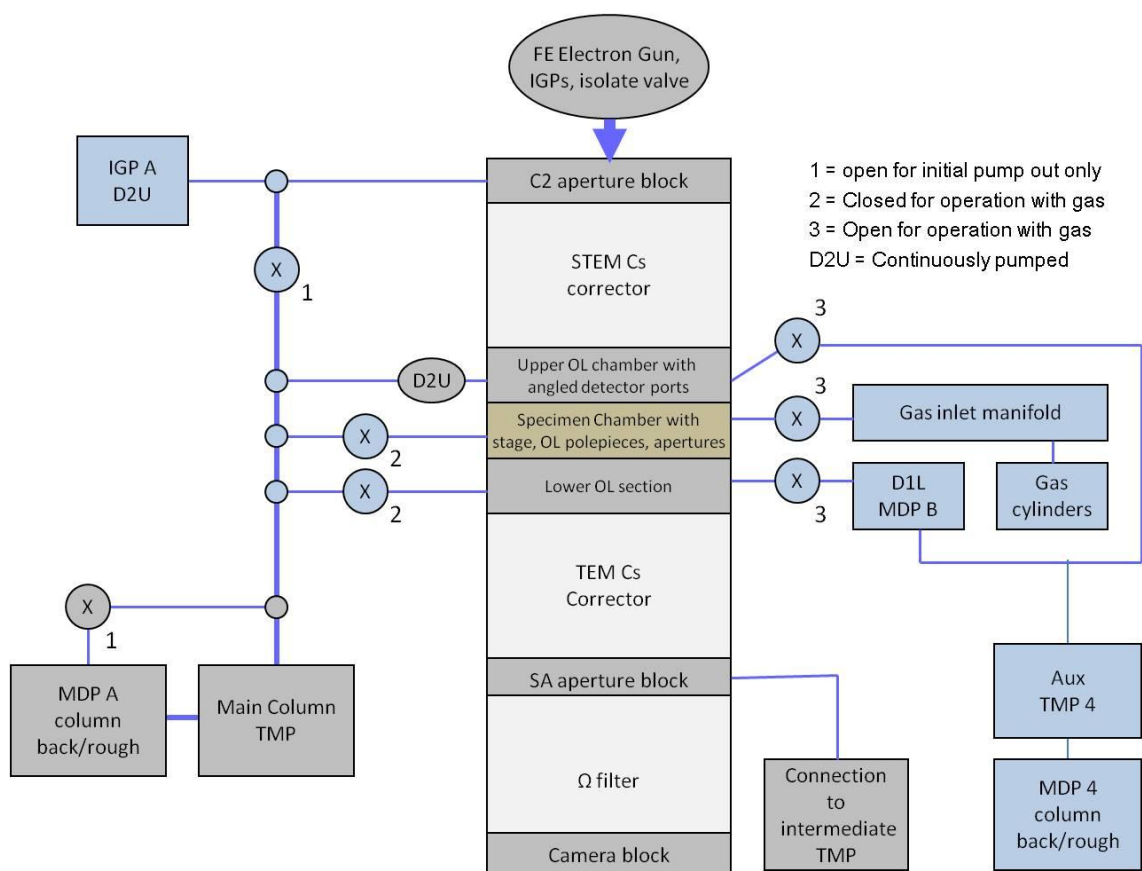


Figure 4.6. Schematic diagram of the double aberration corrected E(S)TEM at the University of York. Reproduced from Gai and Boyes [190].

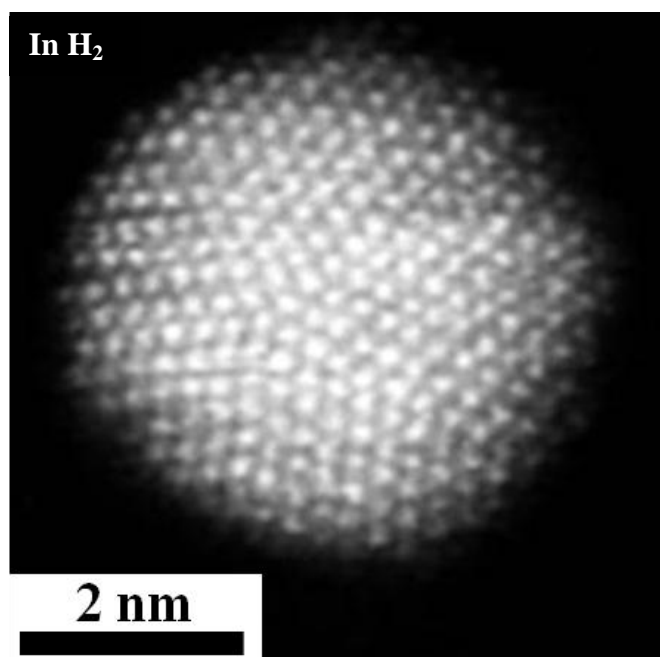


Figure 4.7. Probe corrected atomic resolution HAADF ESTEM of a multiply twinned gold nanoparticle in hydrogen

Figure 4.7 is an example of the performance of the probe corrected HAADF ESTEM, showing clear atomic resolution of a gold decahedral nanoparticle, in which the nature of the multiply twinned structure is clearly revealed in the presence of hydrogen. The exact pressure at the sample, in the range of 0.01 – 0.1 mbar, is still to be precisely calibrated, but typically is ~ 0.05 mbar. This is enough to provide up to 10^5 monolayers of gas per second and therefore to dominate the surface chemistry [190].

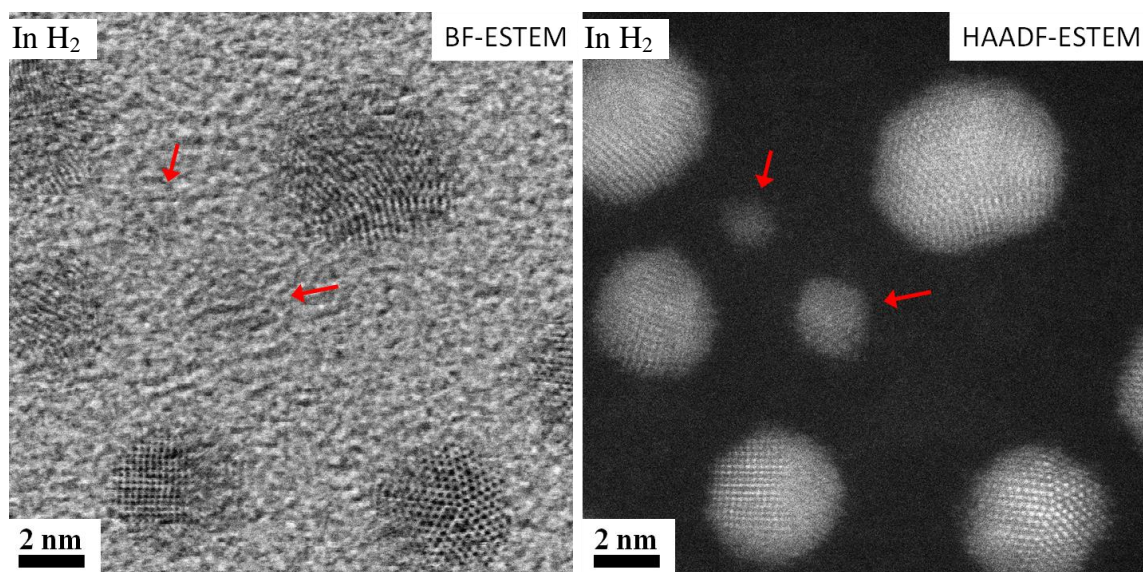


Figure 4.8. Comparison of BF and HAADF ESTEM images of gold nanoparticles in hydrogen shows the advantage of Z contrast for imaging small particles and clusters.

Importantly, the recent modifications not only incorporate the use of a probe C_s corrector, but also allow collection of the full range of high angle elastically scattered electrons by the HAADF detector. This therefore enables atomic resolution Z contrast *in-situ* imaging, and Figure 4.8 clearly shows the advantage of such a technique for identification of small particles and clusters often crucial to catalysis. As well as enabling operation in a controlled gas environment, the wider gap polepiece afforded by aberration correction provides room for the use of a regular commercial heating holder. In the case of the present work, a Gatan 628 tantalum furnace type heating holder has been used, capable of delivering 0.1 nm resolution at controlled temperatures of up to $\sim 900^\circ\text{C}$ [188, 189].

Chapter 5

Structural studies of gold nanoparticles

Studies of gold nanoparticles on two dimensional model supports through aberration corrected transmission electron microscopy (AC-TEM) are presented in the following chapter, including detailed studies of both the internal structure and external surfaces of gold particles in the catalytically active size regime. Sub-angstrom resolution enables clear identification of previously reported active sites, as well as a new structural origin for the enhanced reactivity of small gold particles due to electronic band structure modifications that result from common particle morphologies. The identification of active sites allows for subsequent studies of their stability in Chapter 6.

5.1 Sample preparation

3.5 nm thick amorphous carbon supports were deposited on to holey carbon grids in order to provide reduced background noise and improved resolution of weak phase objects such as small nanoparticles. The thin carbon films also provide a better defined and more uniform support material than conventional carbon TEM grids. Colloidal gold nanoparticles in the size range of 1-10nm suspended in water were then deposited on to the support, as shown in Figure 5.1. Au particles supported on commercially available Si_3N_4 membranes (30 nm) were also used as a basis for comparison.

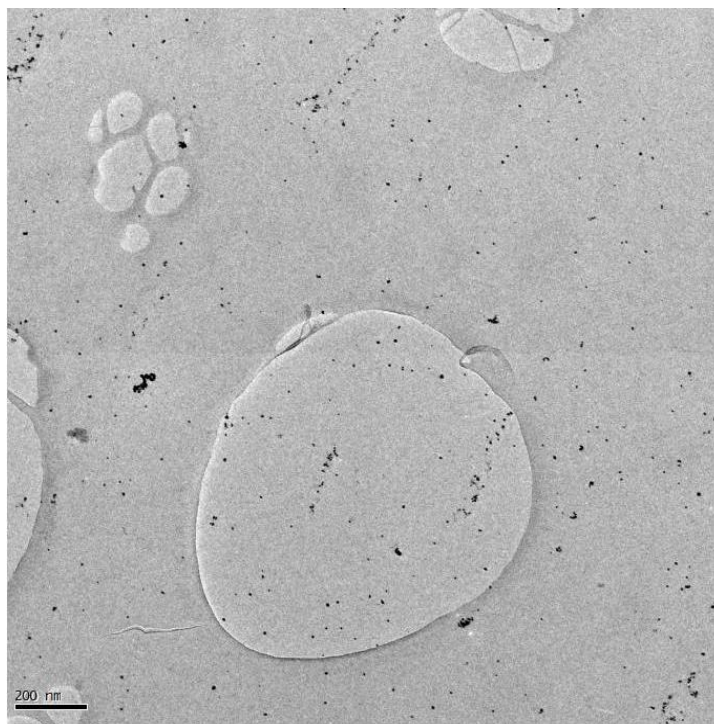


Figure 5.1. Low Magnification image recorded at x10k showing gold nanoparticles on thin carbon film supported on a holey carbon grid.

5.2 Gold particle structures

The Wulff equilibrium shape [96] for FCC metals is an octahedron bound by $\{111\}$ facets, truncated by a cube that adds additional $\{100\}$ surfaces [97]. This single crystal structure is commonly referred to as a truncated octahedron or a cuboctahedron, and an example of such is shown in Figure 5.2. However, at this small size range, surface energy terms provide a substantial contribution to the overall energy of the nanoparticle, meaning that single crystal structures with higher energy surface facets may not be energetically favourable [106]. The inclusion of internal twin boundaries enables alternative particle morphologies with reduced surface energies [110].

In the size range of 2-10 nm the most commonly observed structures of gold are the multiply twinned icosahedra and decahedra [191, 192]. As such structures are crystallographically forbidden, significant internal strain must be incorporated in order to make up for their non-space filling nature [110]. Icosahedra are made up of 20 tetrahedra bound by three $\{111\}$ twin planes. Therefore interpretation of icosahedral

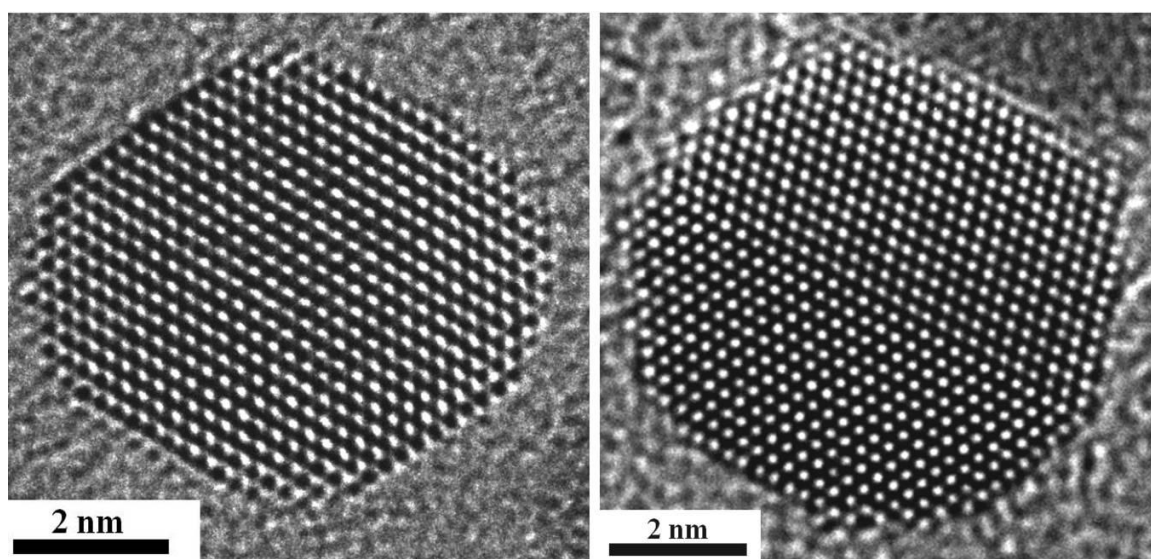


Figure 5.2. Gold nanoparticles in the [110] orientation exhibiting single crystal (left) and single twinned (right) structures.

images is not straight forward, as the overlap of different tetrahedra precludes a common zone axis to the particle. This is demonstrated in Figure 5.3 – showing icosahedra orientated in or close to the 2 fold, 3 fold and 5 fold symmetry axes.

Figure 5.4 is an example of a decahedron, consisting of five crystals each bound by two {111} twin planes, whilst {111} re-entrant facets act to further minimise the particle's

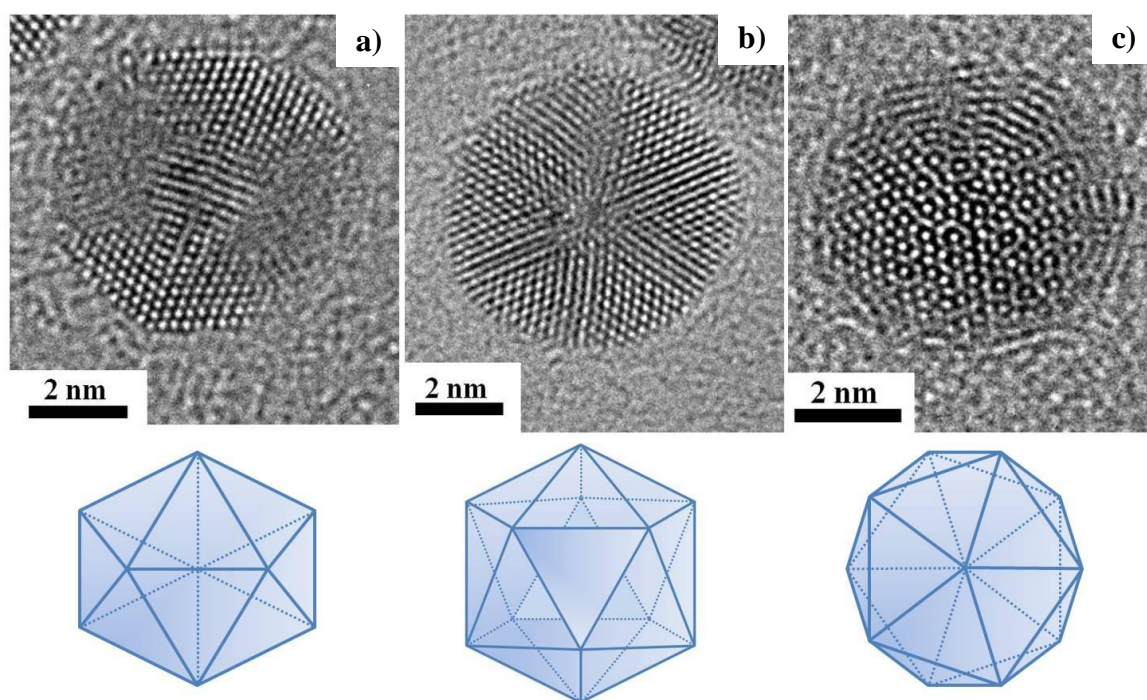


Figure 5.3. Icosahedral gold nanoparticles in or near the 2 fold (a), 3 fold (b), and 5 fold (c) axes.

surface energy [106]. Here the particle is in the [011] zone axis, meaning that each crystal segment is in the same zone axis, with the strain distributed around the rotational axis by a disclination in order to make up for the 7.35° missing angle. A fast Fourier transform (FFT) gives a representation of the optical diffraction pattern (ODP) of the image, with the twinned structure producing several symmetry related diffraction spots.

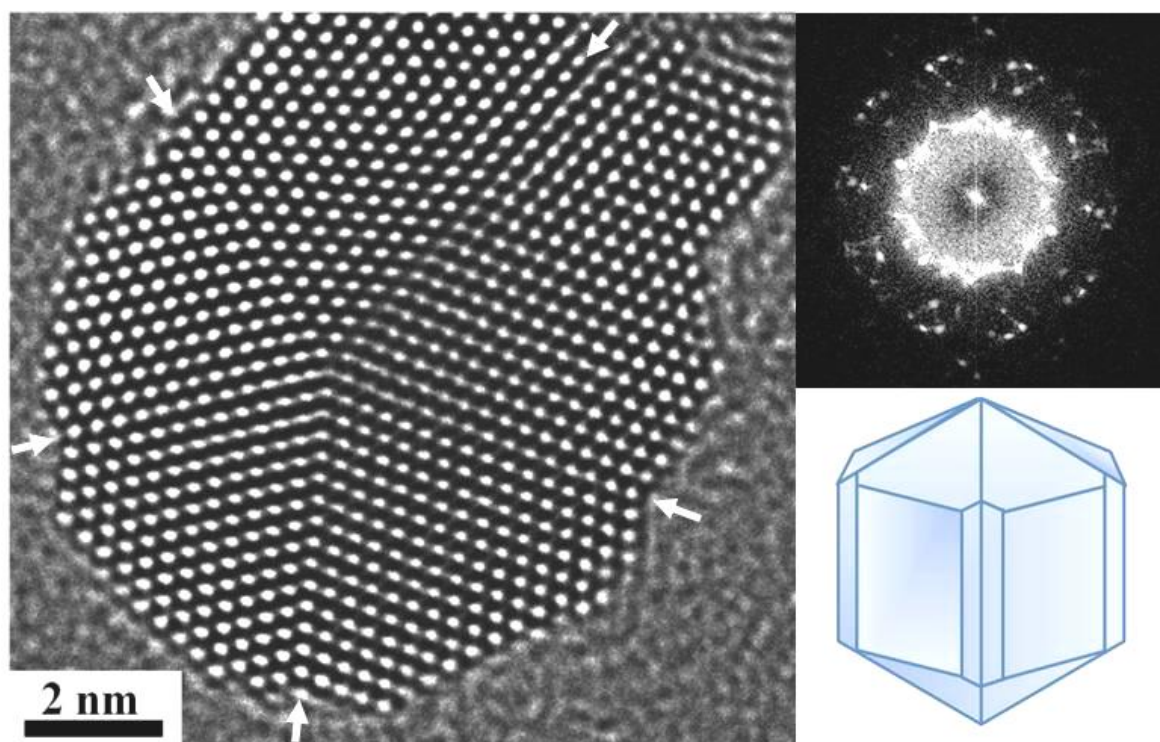


Figure 5.4. A decahedral Au nanoparticle in the [011] orientation with re-entrant facets at the twin boundaries (arrowed) and corresponding FFT and structure schematic.

5.3 The structural origin of gold nano-catalysis

The small energy difference between the most common particle morphologies means that variations in the local environment or the number of atoms present can produce a variety of structures. Figure 5.5 shows an example of a possible twinning dislocation in a gold nanoparticle in the [011] orientation. Such defects may arise due to internal stresses during crystal growth or the initial crystallisation. Tilting of the particle into alternative zone axes needed for full displacement vector analysis is avoided due to concerns over the effect of the electron beam on the particles atomic structure during the long exposure times needed. However, preliminary displacement vector of the partial dislocation bonding the (111) twinning plane can be inferred based on measurements of

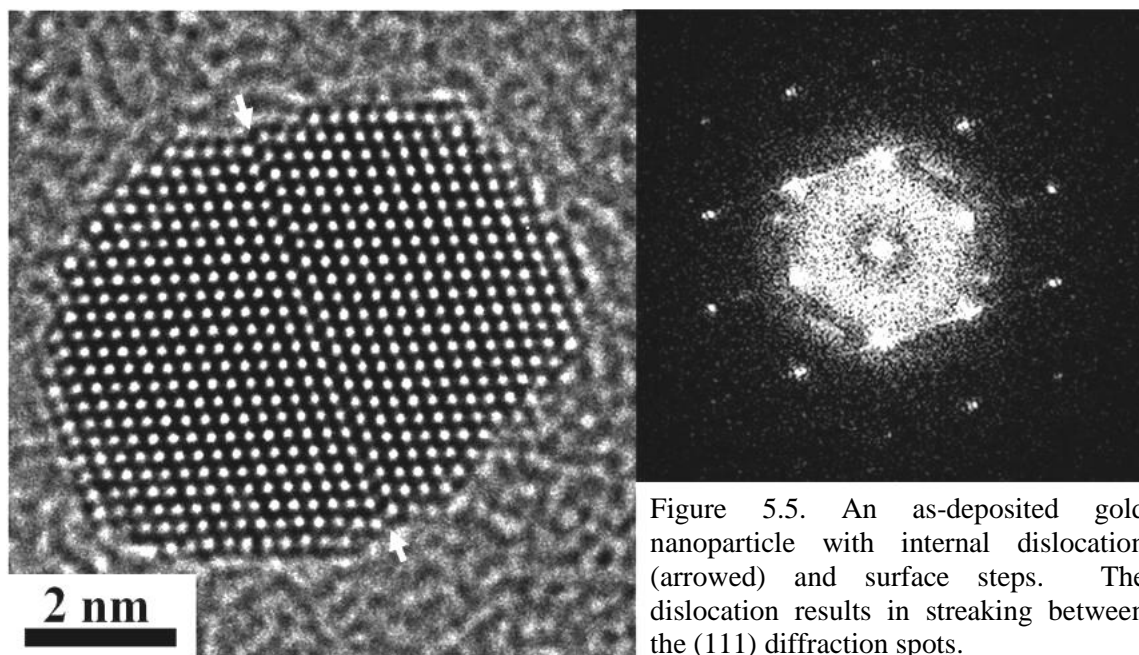


Figure 5.5. An as-deposited gold nanoparticle with internal dislocation (arrowed) and surface steps. The dislocation results in streaking between the (111) diffraction spots.

the atomic scale planar image and corresponding FFT – which is streaked in the (111) direction – and suggests that the Burgers vector of the partial dislocation is of the type $1/6 [211]$. Also clear from the image is the highly stepped nature of the surface. The internal dislocation terminates in a partial terrace at the surface, whilst the rest of the surface is regularly stepped throughout the perimeter of the particle. Such a disordered surface structure generates an abundance of low co-ordinated surface sites thought to be crucial for the catalytic activity of gold nanoparticles. The stability of these active sites will be the subject of study in Chapter 6

5.3.1 The effect of strain on catalytic properties

Despite the promising reported catalytic properties of surfaces with support induced strain [90, 92, 93, 95], their application on a large scale is unlikely, as the strain will be released by the formation of dislocations or reduced by annealing at elevated operating temperatures. Furthermore, the strain will be greatest at the support interface and therefore not easily accessible to incoming gas molecules. However, until now, the effect of strain inherent to crystallographically forbidden particle morphologies has been largely overlooked when considering origins for the surprising catalytic activity of small gold nanoparticles. As we have seen, for the size range in which gold is catalytically active, the most common structures are the icosahedra and decahedra, both of which are known to have substantial intrinsic strain.

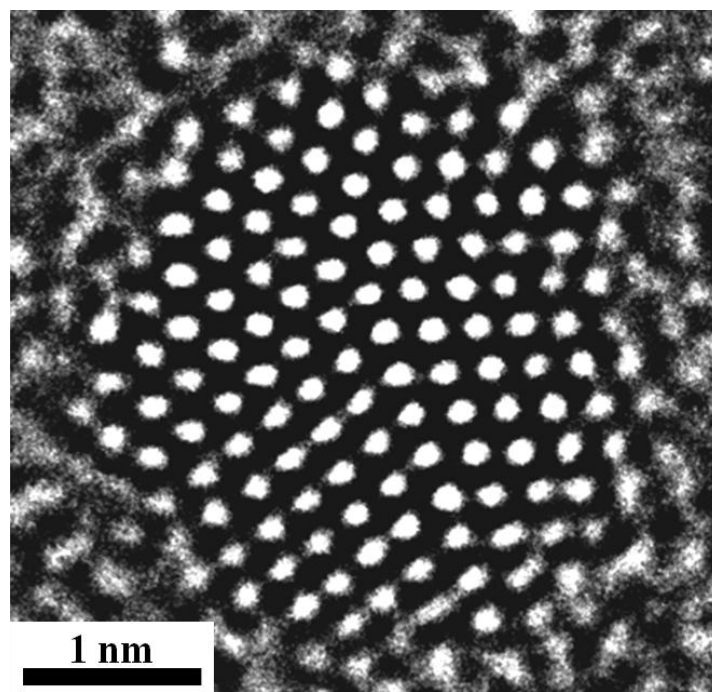


Figure 5.6. 3 nm Au decahedron with re-entrant facets.

Figure 5.6 shows an example of a gold decahedral particle in the [011] orientation supported on 3.5 nm thick amorphous carbon. The directly interpretable single image provided by aberration correction allows for minimal exposure of the particle to the electron beam. The particle is approximately 3 nm in diameter, and shows the classical Marks decahedral structure [106, 110]. However, truly quantitative analysis of the local strain in multiply twinned structures by conventional approaches, such as geometrical phase analysis (GPA) [193], is difficult. The need to define a reference vector leads to imposed discontinuities across the crystal boundaries, as seen in Figure 5.7, whilst the approach also requires an unstrained reference area to be defined, within which it will minimise any phase gradients before comparing with other areas in the image. This is not very practical for a small nanoparticle, let alone one that is internally twinned, with each crystal segment only a few atoms across. The resulting analysis means that one of the crystals appears unstrained due to it including the reference area, whilst the strain map of the rest of the particle is discontinuous at the twin boundary, leading to the observation of apparent strain at the interface. However, the significant internal strain due to the crystallographically forbidden nature of the decahedral particle can still be seen qualitatively when compared with the similar analysis of a single crystal particle.

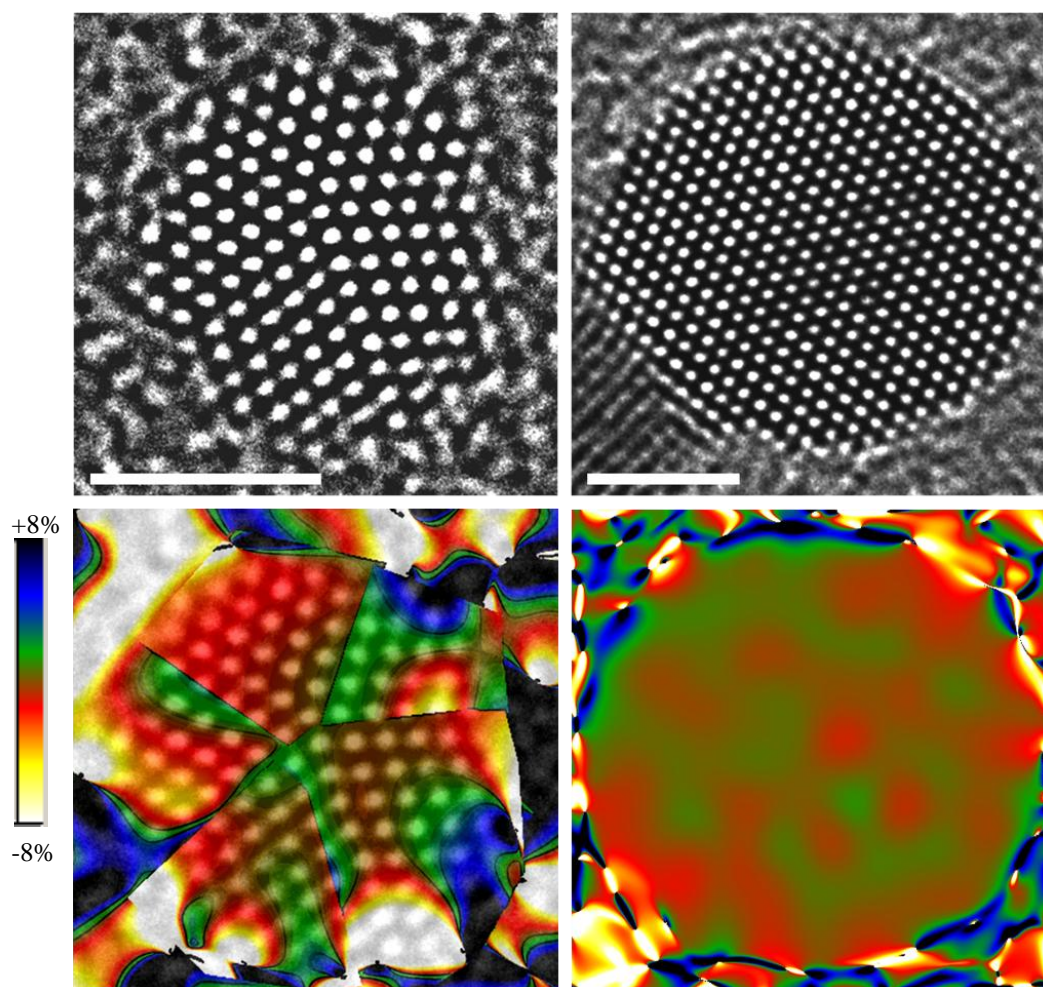


Figure 5.7. Geometrical phase analysis of D_{xy} strain in both decahedral and single crystal structures. Scale bars indicate 2 nm.

5.3.2 Quantitative strain analysis through a real space approach

In order to provide truly quantitative information on the nature of the atomic column displacements that result from inherently strained structures, an alternative approach [194] was developed in order to remove the need for a reference area and reference vector – and therefore any unphysical discontinuities at the crystal boundaries. Working in real space, an initial threshold is put on the image in order to identify the atomic columns, and only intensity values above this threshold are selected. The threshold level was carefully adjusted for each image used and several values were tried in order to obtain the optimum level. At this point each atomic column highlighted was checked manually in order to ensure that all peaks had been identified; no random bright areas had been misidentified as atomic columns; and that there were no spurious peaks

present as a result of intensity variations across the intensity profile of the peak. Plots of the peak intensity integrated across the atomic columns revealed the intensity distributions to be Gaussian and symmetrical about the centre of the peak. Therefore the x - y co-ordinate of each atomic column was defined as the centroid of the intensity above the selected threshold value.

In order to accurately determine the position of each atomic column a high quality spherical aberration free image with consistent phase contrast and minimal delocalisation is essential. The particle must also be orientated in a zone axis in order for clear resolution of the individual columns. The accuracy with which it is possible to define the atomic column co-ordinates is the largest identified source of error and determines the final uncertainty limits in the measured nearest neighbour distance. This is a random error due to the pixel size (0.01nm) and leads to an uncertainty of $\pm 3.5\%$ in the measured nearest neighbour distance. Any strain resulting in a bending of the column is not directly observable and will lead to a slight averaging of the column position.

From this point the x - y co-ordinates of each column are fed into code developed in-house [194] in order to provide the corresponding nearest neighbour distances. Distances are measured only to the immediate neighbouring columns (6 for a bulk column in [011] projection), with a limit on the allowed neighbour distance preventing measurements to second order neighbours and beyond. Understanding of the crystallography of the particle in question allows us to compare each distance measured to the known nearest neighbour distance of bulk gold (0.288 nm) and to analyse both the amount of strain with respect to the bulk value and its location. Whilst the two dimensional image only allows analysis of strain in the x - y plane, it can be assumed that there is minimal strain in the z direction, as the disclination axis is aligned parallel to the direction of the electron beam [194]. For the purpose of correcting measured distances in the x - y projection to real nearest neighbour distances it is assumed there is no strain in the axis parallel to the beam, whilst no such assumption is needed for inter-atomic distances measured between atoms in a plane normal to the beam, as depicted by the black lines in Figure 5.8.

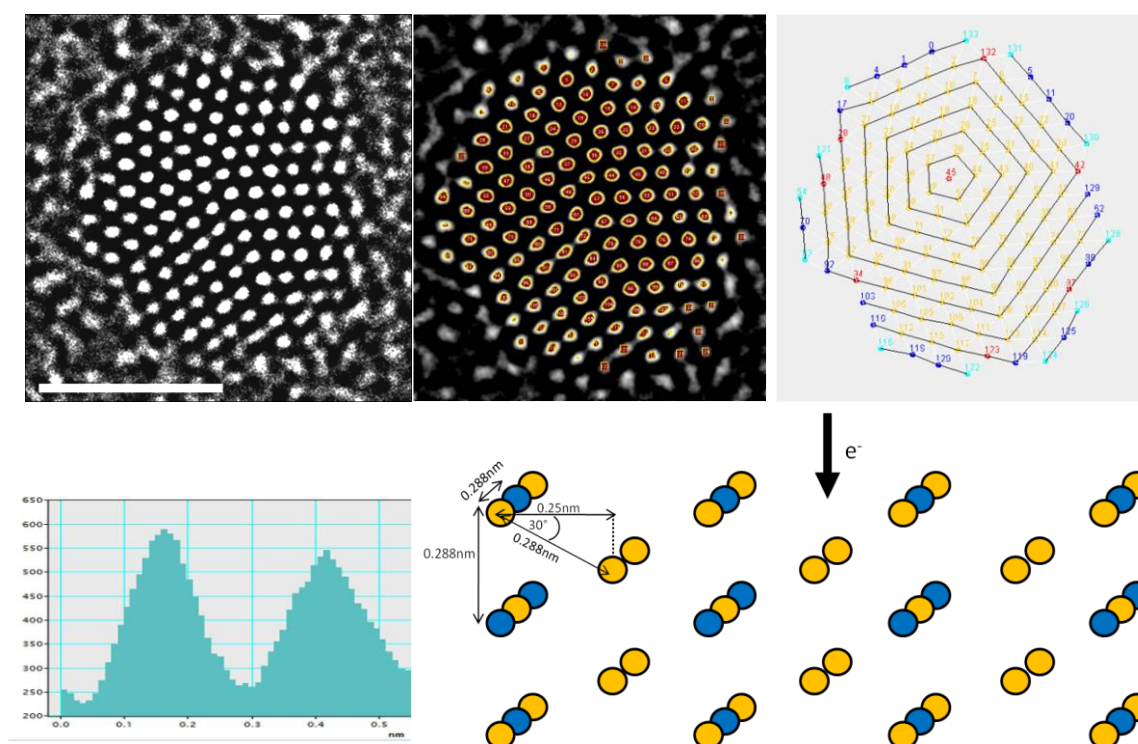


Figure 5.8. Atomic column displacements are measured by identifying the x - y co-ordinates of each column and measuring the distances from one co-ordinate to the next, correcting for crystallographic orientation.

Using the real space approach of measuring atomic column displacements, the corresponding distributions of nearest neighbour distances are plotted in Figure 5.9 for both the decahedral (left) and single crystal (right) particles. The measured atomic spacings for the decahedral structure follow a lognormal distribution, with a mean nearest neighbour distance (with standard error) of 0.290 ± 0.002 nm, whilst the tail of

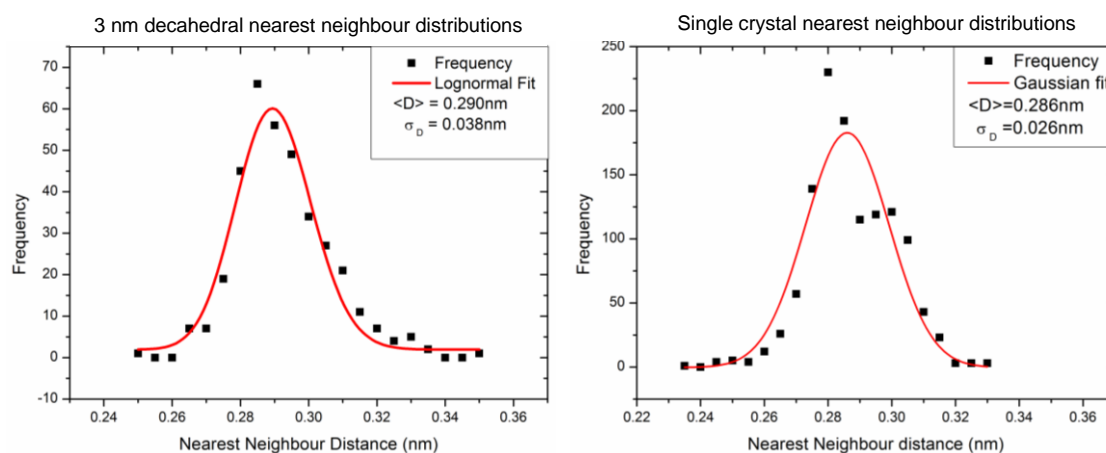


Figure 5.9. Distribution of nearest neighbour distances measured for a 3 nm decahedral particle (left) and a 4 nm single crystal particle (right).

the lognormal curve shows a number of positively strained nearest neighbour distances measured. In comparison, the single crystal structure shows a Gaussian distribution with a mean nearest neighbour distance 0.286 ± 0.001 nm, with the standard deviation being a result of some random error in the analysis that results from the small uncertainty in the column position. However, the range of nearest neighbour distances measured is reduced, whilst the larger distances corresponding to areas of large expansive strain are missing.

For the 3 nm decahedron, average strain measured as a function of distance from the fivefold axis is shown in Figure 5.10, whilst strain maps can be plotted from a xyz matrix containing the atomic column positions and the magnitude of the measured displacements using the OriginLab graphical software. Figure 5.11 shows 3D surface plots of the measured nearest neighbour distances for both the decahedral and single crystal particles. The 3 nm decahedron exhibits regular expansions of up to $15 \pm 3.5\%$, and these highly strained inter-atomic distances predominantly correspond to both circumferential and radial strain at the surface. Corresponding 2D strain maps are provided in Figure 5.12 and both these and Figure 5.11b) show that when the need to define a reference vector is removed, the location of the twin boundaries is not observed, thus showing that the strain is coherent across the twin interface.

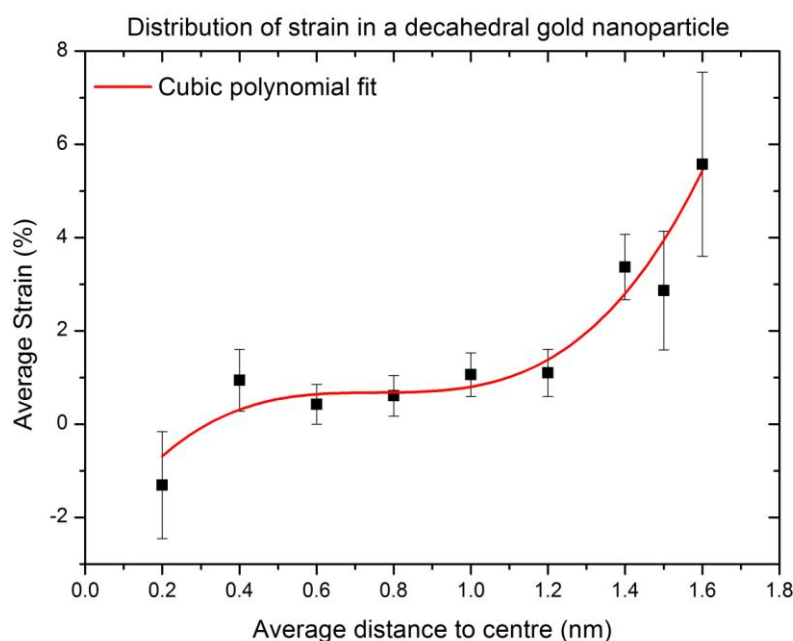


Figure 5.10 Average strain measured as a function of distance from the fivefold axis in a 3 nm decahedral particle.

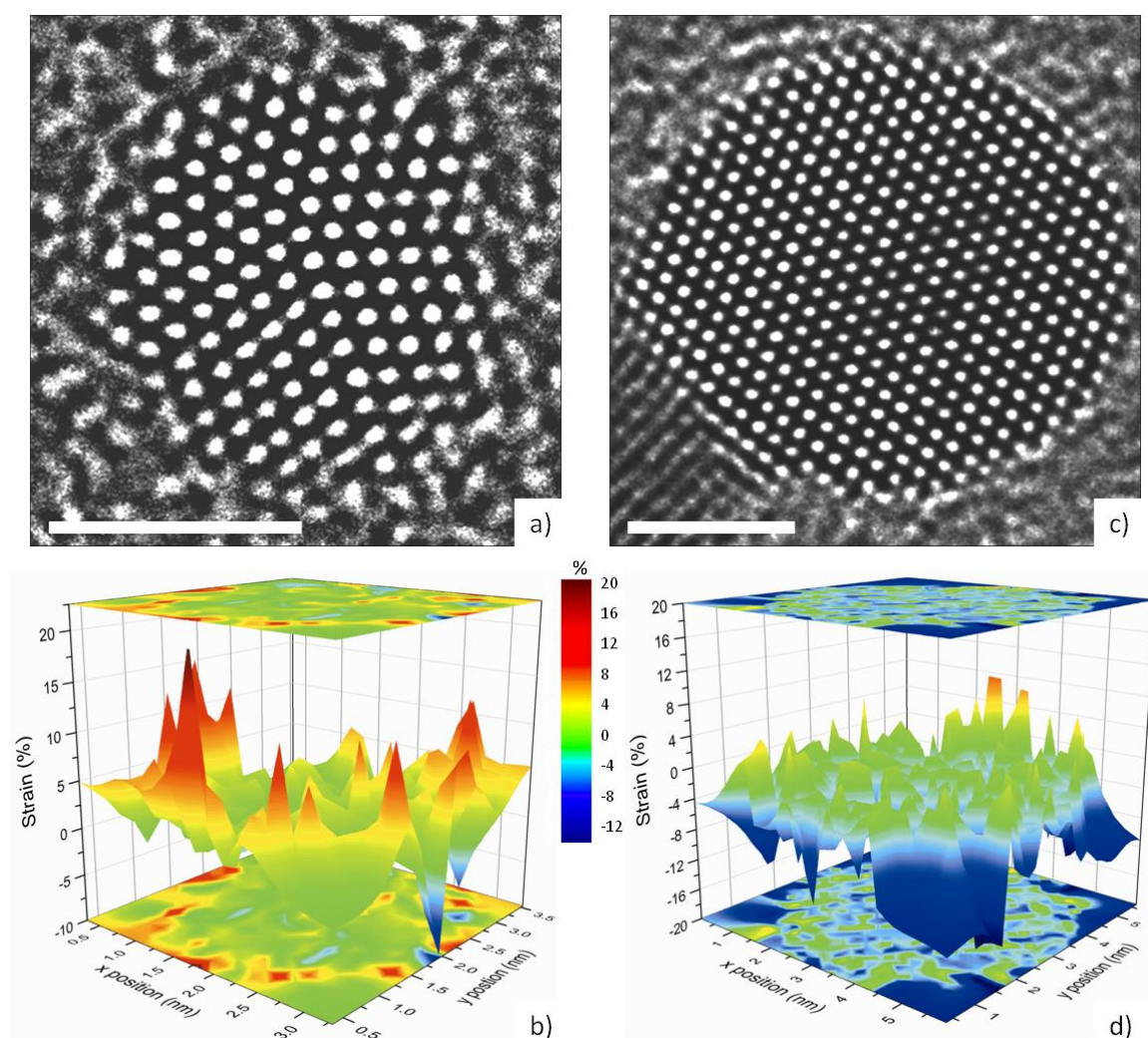


Figure 5.11. AC-TEM images of a decahedral particle (a) and single crystal particle (c) with corresponding strain distributions (b and d). Scale markers indicate 2 nm.

From both Figure 5.10 and Figure 5.11b) some expected compression is observed near the crystallographic centre, whilst an average expansive strain of 5.6% is found at the surface. The large error bar corresponding to the average surface strain value indicates the larger distribution of nearest neighbour distances measured at the surface. The d band model [85] suggests that changes in the local lattice parameter of this magnitude will have a profound influence on the band structure of the particle and thus on their physical and chemical properties. These effects are attributed to the inherent strain associated with the crystallographically forbidden nature of the structure and are larger than anything previously reported due to interface strains [94]. Accordingly they may be amongst the more important factors in practical catalytic applications; since they are both the largest effects known to have been reported to date and they affect directly the

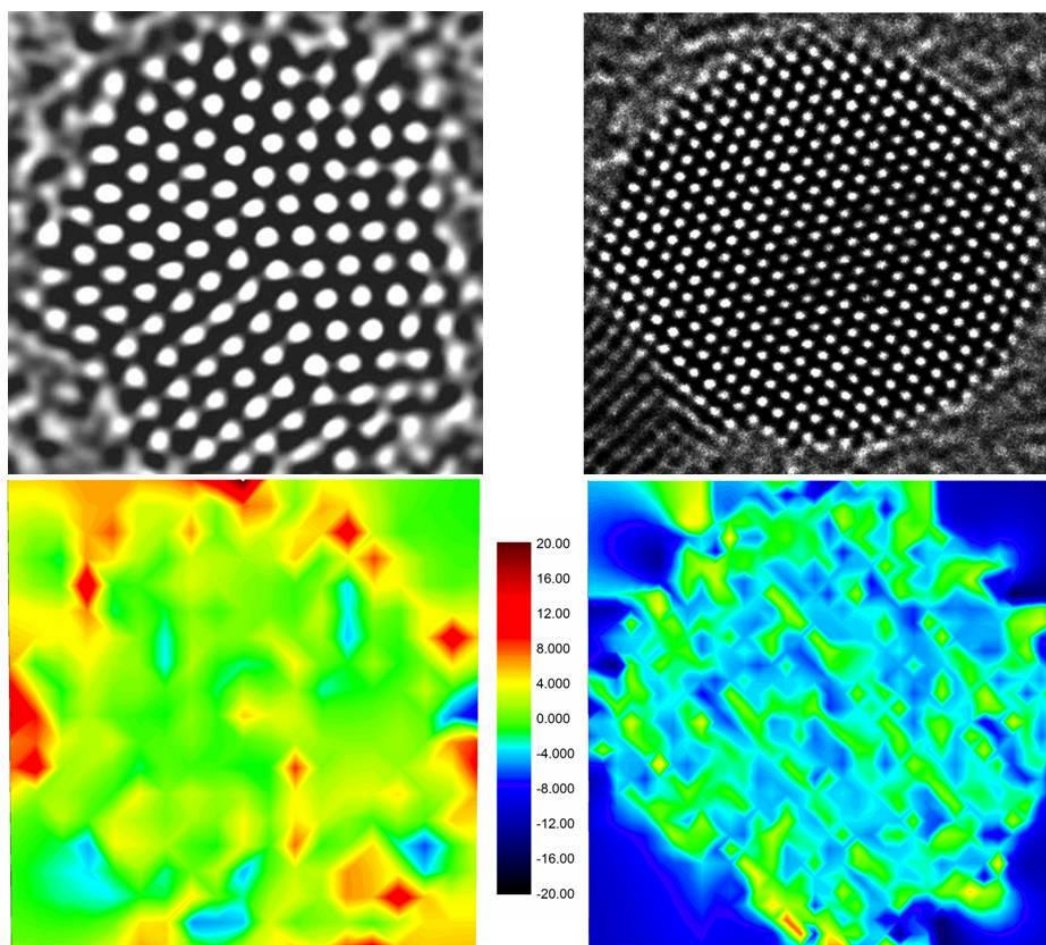


Figure 5.12. 2D strain maps of both decahedral (left) and single crystal (right) structures.

free outer surfaces exposed for reactions with gas molecules.

As a basis for comparison, a single crystal gold nanoparticle in the [011] orientation is shown in Figure 5.11c). This particle is again as-deposited, and prepared and imaged under the same conditions as the decahedral particle. Here the single crystal structure should have no inherent strain, and therefore any strain measured will be a consequence of beam induced atomic rearrangements, an artefact of the analysis or the effect of electronic density redistribution due to surface stress and high surface to volume ratio of the nanoparticle [195]. Analysis of the single crystal structure shows the particle is largely unstrained, whilst some small contraction relative to the bulk nearest neighbour distance (0.288 nm) can be expected at this size range [196]. The surfaces of the single crystal particle are generally unstrained or slightly compressed, whilst the few areas that show expansion at the surface set an upper limit on non-structure specific strain and apparent strain induced by the imaging or analysis process. However, by comparing the

strain maps in Figure 5.11(b) and Figure 5.11(d) it is clear that the single crystal structure, measured in the same way, exhibits nothing like the strain of the crystallographically forbidden decahedral particle, and that the surface of the decahedral particle is highly strained compared to the surface of the single crystal.

Through similar analysis of the larger 9 nm decahedron shown in Figure 5.4, it is possible to study the effect of particle size on the distribution of strain throughout the decahedral structure. Both GPA and real space measurements of atomic column displacements are shown in Figure 5.13, and again it is clear that there is compressive strain surrounding the fivefold axis, with expansive strain observed at the surface. Furthermore, in the real space analysis no strain is detected across the majority of the twin boundaries, with the uppermost tetrahedron exhibiting some small compression at each edge as a result of lattice plane alignment following partial coalescence with another particle. This is in direct contrast with the GPA results, which show strain at the twin boundaries as a result of the reference vector changing at the interface.

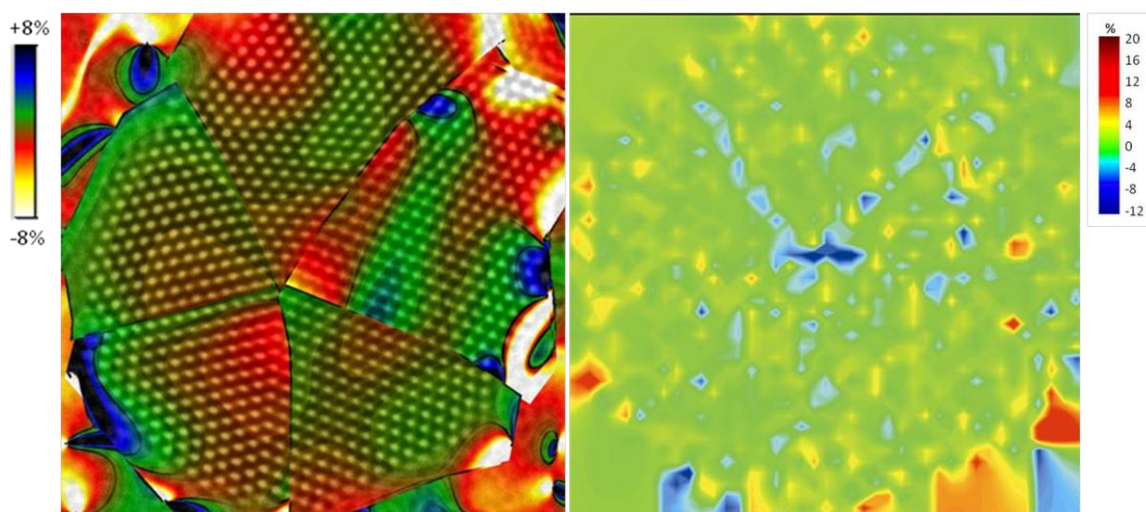


Figure 5.13. GPA (D_{xy} left) and in house (right) strain maps of a Marks decahedral nanoparticle.

The mean atomic column displacements as a function of distance to the centre of the particle for both the 3 nm and 9 nm decahedra are shown in Figure 5.14. Both particles show similar compression of nearest neighbour distances by $\sim 2\%$ at the centre. However, a gradual expansion of nearest neighbour distances is observed in the larger 9 nm decahedron as we move towards the surface, resulting in an average expansive surface strain of $\sim 3\%$. In contrast, the 3 nm decahedron exhibits significantly expanded

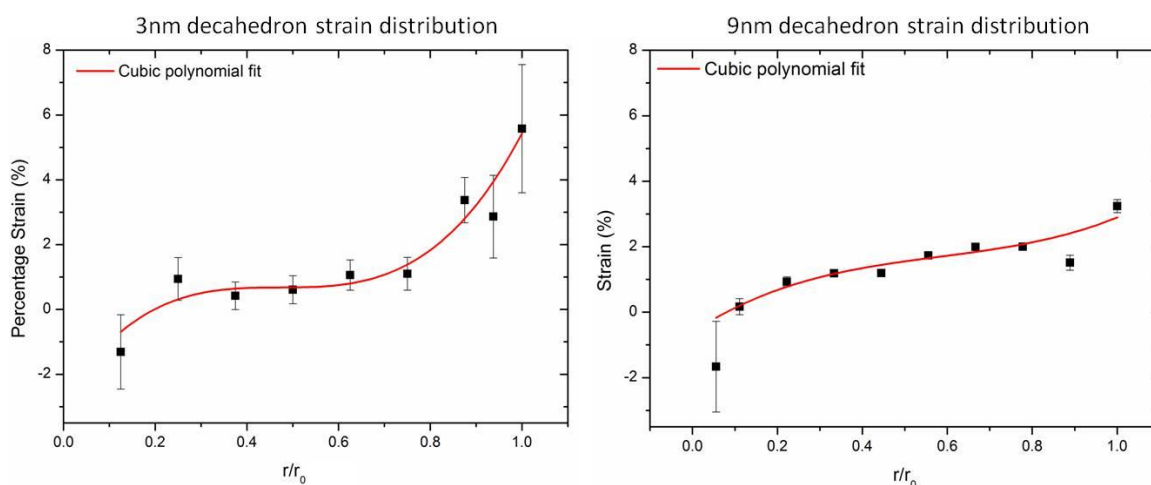


Figure 5.14. Strain measured as a function of distance from the fivefold axis for 3nm (left) and 9nm (right) Au decahedra.

nearest neighbour distances at the surface, with an average surface strain of $\sim 6\%$ and many surface atom column positions strained by more than 10%. Such highly strained surface atoms are expected to act as initial active sites for adsorption of reactant molecules, meaning that the activity of inherently strained structures such as the decahedra will diminish with increasing particle size. This conclusion correlates well with the reported catalytic properties as a function of particle size [46].

5.3.3 Calculations on the effect of strain on catalysis

In order to quantify the effect of such large surface strains intrinsic to the decahedral structure, density functional theory has been used¹ to calculate the adsorption energy for CO on Au(111) surfaces with strain increasing up to 15% [194]. Ground state calculations were carried out by VASP code [197, 198] based on density functional theory (DFT) [199]. The electron-ion interaction was represented by the projector augmented wave (PAW) method [200], and the generalized gradient approximation (GGA) [201] is used for formalism of the exchange-correlation term. Configurations of valence electrons are $5d^{10} 6s^1$ for Au, $2s^2 2p^2$ for C, and $2s^2 2p^4$ for O. Basis functions include plane waves up to kinetic energies of 400 eV. All atomic configuration figures related to DFT calculations were produced using the visualization program VESTA [202].

¹ DFT calculations were provided by collaborators Drs A. Kuwabara and K. Yoshida from the Japan Fine ceramics centre, Nagoya, Japan

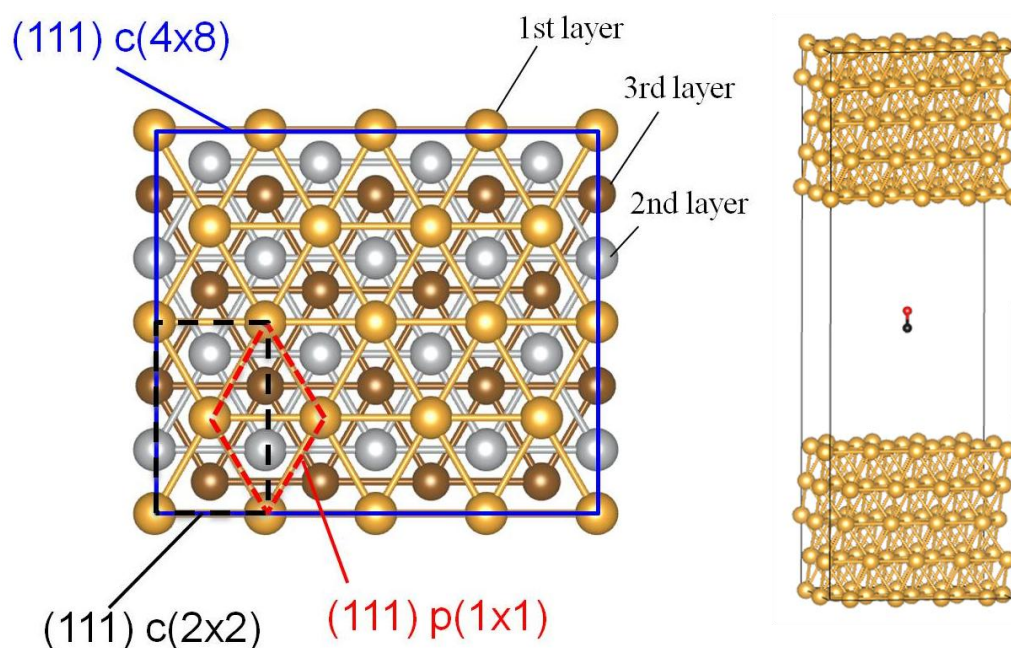


Figure 5.15. Au c(4×8) (111) surface cell used for adsorption

Here we present an investigation of the adsorption energies of CO on both Au (111) and 15% strained Au (111) surfaces. Figure 5.15 shows a slab model used in the present study. This model is a c(4×8) (111) surface cell constructed from an optimized FCC unit cell of a bulk Au ($a=0.4172$ nm) obtained from preliminary calculations. The slab model includes 2 surfaces, 9 layers, and a vacuum layer with a thickness of 1.7 nm. The mesh of k -point sampling in the Brillouin zone was $4 \times 4 \times 1$ based on the Monkhorst-Pack scheme [203]. This set satisfies that convergence of calculated adsorption energy against number of k -points becomes lower than 5 meV. Before adsorption, structural relaxation was carried out for a clean surface by freezing atomic positions at the centre of the slab model until residual forces on all atoms except those that are fixed became less than 0.2 eV/nm.

CO adsorption energies were calculated using:

$$E_{ad} = E(\text{surface with adsorbed CO}) - E(\text{clean surface} + \text{free CO}) \quad (5.1)$$

with the carbon atom bound to an on top site of the Au(111) surface. The initial distance between C and Au atoms was 0.2 nm. Atomic positions of an adsorbed CO molecule and Au atoms in the 4 layers from the adsorption surface were optimized with the same condition as that for the clean surface.

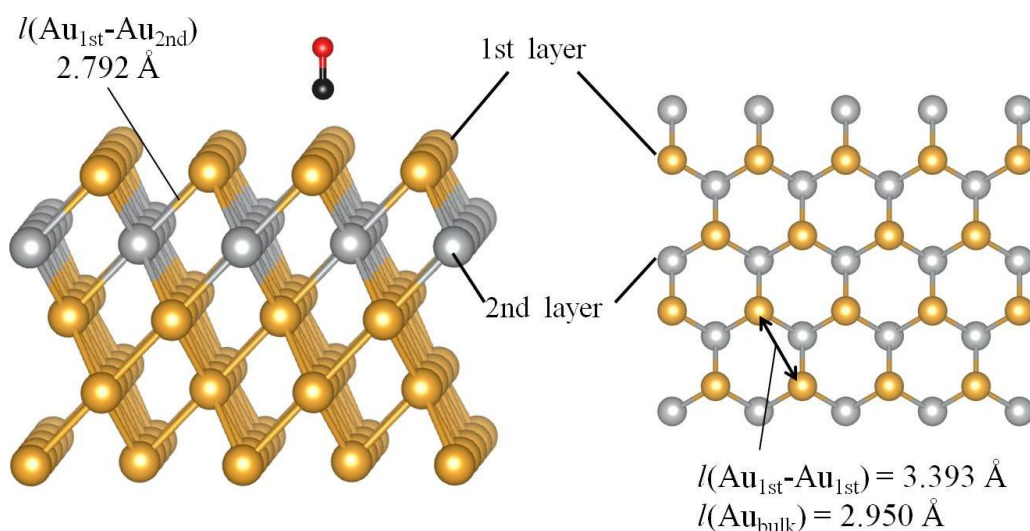


Figure 5.16. Initial configuration of the 15% strained gold slab used.

To investigate the effect of strain on adsorption of CO the Au $c(4 \times 8)$ (111) surface cell was expanded by 5%, 10% and 15% in each direction of the (111) plane. The pristine strained-surface cell was then optimized in the vertical direction to (111) plane, as shown in Figure 5.16. CO adsorption energies on the strained-Au (111) slabs were evaluated under similar calculating conditions to the free-strain surfaces.

For the unstrained Au(111) surface the CO adsorption energy was found to be -0.31eV , in good agreement with previous reports [80]. Upon the introduction of 5% strain, the adsorption energy increases in magnitude to -0.58eV , whilst increasing the strain towards the larger amounts observed at the decahedral surface causes the magnitude of the adsorption energy to increase exponentially, as shown in Figure 5.17. At 10% strain the adsorption energy is -2.72eV and reaches -6.40eV by 15% [194]. Upon adsorption on the heavily strained surfaces the calculations predict significant atomic rearrangement, with nearest neighbour distances contracting towards the bulk values, as seen in Figure 5.18.

Subsequent adsorption energies calculated on these restructured surfaces are significantly reduced and are comparable to those calculated for 5% strain. However, the calculations are performed on a model slab, effectively with infinite lateral dimensions and free from the structural constraints experienced by the decahedral particle. Furthermore, these values are based on a surface expanded in all directions, whilst the expansion of inter-atomic distances observed is inhomogeneous and surface

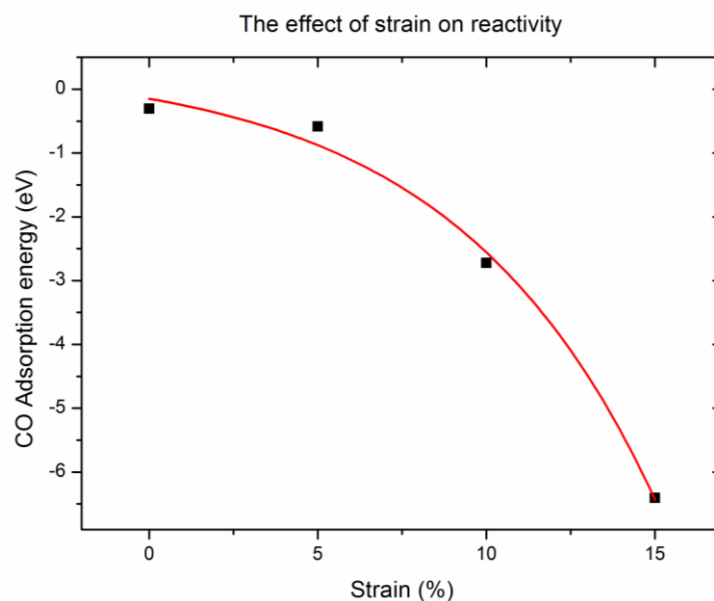


Figure 5.17. DFT calculations of the effect of strain on the adsorption energy for carbon monoxide.

atoms may be heavily strained in relation to one nearest neighbour but less so to another. A detailed theoretical study including the fixed twin boundaries and variable inter-atomic distances measured is beyond the scope of the current study. However, after binding to the strained active site it can be expected that adsorption may act as a trigger for surface atom movement and possibly internal restructuring at higher temperature and pressures.

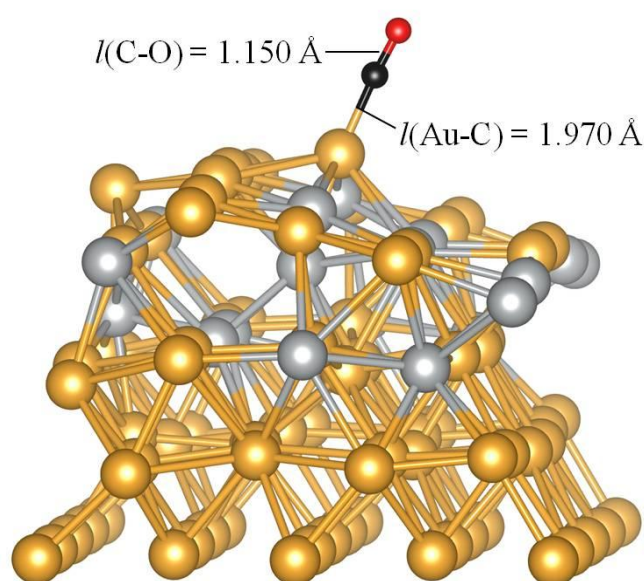


Figure 5.18. Restructuring of 15% strained Au(111) surface upon CO adsorption calculated by DFT

5.4 Chapter conclusions

It is clear that inducing a strain to a metal surface can significantly enhance the performance of a catalytic material. Previous studies seeking to explain the surprising activity of small gold nanoparticles have largely overlooked the effect of strain, and the only strain to be considered has been the relatively small support induced strain. The multiply twinned icosahedral and decahedral structures are regularly observed and are expected to be the most stable forms of gold nanoparticles in the size range for which gold is chemically active. However, the nature of their crystallographically forbidden, non-space filling structure has been until now overlooked when considering the origin of the catalytic activity of small gold nanoparticles.

The results in this chapter quantitatively describe the substantial inherent strain in a decahedral Au particle in the size range for which gold is chemically active. The strain is found to be greatest at the surface, with an average surface strain of 5.6% and many instances of 10% or greater surface expansion measured for a 3 nm particle. DFT calculations show that such surface strain will have a major impact on the adsorption energy of CO and therefore activity for carbon monoxide oxidation. These results provide further explanation of the dramatic increase in the catalytic activity of gold nanoparticles in this size range and further highlight the structural sensitivity of their properties.

Chapter 6

In-situ heating of model gold catalysts

6.1 Structural deactivation mechanisms

The inherently unstable nature of small metal nanoparticles is a major obstacle in the pursuit of active, selective, durable and economical catalysts; as a variety of deactivation mechanisms can contribute to an overall loss of catalytic performance. Poisoning or carbon lay-down can often be alleviated by regeneration of the catalyst in a suitable environment, whilst the effect of traditional sintering mechanisms, such as particle migration and coalescence, and of Ostwald ripening [15, 204], can be reduced by sophisticated supporting materials that provide anchoring sites, either by chemical or topographical means. However, as the activity and selectivity of the catalyst will be governed by the nature and number of the active sites found on the nanoparticles, the evolution of such sites must also be considered at the atomic scale.

6.1.1 Loss of low co-ordinated sites

Highly stepped surfaces of as-deposited particles, such as those shown in figure 5.5, provide many potential active sites for catalysis. However, the stability of such sites under simulated reaction conditions needs to be carefully considered. Low co-ordination surface atoms result in higher surface energies due to the greater number of broken bonds. Whilst particle-support interactions and the presence of additional

surface groups undoubtedly complicate the overall particle energetics [113], on this model system with a weakly interacting support we consider just the contribution of the particles surface energy. By rearranging the expression given in equation 3.6 [109], the surface energy can be described as a function of the co-ordination number of each surface atom i . Summing over the surface of the particle gives:

$$\sigma = \frac{1}{2} \sum_{\text{surface}}^N \frac{(Z_B - Z_i)}{Z_B} \cdot E_{coh} \quad (6.1)$$

where Z_B is the bulk co-ordination number ($Z_B = 12$ for gold), Z_i is the co-ordination of the surface atom and E_{coh} is the cohesive energy between two neighboring atoms. For a gold surface atom the greatest co-ordination number, Z_i , is 9 and found on a $\{111\}$ surface facet. Therefore it can be expected that Au surfaces will attempt to minimise their surface energy by removing under co-ordinated surface atoms and creating $\{111\}$ surface facets.

This process is observed in figure 6.1, where the electron beam provides enough energy to allow surface atoms to overcome the energy barrier associated with surface atom movement. Such an energy barrier will decrease with co-ordination number, meaning the most catalytically active low co-ordination sites are likely to be the first to rearrange towards reduced energy and activity.

Through the use of a heating holder this process can be studied at controlled elevated temperatures and over longer periods of time with minimised electron beam effects. Figure 6.2 is an example of a gold nanoparticle in the $[011]$ orientation that has been heated to 600°C *in-situ* and shows the full extent of energy minimisation as a result of heating. At elevated temperatures surface energy anisotropy is reduced, meaning that inherently strained structures bound by $\{111\}$ surfaces may no longer be energetically favourable. This makes transitions to single crystal particles, such as the cuboctahedral particle shown in Figure 6.2, more likely, as the minimal strain involved with such structures – shown by the corresponding GPA analysis – becomes energetically preferable at higher temperatures to a non-space filling structure bound predominantly by $\{111\}$ surfaces.

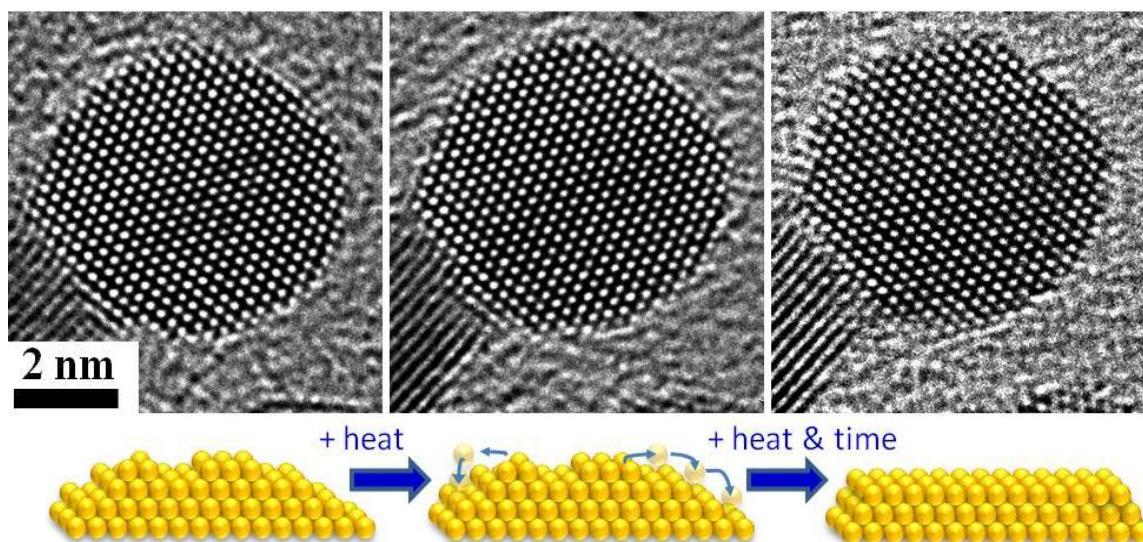


Figure 6.1. Re-arrangement of Au surface atoms towards high co-ordination planar $\{111\}$ surface facets as a result of heating by 200kV electron beam.

The $\{111\}$ and $\{100\}$ surfaces exposed will then minimise their surface energy by creating almost atomically clean facets. This removal of both strain and low co-ordination atoms is expected to lead to a deactivation of the nanoparticle's catalytic activity without any necessarily associated significant increase in size or loss of surface area.

The activity of catalysts is often observed to drop significantly shortly after coming online, before stabilising, and gradually decreasing over time through traditional sintering processes such as particle migration and coalescence or Ostwald ripening,

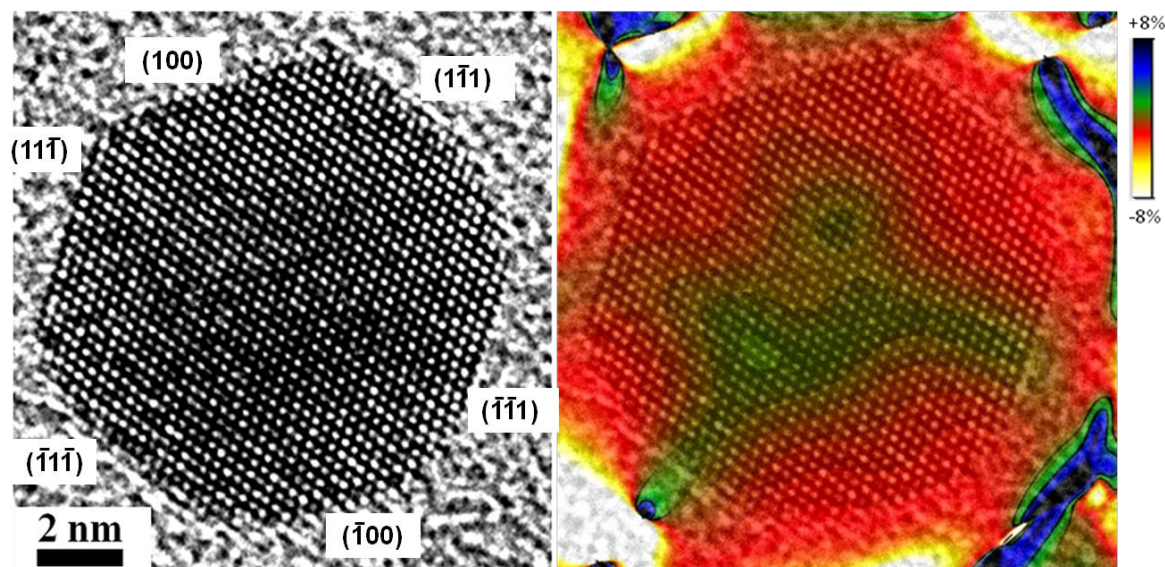


Figure 6.2. A cuboctahedral nanoparticle in the $[011]$ orientation with atomically clean facets observed after heating to 600°C , with GPA analysis (right) showing minimal (D_{xy}) strain.

whilst higher calcination temperatures often result in catalysts with a reduced initial activity [83]. This initial loss of activity may be attributed to structural deactivation mechanisms such as those described above, before the nanoparticles find an energetically favourable morphology and the performance of the nano-catalyst stabilises at a lower level [205].

6.1.2 Relaxation of strain

Several mechanisms through which decahedra may minimise elastic energy have been proposed, including the development of wedge shape stacking faults, decomposing the disclination into two weaker disclinations, development of a central region without a disclination and shifting the pentagonal axis towards the surface [206, 207]. The incorporation of stacking faults and multiple disclinations is known to occur in large decahedra; however the mechanisms by which small decahedra relevant to catalysis reduce their elastic energy is unclear.

Equation 3.8 shows that the elastic energy of decahedra can be reduced by shifting the rotational axis towards the surface of the particle, with the migration of the disclination towards the particle surface expected to occur through the climb of an edge dislocation into the particle towards the rotational axis [110, 208]. Figure 6.3 shows a sequence of *in-situ* images of the same particle throughout a range of temperatures, with the particle exposed to the beam only for the minimum time necessary for imaging at each

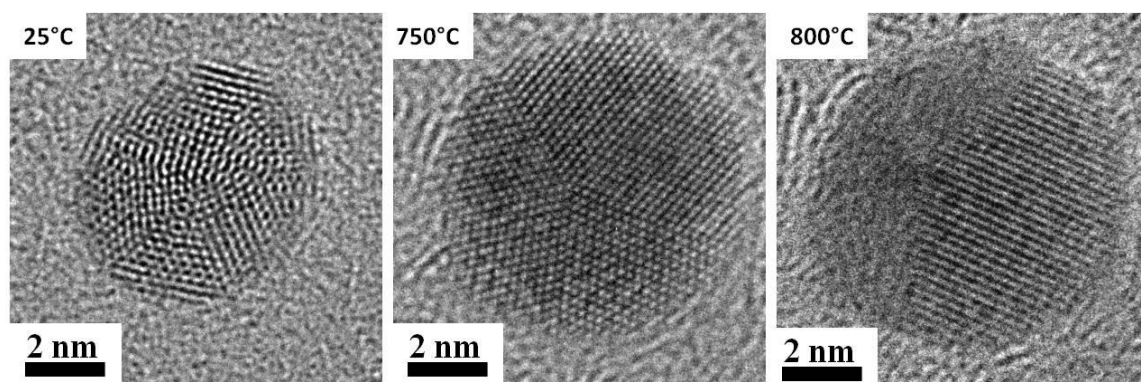
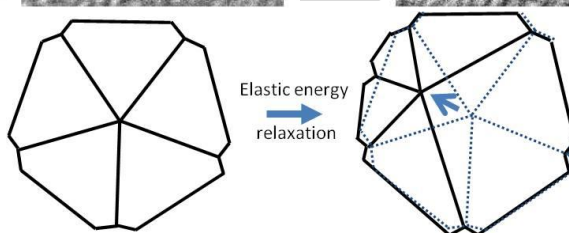


Figure 6.3 *In-situ* heating shows transition from icosahedral to decahedral structure at $\sim 400^\circ\text{C}$, followed by shifting of the fivefold axis between 750°C and 800°C .



temperature step. The particle is initially icosahedral, imaged here off its symmetry axis. At between 300°C and 400°C the particle transforms to the Marks decahedral structure, before remaining structurally stable up to 750°C, whilst the particle has increased in size due to growth consistent with a ripening mechanism. Between 750°C and 800°C, the fivefold axis is observed to shift towards the surface of the particle, allowing for a reduction in elastic stress that results from the inherently strained structure [205].

Higher resolution images obtained *ex-situ* allow more detailed analysis of decahedra with displaced rotational axes and measurement of the resulting atomic displacements. Figure 6.4 shows a decahedral particle with the fivefold axis located less than 1 nm from the lower right corner, alongside measurements of average surface strain plotted as a function of distance from the disclination axis. The surface up to 1 nm from the axis is found to be highly strained, with nearest neighbour distances expanded by ~6% on average, comparable with the surface strain previously measured in a small decahedron 1.5 nm in radius [194]. Further from the axis, the surface strain is approximately halved and is similar to that of the particle in figure 5.4. Furthermore, aberration corrected annular dark field (ADF) STEM, in which for small particles the contrast is dependent on the number of atoms in the column, indicates that the maximum thickness of the particle corresponds to the position of the rotational axis, even when it is displaced towards the surface, as seen in Figure 6.5 [205].

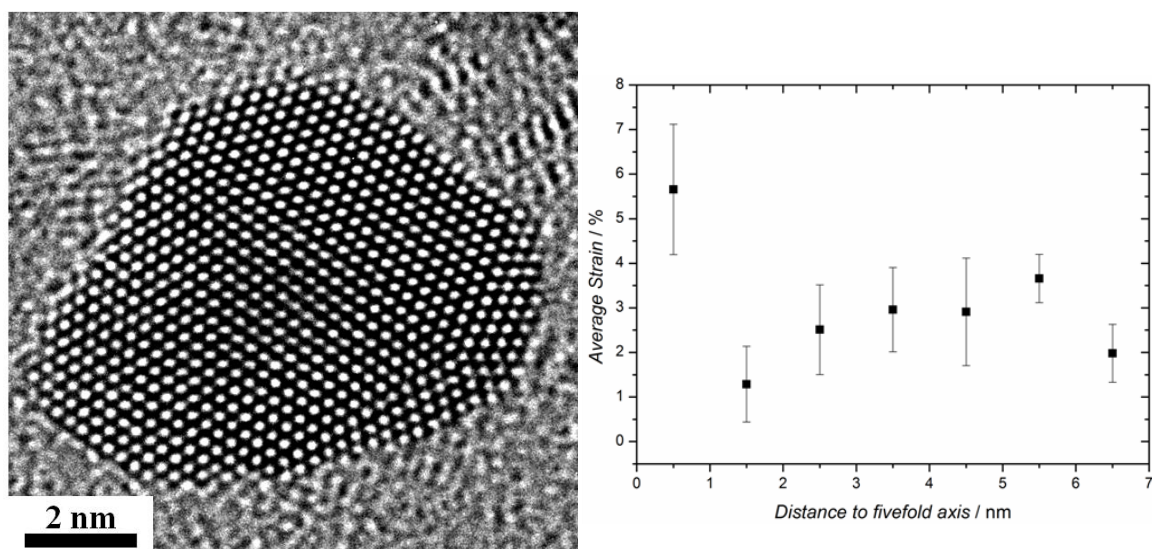


Figure 6.4. A decahedral particle with fivefold axis shifted close to the surface (left) with average surface strain as a function of distance to the axis (right).

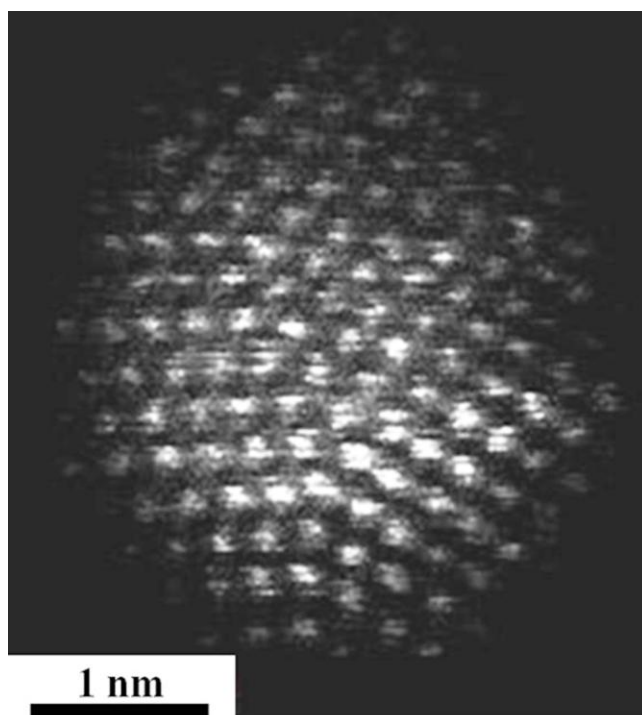


Figure 6.5. ADF STEM image of a decahedral particle. Z contrast dependent intensity reveals maximum thickness at the off-centre fivefold axis.

6.2 Sintering of gold nanoparticles

6.2.1 Particle migration and coalescence

A statistical approach to determining how particle size distributions change as a function of temperature was carried out using *in-situ* HAADF-STEM images taken at low magnification at various positions of the sample. The advantage of this method is that it negates any effects of the electron beam, as each image is obtained from an area of the sample that had previously not been exposed to the beam, whilst the strong Z contrast of the Au particles compared to the support allows for easy identification and analysis of the particles. Also by taking images from various parts of the sample, more representative data is obtained and we ensure that the conclusions drawn are common to the whole sample, rather than just a given local area.

Colloidal Au nanoparticles supported on Si_3N_4 are shown in Figure 6.6, with significant sintering observed between 400°C and 520°C leading to the mean particle size increasing from 7.51nm to 15.2 nm. However, for details of the sintering mechanisms at work, or information regarding the structure of the particles throughout this process,

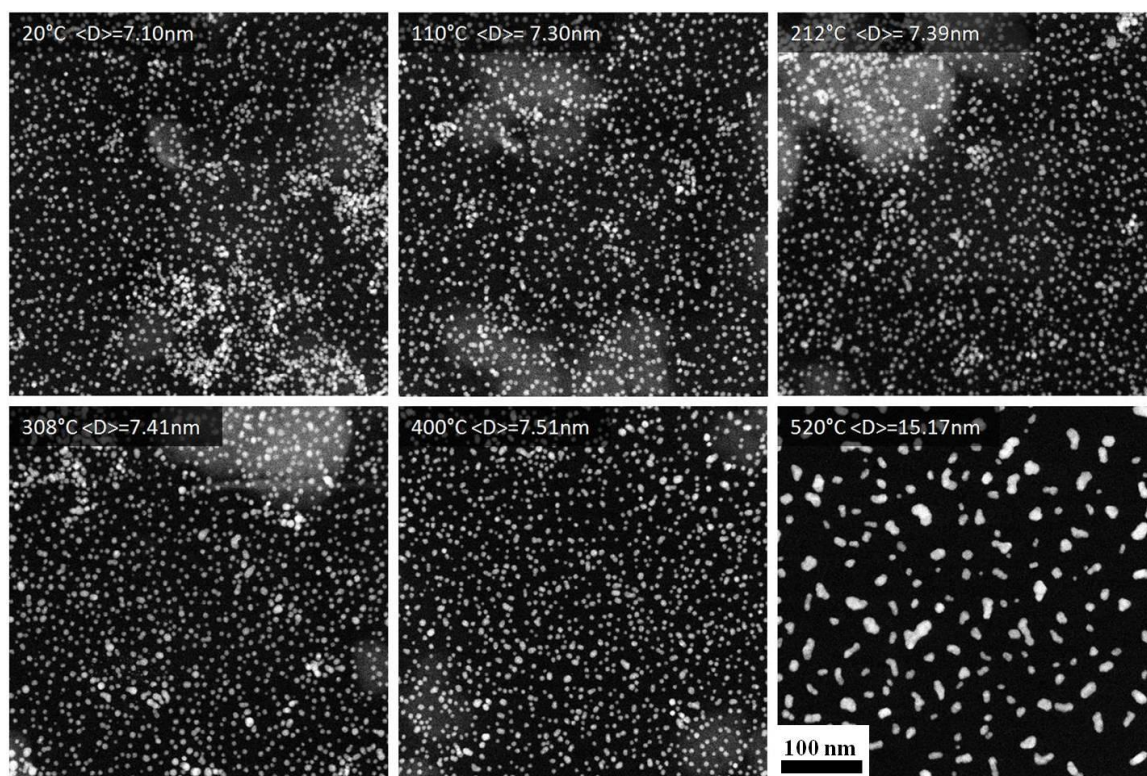


Figure 6.6. *In-Situ* ADF-STEM of Au on Si₃N₄

higher magnification studies are required of the same area throughout a range of temperatures.

In-situ heating of the same area of Au nanoparticles supported on thin carbon is shown in Figure 6.7. Sintering is observed to occur predominantly through particle migration and coalescence, with an increase in mean particle diameter from 3.37 nm to 5.22 nm and a 53% reduction in the number of particles present in the area observed. The relatively weak interaction between the particle and the amorphous carbon support makes the particles easily mobile at these temperatures, therefore enabling coalescence.

Figure 6.8 shows Au particles supported on carbon at 25°C and 700°C. As particles migrate and come in to contact there is a parallel alignment of the {111} crystal planes; facilitating the minimisation of surface area through coalescence. This is consistent with previous observations [188].

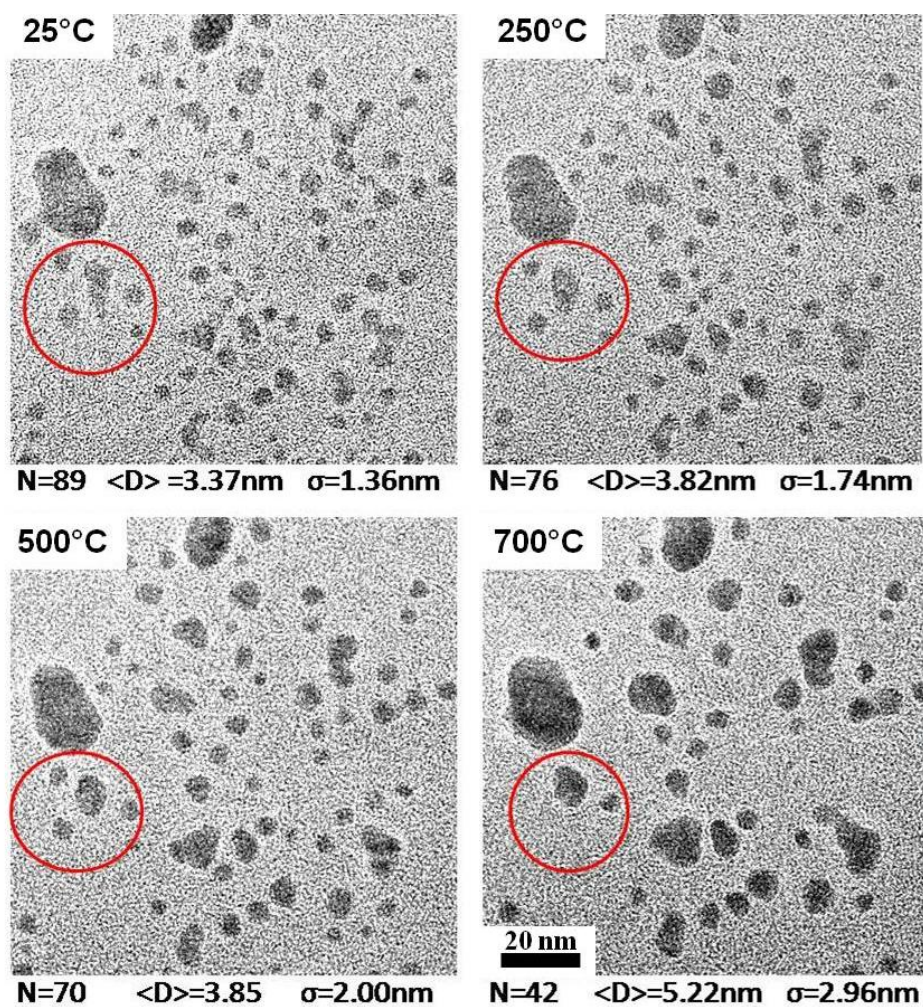


Figure 6.7. *In-Situ* TEM of Au on carbon

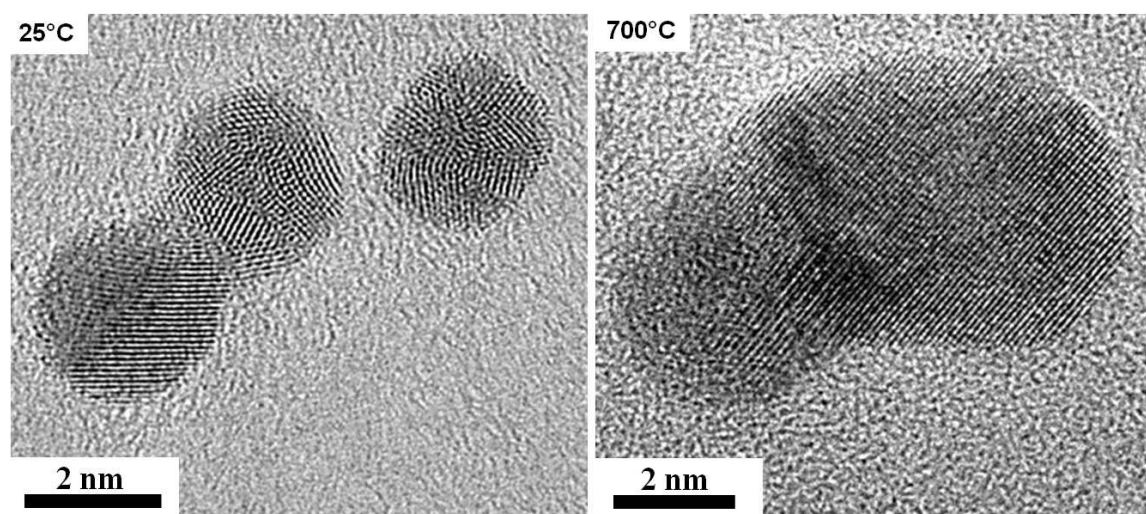


Figure 6.8. *In-Situ* TEM shows Au nanoparticles coalescence via the parallel alignment of {111} planes.

6.2.2 Ostwald Ripening

Ostwald ripening is a well known deactivation mechanism for nano-catalysts. The atomic or small cluster transport from one particle to another causes some particles to grow at the expense of others that shrink and may eventually disappear – leading to an overall loss of surface area available for reactions.

The same area of gold nanoparticles on Si_3N_4 membranes is shown throughout a range of temperatures in Figure 6.9, and from these images it appears the particles are much more stable than those reported earlier in figure 6.6. This is attributed to a build up of contamination under the electron beam over the prolonged exposures used, which then prevents particle migration. These results therefore show how the electron beam can influence the results obtained and highlight the importance of checking *in-situ* observations with reference areas not exposed to the beam, and inform the *in-situ*

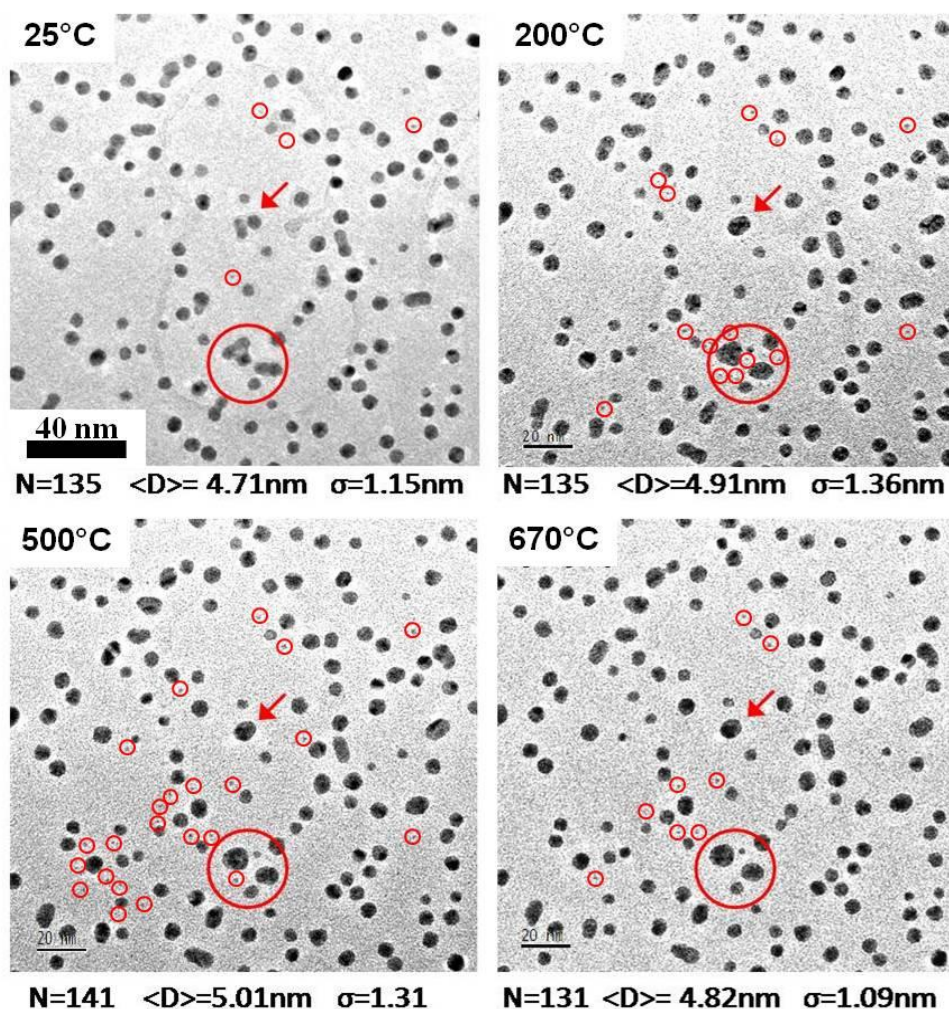


Figure 6.9. *In-Situ* TEM of 5nm Au on Si_3N_4 . Red circles indicate clusters < 1nm.

methods used in Chapter 8 for studying the stability of real metal-oxide supported nano-catalysts.

Despite the stabilising effects of the contamination drawn in by the electron beam, some particle migration and coalescence is observed at $\sim 180^\circ\text{C}$, followed by predominantly Ostwald Ripening at higher temperatures. Between 200°C and 500°C the number of small particles and clusters, approximately 1nm in diameter, is significantly increased. This is indicative of Ostwald Ripening, resulting in an almost bimodal particle size distribution. However these small particles and clusters observed are not previously larger particles that have reduced in size, but the build up of atoms or small clusters that have migrated from their original particle and become trapped on the Si_3N_4 surface. The stability of these clusters up to 500°C suggests that they are well anchored on the support, possibly nucleating on point defects induced by the beam. Above 500°C , the trapped clusters and small particles have sufficient energy to continue to migrate across the surface and rejoin a larger particle, as seen in the marked reduction of 1nm particles present above 500°C . From 200°C onwards the mean particle diameter is constant, within error, whilst the standard deviation of the particle size increases from 1.15nm to 1.36 nm, before reducing back to 1.09 nm at 670°C , consistent with the above conclusions.

The migration of atomic species and small clusters from their original particle can be understood further through atomic resolution *in-situ* imaging. Figure 6.10 is an *in-situ* sequence showing two small Au nanoparticles less than 2nm in diameter, undergoing structural rearrangements from (a) to (c) under beam heating. Figure 6.10(b) informs the intermediate stage, with disordered particle structures observed and evidence of single atoms migrating from the particles (appearing as black dots on the thin amorphous carbon film under slightly negative defocus). The driving force for the removal of atoms away from the particle is proposed to be either minimisation of the particles surface energy, meaning surface ad-atoms and steps will be removed in order to create atomically clean facets, or structural transitions in which the number of atoms required for the new minimum energy structure may be slightly different. The resulting free atoms then migrate across the support until joining another particle.

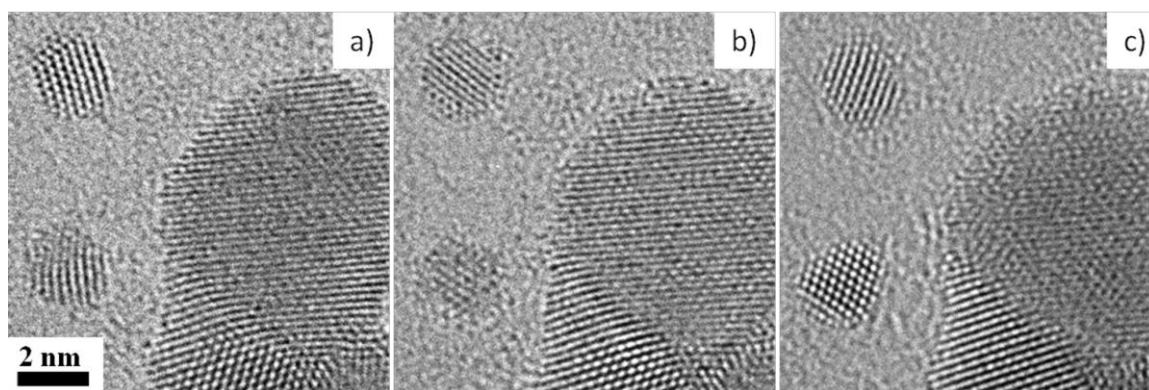


Figure 6.10. Two small nanoparticles are observed to change structure from (a) to (c) as a result of heating. Image (b) informs the intermediate stage, as the removal of a few surface atoms causes a different particle structure to be energetically favourable. Evidence of the migration of single atoms is seen in (b), with single atoms appearing as black dots in the under focussed condition.

Whilst overall loss of surface area and hence activity is often the result of Ostwald ripening, the existence of single atoms and small clusters on the surface of the support during the intermediate stage has interesting implications for catalysis, with recent work attributing excellent catalytic performance to the presence of single atoms or small clusters [75, 132, 174]. Through the use of a support material with an abundance of anchoring sites, such as oxygen vacancies in reducible metal-oxide supports, migrating atoms may be stabilised on such defects and provide further active sites for adsorption, with the nanoparticles main role in this case being to act as a reservoir of potential atoms and clusters.

6.3 Chapter conclusions

Both expansive surface strain and low co-ordination surface atoms are known to enhance the catalytic activity of small gold nanoparticles. Through *in-situ* aberration corrected electron microscopy the stability of these active sites has been studied as a function of temperature. Minimisation of surface energy leads to the removal of under co-ordinated surface atoms in favour of atomically clean facets, and such a process is proposed to contribute to the often observed initial drop in activity of nano-catalysts. The significant elastic strain energy inherent to the non-space filling decahedral structure is reduced by heating, and the mechanism by which this occurs in small decahedra relevant to catalysis is observed to be a shifting of the disclination axis towards the surface. Furthermore the reduction in surface energy anisotropy at higher

temperatures may lead to structural transitions away from intrinsically strained morphologies.

Model systems of Au particles on two dimensional supports allow for insight at the atomic level into both coalescence and Ostwald ripening sintering mechanisms. These results also show how the electron beam can have a stabilising effect on the particles, either by drawing in contamination or creating a defective support surface with a greater density of anchoring sites for small particles, and these results will inform the studies of industrial catalysts in Chapter 8. Careful consideration of the stability of the identified active sites, coupled with further understanding of sintering processes that result in a loss of catalytically active surface area, should allow for the development of more active, durable and economically viable catalysts.

Chapter 7

Nano-ceria supported gold catalysts

The exceptional catalytic properties of gold supported on nano-crystalline ceria offer great promise for the economical production of hydrogen via the water-gas shift reaction, as well as being an excellent low temperature CO oxidation catalyst to remove poisonous carbon monoxide from the hydrogen stream in fuel cells [125, 131]. The high activity with very low Au loadings of such catalysts may facilitate a large reduction in the cost of fuel cells, which is certainly needed if fuel cell technology is to become commercially viable [63]. As discussed in Chapter three, there is still no agreement in the literature on the nature of the active site of Au/CeO₂ catalysts. The presence of cationic gold seems to be accepted as a prerequisite for high activity, but whether this is in the form of single atoms [132] or clusters [136], and whether these act as the active species [140] or a precursor [65] for the active phase is unclear. In the following chapter, aberration corrected TEM and HAADF STEM are used to characterise these catalysts at the atomic scale, whilst the atomic number dependent contrast of HAADF STEM imaging offers an insight into the nature of the Au species and its interaction with the supporting ceria.

7.1 Sample preparation

The Au/CeO₂ samples discussed in the following chapter were prepared and provided by collaborator Dr Shiju [209]. The ceria nanocrystals were prepared by precipitation

of cerium nitrate, followed by deposition of the Au (~ 2 weight %) by insipient wetness of the ceria with an aqueous solution of HAuCl₄. The resulting material was calcined at 400°C.

XPS analysis (provided by Johnson Matthey Plc) showed a peak at ~ 86 eV, consistent with the presence of gold in the Au⁺³ state (see Figure 3.11 for reference). Therefore the highly dispersed cationic gold supported on nano-ceria is in the same form as previous Au/ceria catalysts reported to have exceptional activity for the water-gas shift reaction.

7.2 Structural analysis through electron microscopy

As we can see from Figure 7.1, the as-prepared sample is made up of very small ceria crystallites, typically < 10 nm in diameter. The small size of the ceria crystals not only makes for a very high surface area catalyst, but also provides a high proportion of under co-ordinated corner atoms. These corner atoms, as well as low co-ordination atoms found at surface steps and terraces, are expected to facilitate the formation and filling of vacancies in the surrounding oxygen sites [126].

Analysis of a series of images in Figure 7.2, taken over the course of approximately two minutes, show movement of surface cerium atoms, as irradiation by the electron beam

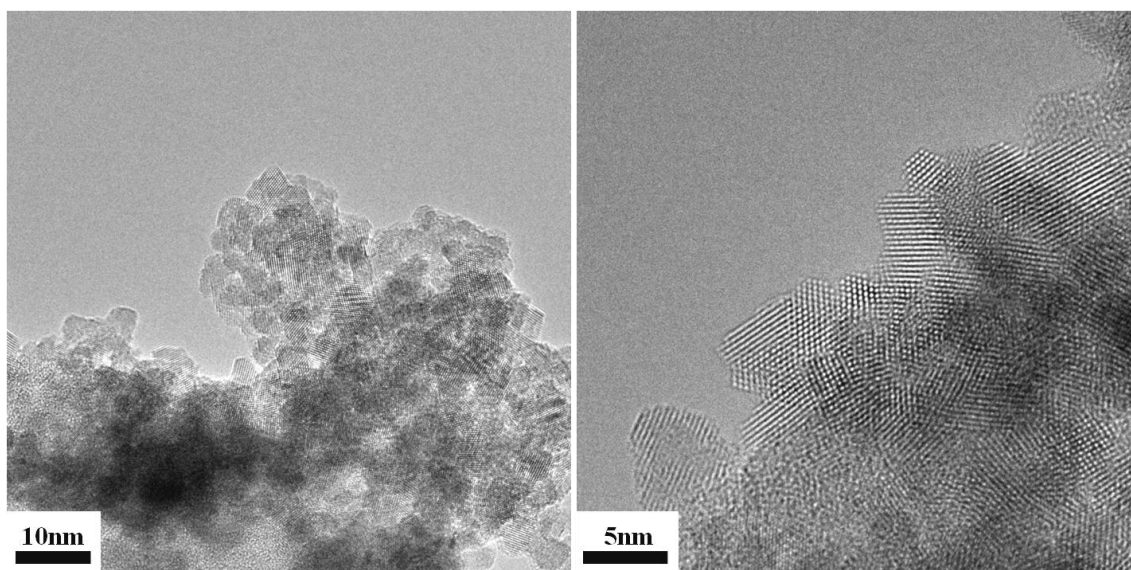


Figure 7.1. TEM images showing the nano-crystalline ceria support

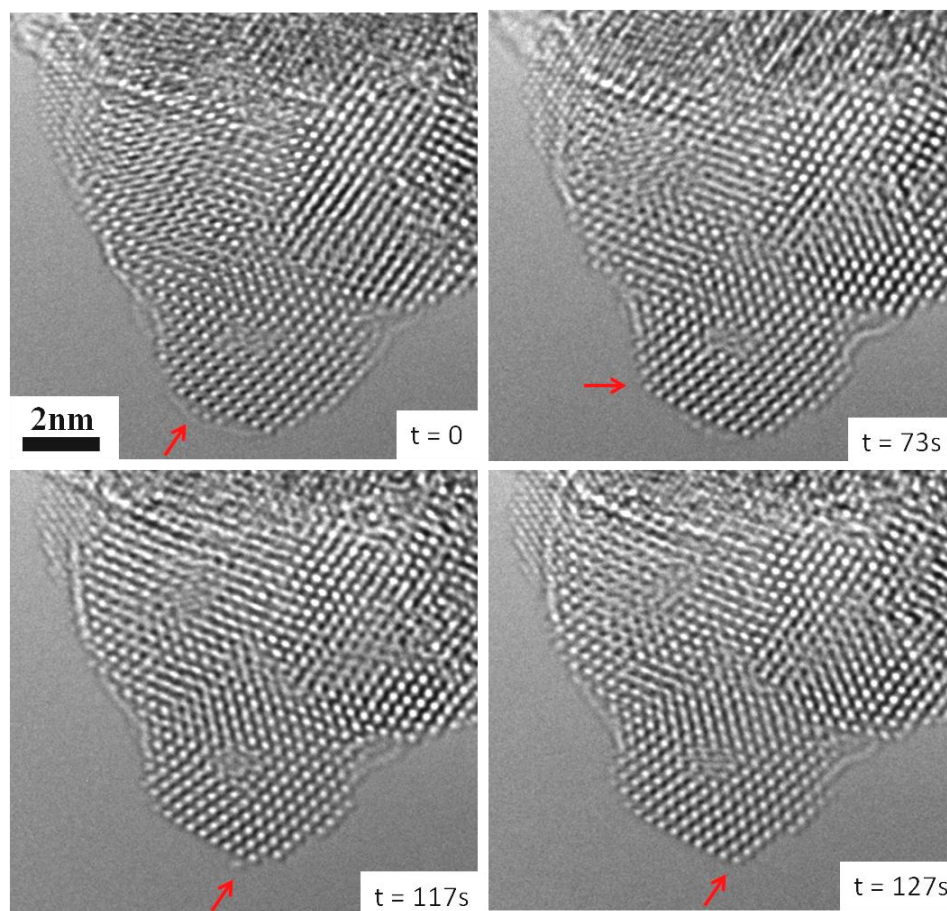


Figure 7.2. Electron beam induced surface atom movement of nano-ceria.

provides sufficient energy for the ceria crystal to minimise its surface energy by removing low co-ordination atoms in favour of atomically clean facets. The top two images show that surface atom movement occurs initially on the (001) surface, which is higher in energy and therefore less stable, followed by removal of surface steps and filling of the corner atom position along the (111) surface.

The observation of surface atom instability has important implications for the electron beam exposure times used. Through reconstruction of the exit wavefunction of the electron beam, Haigh *et al* [210] directly showed that the ceria {111} surface is oxygen terminated, whereas the {001} surface is cerium terminated. However, such a technique requires the acquisition of a through focal series of images, making surface atom movement as a result of electron beam irradiation likely on small ceria crystallites. Consequently, exposure to the electron beam was kept to a minimum for the following studies.

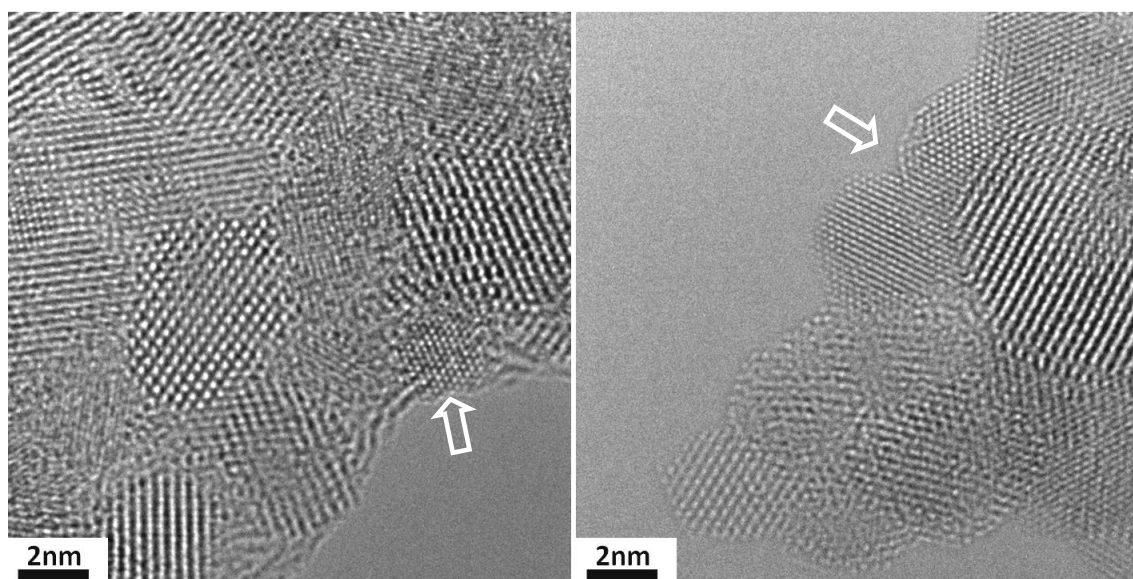


Figure 7.3. TEM observations of metallic Au particles on ceria.

Measurements of lattice parameters observed in atomic resolution TEM images reveal the presence of small gold nanoparticles that are already formed in the precursor sample, and examples of these are indicated in Figure 7.3.

The use of HAADF STEM coupled with localised chemical analysis further verifies the presence of metallic gold particles in both the precursor (Figure 7.4) and calcined (Figure 7.5) samples. The circled particle in Figure 7.4 is not only brighter in the Z

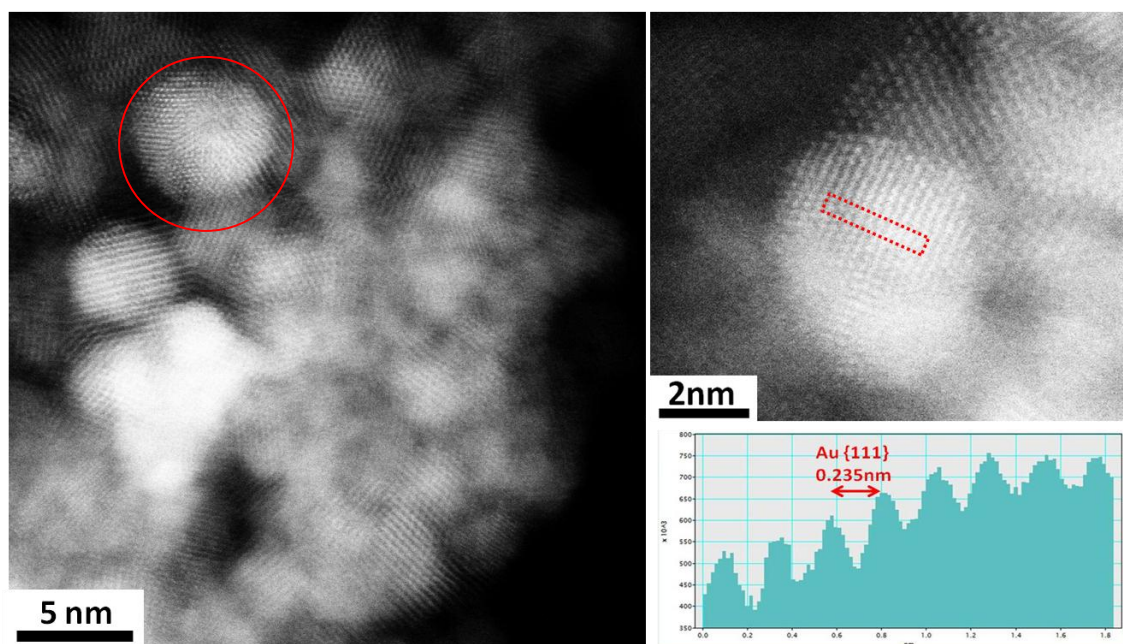


Figure 7.4. HAADF STEM reveals presence of Au nanoparticles in the precursor sample.

contrast image, but appears to be icosahedral in structure, imaged close to the two fold symmetry axis (see figure 5.3a for reference). Furthermore, the atomic resolution HAADF STEM image reveals lattice spacings matching the Au(111) spacing of 0.235 nm, whilst localised EDX analysis of the calcined sample in Figure 7.5 shows strong Au peaks in points 2 and 3, compared with the reference area in point 1.

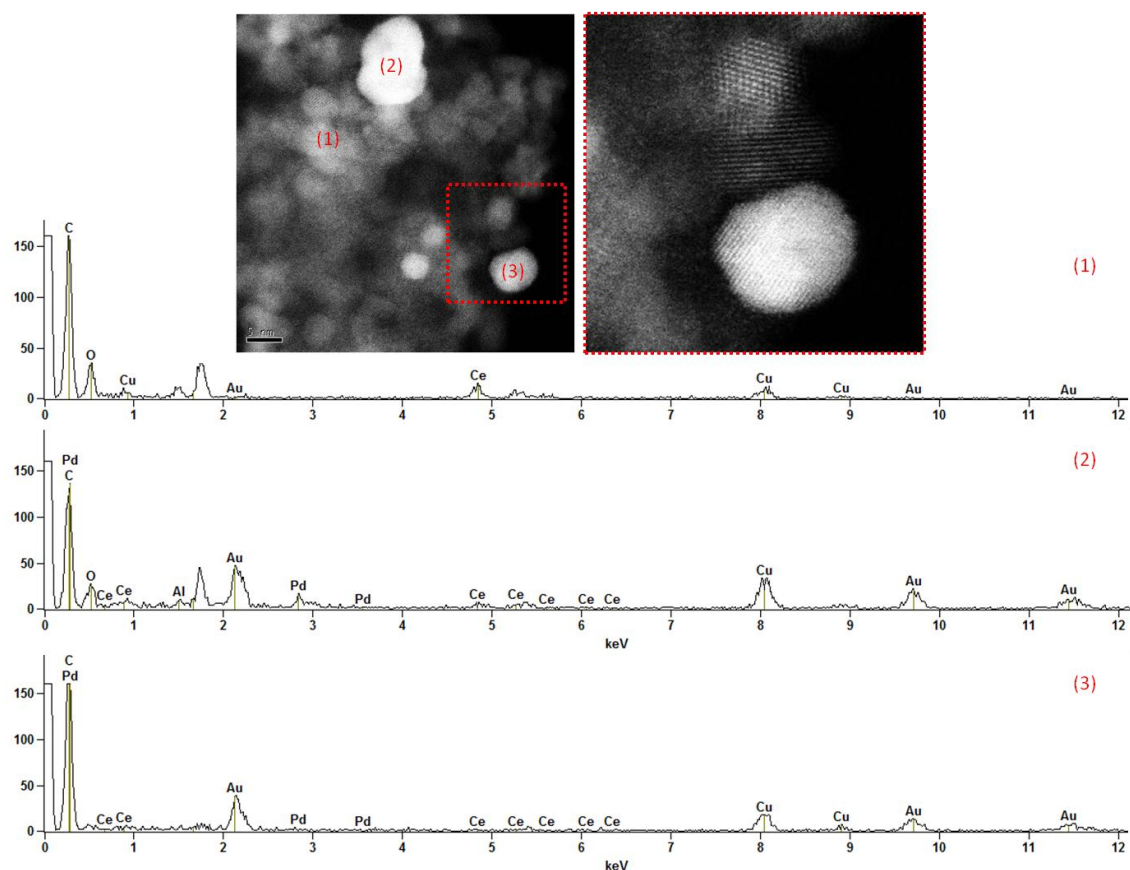


Figure 7.5. STEM-EDX of the calcined sample reveals the presence of metallic gold particles.

7.2.1 Imaging oxygen atoms in AC-HRTEM

The recent development of negative spherical aberration imaging (NCSI) [167] made possible by aberration correction allows accurate observation of oxygen atom positions in the metal oxide support; opening up new possibilities for *in-situ* study of reduction and oxidation processes critical to many catalytic reactions. In Figure 7.6 we can see a slightly over focussed image on the left, in which the cerium and oxygen atomic columns in [011] orientation are not perfectly resolved, appearing instead as a bright dot consisting of both cerium and oxygen atoms. Through careful control of the defocus to marginally above zero ($\sim +5$ nm), the individual columns are now resolved, with the previous over focussed bright dots splitting into one cerium and two oxygen columns.

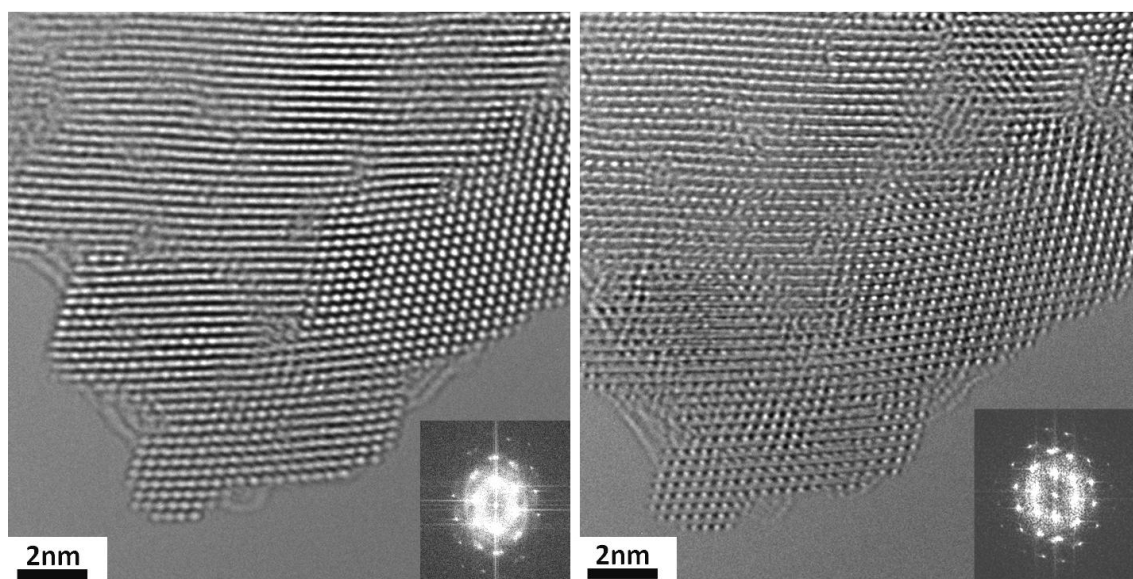


Figure 7.6. Revealing oxygen atoms through AC-HRTEM

Ceria crystals in the [001] zone axis perhaps offer clearer resolution of the oxygen columns due to the maximised distance between the cerium and oxygen positions in this projection. This is shown in Figure 7.7, in which the oxygen columns are clearly resolved, whilst a HRTEM multislice simulation (inset) calculated using the JEMS image simulation software [211], (thickness = 12 nm, defocus = +10 nm) closely matches the experimental image.

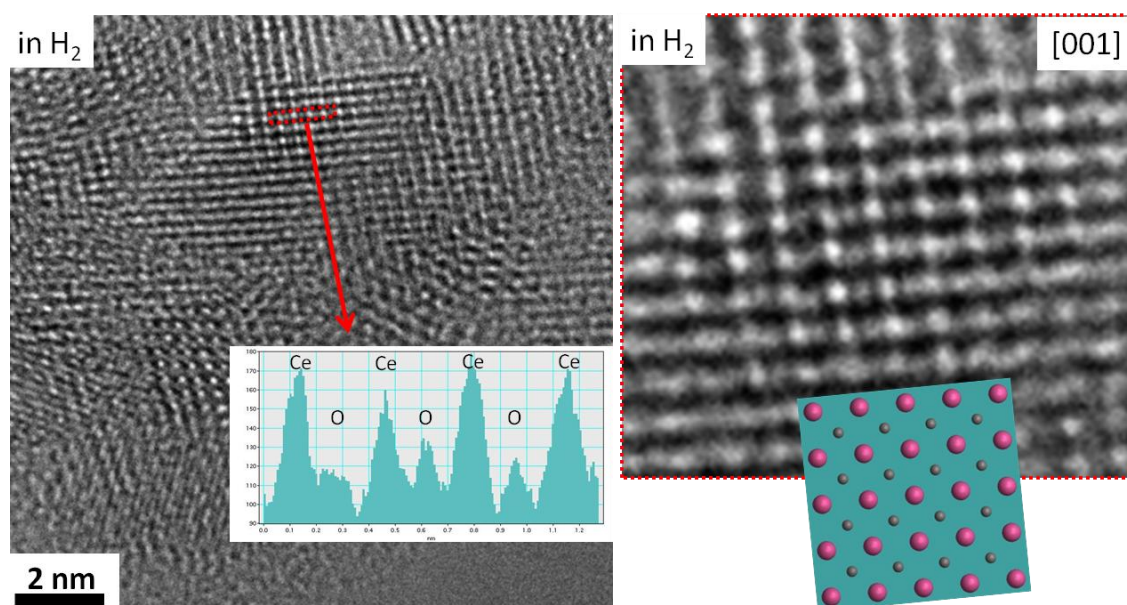


Figure 7.7. Imaging of bulk oxygen atoms in CeO₂ [001] with corresponding multislice simulation (inset).

Modifications to the microscope [188] allow the introduction of small pressures of gas to the sample with minimal effect on the imaging performance. A CeO_2 crystal, again in the [001] orientation, is shown in hydrogen in Figure 7.8. The internal structure, including the position of the oxygen columns, is clearly resolved and directly interpretable from the individual image frame. This is key for future *in-situ* studies, in which the dynamical environment rarely allows for the acquisition of through focal series, whilst the extended exposure of the electron beam is generally unwanted. This capability makes the direct *in-situ* observation of oxygen defect formation, as well as structural changes as a result of reduction or oxidation, possible. However, the elevated temperatures such processes often require, such as bulk $\text{CeO}_2 \leftrightarrow \text{Ce}_2\text{O}_3$, necessitate the use of a heating holder, currently adding further instabilities and limits to the resolution.

Unfortunately, using this single image technique, identification of surface oxygen atoms has proved elusive. This is illustrated by Figure 7.9, which again shows a small ceria crystal in the [011] zone axis, with bulk oxygen columns clearly visible. However, at the edge of the {111} surfaces there is no evidence of the expected oxygen atoms. It seems that from the single TEM image, the presence of oxygen atoms does not have a large enough effect on the phase of the electron wavefunction to be detectable, and that reconstruction of the exit wavefunction is needed. This is largely due to the loss of electron channelling through the specimen at the surface, whilst the surface is likely to

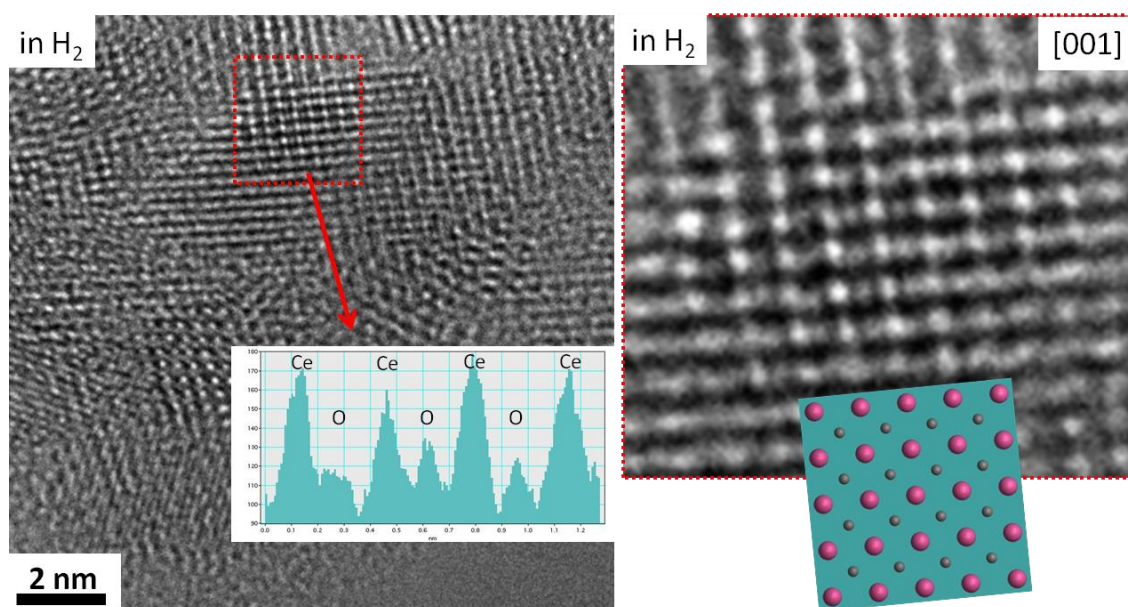


Figure 7.8. Bulk oxygen atoms in CeO_2 observed *in-situ* in Hydrogen.

be the thinnest area of the crystal, and therefore have the fewest number of atoms in each column with which the electron wavefunction can interact. Therefore, direct observation of the formation and filling of surface oxygen vacancies under a gas environment was not possible in the present study. Future work may utilise exit wave restoration for the *in-situ* study of the position and stability of surface oxygen atoms. However careful calibration of the electron beam effects will be needed, as well as possible modifications to the imaging conditions – such as the energy of the electron beam and the number of images needed for exit wave restoration.

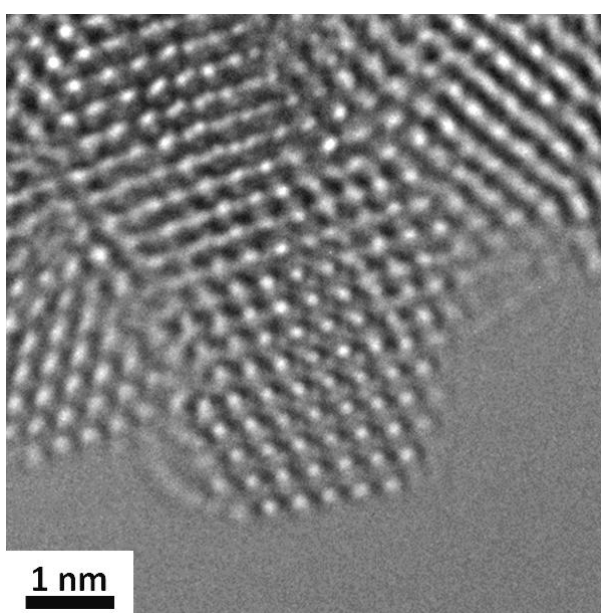


Figure 7.9. AC-HRTEM reveals bulk oxygen atoms, but surface oxygen atoms remain elusive from the single image.

7.2.2 Identifying the active site – single atom detection through HAADF STEM

Whilst some small metallic gold nanoparticles are observed through HRTEM, previous studies have shown that the removal of metallic gold had no effect on the resulting catalysts activity, and therefore metallic particles were not the predominant active species for the water-gas shift reaction [132]. Further to this, XPS analysis indicates a strong presence of Au^{+3} , and it is this cationic gold that can be expected to be critical for high catalytic activity [132, 136, 140, 141]. The dependence of image contrast on atomic number in HAADF STEM makes possible the identification of heavy single atoms [174] or small clusters [75] on a lighter support. Despite ceria having a significantly higher atomic number than iron oxide or other supporting materials that

this technique has been successfully applied to in the literature, the atomic number difference of Au ($Z=79$) to Ce ($Z=58$) should make possible the identification of any small clusters or single Au atoms on thin ceria supporting crystals.

As the intensity of the HAADF STEM image is dependent on the total number of protons in the atomic column, any local thickness variations will also lead to changes in intensity of the observed columns. This can be seen in Figure 7.10, and clearly shows that any observed intensity increase must be in relation to a flat and therefore uniform intensity background in order for it to be attributable to the presence of gold.

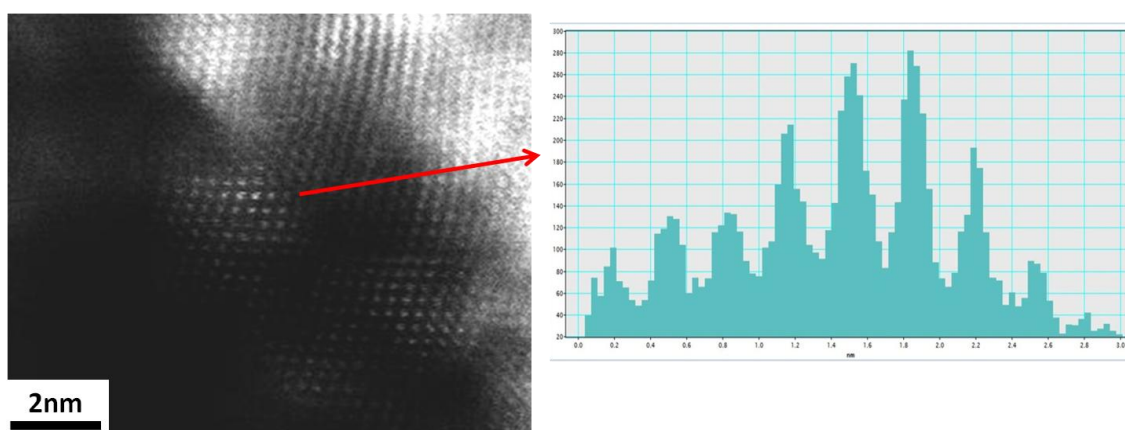


Figure 7.10. Z contrast STEM is sensitive to thickness variations as well as increasing atomic number, as shown by the intensity profile (right) across the ceria crystal.

Analysis of many atomic resolution HAADF STEM images of the Au/CeO₂ precursor sample in this case *did not* reveal the presence of any small Au clusters. However, by carefully selecting thin areas of the supporting ceria with minimal thickness variations, the presence of Au single atoms can be investigated through analysis of any observed contrast increase. Figure 7.11 shows an example of two such areas chosen. Line profiles of the measured atomic column intensities reveal an increase in intensity of certain individual columns by $\sim 40\%$ in relation to their surrounding neighbours. This intensity increase is relative to either a uniform intensity of neighbouring columns or at times a slightly decreasing intensity of the line profile that results from a small reduction in thickness. Therefore the relatively large intensity increase observed in certain atomic columns is greater than anything that can be related to thickness variations, since such a large change in the number of atoms from one column to the next is unphysical.

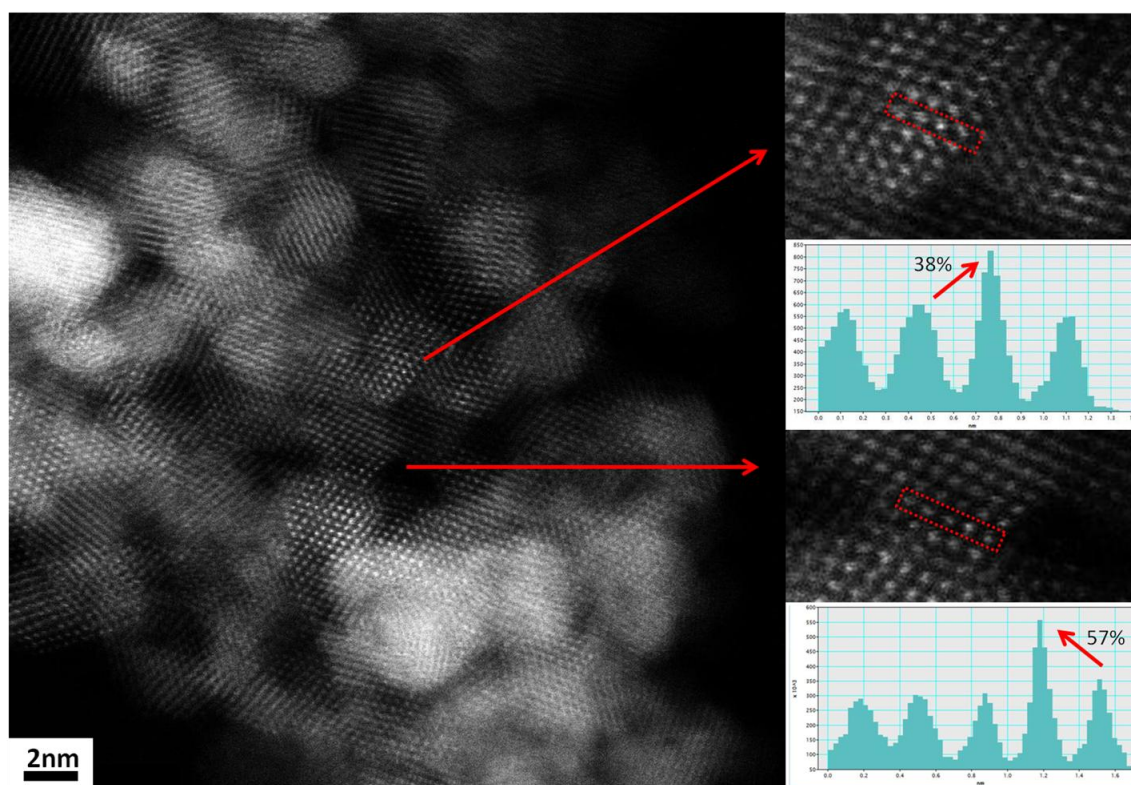


Figure 7.11. Atomic resolution HAADF-STEM imaging reveals bright columns, indicating the presence of single Au atoms.

Furthermore, each atomic column comprises several pixels in the image, with the intensity of each column resulting from multiple probe positions each causing many elastic scattering events that are detected by random parts of the annular detector. Therefore, the increase in intensity of certain columns cannot be attributed to a random error in the detector response or the image processing. The chances of multiple pixels, some of which are on different scanning lines (and therefore obtained 20 milliseconds apart), each having a random increase in measured intensity compared to the expected background intensity levels is very low. Consequently, the observed increase in atomic column intensities can be attributed to the presence of single gold atoms, whose higher atomic number increases the overall atomic weight, and therefore intensity, of the columns in the HAADF STEM image. It is also observed that these increased intensities correspond exactly to the expected position of the cerium column, as opposed to the oxygen column position or causing a spreading of the measured intensity profile. The evidence therefore suggests that the cationic gold is in the form of single gold atoms that substitute for Ce sites, as opposed to being anchored on oxygen vacancies or being in the form of Au clusters. This observation is in agreement with theoretical

calculations that suggest substituting into a cerium vacancy is the most energetically favourable position for a single Au atom supported on CeO₂ [135, 137].

In the present study, the observed intensity difference between Ce columns and Ce columns proposed to contain a single Au atom is a relative intensity difference, with its magnitude a consequence of, amongst other things, the image acquisition and processing conditions. The image acquisition software available as standard on current electron microscopes removes much of the background signal, and therefore stretches the observed intensity difference. The available dynamic range is insufficient to enable inclusion of a full range of detected intensities, meaning the measured intensity differences are relative as opposed to absolute. As such, comparisons of conventionally acquired HAADF STEM images, such as those presented here, with simulations do not agree quantitatively, meaning the images can only be interpreted in a qualitative manner. However, the intensity difference observed is many times larger than any small fluctuations between other neighbouring columns proposed to contain just Ce atoms, and as such cannot be attributed to local changes in thickness or any statistical affect of the imaging acquisition or processing conditions.

Recently, the work of Lebeau *et al* [180, 181, 184, 212] has led to the ability to quantify the experimentally observed intensity in HAADF STEM images; opening up the possibility of quantitatively measuring atomic column composition as well as thickness from a single image. By plotting the measured column intensity as a function of the initial probe intensity, the image is placed on an absolute scale, allowing direct comparison with simulations. As discussed in Chapter 4, several experimental factors must first be carefully calibrated in order to apply this approach, whilst theoretical calculations must use the frozen-phonon model in order to accurately model the thermal diffuse scattering events [183]. However, future work utilising this method will be able to quantitatively measure the Z dependent contrast and therefore chemical composition of many materials, offering a powerful new tool for characterisation of single atom catalysts.

As we know from XPS data, as well as similar previous reports [132, 136], much of the gold in the as-prepared sample is cationic; and the presence of cationic gold very

strongly correlates with high catalytic activity. Through both aberration corrected TEM and HAADF STEM analysis, we saw no evidence of small Au clusters, but do provide strong evidence for the existence of single gold atoms that substitute for cerium atomic positions. The resulting $\text{Au}_x\text{Ce}_{1-x}\text{O}_2$ surface is one of several hypotheses previously reported to explain the remarkable activity of Au/ceria catalysts, and here we provide direct evidence to support this through electron microscopy.

The substitution of Au into the cerium position leads to a very strong interaction between the gold and ceria, and is expected to further weaken the bonding of surrounding oxygen species, thus enabling their involvement in oxidation reactions [131]. However, whilst some groups believe that the Au^{+3} , shown here to be in the form of single atoms, remains as the key active site [132, 140], others believe that cationic gold is merely the precursor for the active species, which consists of larger clusters that are anchored on the substitutional gold site, and therefore maintain the strong interaction with the support [65, 141]. To resolve this, studies of the stability of the identified single Au atoms under reaction conditions are needed, with *in-situ* electron microscopy perhaps the most likely technique to provide a definitive answer as to the nature and evolution of the active site under simulated reaction conditions.

7.2.3 Stability of the active site under simulated reaction conditions

In the present study, direct simulation of the water-gas shift reaction conditions was not possible, as the use of carbon monoxide and water vapour were not compatible with the present *in-situ* design. However, hydrogen is analogous to carbon monoxide in that it creates a strongly reducing atmosphere, and it is this which is likely to be the key factor in reducing surface oxygen and possibly destabilising the atomically dispersed gold species. The presence of water vapour in the gas stream has been suggested to cause deactivation through reducing the interaction of the gold with the support [141]. However, as the nature of the active gold is still not clear, speculating on subtle deactivation processes may be somewhat premature. Therefore, we will initially investigate the effect of heating and a reducing environment on the stability of gold single atoms.

Following heating to 400°C in hydrogen, small metallic particles were observed, as seen in Figure 7.12. However, the crystallisation of such particles was not observed *in-situ*, and similar particles were seen in the precursor and are thought to be unimportant for activity [132]. Whilst the formation of larger clusters and particles may be detected

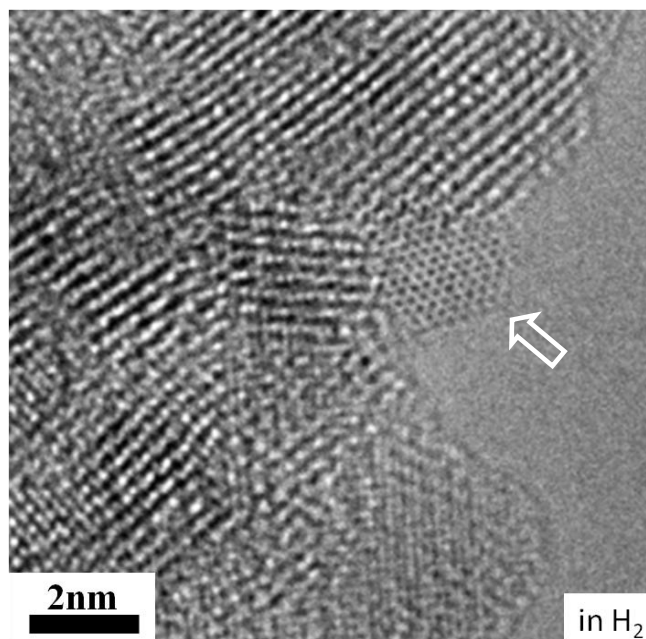


Figure 7.12. Small Au particle after *in-situ* heating to 400°C in H₂.

using TEM imaging, the presence of single atoms or very small clusters requires the atomic number dependent contrast of HAADF STEM. The use of HAADF STEM as an *in-situ* imaging tool traditionally has not been common practice, and it is only recently in York that the first aberration corrected STEM with *in-situ* gas capabilities has been developed. However, the resolution of STEM images is particularly susceptible to any mechanical or electrical instability, and at the present time the HAADF STEM performance possible with the use of the regular Gatan heating holder at elevated temperatures is insufficient to provide images of similar quality as to those discussed in section 7.2.2. Therefore, after heating to 400°C in hydrogen, the sample was allowed to cool before imaging. However, this was done inside the microscope, meaning the sample was at no point exposed to air or any other oxidising environment.

HAADF STEM analysis of the cooled sample, following heating to 400°C in hydrogen, showed similar increases in column intensity to those observed in the precursor sample.

Figure 7.13 shows an example of a column that is approximately 40% brighter than its neighbouring columns, similar to the level of intensity increases observed in section 7.2.2. Without knowing the position of the gold atom before heating in hydrogen, it is not possible to establish the stability of the single atom with absolute certainty, but we

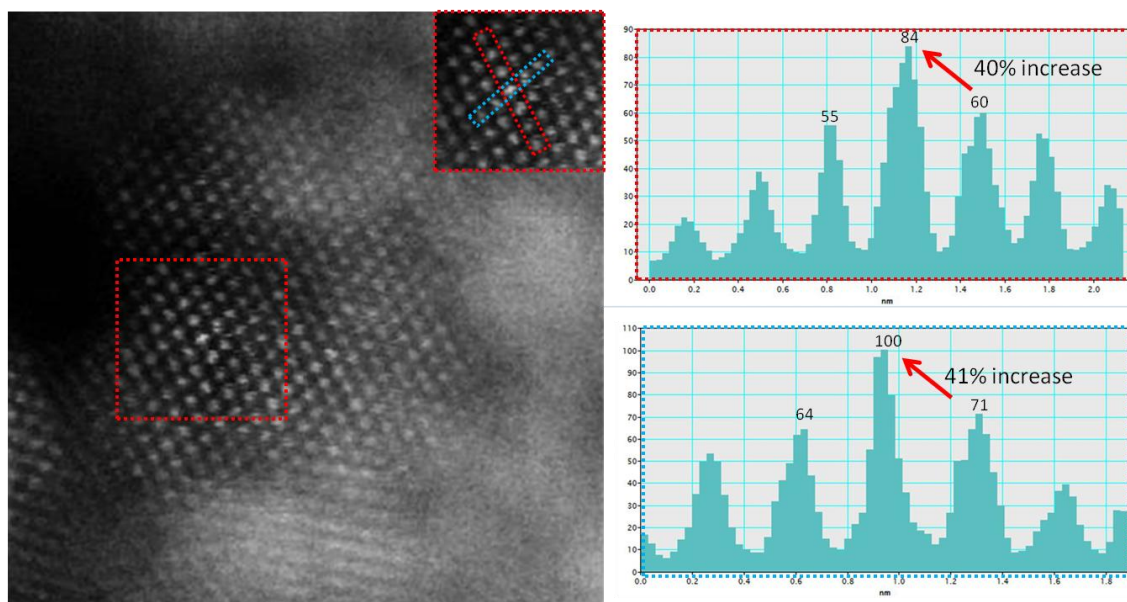


Figure 7.13. Bright contrast from some columns suggests some single Au atoms remain stable after heating in H_2 to $400^\circ C$.

do not observe the agglomeration of single atoms to form small clusters or even larger particles under these conditions. Again, the brighter contrast appears in the position of the cerium column; indicating the single Au atom is substituting for a Ce atom position. If the single gold atoms remain stable under water-gas shift conditions, they can be expected to act as an active site for CO adsorption, whilst subsequent oxidation of the CO molecule can proceed via bonding with one of the surrounding loosely bound surface oxygen atoms.

Further evidence of single atoms existing after heating in hydrogen is shown in Figure 7.14, where the increase in intensity observed is relative to a decreasing intensity background that results from a reduction in thickness of the supporting ceria crystal. Therefore the observed intensity increase of one particular column is in spite of reducing thickness, as opposed to possibly being attributable to any local thickness increase. Clearly, much further work is needed to establish the prolonged stability of the single Au atoms, whilst comparisons with samples reacted *ex-situ* in W-G-S

conditions will determine the relevance of the *in-situ* samples heated in hydrogen. In particular, the role of water vapour and possibly higher pressures may lead to very different stabilities and activation/deactivation mechanisms.

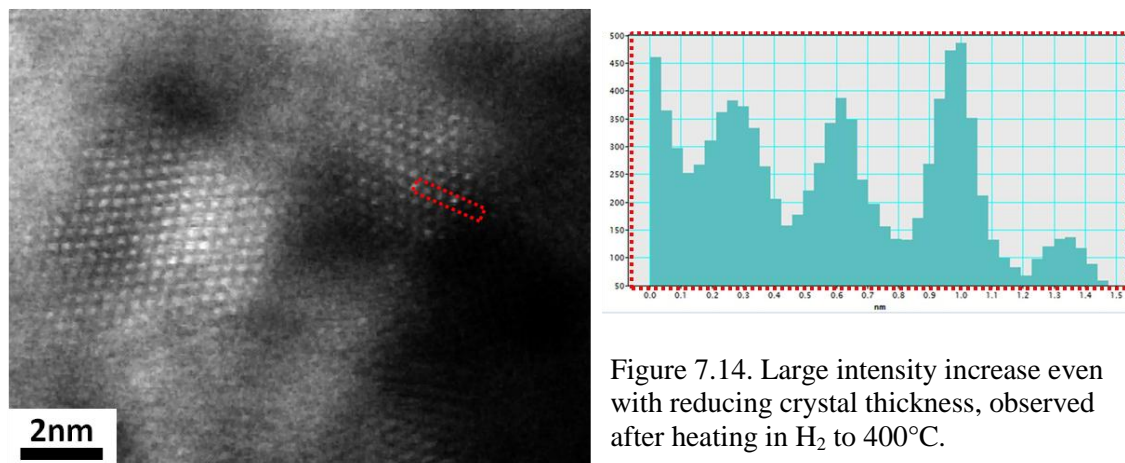


Figure 7.14. Large intensity increase even with reducing crystal thickness, observed after heating in H_2 to $400^\circ C$.

7.3 Chapter conclusions

In this chapter, AC-E(S)TEM has been used to characterise Au/ceria catalysts of significant interest for CO oxidation and hydrogen production through the water-gas shift reaction. The ceria surfaces are shown to be sensitive to prolonged exposure to electron beam, with surface atom movement observed on both $\{100\}$ and $\{111\}$ surfaces. The use of negative spherical aberration imaging allows for clear identification of oxygen atoms, and this technique has been successfully applied to image lattice oxygen atoms in a gas environment. However, surface oxygen atoms could not be resolved in the individual image frame, and may still require reconstruction of the exit wave of electron beam [210]. The ability to resolve the position of oxygen atoms in the presence of a controlled gas environment will be particularly useful for the study of redox reactions, whilst insights into the formation and filling of oxygen vacancies at the surface of oxides such as ceria may prove critical to furthering our understanding of various catalytic processes. Here, exit wave restoration may be particularly useful, providing the number of images required can be sufficiently reduced so as to minimise the invasive effects of the electron beam.

The Z contrast nature of HAADF STEM imaging has been utilised to resolve the nature of the active site in Au/ceria W-G-S catalysts. Small clusters of Au were not detected,

however significant intensity increases of individual atomic columns were observed. These intensity increases could not be attributed to thickness variations or imaging artefacts, and as such are attributed to the presence of single Au atoms that substitute for Ce sites. This closely correlates with the presence of cationic Au as shown by XPS, and it is this cationic Au that is thought to be the cause of the reported high activities of such catalysts [132, 136]. However, currently it is unclear whether the single Au atoms act as the active site, or as a precursor for nucleation of the active phase, in which the substitutional Au atoms cause the surrounding oxygen surface atoms to be more weakly bound and therefore more reactive.

The recent development of aberration corrected environmental HAADF STEM [190] now makes possible observations of supported single atoms *in-situ*. Future developments, such as heating holders designed for use in ESTEM, will lead to improvements in the capability of the technique, and should allow definitive answers to questions regarding the nature and the stability of the active site under reaction conditions.

Chapter 8

Activation and Deactivation of Ni catalysts

The activation process required to transform the precursor into the catalytically active phase can play a major role in determining the final size, structure and distribution of catalytic nanoparticles, whilst the performance of nano-catalysts is typically observed to diminish over time as a result of a variety of possible deactivation mechanisms. In the following chapter, nickel supported on alumina catalysts provided by Johnson Matthey Plc (JM), as well as a model system, are used to study both the reduction process of NiO to the active Ni metal and the subsequent sintering that occurs upon reduction. Although these *in-situ* studies are carried out at much lower pressures than would be used industrially, the gas-solid interface is critical to many dynamic chemical processes. Atomic resolution imaging under reaction conditions in ETEM allows the direct observation of the dynamic structural evolution at the solid catalyst surface and provides insights into activation and deactivation mechanisms, including sintering.

8.1 Sample preparation and initial characterisation

In the following chapter results are presented from two Ni/alumina samples provided by JM, as well as a model NiO powder purchased from Aldrich for comparative studies on a model system. The first sample discussed is a NiO precursor supported on a high surface area alumina made by co-precipitation for industrially relevant hydrogenation reactions. The samples come in powder or pellet form, which are then dispersed in

ethanol and ground in a pestle and mortar before being deposited on to a standard TEM holey carbon grid. X-ray diffraction (XRD) shown in Figure 8.1 (provided by JM) of the sample reveals that the alumina support is a mixed phase delta/theta alumina, and as such will be labelled as Ni/ δ -Al₂O₃. The small crystal size and porous nature of the δ -alumina provides a very high surface area support, whilst the 2-5 nm particles present are clearly observed using Z contrast STEM. Characterisation of the small particles using AC-TEM is shown in Figure 8.2, with particles imaged in the [011] (above) and [001] (below) orientations. Analysis of the corresponding fast Fourier transforms show the particles are NiO and bound predominantly by {001} non-polar surfaces, which are expected to be the most stable for the NiO cubic rock-salt structure [213].

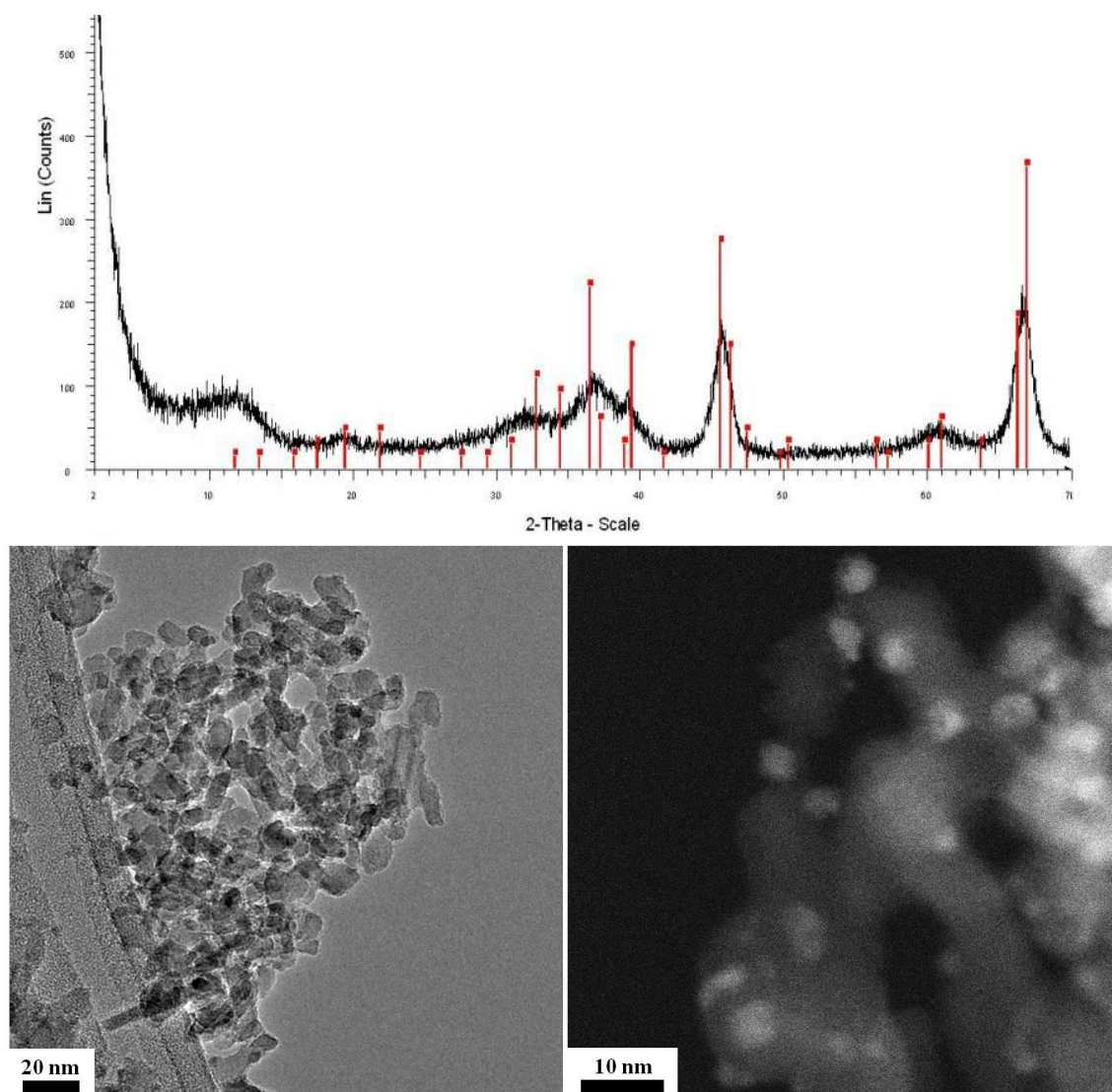


Figure 8.1. XRD analysis (above) identifies the Al₂O₃ support as a mixed phase delta-theta alumina. TEM and HAADF STEM (below) show the crystallite size of both the support and NiO particles present in the precursor.

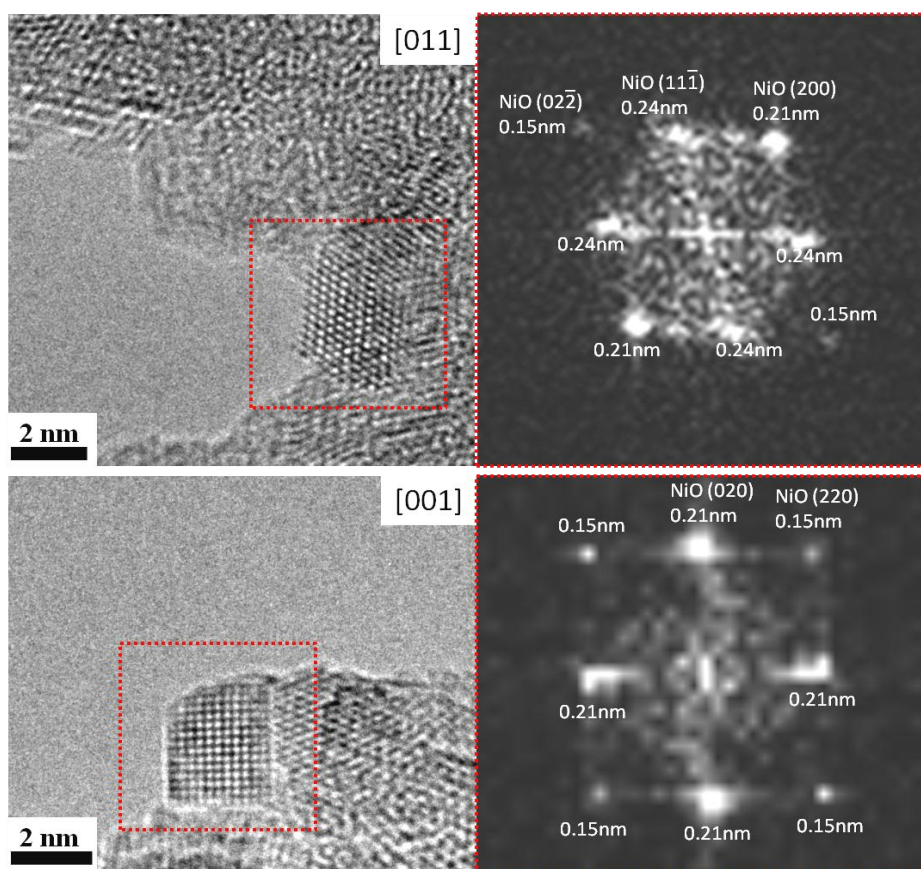


Figure 8.2. AC-HRTEM with analysis of the corresponding FFTs clearly reveal the small particles are NiO, imaged here in the [011] (above) and [001] (below) orientations.

The nature of δ -Alumina makes for an excellent high surface area catalyst support. However, the supports porosity and small crystal size, with many overlapping crystals in a variety of orientations, often makes interpretation of images of the small supported particles inconclusive. Ni catalysts supported on alpha alumina (α -alumina) are often used for high temperature reactions, such as steam reforming, due to their excellent thermal stability. Here, the supporting alumina crystals are much larger and therefore allow easier interpretation of the data, particularly for *in-situ* studies of particle stabilities. XRD analysis in Figure 8.3 shows that the supporting alumina is in the alpha phase, whilst the large crystal size of the support can clearly be seen in the micrographs (below). Also observed is the distribution of the NiO prepared using a deposition-precipitation technique, and this sample will be referred to hereafter as Ni(DP)/ α -alumina.

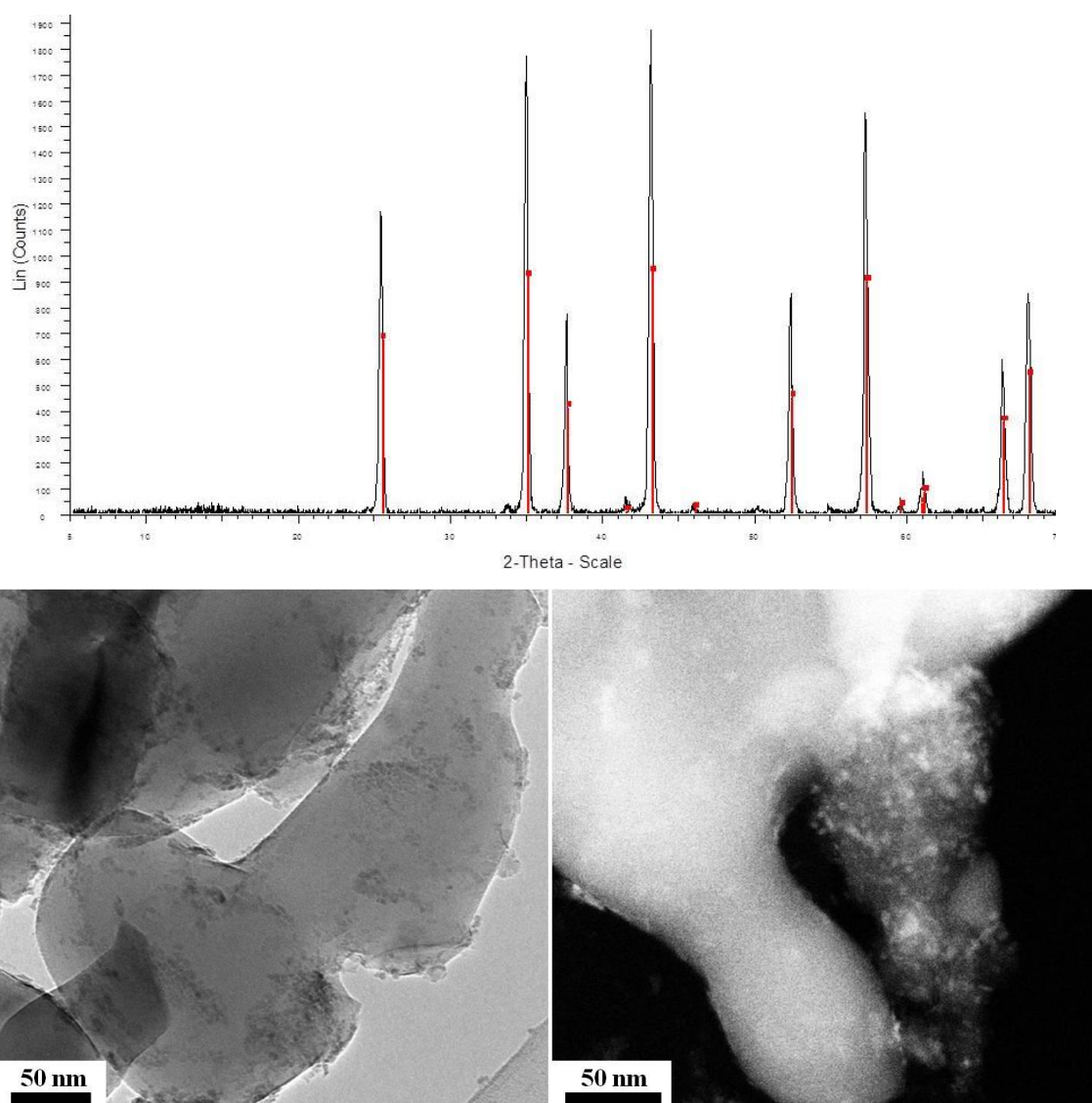


Figure 8.3. XRD analysis provided by JM (above) shows the support is alpha alumina. HRTEM and HAADF STEM images (below) show the large crystallite size of the α -alumina support as well as the distribution of the NiO.

High magnification AC-TEM images of the Ni(DP)/ α -alumina precursor are shown in Figure 8.4, and analysis of the image and corresponding FFT confirm the particles are NiO. Very small NiO particles (< 2 nm) are observed to be present on the surface of the support, as shown in Figure 8.4 (top), but not with the frequency that might be expected from an approximately 10% atomic weight catalyst. This indicates that not all of the deposited NiO is in the form of discrete particles, but may be atomically dispersed or exist as layers on the support. Evidence for this is provided in Figure 8.4, with the bottom left image showing a small layer of NiO on the support (arrowed), whilst on the bottom right we can see larger agglomerates of NiO.

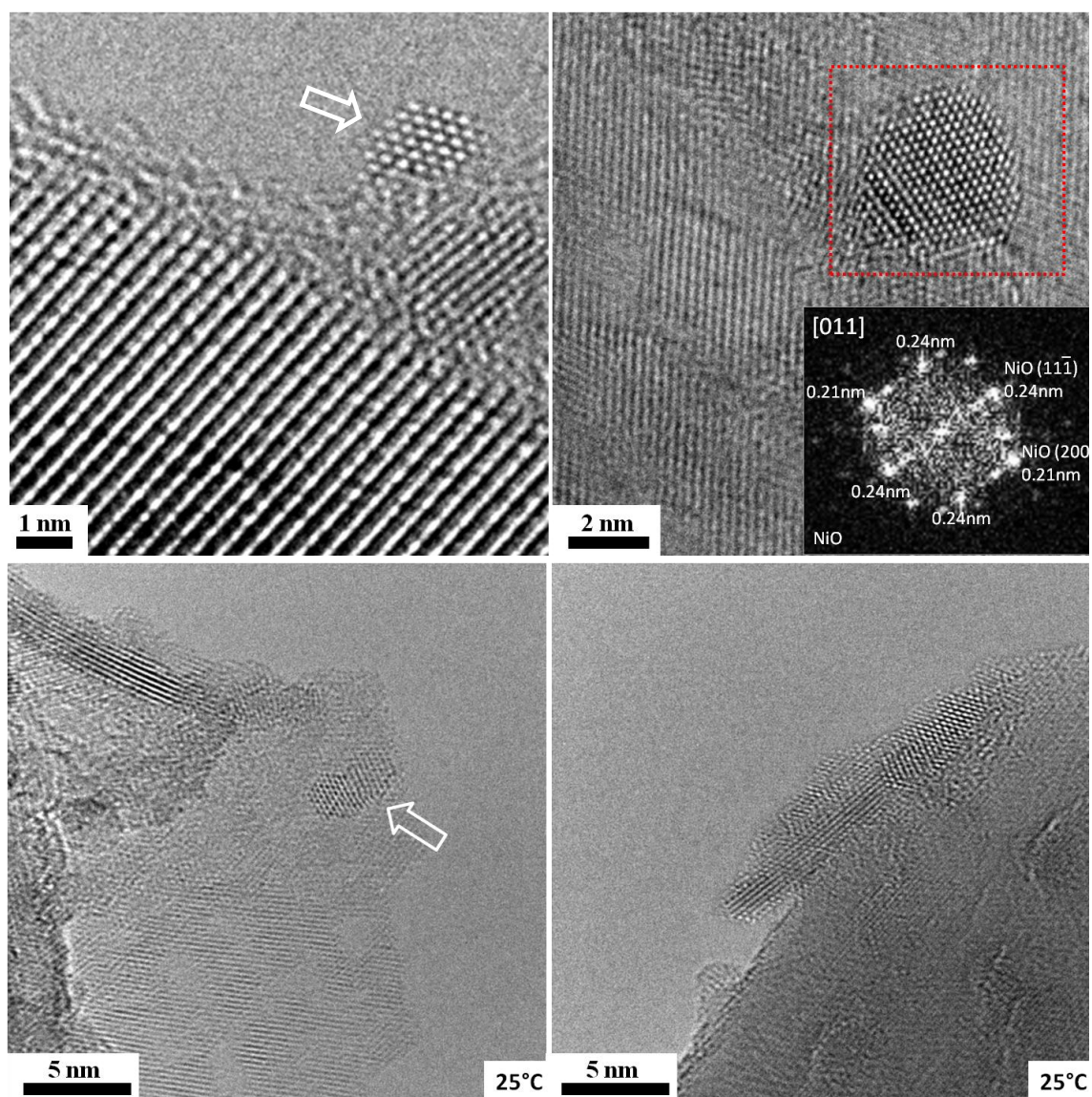


Figure 8.4. Very small NiO particles are observed on the surface of the α -alumina by AC-HRTEM (above), whilst other areas suggest the presence of highly dispersed layers of NiO on the support (below).

8.2 Reduction of NiO to the active phase

8.2.1 Reduction of industrial NiO/Alumina catalysts

As the experimental work presented in this thesis was conducted concurrently with modifications to allow the insertion of controlled gas environments into the microscope, data was acquired both before and after the gas capability was implemented [190]. As such, experiments performed before the modifications were conducted in vacuum, with higher temperatures used to drive the reduction process. Figure 8.5 shows the same

particle from the Ni/ δ -Al₂O₃ sample over the course of 9 minutes at 600°C in vacuum. As the fast Fourier transforms are taken from a small selected area of the *in-situ* image, there is an approximate $\pm 10\%$ error in the measurements of the diffraction spots, mainly resulting from the large pixel size of the FFT. Further complications occur due to the overlap of expected lattice spacings for NiO(200) and Ni(111) (0.209 nm and 0.203 nm respectively), as well as possible contributions from the support. However, the particle is initially still in the NiO form, as shown by the match (within error) of the diffraction spots in the FFT with that expected from NiO in the [011] orientation. After 9 minutes at 600°C the particle has changed significantly, exhibiting both different internal structure and external surfaces. Analysis of the FFT is somewhat inconclusive, as the

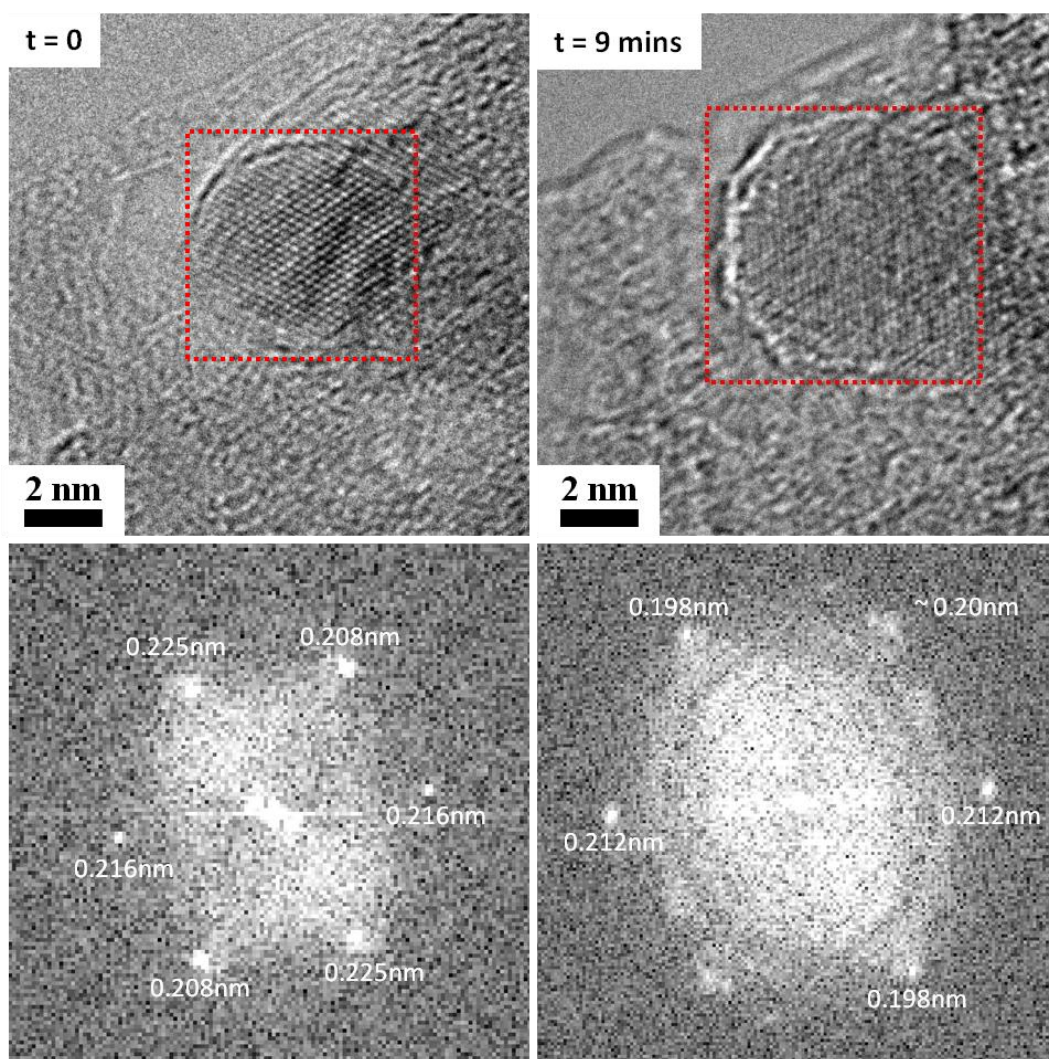


Figure 8.5. A sequence of images (with corresponding FFT) of the same particle at 600°C in vacuum taken 9 minutes apart. The particle is initially NiO but is observed to undergo a transformation after ~ 9 mins. Analysis of the latter FFT reveals spots consistent with the $\{111\}$ spacing of Ni, whilst the change in structure towards $\{111\}$ facets can clearly be seen.

diffraction spots are within error of both the Ni{111} and NiO{200} spacings, whilst the spatial frequencies and angles between the spots do not directly correspond to a consistent orientation of either Ni or NiO. Therefore the diffraction spots may originate from a mixture of both Ni and NiO in different orientations. However, the spatial frequencies measured are consistent with the presence of Ni{111}. Furthermore, the change in surface structure can be expected from a NiO to Ni transition, as the most energetically stable surface facet goes from {001}(NiO) to {111}(Ni).

Upon heating to the much lower temperature of 400°C in H₂, metallic Ni particles are observed to form on the Ni(DP)/ α -alumina sample. An example of the same area at room temperature and 400°C in H₂ is shown in Figure 8.6. The density of Ni particles formed after reduction is much greater than that of the initial NiO particles observed, suggesting that much of the NiO is initially atomically dispersed, or exists as layers or agglomerates that form small particles upon reduction. The areas in the precursor that appear darker in the mass-thickness contrast image correspond to more dense areas of Ni particles in the reduced sample, whilst the distribution of Ni particles indicates that when reduced, the dispersed Ni is able to migrate across the support before reaching a nucleation point and forming a metallic particle. Higher magnification images shown in Figure 8.7 confirm the particles are reduced Ni, and show that they are approximately hemispherical in nature and typically 2-5 nm in diameter.

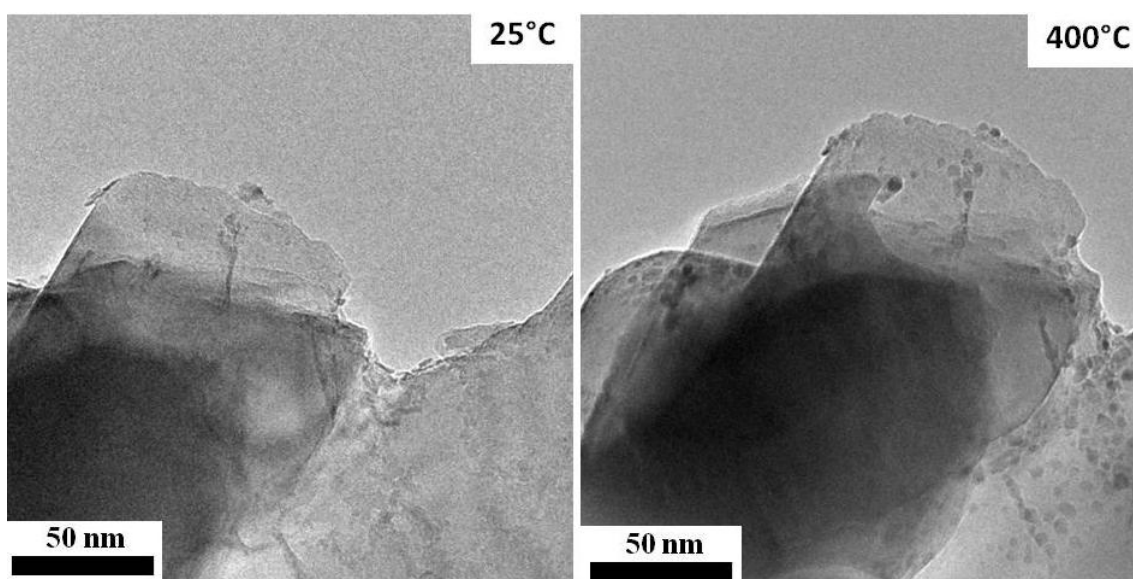


Figure 8.6. The formation of discrete Ni particles is observed upon heating to 400°C in H₂.

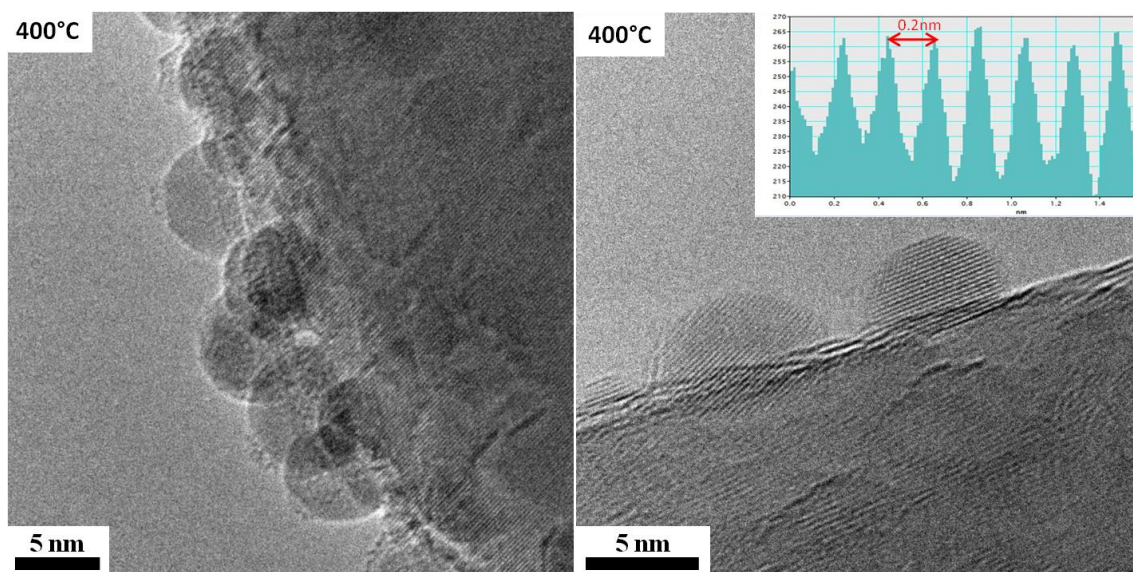


Figure 8.7. The Ni particles are ~ hemispherical with a diameter of 2-5 nm. Measurements of the observed lattice spacings confirm the particles are metallic Ni.

8.2.2 *In-situ* reduction of model NiO particles

As a basis for comparison, NiO powder was used as a model system. The wide range of particle sizes present enable additional studies of the effect of particle size on the reduction of NiO to Ni, whilst the removal of the support material provides a major simplification of the system, allowing direct interpretation of the lattice spacings or diffraction patterns experimentally observed. Preliminary experiments done in selected area diffraction (SAD) mode were used to establish the temperature regime at which reduction occurred in H₂. The advantage of such a technique is that in the absence of the alumina support, the diffraction patterns give easily interpretable area averaged data to high spatial frequencies in the *in-situ* environment, negating the need for atomically resolved images or particles in desirable orientations. Additionally, the experiment can be conducted with minimal effects of the electron beam, and can quickly provide structural information from a wide range of areas. This allows much better sampling than an imaging approach, and provides information regarding the homogeneity of the sample as well as the temperature and time scales needed for reduction.

The NiO powder was observed to begin to reduce in H₂ at approximately 350°C, with complete reduction of most areas by 450°C. An example of two SAD patterns is shown in Figure 8.8, with clear matches with the theoretical patterns occurring for NiO at room

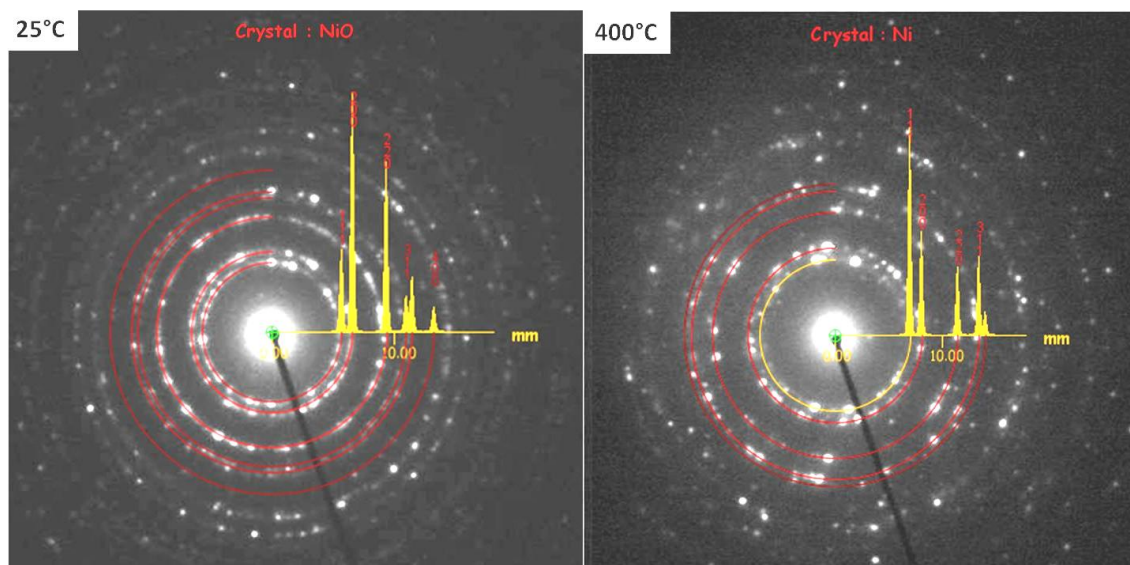


Figure 8.8. Diffraction patterns obtained at room temperature and at 400°C in H₂ of NiO powder provide unambiguous proof of the reduction of NiO to Ni.

temperature (left) and Ni at 400°C (right). The difference between the two patterns is highlighted in Figure 8.9, where at 400°C the inner most ring, corresponding to the NiO(111) spacing, has disappeared, whilst a ring at the expected Ni(200) spacing appears. However, it should be noted that at this temperature and pressure, not all of the NiO was fully reduced, with some areas showing both Ni and NiO diffraction rings.

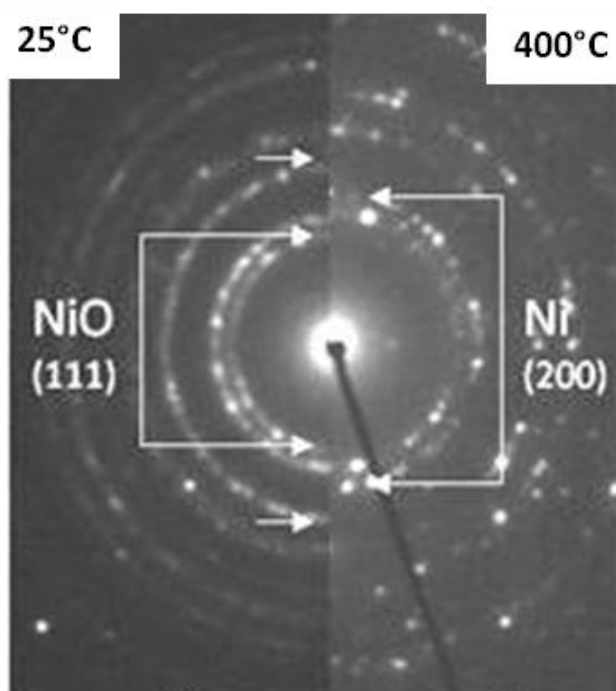


Figure 8.9. *In-situ* selected area diffraction clearly shows the reduction of NiO to Ni at ~400°C, as the NiO(111) ring disappears and the Ni(200) ring appears.

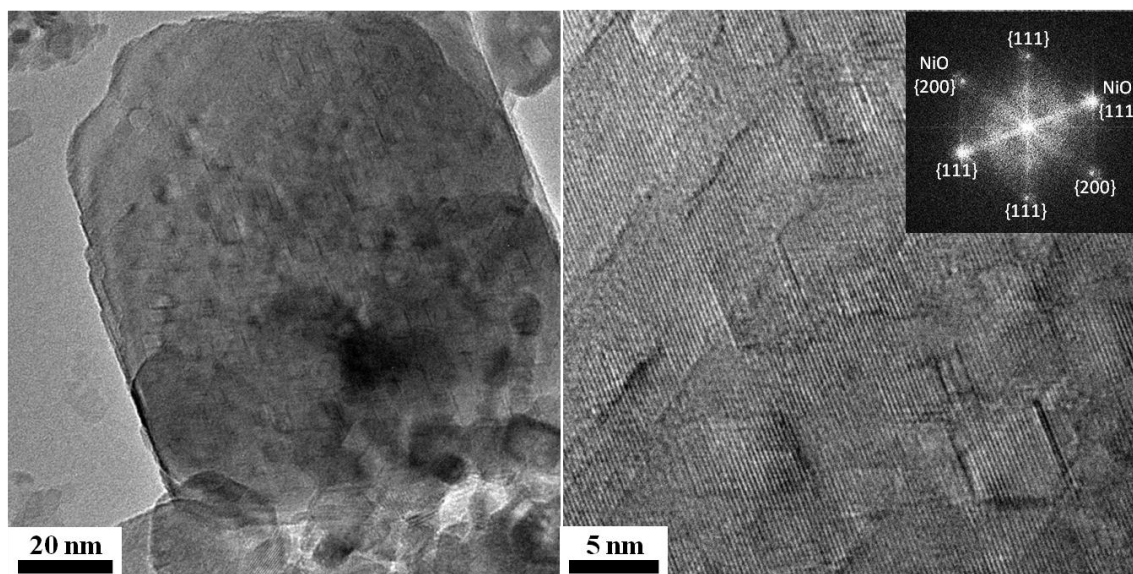


Figure 8.10. A large NiO particle after heating to 500°C in H₂. The particle is still NiO, however symmetry related defects are observed along the $\langle 111 \rangle$ directions. The defects appear to start from the surface, suggesting they are formed as a result of the reduction process.

The remaining NiO corresponded to the larger particles originally present in the sample; and it is expected that higher temperatures, pressures or extended exposure to the reducing environment may be needed to fully reduce these larger crystals. An example of a large particle still in the NiO phase is shown in Figure 8.10, with the FFT taken from the higher magnification image (right) clearly matching NiO in the $[01\bar{1}]$ projection. Also clear from the high magnification image are a high proportion of extended symmetry-related defects along the $\langle 111 \rangle$ directions, as is further evidenced by the streaking observed in the FFT between the $\{111\}$ diffraction spots. These extended defects are expected to occur in order to accommodate the growing concentration of oxygen vacancies in the crystal that result from interaction with the reducing environment. In the present study it has not been possible to accurately determine the Burger's vector of the defect from the 2D image, and future work utilising a double tilt heating holder (not currently available) and diffraction contrast imaging will seek to further determine the nature of the extended defects that occur in larger particles during the reduction process.

A smaller particle at 600°C in vacuum is shown in Figure 8.11. Measurements of the lattice spacings observed in the top and bottom part of the particle show them to match the Ni(111) spacing. However, the image shows a band in the middle of the particle

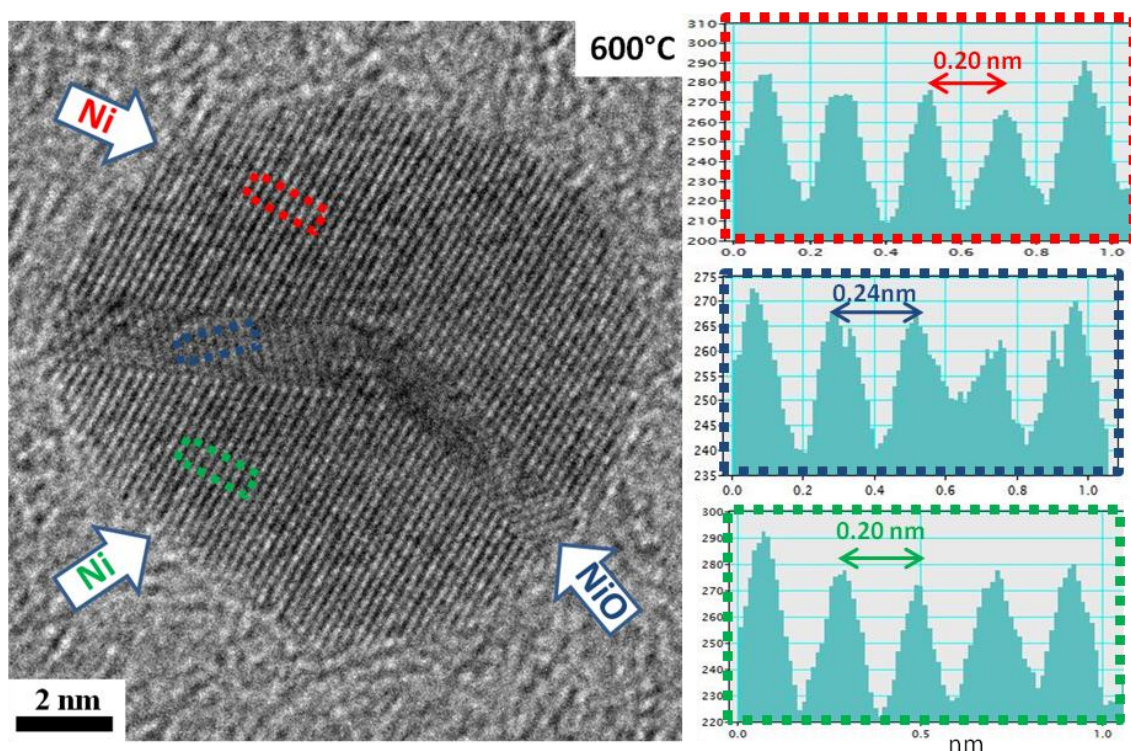


Figure 8.11. Analysis of a particle heated to 600°C in vacuum shows that it is predominantly reduced Ni, however an internal section reveals lattice spacings greater than can be attributed to Ni, suggesting the presence of some remaining NiO.

that is clearly a different crystal to the areas above and below. Measurements of the lattice spacings from this section are difficult due to its small size and instabilities introduced by the heating holder, however they appear to be larger than any spacings than those that would be present in Ni, and may therefore be explained by the residual presence of unreduced NiO, with the observed spacings being NiO(111).

8.2.3 Towards a reduction mechanism

From the results presented in Section 8.2, it seems that there is more than one mechanism by which the oxide may be reduced to form the active metallic phase. For the Ni(DP)/ α -alumina sample, the highly dispersed nature of the NiO precursor means that upon reduction, the Ni is in the form of atoms or small clusters that are free to migrate on the surface of the support, before reaching a nucleation point and forming the small hemispherical particles observed. Therefore the size and distribution of the reduced Ni particles may be controlled by the initial NiO loading, as well as the density of likely nucleation points on the support. The NiO on the Ni/ δ -Al₂O₃ sample is deposited in the form of small nanoparticles, and these are observed to reduce directly

to Ni. However, in both cases the resulting small Ni nanoparticles appear to be free of any internal defects as a result of the reduction process. In contrast, larger particles observed in the NiO powder require higher temperatures or pressures to fully reduce, with the reduction appearing to proceed via a defect mechanism. Although further analysis is needed to determine the Burger's vector of the defect, they are along the $\langle 111 \rangle$ directions and accommodate the growing number of anion vacancies in the crystal structure [214].

Therefore, the effect of particle size seems to play a crucial role in not just the rate of reduction but also the mechanism by which the particle is reduced. In order for complete reduction, the bulk oxygen atoms must either migrate out to the surface of the crystal – where they can react with the dissociated hydrogen at the particle surface to form H_2O – or the H atoms must diffuse into the particle until they reach the remaining oxygen, before reacting and diffusing out of the particle, presumably as OH [12]. Whichever of these is the case; the migration distance of the O, H or OH species from the particle surface to the Ni/NiO boundary will determine the ease with which the reduction process can proceed.

NiO particles of just a few nanometres – such as those present in the JM catalysts – appear to reduce without the need for the formation of extended defects. The high surface to volume ratio of small nanoparticles means that they have proportionately more atoms at the surface, whilst the migration distance of the diffusing species is a significant proportion of the particle radius, allowing relatively fast reduction to metallic Ni. For larger NiO particles undergoing reduction, the growing number of oxygen vacancies diffusing into the bulk is accommodated for by the formation of extended anion-deficient defects. These defects can be expected to eventually order, leading to Ni, but the process requires more time and possibly higher temperatures.

In the case of larger NiO particles, the particle radius is much greater than the migration distance of the diffusing species, making it difficult for the bulk oxygen atoms to reach the reactive hydrogen. The diffusion of oxygen vacancies into the crystal presents a path for a given bulk oxygen atom to reach the particle surface and the reactive hydrogen; albeit potentially one with several energy expensive bond breaking and

forming steps. The formation of extended defects, such as those shown in Figure 8.10, may provide a path with reduced activation energy associated with the oxygen diffusion, thereby facilitating the removal of oxygen from the bulk of the crystal.

Further work is clearly needed to more fully investigate the effect of particle size on the reduction mechanism. The future use of a double tilt heating holder, coupled with experiments using nanobeam diffraction, diffraction contrast and atomic resolution imaging should allow direct characterisation of the nature of the defects formed. Complimentary calculations on the energetics of oxygen removal through the variety of proposed processes may also provide further insight when combined with the experimental *in-situ* observations.

8.3 Sintering of Ni catalysts

After the catalyst is activated and brought online, the initial activity is observed to decrease over time due to various possible deactivation mechanisms. Perhaps the most problematic of these is thermal deactivation, or sintering, as it leads to an irreversible loss of surface area available for reactions. Results of particle stabilities for the Ni(DP)/ α -alumina sample are presented in the following section. The larger crystal size of the α -alumina support allows for easier interpretation of any observed changes in the particle size or position, whilst the realistic nature of the metal-support interaction much more closely resembles that of an industrial Ni/alumina catalyst than two dimensional amorphous model supports often used in microscopy studies [35].

As the desired lifetime of catalysts can often be several months or years, sintering observations would ideally replicate this time frame. Clearly this is not practical for *in-situ* microscopy experiments, and can instead be studied by *ex-situ* observations of the fresh and aged catalyst. However, as discussed in Chapter 2, *ex-situ* analysis – such as inferring sintering mechanisms based on the resulting particle size distribution – can lead to misleading results, and *in-situ* observations are needed to understand the mechanism by which particle growth occurs. Constraints on available microscopy time mean *in-situ* observations are of the catalyst in its infancy. However, such observations

can be used to directly observe the sintering process, and indeed the rate of deactivation of the catalyst is greatest immediately after activation.

Figure 8.12 shows the same area of the Ni(DP)/ α -alumina catalyst over the course of 4 hours at 400°C in H₂. The images were acquired with minimal exposure to the electron beam, with the beam turned off between images. Therefore any observed changes in the Ni particles are a direct result of continued exposure to the reaction environment. At $t=0$, the sample is imaged as soon as is practical after the temperature of 400°C has been reached and reduction and formation of metallic Ni particles has occurred. After 1.5 hours, the Ni particles have changed substantially. For example, in the area highlighted, there is approximately half the number of particles remaining, with several of the smaller particles having disappeared and the larger particles remaining in the same place on the support. After 4 hours, little change is observed from the situation after 1.5 hours, and therefore more detailed studies of the same area have concentrated on the initial 90 minutes after reduction.

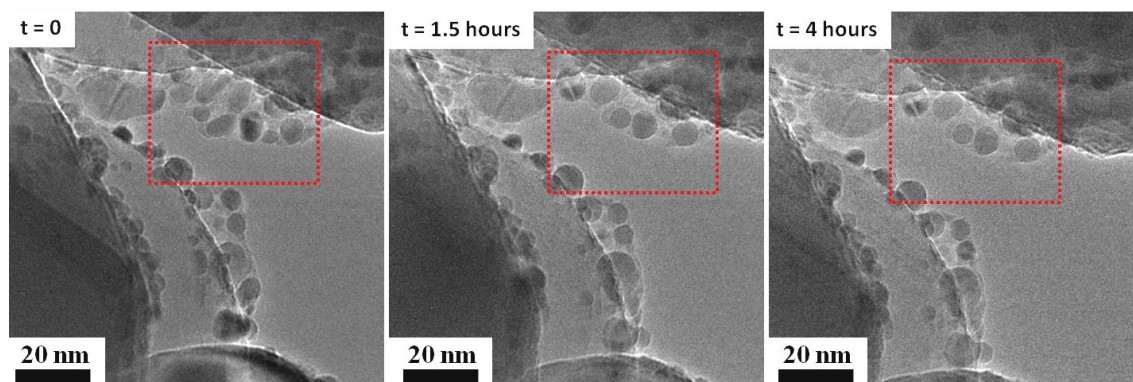


Figure 8.12. Sintering of Ni particles at 400°C over the course of 4 hours showed significant sintering and loss of surface area over the first 90 mins, followed by much improved stability.

A further example of an area exposed to the electron beam for the minimum time necessary is shown in Figure 8.13, and again significant loss of Ni particles over the course of the 90 minutes is observed at 400°C in H₂. Again, many of the small particles have disappeared, whilst those that remain appear to be located at the same position on the support, such as those arrowed. These observations are consistent with sintering through an Ostwald ripening mechanism, although could possibly be explained by migration of smaller particles and relative stability of the larger particles that remain effectively immobile. Therefore, continuous observation of the same area throughout

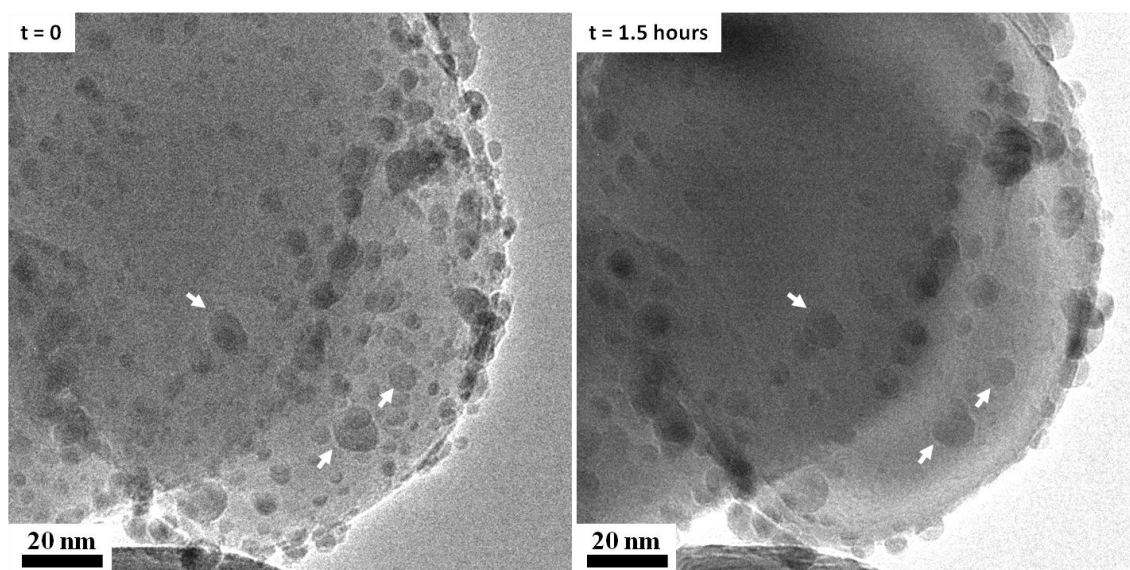


Figure 8.13. A reference area only exposed to the electron beam at the start and end points showed significant sintering as a result of the reaction conditions.

the sintering process is needed. However Figure 8.13 provides a reference area with which to compare the *in-situ* results, ensuring that both observations are consistent and that the electron beam is playing a minimally invasive role.

A sequence of images taken from an *in-situ* movie acquired at 400°C in H₂ is shown in Figure 8.14. Looking at the difference between the initial distribution of Ni particles and those after a similar time as in Figure 8.13, we see a comparable loss of particles present, whilst the remaining particles appear immobile on the support, showing that under these imaging conditions, continued exposure to the electron beam has a minimal effect on both the rate and mechanism of particle sintering.

From the *in-situ* video we directly observe sintering through an Ostwald ripening mechanism, with no evidence of particle migration and coalescence. This suggests that there is a strong interaction between the Ni particles and the supporting alumina, causing the particles to be well anchored on the support. Although the strength of this interaction prevents particle migration and coalescence by rendering the particles effectively immobile on the support, it encourages sintering via Ostwald ripening, as the interaction between the Ni and the alumina provides the driving force for atomic migration of surface atoms on to the support. A classical example of this can be seen in the particles labelled A and B, where the smaller particle A shrinks and has disappeared

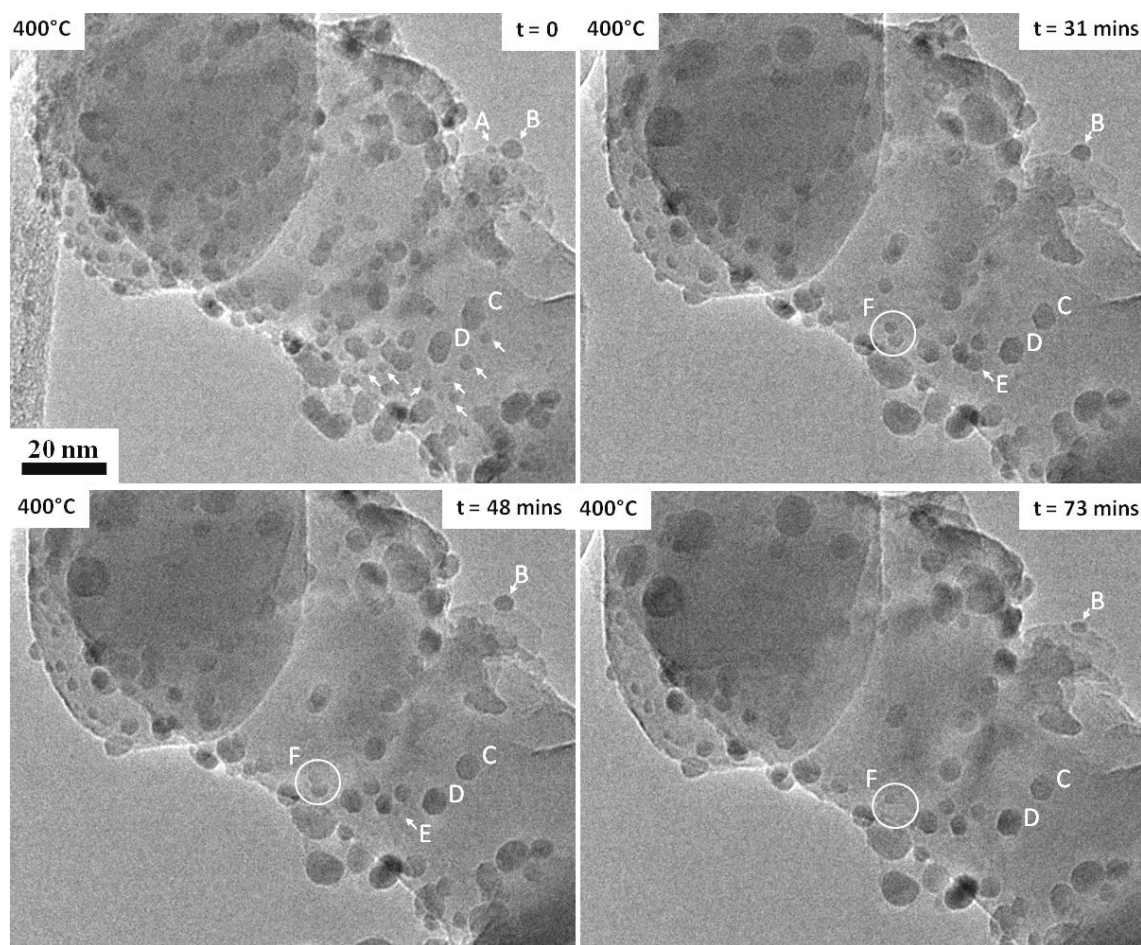


Figure 8.14. *In-situ* observations of the same area in H_2 at $400^\circ C$ reveal sintering through an Ostwald ripening process. The observations do not match the simplified models of Ostwald ripening, as clearly more than just size determines the particle stability.

after 30 minutes. Several other small particles, typically < 2 nm, are arrowed in the initial image, and are observed to be the first to disappear under the sintering conditions. This is consistent with the classical theory of Ostwald ripening, in which the smallest particles have the highest potential energy (as shown by the Gibbs-Thomson relationship in equation 2.5) and will therefore be the least stable, as predicted by equation 2.12.

However, one striking observation from the *in-situ* video is the rate at which particle decay occurs. Classically, Ostwald ripening is thought of as the constant exchange of atoms between particles; with the net effect of atoms migrating from the smaller particles (with higher potential energy) to the larger particles, and therefore causing the less stable small particles to shrink whilst the larger ones grow. However, from the *in-situ* video, small particles are observed to undergo relatively sustained periods of

stability before rapidly shrinking and disappearing. For example, the particle labelled E is approximately 4.5 nm and appears to remain stable for 48 minutes, with no measurable change in particle size. At this point, the particle decays rapidly, and has disappeared completely after a further three minutes. This is just one of several examples of rapid particle decay following sustained periods of stability observed, and indeed similar decay times for Ni on MgAl₂O₄ were reported by Challa *et al* [42]. They find that equation 2.14 can be used to describe the observed decay rates, with the non-linear Gibbs-Thomson relation explaining the exponential increase in the rate of decay as the particle shrinks; although different values of the supposed constants in the K_{int} term given in equation 2.13 are needed when describing the decay rates of other particles. However, the sudden onset of particle decay after sustained periods of stability is yet to be explained in the literature, with the current evidence suggesting there may be a trigger that causes the loss of stability of an individual particle.

Further differences from the classical theory of Ostwald ripening, which describes particle radius as being the only variable parameter governing particle stability, are highlighted by the two particles circled in F. Again the two particles remain relatively stable for extended periods of time, with no shrinking of either particle observed for the first 53 minutes. At this point, it is actually the slightly larger particle (the lower one in the image), approximately 4 nm in diameter as opposed to the 3 nm particle nearby, that is observed to rapidly decay and disappear after a further two minutes. According to theory, and expressions such as equation 2.12, the smaller particle would be expected to be the least stable, whilst the rapid decay after prolonged periods of stability again indicate that there must be a trigger for the shrinking of the particle due to atomic migration.

Particles that remained stable throughout exposure to the sintering conditions in the allotted time, such as particles C and D, appear to quickly adopt a faceted morphology and then maintain their size and surface structure throughout the experiment. By minimising surface energy through the creation of low index surface facets, the particle's surface atoms will be in a minimum energy state. This is therefore likely to have a major impact on the energy barrier for the migration of surface atoms required to facilitate Ostwald ripening. From equations 2.12 and 2.13, we can see that the stability

of a particle is dependent on a prefactor, v_p , that governs the rate at which a metal surface atom may diffuse from the particle on to the support. In the literature, this term is treated as a constant for a given supported metal particle system. However, the observation that the most stable particles appear to be those with minimum energy surface facets suggests that this parameter is dependent on the surface energy and therefore surface structure of the particles. Therefore differing surface energies may explain the relative instability of some particles that are of a comparable or even slightly larger size than their more stable neighbours.

The sudden loss of particle stability may be explained by a change in surface energy, and therefore the v_p prefactor, of a given particle. The migration of just one or two atoms from a closely packed surface is likely to increase the mobility of the neighbouring atoms, possibly reducing the energy barrier for surface atom diffusion on to the support below the kinetic energy of surface atoms at the reaction temperature. Therefore one hypothesis for the sudden onset of particle decay is a domino type effect upon the loss of one or two surface atoms, causing a change in the v_p term and facilitating the onset of large scale atomic migration.

An additional complication in developing a full understanding of relative particle stabilities comes from the contact angle parameter, θ . Like the v_p term, this parameter is treated as a constant in the literature, however it is likely that θ will vary with particle size [43], whilst inhomogeneities in the surface of the alumina will lead to a variety of possible interactions between the particle and the support. From the present results, the role of variable particle surface energetics and support interactions is proposed as a hypothesis to explain the difference in particle stabilities observed, and further experimental data, preferably with atomic resolution, will probe the effects of these, and possibly other parameters. Acquiring such data at sufficiently high magnifications whilst maintaining minimal effects of the electron beam may prove challenging, and careful comparisons with reference experiments without the beam will be needed [190].

The particle size distributions (PSD) for the images shown in Figure 8.14 of the sample immediately after reduction and after sintering for 1 hour at 400°C in H₂ are shown in Figure 8.15. Both distributions are lognormal in nature, again highlighting the danger

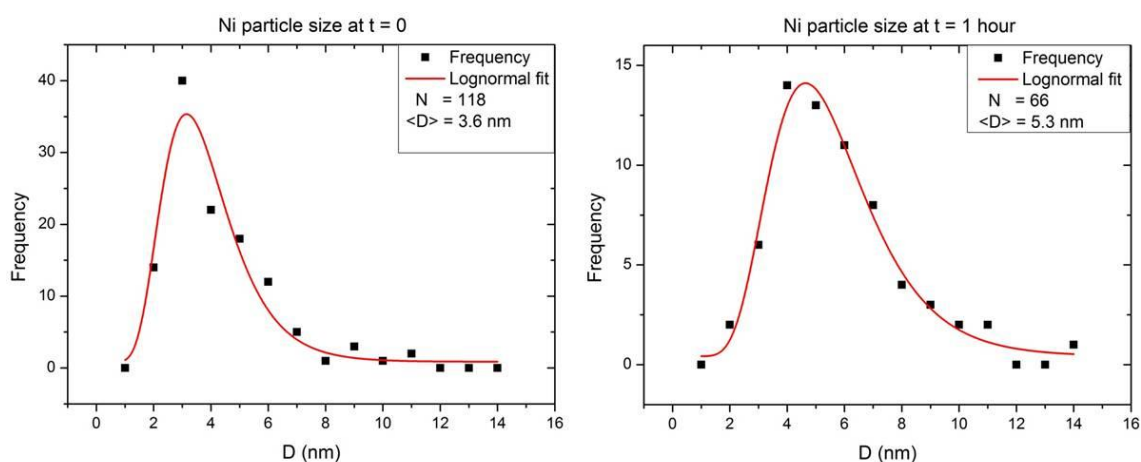


Figure 8.15. Particle size distributions of the same area as shown in figure 8.14 at $t = 0$ and $t = 1$ hour.

of inferring the sintering mechanism based on the resulting PSD. The evolution of the PSD is clearly time dependent, and indeed after 1 hour could be thought of as being in the intermediate stage between the initial log normal distribution and the theoretically predicted Lifshitz-Slyozov-Wagner distribution [28, 29] expected as a result of Ostwald ripening. The mean particle size in the region of interest increases from 3.6 nm to 5.3 nm, whilst the total number of particles present is approximately halved.

Based on the measured PSD, and assuming the particles to be hemi-spherical (as indicated by images such as Figure 8.7), the total volume of Ni present in the region of interest is found to increase from approximately 4000 nm^3 to 4900 nm^3 over the course of sintering for an hour. The apparent gain in mass means the measured overall surface area remains approximately constant, despite the mean particle size increasing. Clearly, we would expect mass to be conserved in the system, suggesting that additional factors either not considered or observed are at play.

The most obvious explanation is that there is a limit on the size of particles that are detected using the TEM technique at this magnification. Certainly any small clusters or particles $< 1 \text{ nm}$ are not observed in the image, and indeed a significant number of these present in the freshly reduced sample may help explain the apparent gain in Ni mass as they then sinter and join larger particles. However, the large difference in volume of Ni before and after sintering means that it would take ~ 2000 particles of 1 nm diameter to conserve mass, which seems unlikely to be the case. Therefore, whilst the lack of

sensitivity to particles that are 1 nm or less in diameter may contribute to the volume discrepancy observed, it will not be the dominant cause.

A more plausible explanation comes from the reduction rate of NiO. As we saw in the previous section, some NiO may require extended exposure times, or higher temperatures or pressures in order to reduce to the active metal. The slow reduction rate of some NiO is shown in Figure 8.16, which shows the presence of small NiO crystals observed after the sample was heated in H₂ at 400°C for 4 hours. As reduced Ni will not oxidise without heating in an oxidising environment, it can be assumed that the observed NiO crystals remained in the NiO phase throughout the reduction and sintering experiment. Therefore we can expect that not all of the NiO is initially reduced, and the following observations are of the combined effect of continued reduction plus sintering of the reduced Ni.

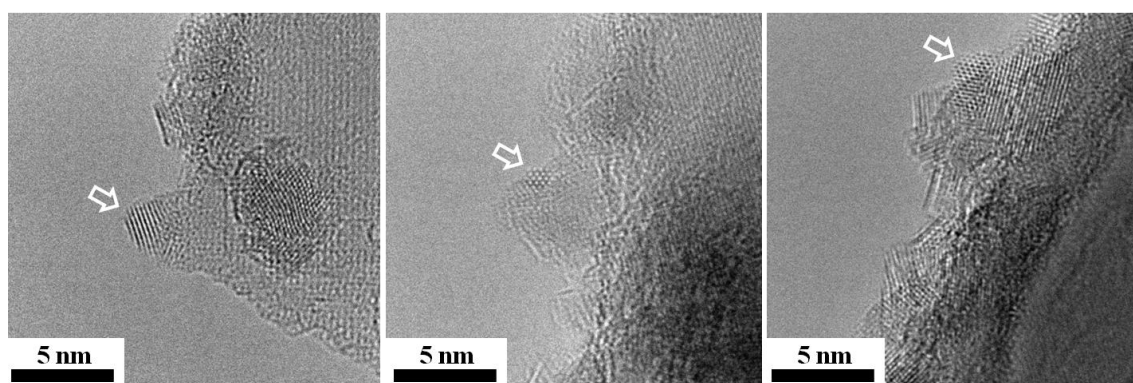


Figure 8.16. AC-HRTEM images after heating reveal the presence of some NiO remaining, suggesting that not all the NiO was reduced.

8.4 Chapter conclusions

The activation process for supported metal catalysts can have a major influence on the resulting particle size and morphology of the active particles. In this chapter, observations of the reduction process of NiO to Ni for a variety of NiO particle sizes are reported, with the results suggesting a size dependent reduction mechanism. For small NiO crystals, such as those present in the catalysts provided by JM, the migration distance of the oxygen atoms is a significant proportion of the particle radius, therefore allowing the straightforward removal of oxygen atoms from the bulk. However, when the particle size becomes sufficiently large, the particle radius is much greater than the

migration distance of the oxygen atoms. In this case, the formation of extended defects accommodates the growing number of anion vacancies in the crystal, and potentially provides a path with reduced activation energy for the diffusing oxygen.

Thermal deactivation, or sintering, that occurs upon reduction can lead to a significant loss of available surface area and therefore activity of the catalyst. For Ni/alumina catalysts at 400°C in H₂, sintering is observed to proceed via an Ostwald ripening mechanism. The lack of particle migration observed suggests that there is a strong particle-support interaction, anchoring the particles and therefore preventing coalescence. However, this strong interaction may encourage Ostwald ripening, as it provides a driving force for migration of surface atoms on to the support. The *in-situ* observations of Ostwald ripening present several results not consistent with the sintering models reported in the literature, and it is clear that size is not the only factor that governs particle stability. The relative periods of particle stability, followed by rapid particle decay suggests that there may be a trigger for the onset of atomic migration, whilst the most stable particles appear to be those with faceted surfaces and therefore minimised surface energy. It is proposed that differences in the surface energetics of each nanoparticle will lead to a variable prefactor, v_p , that will determine the energy barrier for diffusion of surface atoms on to the support. Additionally, the loss of one or two surface atoms may cause a perturbation in the energy of the remaining surface atoms, and this is proposed as a mechanism to explain the sudden onset of particle decay observed.

Chapter 9

Final Remarks and Further Work

The discovery of the catalytic activity of small gold nanoparticles sparked a wealth of research in the area; both to understand the physical origins of the change in chemical properties and to exploit them for many possible commercial applications. Perhaps the most important of these applications is gold's exceptional activity and selectivity for the low temperature oxidation of carbon monoxide; and the efficient low temperature removal of poisonous CO from the hydrogen stream in fuel cells would overcome one of the current barriers to the commercial viability of fuel cell technologies.

In this work, a new mechanism is introduced to further explain the sudden onset of catalytic activity of small gold nanoparticles. The inherently strained decahedron is known to be one of the most commonly observed structures in the size range for which gold is catalytically active. Through measurements of atomic column displacements observed in the aberration corrected TEM images, the magnitude of this strain has been quantified and then related to activity for CO oxidation through DFT calculation based on the experimental observations. It is found that the large expansive strain observed at the surface of small gold decahedra significantly modifies the electronic band structure, shifting the *d* band towards the Fermi level and therefore increasing the strength of the surface-molecule interaction. This mechanism offers a further explanation of the

exceptional catalytic activities of certain gold nanoparticles in this size range, and coupled with the similar effects of under co-ordinated surface atoms, can explain the surprising catalytic properties reported.

In-situ heating studies have shown that the decahedral structure is thermally stable throughout a wide range of temperatures, however further work is required to study the combined effects of temperature and various gas environments on the structure of small gold nanoparticles. Different environments are likely to significantly modify both the external surfaces and internal structure of catalytic particles, and therefore their catalytic properties. Additionally, interactions with various possible supports may cause atomic displacements due to lattice mismatch, whilst potentially modifying the minimum energy structure in a given environment.

Exceptional activities of Au/ceria catalysts for the water-gas shift reaction have been reported, with the presence of cationic gold thought to further reduce the strength of the surface oxygen binding energies, thereby increasing activity by readily donating and accepting atomic oxygen. The Au species may then act as active sites for the adsorption of CO, with the adsorbed molecule oxidised by the surrounding oxygen from the ceria surface. Z contrast HAADF STEM has been used to study the nature of the cationic Au species in such catalysts, with evidence presented for the substitution of single Au atoms for Ce sites. The potential optimum use of precious metal loadings by supported single atom catalysts offers not only exceptional catalytic properties, but also a dramatic reduction in cost of the catalyst.

In future work, the application of quantitative HAADF STEM, following the approach of LeBeau *et al*, should allow a more rigorous determination of the existence of single atoms on a support. The development of new heating holders compatible with atomic resolution ESTEM will enable studies of the stability of single atoms *in-situ*. Coupled with comparisons with *ex-situ* reacted samples under water-gas shift conditions, this should allow further insight as to whether single atoms remain stable and act as the active site, or are only present in the precursor and act as a nucleation point for the formation of metallic clusters with the desired particle-support interaction.

The reduction of NiO to the active metallic Ni is observed *in-situ*, and a size dependent defect mechanism is proposed. For small NiO particles in a reducing environment, reduction to Ni is expected to be facile, resulting in the production of small, defect free Ni particles, whilst atomically dispersed NiO is observed to form well dispersed small Ni particles that nucleate upon reduction. In contrast, larger NiO crystals are much more difficult to reduce, and appear to transform to Ni via a defect mechanism. For such particles, the migration distance for diffusing O species is much less than the particle radius, and it is proposed that the formation of extended defects facilitates the removal of oxygen by reducing the energy involved in the bond breaking and bond forming steps for the diffusing species.

Further studies of the reduction process, utilising a combination of nanobeam diffraction; diffraction contrast; and atomic resolution imaging, would allow the Burger's vector of the defects to be established, and therefore a more complete mechanism to be formulated. The effect of particle size on the mechanism for reduction needs further study, both to establish if there is a critical particle size at which extended defects are formed, and to further study the reduction process of very small nanoparticles more relevant to industrial catalysts. The latter of these is a particular challenge, due to the potentially fast nature of the process; the sensitivity of the particles to the electron beam; and the difficulty in interpreting *in-situ* images of supported small particles. For these reasons, time resolved *in-situ* experiments in nanobeam diffraction mode may be the most likely technique to provide clear structural information from individual particles.

Upon reduction, catalytic Ni particles supported on alumina are observed to sinter through an Ostwald ripening mechanism, although several differences are observed from the classical sintering theory. Particles are observed to undergo relatively sustained periods of stability, before rapidly decaying and disappearing, whilst particles that remain stable appear to exhibit clear surface facets. Therefore, it is proposed that differences in local surface energies, as well as size, may govern the stability of small supported nanoparticles under reaction conditions, with the rapid onset of particle decay suggested to be triggered by the removal of one or two surface atoms – significantly increasing the mobility of other surrounding surface atoms. Future work may utilise

higher magnification images, preferably with atomic resolution, to study the onset of particle decay, whilst the effect of variable contact angles is another possible cause of differences in particle stability that warrants further study.

The recent development of aberration corrected ESTEM at the university of York opens up exciting opportunities to exploit the Z contrast nature of HAADF STEM images for *in-situ* study of materials. This new technique will be particularly well suited to many heterogeneous catalysts that consist of a dispersed heavy metal on a lighter support. The current trend towards catalysis by small clusters and even single atoms make the identification of such small species particularly critical, and HAADF STEM is uniquely suited to such studies. Atomically resolved HAADF STEM images acquired *in-situ* allow for direct observation of the nature and stability of such species under simulated reaction conditions. Furthermore, the inter-particle transport of single atoms and small clusters plays a crucial role in the deactivation of many industrially important catalysts, and AC-ESTEM is the most likely tool to allow the direct visualisation of which atoms migrate, where they come from and where they go. The development of ultra stable heating holders specifically designed for ESTEM applications may present the biggest challenge to enable such experiments under conditions of elevated temperature as well as controlled environment.

List of acronyms

AC	Aberration corrected
ADF	Annular dark field
BF	Bright Field
CTF	Contrast transfer function
DFT	Density functional theory
EDX	Energy dispersive X-ray spectroscopy
EELS	Electron energy loss spectroscopy
E(S)TEM	Environmental (scanning) transmission electron microscopy
FEG	Field emission gun
FCC	Face centred cubic
FFT	Fast Fourier Transform
GGA	Generalised gradient approximation
GPA	Geometrical phase analysis
HAADF	High angle annular dark field
HRTEM	High resolution transmission electron microscopy
JM	Johnson Matthey Plc
L-S-W	Lifshitz-Slyozov-Wagner model
MTP	Multiply twinned particle
NCSI	Negative spherical aberration imaging
ODP	Optical diffraction pattern
PAW	Projector augmented wave method
PEM	Polymer electrolyte membrane
PGM	Platinum group metals
PROX	Preferential oxidation of carbon monoxide
PVC	Polyvinyl chloride
SAD	Selective area diffraction
SCO	Selective carbon monoxide oxidation
SMSI	Strong metal-support interaction
STEM	Scanning transmission electron microscope

TEM	Transmission electron microscope
TOF	Turnover frequency
TWC	Three way catalyst
WGS	Water-gas shift reaction
XPS	X-ray photoelectron spectroscopy
XRD	X-ray Diffraction

List of symbols

a	Interatomic spacing
$A(k)$	Aperture function
$A(x,y)$	Amplitude
$B(k)$	Aberration function
β	Semi angle of collection
c	Speed of light
C_c	Chromatic aberration coefficient
C_s	Spherical aberration coefficient
$\chi(k)$	Total phase shift
d	Diameter
d_{atom}	Atomic diameter
dis	dispersion - the fraction of atoms exposed to the surface
dis_0	Initial dispersion
dis_{eq}	Dispersion at infinite time
D_s	Surface atom diffusion coefficient
δ	Resolution
e	Electron charge
E	Energy
ΔE	Energy loss
\mathbf{E}	Electric field
$E(k)$	Envelope function
E_0	Initial beam energy
E_a	Activation energy
E_{ad}	Adsorption energy
E_{coh}	Cohesive energy between neighbouring atoms
E_d	Desorption energy
E_{diff}	Diffusion activation energy
E_r	Reaction barrier
eV	Electron volt

$\delta\varepsilon_d$	Shift in the d band centre
ε_a	Electronic adsorbate level
ε_d	Centre of d band
\mathbf{F}	Force
Δf	Defocus
G	Shear modulus
γ	surface free energy
h	Planck's constant
$h(x,y)$	Point spread function
h_i	Distance from the particle centre to the facet i
ΔH_{sub}	Bulk sublimation enthalpy
I	Intensity
k	spatial frequency
k_B	Boltzmann's constant
k_s	sintering rate constant
λ	Wavelength
m	Sintering order
m_0	Rest mass
μ	Chemical potential energy
n	Refractive index
N	number of broken bonds
ν	Poisson's ratio
ω	strength of the disclination
Ω	The solid angle of collection
$\varphi_i(x,y)$	Phase dependent on thickness
Ψ	Wavefunction
Q	activation energy for surface diffusion
r	Radius
r^*	Critical radius
R	The universal gas constant
ρ	Bulk volume per atom of the metal
σ	Scattering cross section
T	Temperature
$T(k)$	Contrast transfer function
θ	Contact angle
θ	Scattering angle

\mathbf{v}	Velocity
V	coupling matrix element
$V(x,y,z)$	potential energy
v_p	Pre-factor for atomic diffusion on to the support
x	Distance of the disclination from the centre of the cylinder
Z	Atomic number
Z_B	Bulk co-ordination number
Z_i	Co-ordination number of the surface atom i

Bibliography

1. M.I. Acmite, *Market Report: Global Catalyst Market*. 2011.
2. J.J. Berzelius, *Annls. Chim. Phys.*, 1836. **61** 146.
3. H. Davy, *Phil. Trans. Roy. Soc.*, 1817. **107** 77.
4. M. Faraday, *Phil. Trans. Roy. Soc.*, 1834. **124** 55.
5. M. Haruta, et al., *Gold catalysts prepared by coprecipitation for low-temperature oxidation of hydrogen and of carbon monoxide*. *Journal of Catalysis*, 1989. **115** 301-309.
6. M. Raney, *Method of producing finely divided nickel*, U.S. Patent Office. 1927: 1628190.
7. S. Sane, et al., *Raney metal catalysts: I. comparative properties of raney nickel proceeding from Ni-Ai intermetallic phases*. *Applied Catalysis*, 1984. **9** 69-83.
8. D. Potoczna-Petru and L. Kępiński, *Reduction study of Co₃O₄ model catalyst by electron microscopy*. *Catalysis Letters*, 2001. **73** 41-46.
9. S. Chenna, R. Banerjee, and P.A. Crozier, *Atomic-Scale Observation of the Ni Activation Process for Partial Oxidation of Methane Using In Situ Environmental TEM*. *ChemCatChem*, 2011. **3** 1051-1059.
10. J.A. Rodriguez, et al., *Experimental and Theoretical Studies on the Reaction of H₂ with NiO: Role of O Vacancies and Mechanism for Oxide Reduction*. *Journal of the American Chemical Society*, 2001. **124** 346-354.
11. J.T. Richardson, R.M. Scates, and M.V. Twigg, *X-ray diffraction study of the hydrogen reduction of NiO/ α -Al₂O₃ steam reforming catalysts*. *Applied Catalysis A: General*, 2004. **267** 35-46.
12. S.S.A. Syed-Hassan and C.-Z. Li, *Effects of crystallite size on the kinetics and mechanism of NiO reduction with H₂*. *International Journal of Chemical Kinetics*, 2011. **43** 667-676.
13. J.T. Richardson and M.V. Twigg, *Reduction of impregnated NiO/ α -Al₂O₃ association of Al³⁺ ions with NiO*. *Applied Catalysis A: General*, 1998. **167** 57-64.
14. J.T. Richardson, et al., *Reduction of model steam reforming catalysts: NiO/ α -Al₂O₃*. *Applied Catalysis A: General*, 1994. **110** 217-237.
15. P. Wynblatt and N.A. Gjostein, *Particle growth in model supported metal catalysts—I. Theory*. *Acta Metallurgica*, 1976. **24** 1165-1174.

16. P. Wynblatt, R.A.D. Betta, and N.A. Gjostein, *The Physical Basis for Heterogeneous Catalysis*, ed. E. Drauglis and R.I. Jaffee. 1975, New York: Plenum Press.
17. E.E. Gruber, *Calculated Size Distributions for Gas Bubble Migration and Coalescence in Solids*. Journal of Applied Physics, 1967. **38** 243-250.
18. L. Willertz and P. Shewmon, *Diffusion of helium gas bubbles in gold and copper foils*. Metallurgical and Materials Transactions B, 1970. **1** 2217-2223.
19. K.Y. Chen and J.R. Cost, *Coalescence of helium bubbles in aluminum*. Journal of Nuclear Materials, 1974. **52** 59-74.
20. F.A. Nichols, *Coalescence of Two Spheres by Surface Diffusion*. Journal of Applied Physics, 1966. **37** 2805-2808.
21. F.A. Nichols and W.W. Mullins, Trans. AIME, 1965. **233** 1840.
22. P. Wynblatt and N.A. Gjostein, *Supported metal crystallites*. Progress in Solid State Chemistry, 1975. **9** 21-58.
23. C.G. Granqvist and R.A. Buhrman, *Statistical model for coalescence of islands in discontinuous films*. Applied Physics Letters, 1975. **27** 693-694.
24. S.E. Wanke and P.C. Flynn, *The Sintering of Supported Metal Catalysts*. Catalysis Reviews, 1975. **12** 93-135.
25. G.A. Fuentes and E.D. Gamas, *Catalyst Deactivation*. Vol. 68. 1991, Amsterdam: Elsevier.
26. J. Sehested, et al., *Sintering of nickel steam-reforming catalysts: effects of temperature and steam and hydrogen pressures*. Journal of Catalysis, 2004. **223** 432-443.
27. T.W. Hansen, *Sintering and Particle Dynamics in Supported Metal Catalysts*. 2006, Haldor Topsoe A/S, DTU.
28. I.M. Lifshitz and V.V. Slyozov, *The kinetics of precipitation from supersaturated solid solutions*. Journal of Physics and Chemistry of Solids, 1961. **19** 35-50.
29. C.Z. Wagner, Elektrochemie, 1961. **65** 581.
30. Y. De Smet, L. Deriemaeker, and R. Finsy, *A Simple Computer Simulation of Ostwald Ripening*. Langmuir, 1997. **13** 6884-6888.
31. Y. De Smet, et al., *Ostwald Ripening in the Transient Regime: A Cryo-TEM Study*. Langmuir, 1999. **16** 961-967.
32. A.G. Sault and V. Tikare, *A New Monte Carlo Model for Supported-Catalyst Sintering*. Journal of Catalysis, 2002. **211** 19-32.
33. A. Howard, C.E.J. Mitchell, and R.G. Egdell, *Real time STM observation of Ostwald ripening of Pd nanoparticles on TiO₂ at elevated temperature*. Surface Science, 2002. **515** L504-L508.
34. P.L. Gai and E.D. Boyes, *Electron Microscopy in Heterogeneous Catalysis*. Microscopy in Materials Science, ed. B. Cantor, M.J. Goringe, and J.A. Eades. 2003, Bristol and Philadelphia: IoP.

35. S.B. Simonsen, et al., *Direct Observations of Oxygen-induced Platinum Nanoparticle Ripening Studied by In Situ TEM*. Journal of the American Chemical Society, 2010. **132** 7968-7975.
36. A.K. Datye, et al., *Particle size distributions in heterogeneous catalysts: What do they tell us about the sintering mechanism?* Catalysis Today, 2006. **111** 59-67.
37. R. Meyer, et al., *An ab initio analysis of adsorption and diffusion of silver atoms on alumina surfaces*. Surface Science, 2007. **601** 134-145.
38. N. Aaron Deskins, D. Mei, and M. Dupuis, *Adsorption and diffusion of a single Pt atom on γ -Al₂O₃ surfaces*. Surface Science, 2009. **603** 2793-2807.
39. W. Qin-bo, et al., *On the critical radius in generalized Ostwald ripening*. Journal of Zhejiang University - Science B, 2005. **6** 705-707.
40. C.T. Campbell, S.C. Parker, and D.E. Starr, *The Effect of Size-Dependent Nanoparticle Energetics on Catalyst Sintering*. Science, 2002. **298** 811-814.
41. S.C. Parker and C.T. Campbell, *Kinetic model for sintering of supported metal particles with improved size-dependent energetics and applications to Au on TiO₂(110)*. Physical Review B, 2007. **75** 035430.
42. S.R. Challa, et al., *Relating Rates of Catalyst Sintering to the Disappearance of Individual Nanoparticles during Ostwald Ripening*. Journal of the American Chemical Society, 2011. **133** 20672-20675.
43. A. Delavaria, *Ph.D thesis*. 2010, University of New Mexico: Albuquerque, NM.
44. M. Haruta, et al., Chem. Lett., 1987 405-408.
45. G.J. Hutchings, J. Catal, 1985. **96** 292-295.
46. M. Haruta, et al., *Low-Temperature Oxidation of CO over Gold Supported on TiO₂, α -Fe₂O₃, and Co₃O₄*. Journal of Catalysis, 1993. **144** 175-192.
47. M. Haruta, *Gold as a low-temperature oxidation catalyst: factors controlling activity and selectivity*, in *Studies in Surface Science and Catalysis*, S.T.O.A.M.G. R.K. Grasselli and J.E. Lyons, Editors. 1997, Elsevier. p. 123-134.
48. M. Haruta, *Size- and support-dependency in the catalysis of gold*. Catalysis Today, 1997. **36** 153-166.
49. M. Okumura, T. Akita, and M. Haruta, *Hydrogenation of 1,3-butadiene and of crotonaldehyde over highly dispersed Au catalysts*. Catalysis Today, 2002. **74** 265-269.
50. N.R. Collins, et al., *Advanced Three-Way Catalysts - Optimisation by Targeted Zoning of Precious Metal* SAE Technical Paper Series, 2005. **2005-01** 2158.
51. G. Pattrick, et al., *The potential for use of gold in automotive pollution control technologies: a short review*. Topics in Catalysis, 2004. **30-31** 273-279.
52. D. Andreeva, et al., *Low-Temperature Water-Gas Shift Reaction over Au/ α -Fe₂O₃*. Journal of Catalysis, 1996. **158** 354-355.

53. A. Russell and W.S. Epling, *Diesel Oxidation Catalysts*. Catalysis Reviews, 2011. **53** 337-423.
54. M.B. Cortie and E. Van der Lingen, *Mat. Forum.*, 2002. **26** 1-14.
55. G.C. Bond and D.T. Thompson, *Catal. Rev. Sci. Eng.*, 1999. **41** 319.
56. G. Hutchings, *Catalysis: A golden future*. Gold Bulletin, 1996. **29** 123-130.
57. D.T. Thompson, *Gold Bull.*, 1998. **31** 111-118.
58. T. Hayashi, K. Tanaka, and M. Haruta, *J. Catal.*, 1998. **31** 566-575.
59. D.A.H. Cunningham, et al., *Structural Analysis of Au/TiO₂ Catalysts by Debye Function Analysis*. Journal of Catalysis, 1999. **183** 24-31.
60. P. Landon, et al., *Direct formation of hydrogen peroxide from H₂/O₂ using a gold catalyst*. Chemical Communications, 2002 2058-2059.
61. M. Rossi. in *Gold*. 2003. Vancouver.
62. J. Jia, et al., *Selective Hydrogenation of Acetylene over Au/Al₂O₃ Catalyst*. The Journal of Physical Chemistry B, 2000. **104** 11153-11156.
63. U.S. Department of Energy, *Fuel Cell Report to Congress*. 2003.
64. D. Andreeva, et al., *Low-temperature water-gas shift reaction over Au/CeO₂ catalysts*. Catalysis Today, 2002. **72** 51-57.
65. R. Burch, *Gold catalysts for pure hydrogen production in the water-gas shift reaction: activity, structure and reaction mechanism*. Physical Chemistry Chemical Physics, 2006. **8** 5483-5500.
66. T. Akita, K. Tanaka, and M. Kohyama, *TEM and HAADF-STEM study of the structure of Au nano-particles on CeO₂*. Journal of Materials Science, 2008. **43** 3917-3922.
67. M.M. Schubert, et al., *Activity, Selectivity, and Long-Term Stability of Different Metal Oxide Supported Gold Catalysts for the Preferential CO Oxidation in H₂-Rich Gas*. Catalysis Letters, 2001. **76** 143-150.
68. H.S. Oh, et al., *Catalysis by gold and silver*. EuropaCat, Limerick, Ireland, 2001 19-0-19.
69. G.C. Bond, *Catalysis Today*, 2002. **72** 5.
70. M. Valden, X. Lai, and D.W. Goodman, *Science*, 1998. **281** 1647.
71. Y. Maeda, et al., *Local barrier height of Au nanoparticles on a TiO₂ (110)-(1x2) surface*. Applied Surface Science, 2004. **222** 409-414.
72. X.F. Lai and D.W. Goodman, *Structure-reactivity correlations for oxide-supported metal catalysts: new perspectives from STM*. Journal of Molecular Catalysis a-Chemical, 2000. **162** 33-50.
73. G.R. Bamwenda, et al., *The influence of the preparation methods on the catalytic activity of platinum and gold supported on TiO₂ for CO oxidation*. Catalysis Letters, 1997. **44** 83-87.

74. B. Zhang, W. Zhang, and D.S. Su, *Towards a More Accurate Particle Size Distribution of Supported Catalyst by using HAADF-STEM*. ChemCatChem, 2011. **3** 965-968.
75. A.A. Herzing, et al., *Identification of Active Gold Nanoclusters on Iron Oxide Supports for CO Oxidation*. Science, 2008. **321** 1331-1335.
76. M. Haruta, J. New. Mater. Electrochem. Syst., 2004. **163** 7.
77. C.R. Henry, *Catalytic activity of supported nanometer-sized metal clusters*. Applied Surface Science, 2000. **164** 252-259.
78. I.N. Remediakis, N. Lopez, and J.K. Norskov, Angew. Chem., 2005. **44** 1824.
79. S.N. Rashkeev, et al., Phys. Rev., 2007. **76** 035438.
80. M. Mavrikakis, P. Stoltze, and J.K. Norskov, *Making gold less noble*. Catalysis Letters, 2000. **64** 101-106.
81. G. Mills, M.S. Gordon, and H. Metiu, *Oxygen adsorption on Au clusters and a rough Au(111) surface: The role of surface flatness, electron confinement, excess electrons, and band gap*. Journal of Chemical Physics, 2003. **118** 4198-4205.
82. N. Lopez, et al., *On the origin of the catalytic activity of gold nanoparticles for low-temperature CO oxidation*. Journal of Catalysis, 2004. **223** 232-235.
83. R. Zanella, et al., *Characterization and reactivity in CO oxidation of gold nanoparticles supported on TiO₂ prepared by deposition-precipitation with NaOH and urea*. Journal of Catalysis, 2004. **222** 357-367.
84. M.S. Chen and D.W. Goodman, *Structure–activity relationships in supported Au catalysts*. Catalysis Today, 2006. **111** 22-33.
85. A. Ruban, et al., *Surface electronic structure and reactivity of transition and noble metals*. Journal of Molecular Catalysis a-Chemical, 1997. **115** 421-429.
86. B. Hammer and J.K. Nørskov, *Electronic factors determining the reactivity of metal surfaces*. Surface Science, 1995. **343** 211-220.
87. B. Hammer, O.H. Nielsen, and J.K. Nørskov, *Structure sensitivity in adsorption: CO interaction with stepped and reconstructed Pt surfaces*. Catalysis Letters, 1997. **46** 31-35.
88. V. Pallassana, et al., *Theoretical analysis of hydrogen chemisorption on Pd(111), Re(0001) and Pd_{ML}/Re(0001), Re_{ML}/Pd(111) pseudomorphic overlays*. Physical Review B, 1999. **60** 6146-6154.
89. M. Mavrikakis, B. Hammer, and J.K. Norskov, *Effect of strain on the reactivity of metal surfaces*. Physical Review Letters, 1998. **81** 2819-2822.
90. M. Gsell, P. Jakob, and D. Menzel, *Effect of Substrate Strain on Adsorption*. Science, 1998. **280** 717-720.
91. L.A. Kibler, et al., *Tuning Reaction Rates by Lateral Strain in a Palladium Monolayer*. Angewandte Chemie International Edition, 2005. **44** 2080-2084.

-
92. A. Schlapka, et al., *Surface Strain versus Substrate Interaction in Heteroepitaxial Metal Layers: Pt on Ru(0001)*. Physical Review Letters, 2003. **91** 016101.
93. J. Greeley, W.P. Krekelberg, and M. Mavrikakis, *Strain-Induced Formation of Subsurface Species in Transition Metals*. Angewandte Chemie International Edition, 2004. **43** 4296-4300.
94. S. Giorgio, et al., *Au particles supported on (110) anatase-TiO₂*. Materials Science and Engineering: A, 2001. **297** 197-202.
95. Y. Xu and M. Mavrikakis, *Adsorption and dissociation of O₂ on gold surfaces: Effect of steps and strain*. Journal of Physical Chemistry B, 2003. **107** 9298-9307.
96. G. Wulff, *Z. Kristallogr. Mineral*, 1901. **34** 449-530.
97. C.R. Henry, *Morphology of supported nanoparticles*. Progress in Surface Science, 2005. **80** 92-116.
98. A.S. Barnard, et al., *Nanogold: A Quantitative Phase Map*. Acs Nano, 2009. **3** 1431-1436.
99. W.L. Winterbottom, *Equilibrium shape of a small particle in contact with a foreign substrate*. Acta Metallurgica, 1967. **15** 303-310.
100. L.D. Marks, *Particle size effects on Wulff constructions*. Surface Science, 1985. **150** 358-366.
101. D.J. Smith and L.D. Marks, *High resolution studies of small particles of gold and silver: II. Single crystals, lamellar twins and polyparticles*. Journal of Crystal Growth, 1981. **54** 433-438.
102. L.D. Marks and A. Howie, *Multiply-Twinned Particles in Silver Catalysts*. Nature, 1979. **282** 196-198.
103. S. Iijima and T. Ichihashi, *Structural instability of ultrafine particles of metals*. Physical Review Letters, 1986. **56** 616-619.
104. S. Giorgio, et al., *Environmental electron microscopy (ETEM) for catalysts with a closed E-cell with carbon windows*. Ultramicroscopy, 2006. **106** 503-507.
105. K.P. McKenna, *Gold nanoparticles under gas pressure*. Physical Chemistry Chemical Physics, 2009. **11** 4145-4151.
106. L.D. Marks, *Surface structure and energetics of multiply twinned particles*. Philosophical Magazine A, 1984. **49** 81 - 93.
107. W. Eberhardt, *Clusters as new materials*. Surface Science, 2002. **500** 242-270.
108. T.X. Li, et al., *A genetic algorithm study on the most stable disordered and ordered configurations of Au₃₈₋₅₅*. Physics Letters A, 2000. **267** 403-407.
109. I. Galanakis, N. Papanikolaou, and P.H. Dederichs, *Applicability of the broken-bond rule to the surface energy of the fcc metals*. Surface Science, 2002. **511** 1-12.

110. A. Howie and L.D. Marks, *Elastic Strains and the Energy-Balance for Multiply Twinned Particles*. Philosophical Magazine a-Physics of Condensed Matter Structure Defects and Mechanical Properties, 1984. **49** 95-109.
111. A. Richter, et al., *On the Screening Length of Disclinations in Amorphous Structures*. physica status solidi (b), 1987. **143** 43-53.
112. H.B. Liu, et al., *Melting behavior of nanometer sized gold isomers*. Surface Science, 2001. **491** 88-98.
113. B. Zhang, et al., *Structural Dynamics of Low-Symmetry Au Nanoparticles Stimulated by Electron Irradiation*. Chemistry – A European Journal, 2011. **17** 12877-12881.
114. J.M. Soler, I.L. Garzon, and J.D. Joannopoulos, *Structural patterns of unsupported gold clusters*. Solid State Communications, 2001. **117** 621-625.
115. U. Heiz, et al., *Tuning the oxidation of carbon monoxide using nanoassembled model catalysts*. Chemical Physics, 2000. **262** 189-200.
116. S.D. Lin, M. Bollinger, and M.A. Vannice, *Low temperature CO oxidation over Au/TiO₂ and Au/SiO₂ catalysts*. Catalysis Letters, 1993. **17** 245-262.
117. M.M. Schubert, et al., *CO Oxidation over Supported Gold Catalysts—“Inert” and “Active” Support Materials and Their Role for the Oxygen Supply during Reaction*. Journal of Catalysis, 2001. **197** 113-122.
118. S.-J. Lee and A. Gavriilidis, *Supported Au Catalysts for Low-Temperature CO Oxidation Prepared by Impregnation*. Journal of Catalysis, 2002. **206** 305-313.
119. M. Okumura, et al., *Chemical vapor deposition of gold on Al₂O₃; SiO and TiO₂ ; for the oxidation of CO and of H₂ .* Catalysis Letters, 1998. **51** 53-58.
120. S. Schimpf, et al., *Supported gold nanoparticles: in-depth catalyst characterization and application in hydrogenation and oxidation reactions*. Catalysis Today, 2002. **72** 63-78.
121. Y. Yuan, et al., Catal. Lett., 1996. **42** 15.
122. W.D. Williams, et al., *Metallic Corner Atoms in Gold Clusters Supported on Rutile Are the Dominant Active Site during Water–Gas Shift Catalysis*. Journal of the American Chemical Society, 2010. **132** 14018-14020.
123. J.-D. Grunwaldt, et al., *Preparation of Supported Gold Catalysts for Low-Temperature CO Oxidation via “Size-Controlled” Gold Colloids*. Journal of Catalysis, 1999. **181** 223-232.
124. J.-D. Grunwaldt, et al., *Comparative Study of Au/TiO₂ and Au/ZrO₂ Catalysts for Low-Temperature CO Oxidation*. Journal of Catalysis, 1999. **186** 458-469.
125. S. Carrettin, et al., *Nanocrystalline CeO₂ Increases the Activity of Au for CO Oxidation by Two Orders of Magnitude*. Angewandte Chemie International Edition, 2004. **43** 2538-2540.
126. A. Migani, et al., *Greatly facilitated oxygen vacancy formation in ceria nanocrystallites*. Chemical Communications, 2010. **46** 5936-5938.

-
127. G.N. Vayssilov, et al., *Support nanostructure boosts oxygen transfer to catalytically active platinum nanoparticles*. *Nat Mater*, 2011. **10** 310-315.
128. J. Guzman, S. Carretin, and A. Corma, *Spectroscopic Evidence for the Supply of Reactive Oxygen during CO Oxidation Catalyzed by Gold Supported on Nanocrystalline CeO₂*. *Journal of the American Chemical Society*, 2005. **127** 3286-3287.
129. R.D. Monte and J. Kaspar, *Nanostructured CeO₂-ZrO₂ mixed oxides*. *Journal of Materials Chemistry*, 2005. **15** 633-648.
130. M. Boaro, et al., *Electrical and oxygen storage/release properties of nanocrystalline ceria-zirconia solid solutions*. *Solid State Ionics*, 2002. **147** 85-95.
131. Q. Fu, A. Weber, and M. Flytzani-Stephanopoulos, *Nanostructured Au-CeO₂ Catalysts for Low-Temperature Water-Gas Shift*. *Catalysis Letters*, 2001. **77** 87-95.
132. Q. Fu, H. Saltsburg, and M. Flytzani-Stephanopoulos, *Active Nonmetallic Au and Pt Species on Ceria-Based Water-Gas Shift Catalysts*. *Science*, 2003. **301** 935-938.
133. Z.-P. Liu, S.J. Jenkins, and D.A. King, *Origin and Activity of Oxidized Gold in Water-Gas-Shift Catalysis*. *Physical Review Letters*, 2005. **94** 196102.
134. A.M. Venezia, et al., *Relationship between Structure and CO Oxidation Activity of Ceria-Supported Gold Catalysts*. *The Journal of Physical Chemistry B*, 2005. **109** 2821-2827.
135. C. Zhang, et al., *Structure of gold atoms on stoichiometric and defective ceria surfaces*. *The Journal of Chemical Physics*, 2008. **129** 194708-8.
136. D. Tibiletti, et al., *DFT and In Situ EXAFS Investigation of Gold/Ceria-Zirconia Low-Temperature Water Gas Shift Catalysts: Identification of the Nature of the Active Form of Gold*. *The Journal of Physical Chemistry B*, 2005. **109** 22553-22559.
137. M.F. Camellone and S. Fabris, *Reaction Mechanisms for the CO Oxidation on Au/CeO₂ Catalysts: Activity of Substitutional Au³⁺/Au⁺ Cations and Deactivation of Supported Au⁺ Adatoms*. *Journal of the American Chemical Society*, 2009. **131** 10473-10483.
138. A. Fonseca, et al., *Ceria-zirconia supported Au as highly active low temperature Water-gas shift catalysts*. *Topics in Catalysis*, 2007. **44** 223-235.
139. X. Wang, et al., *In situ time-resolved characterization of Au-CeO₂ and AuO_x-CeO₂ catalysts during the water-gas shift reaction: Presence of Au and O vacancies in the active phase*. *The Journal of Chemical Physics*, 2005. **123** 221101-5.
140. W. Deng, et al., *Reaction-Relevant Gold Structures in the Low Temperature Water-Gas Shift Reaction on Au-CeO₂*. *The Journal of Physical Chemistry C*, 2008. **112** 12834-12840.

141. A. Goguet, et al., *Deactivation Mechanism of a Au/CeZrO₄ Catalyst During a Low-Temperature Water Gas Shift Reaction*. The Journal of Physical Chemistry C, 2007. **111** 16927-16933.
142. R. Leppelt, et al., *Kinetics and mechanism of the low-temperature water–gas shift reaction on Au/CeO₂ catalysts in an idealized reaction atmosphere*. Journal of Catalysis, 2006. **244** 137-152.
143. T. Shido and Y. Iwasawa, *Reactant-Promoted Reaction Mechanism for Water-Gas Shift Reaction on Rh-Doped CeO₂*. Journal of Catalysis, 1993. **141** 71-81.
144. G. Jacobs, et al., *Low-Temperature Water-Gas Shift: In-Situ DRIFTS–Reaction Study of a Pt/CeO₂ Catalyst for Fuel Cell Reformer Applications*. The Journal of Physical Chemistry B, 2003. **107** 10398-10404.
145. W. Deng and M. Flytzani-Stephanopoulos, *On the Issue of the Deactivation of Au–Ceria and Pt–Ceria Water–Gas Shift Catalysts in Practical Fuel-Cell Applications*. Angewandte Chemie International Edition, 2006. **45** 2285-2289.
146. A. Einstein, *On a Heuristic point of view concerning the production and transformation of light*. Annalen der Physik, 1905. **17** 132-148.
147. L. de Broglie, *The wave nature of the electron*. Nobel Lecture, 1929. **12**.
148. P.B. Hirsch, et al., *Electron Microscopy of Thin Crystals*. 1965, London: Butterworths.
149. J.W. Edington, *Practical Electron Microscopy in Materials Science*. 1976, Herndon: TechBooks.
150. J.M. Cowley, *Diffraction Physics*. 1975, Amsterdam: North Holland Publishing company.
151. D.B. Williams and B.C. Carter, *Transmission Electron Microscopy*. 1996, New York: Plenum Press.
152. G. Van Tendeloo, D. Van Dyck, and S.J. Pennycook, eds. *Handbook of Nanoscopy*. Vol. 1. 2012, Wiley: Weinheim.
153. S.J. Pennycook and P.D. Nellist, eds. *Scanning Transmission Electron Microscopy*. 2011, Springer: New York.
154. M.G.J. Mosely, *The High Frequency Spectra of the Elements*. Phil. Mag. A, 1913 1024.
155. D. Van Dyck and A.F. de Jong, *Ultimate resolution and information in electron microscopy: general principles*. Ultramicroscopy, 1992. **47** 266-281.
156. D. van Dyck, *Atomic resolution electron microscopy*, in *Handbook of Nanoscopy*. 2012, Wiley: Weinheim.
157. O. Scherzer, *Sparische und Chromatische Korrektur von Elektronen-linsen*. Optik, 1947. **2** 114-132.
158. O. Scherzer, *The Theoretical Resolution Limit of the Electron Microscope*. Journal of Applied Physics, 1949. **20** 20-29.
159. H. Rose, *Outline of a spherically corrected semiaplanatic medium-voltage transmission electron microscope*. Optik, 1990. **85** 19-24.

-
160. M. Haider, et al., *Electron microscopy image enhanced*. Nature, 1998. **392** 768-769.
 161. M. Haider, et al., *A spherical-aberration-corrected 200kV transmission electron microscope*. Ultramicroscopy, 1998. **75** 53-60.
 162. H.H. Rose, *Optics of high-performance electron microscopes*. Science and Technology of Advanced Materials, 2008. **9** 014107.
 163. M. Lentzen, *The tuning of a Zernike phase plate with defocus and variable spherical aberration and its use in HRTEM imaging*. Ultramicroscopy, 2004. **99** 211-220.
 164. K.W. Urban, et al., *Negative spherical aberration ultrahigh-resolution imaging in corrected transmission electron microscopy*. Philosophical Transactions of the Royal Society A: Mathematical, Physical and Engineering Sciences, 2009. **367** 3735-3753.
 165. K.W. Urban, *Studying Atomic Structures by Aberration-Corrected Transmission Electron Microscopy*. Science, 2008. **321** 506-510.
 166. C.L. Jia, M. Lentzen, and K. Urban, *Atomic-Resolution Imaging of Oxygen in Perovskite Ceramics*. Science, 2003. **299** 870-873.
 167. K.J. Urban, et al., *Ultrahigh-Resolution Transmission Electron Microscopy at Negative Spherical Aberration*, in *Handbook of Nanoscopy*, G. Van Tendeloo, D. Van Dyck, and S.J. Pennycook, Editors. 2012, Wiley: Weinheim.
 168. D.A. Muller, et al., *Atomic-Scale Chemical Imaging of Composition and Bonding by Aberration-Corrected Microscopy*. Science, 2008. **319** 1073-1076.
 169. K. Kimoto, et al., *Element-selective imaging of atomic columns in a crystal using STEM and EELS*. Nature, 2007. **450** 702-704.
 170. A.V. Crewe, J. Wall, and J. Langmore, *Visibility of Single Atoms*. Science, 1970. **168** 1338-1340.
 171. R. Erni, et al., *Atomic-Resolution Imaging with a Sub-50-pm Electron Probe*. Physical Review Letters, 2009. **102** 096101.
 172. S. Van Aert, et al., *Three-dimensional atomic imaging of crystalline nanoparticles*. Nature, 2011. **470** 374-377.
 173. K. van Benthem, et al., *Three-dimensional ADF imaging of individual atoms by through-focal series scanning transmission electron microscopy*. Ultramicroscopy, 2006. **106** 1062-1068.
 174. B.T. Qiao, et al., *Single-atom catalysis of CO oxidation using Pt(1)/FeO(x)*. Nature Chemistry, 2011. **3** 634-641.
 175. O.L. Krivanek, et al., *Atom-by-atom structural and chemical analysis by annular dark-field electron microscopy*. Nature, 2010. **464** 571-574.
 176. M.J. Hÿtch and W.M. Stobbs, *Quantitative comparison of high resolution TEM images with image simulations*. Ultramicroscopy, 1994. **53** 191-203.
 177. A. Howie, *Hunting the Stobbs factor*. Ultramicroscopy, 2004. **98** 73-79.

-
178. P.D. Nellist, *The Principles of STEM imaging*, in *Scanning Transmission Electron Microscopy*, S.J. Pennycook and P.D. Nellist, Editors. 2011, Springer: New York.
179. D.O. Klenov and S. Stemmer, *Contributions to the contrast in experimental high-angle annular dark-field images*. *Ultramicroscopy*, 2006. **106** 889-901.
180. J.M. LeBeau, et al., *Standardless Atom Counting in Scanning Transmission Electron Microscopy*. *Nano Letters*, 2010. **10** 4405-4408.
181. J.M. LeBeau and S. Stemmer, *Experimental quantification of annular dark-field images in scanning transmission electron microscopy*. *Ultramicroscopy*, 2008. **108** 1653-1658.
182. R.F. Loane, P. Xu, and J. Silcox, *Thermal vibrations in convergent-beam electron diffraction*. *Acta Crystallographica Section A*, 1991. **47** 267-278.
183. R.F. Loane, P. Xu, and J. Silcox, *Incoherent imaging of zone axis crystals with ADF STEM*. *Ultramicroscopy*, 1992. **40** 121-138.
184. J.M. LeBeau, et al., *High-angle scattering of fast electrons from crystals containing heavy elements: Simulation and experiment*. *Physical Review B*, 2009. **79** 214110.
185. E.P. Butler and K.F. Hale, *Dynamic Experiments in Electron Microscopy*. 1981, Amsterdam: North Holland.
186. E.D. Boyes and P.L. Gai, *Environmental high resolution electron microscopy and applications to chemical science*. *Ultramicroscopy*, 1997. **67** 219-232.
187. E.D. Boyes and P.L. Gai, *Controlled environment [ECELL] HREM for dynamic in-situ chemical reaction studies with STEM and PEELS/GIF*. *Electron Microscopy 1998*, Vol 3, 1998 511-512.
188. P.L. Gai and E.D. Boyes, *Advances in Atomic Resolution In Situ Environmental Transmission Electron Microscopy and 1 angstrom Aberration Corrected In Situ Electron Microscopy*. *Microscopy Research and Technique*, 2009. **72** 153-164.
189. P.L. Gai and E.D. Boyes, *Angstrom analysis with dynamic in-situ aberration corrected electron microscopy*. *Journal of Physics: Conference Series*, 2010. **241** 012055.
190. P.L. Gai and E.D. Boyes, *Atomic Resolution Environmental Transmission Electron Microscopy*, in *Handbook of Nanoscopy*, G. Van Tendeloo, D. Van Dyck, and S.J. Pennycook, Editors. 2012, Wiley: Weinheim.
191. L.D. Marks and D.J. Smith, *High resolution studies of small particles of gold and silver: I. Multiply-twinned particles*. *Journal of Crystal Growth*, 1981. **54** 425-432.
192. R. Esparza, et al., *Structural analysis and shape-dependent catalytic activity of Au, Pt and Au/Pt nanoparticles*. *Matéria (Rio de Janeiro)*, 2008. **13** 579-586.
193. C.L. Johnson, et al., *Effects of elastic anisotropy on strain distributions in decahedral gold nanoparticles*. *Nat Mater*, 2008. **7** 120-124.

-
194. M.J. Walsh, et al., *On the Structural Origin of the Catalytic Properties of Inherently Strained Ultrasmall Decahedral Gold Nanoparticles*. Nano Letters, 2012. **12** 2027-2031.
195. C.W. Mays, J.S. Vermaak, and D. Kuhlmann-Wilsdorf, *On surface stress and surface tension: II. Determination of the surface stress of gold*. Surface Science, 1968. **12** 134-140.
196. W.H. Qi and M.P. Wang, *Size and shape dependent lattice parameters of metallic nanoparticles*. Journal of Nanoparticle Research, 2005. **7** 51-57.
197. G. Kresse and J. Furthmüller, *Efficient iterative schemes for ab initio total-energy calculations using a plane-wave basis set*. Physical Review B, 1996. **54** 11169-11186.
198. G. Kresse and J. Furthmüller, *Efficiency of ab-initio total energy calculations for metals and semiconductors using a plane-wave basis set*. Computational Materials Science, 1996. **6** 15-50.
199. W. Kohn and L.J. Sham, *Self-Consistent Equations Including Exchange and Correlation Effects*. Physical Review, 1965. **140** A1133-A1138.
200. G. Kresse and D. Joubert, *From ultrasoft pseudopotentials to the projector augmented-wave method*. Physical Review B, 1999. **59** 1758-1775.
201. J.P. Perdew, K. Burke, and M. Ernzerhof, *Generalized Gradient Approximation Made Simple*. Physical Review Letters, 1996. **77** 3865-3868.
202. K. Momma and F. Izumi, *VESTA 3 for three-dimensional visualization of crystal, volumetric and morphology data*. Journal of Applied Crystallography, 2011. **44** 1272-1276.
203. H.J. Monkhorst and J.D. Pack, *Special points for Brillouin-zone integrations*. Physical Review B, 1976. **13** 5188-5192.
204. E. Ruckenstein and D.B. Dadyburjor, *Sintering and Redispersion in Supported Metal Catalysts*. Reviews in Chemical Engineering, 1983. **1** 251-356.
205. M.J. Walsh, et al., *On the effect of atomic structure on the activity and deactivation of catalytic gold nanoparticles* ChemCatChem, 2012. **Accepted**.
206. V.G. Gryaznov, et al., *Pentagonal symmetry and disclinations in small particles*. Crystal Research and Technology, 1999. **34** 1091-1119.
207. L.D. Marks, P.M. Ajayan, and J. Dundurs, *Quasi-melting of small particles*. Ultramicroscopy, 1986. **20** 77-82.
208. R. de Wit, ed. *Fundamental Aspects of Disclination Theory* ed. J.A. Simmons, R. de Wit, and R. Bullough. Vol. 1. 1969, NBS Spec. Publ. 317. 677-680.
209. E. Testa, et al. *The composition analysis of supported nanocatalysts using aberration corrected transmission electron microscopy: nanostructures of gold supported on nano-ceria (Au/CeO₂) and gold-palladium supported on nano-ceria (Au-Pd/CeO₂)*. in *Microscience*. 2010: Royal Microscopical Society.
210. S.J. Haigh, et al., *Imaging the Active Surfaces of Cerium Dioxide Nanoparticles*. ChemPhysChem, 2011. **12** 2397-2399.

211. P.A. Stadelmann, *EMS - a software package for electron diffraction analysis and HREM image simulation in materials science*. Ultramicroscopy, 1987. **21** 131-145.
212. J.M. LeBeau, et al., *Quantitative Atomic Resolution Scanning Transmission Electron Microscopy*. Physical Review Letters, 2008. **100** 206101.
213. M. Yan, et al., *Atomistic studies of energies and structures of (hk0) surfaces in NiO*. Philosophical Magazine A, 1995. **72** 121-138.
214. P.L. Gai and K. Kourtakis, *Solid-State Defect Mechanism in Vanadyl Pyrophosphate Catalysts: Implications for Selective Oxidation*. Science, 1995. **267** 661-663.